Crystallography Reports, Vol. 48, No. 1, 2003, pp. 1–7. Translated from Kristallografiya, Vol. 48, No. 1, 2003, pp. 7–13.

CRYSTAL CHEMISTRY

Evaluation of the Parameters of Cation Distribution in $Y_3A_{5-z}B_zO_{12}$ Solid Solutions

O. Yu. Goncharov

Physicotechnical Institute, Ural Division, Russian Academy of Sciences, ul. Kirova 132, Izhevsk, 426000 Russia

e-mail: olaf@nm.ru

Received January 19, 2000; in final form, April 25, 2002

Abstract—Crystal chemical models are proposed for describing the regularities in the distributions of ions and point defects in solid solutions of yttrium aluminum, yttrium gallium, and yttrium iron garnets. The concentration dependences of the distributions of ions and point defects in solid solutions are evaluated in terms of multidimensional nonlinear optimization. © *2003 MAIK "Nauka/Interperiodica".*

INTRODUCTION

Rare-earth garnets—aluminates, gallates, and ferrites—are widely used as laser crystals, substrates for growing epitaxial films, and magnetic and magnetooptical materials. The physicochemical properties of garnets are usually controlled by varying their composition with the aim of preparing isomorphous solid solutions [1–4] and by choosing the appropriate conditions of synthesis and subsequent treatment of the materials in such a way as to provide the formation of specific point defects and crystalline ordering or, in other words, to ensure a particular distribution of ions and defects over crystallographically nonequivalent positions in the garnet structure. The garnet unit cell (space group *Ia*3*d*) contains eight formula units $\{C_3\}[A_2](D_3)O_{12}$; i.e., the isomorphous substitution and defect formation can occur in both anionic and cationic sublattices, namely, in the dodecahedral {*C*}, octahedral [*A*], and tetrahedral (*D*) sublattices.

In isomorphous solid solutions of rare-earth aluminates, gallates, and garnet-type ferrites, the distribution of ions over the sublattices has been examined by Mössbauer spectroscopy, X-ray diffraction, neutron diffractometry, and low-temperature magnetic techniques [5–15]. Reasoning from an analysis of the experimental data obtained, a number of thermodynamic models of cation distribution over octahedral and tetrahedral positions of the garnet structure were proposed earlier in [16–19]. Apart from the aforementioned methods, defect structures of garnets have been investigated using quasi-chemical methods based on the dependence of the electrical conductivity and other physicochemical properties of crystals on the oxygen partial pressure [20–39]. Donnerberg and Catlow [40] estimated the energies of formation of point defects in yttrium iron garnet (YIG) and drew some inferences regarding the most probable reactions of defect formation. It should be noted that the coexistence of different-type defects in garnets makes the interpretation of experimental data more difficult, as is the case with other multicomponent and multisublattice crystals. In order to elucidate the origin and mechanism of crystalline ordering, it is necessary to know not only the location of ions and defects of each type but also their concentrations. This information can be obtained using only a combination of different experimental techniques, which frequently offer contradictory results.

The aim of the present work was to evaluate the concentration dependences of the distributions of ions and point defects in $Y_3A_{5-z}B_zO_{12}$ quasi-binary solid solutions, where *A* and B^{3+} are Al, Ga, or Fe. For this purpose, the crystal chemical models, which allow for the presence of defects and crystalline ordering in $Y_3A_{5-z}B_zO_{12}$ solid solutions, were constructed on the basis of the available experimental data. The parameters of the crystal chemical models were calculated by the nonlinear optimization technique.

CRYSTAL CHEMICAL MODELS

Let us consider some regularities in the distribution of ions and point defects in $Y_3Fe_{5-z}Al_zO_{12}$, $Y_3Fe_{5-z}Ga_zO_{12}$, and $Y_3Ga_{5-z}Al_zO_{12}$ (z = 0–5) solid solutions. It is well known that Fe^{3+}, Ga^{3+}, and Al^{3+} ions in the garnet structure occupy positions of two sorts, namely, the octahedral [*A*] and tetrahedral (*D*) positions [5–16, 18]. In the crystal structure, the sort of positions preferably occupied by particular ions is determined primarily by the size factor, i.e., the ionic radius. Earlier [5–12], it was demonstrated that, in $Y_3Fe_{5-z}Al_zO_{12}$ and $Y_3Fe_{5-z}Ga_zO_{12}$ garnets, the larger sized Fe^{3+} ions predominantly occupy the large-sized [*A*] tetrahedral positions, whereas Al^{3+} and Ga^{3+} ions with smaller sizes are located at the (*D*) octahedral positions. According to Marezio *et al.* [13] and Gautier *et al.* [14], the size principle does not hold in yttrium aluminum gallium gar-

nets of the general formula $Y_3Ga_{5-z}Al_zO_{12}$; in this case, gallium ions predominantly occupy tetrahedral positions, thus displacing aluminum ions to octahedral positions.

Although the defect structure of the solid solutions under consideration is poorly understood, it is clear that the solid solutions should inherit defects of their constituents, i.e., $Y_3Al_5O_{12}$, $Y_3Ga_5O_{12}$, and $Y_3Fe_5O_{12}$. As was noted above, the type and concentration of defects are governed by the synthesis conditions. For example, in rare-earth aluminum garnet single crystals grown from a melt, the stoichiometry was violated, because the rare-earth ions occupied up to 5% of the octahedral positions [20–23, 25]. It should be noted that cation defects of other types and anionic vacancies are characterized by a considerably smaller content [25, 26, 33]. For the most part, cation defects exhibit an impurity nature [24]. Until recently, the nature of intrinsic defects has remained unclear. These can be aluminum vacancies [26] or Al^{2+} and Al^{+} ions formed in place of Al^{3+} ions in the octahedral positions [41]. The latter assumption is confirmed by the fact that the color of yttrium aluminum garnet (YAG) crystals is affected by the dipole-type defect centers, which disappear upon annealing [27]. These centers can be generated by combining anion and cation defects into Al^{2+}–O^{-} or Al^{+}–anionic vacancy pairs. The formation of Al^{2+} and Al^{+} defects was also assumed in other aluminates, for example, in $YAlO_3$ [42]. A change in the synthesis conditions brings about transformations of the defect structure of aluminum garnets. Indeed, the content of rare-earth ions in the octahedral positions in YAG single crystals grown from a solution in the melt is substantially smaller than that in garnets grown from the melt [23].

The defect structure of rare-earth gallium garnets is also governed by the synthesis conditions. In gallium garnet single crystals grown from a melt, the rare-earth ions occupy up to 5% of the octahedral positions [21–23, 25, 29]. This is associated with the deviation of the congruently melting composition from the stoichiometric composition (toward an excess of the rare-earth element). As regards the gallium garnet single crystals grown from a solution in the melt and the polycrystals prepared by sintering of oxides (or other readily decomposing compounds), they contain no rare-earth ions in the octahedral positions [7, 15, 23]. However, a partial evaporation of gallium oxide in the course of synthesis can lead to in the formation of anionic and gallium vacancies [28, 30], which are predominantly located at the octahedral positions [31, 41]. Therefore, in order to decrease the vacancy concentration, the synthesis, as a rule, is performed at an elevated pressure and in an atmosphere enriched with oxygen.

The type and concentration of defects formed in rare-earth garnet-type ferrites also depend on the oxygen partial pressure [32–36]. However, anionic vacancies and Fe^{2+} ions formed upon a change in the charge of a number of Fe^{3+} ions in the octahedral positions are observed in the structure even after annealing of YIG in an oxygen atmosphere [43]. With a decrease in the oxygen pressure ($P_{O_2} < 10^{3.7}$ Pa [36]), the formation of anionic vacancies is partly compensated for by the transfer of a number of iron ions to interstices. The experimental results [21] and theoretical data [40] obtained a few years ago showed that rare-earth ions in garnet-type ferrites can occupy octahedral positions. More recently, this assumption was confirmed in [37–39]. In particular, it was proved that the concentration of defects of the aforementioned types depends on the synthesis conditions. The content of rare-earth ions in octahedral positions in garnet ferrite single crystals grown from a melt is higher than that in both the crystals grown from a solution in the melt and the samples synthesized by sintering of oxides.

From the above review of the data available in the literature, it follows that yttrium aluminum, yttrium gallium (YGG), and yttrium iron garnets are characterized by stoichiometry violation due to a partial filling of octahedral positions with rare-earth ions. Moreover, the formation of anionic vacancies in YGG and YIG is accompanied by the appearance of gallium vacancies and [Fe^{2+}] ions, respectively. The content of intrinsic defects in YAG, as a rule, is insignificant. Since the garnet solid solutions inherit defects of the aforementioned types and the ions are distributed over the sublattices, the crystal chemical models of these solutions can be represented as follows:

$$\{Y_3\}[Fe^{3+}_{2-x-n-\lambda}Fe^{2+}_{\lambda}Y_nAl_x](Fe_{3-y}Al_y)O_{12-\delta}, \quad \delta = 0.5\lambda \tag{1}$$

for yttrium aluminum ferrites,

$$\{Y_3\}[Fe^{3+}_{2-x-n-\lambda}Fe^{2+}_{\lambda}Y_nGa_{x-\beta}\square^{Ga}_{\beta}](Fe_{3-y}Ga_y)O_{12-\delta}, \quad \delta = 0.5\lambda + 1.5\beta \tag{2}$$

for yttrium gallium ferrites, and

$$\{Y_3\}[Ga^{3+}_{2-x-n-\lambda}\square^{Ga}_{\lambda}Y_nAl_x](Ga_{3-y}Al_y)O_{12-\delta}, \quad \delta = 1.5\lambda \tag{3}$$

for yttrium aluminum gallates.

The crystal chemical formulas (1)–(3) for the $Y_3A_{5-z}B_zO_{12}$ quasi-binary solid solutions formed by the $Y_3A_5O_{12}$ and $Y_3B_5O_{12}$ components can be written in the general form

$$Y_3[A_{2-x-n-\lambda-\beta}B_{x-\beta}Y_nA^d_{\lambda}B^d_{\beta}](A_{3-y}B_y)O_{12-\delta}, \tag{4}$$

where A^d and B^d stand for the defects in the positions of the corresponding ions and $z = x + y$ is the content of the $Y_3B_5O_{12}$ component in the solid solution.

COMPUTATIONAL TECHNIQUE

The unit cell parameter a is a sensitive characteristic that responds to the presence of point defects in the crystal and to a change in the distribution of ions and defects over crystallographically nonequivalent positions. For example, the concentration of vacancies in metals can be determined from the temperature dependence of the parameter a [44]. In [41, 43, 45], the content of point defects in garnets was estimated using a procedure based on a comparison of the experimental unit cell parameter a_{exp} with the parameter calculated from the analytical relationship [46]

$$a = b_1 + b_2 r_c + b_3 r_a + b_4 r_d + b_5 r_c r_a + b_6 r_c r_d, \quad (\text{Å}) \quad (5)$$

where $b_1 = 7.02954$; $b_2 = 3.31277$; $b_3 = 2.49398$; $b_4 = 3.34124$; $b_5 = -0.87758$; $b_6 = -1.38777$; and r_c, r_a, and r_d are the weighted mean effective ionic radii of the cations [47] occupying the $\{C\}$, $[A]$, and (D) positions, respectively. If g_j is the fraction of ions (or vacancies) of the jth sort with the radius r_j in the ith crystallographic position, we have $r_i = \sum_j g_j r_j$.

It was assumed that the deviation of the parameter a_{exp} from the parameter a calculated using relationship (5) for the defect-free composition is determined by the type and concentration of defects in the garnet. In [41, 43, 45], the authors substituted the experimental values a_{exp} into relationship (5) and evaluated the contents g_j of defects of the predominant types in a number of garnets.

For solid solutions, the concentration parameters x, y, n, λ, and β of the crystal chemical model (4) cannot be evaluated merely from relationship (5). Therefore, it is necessary to use additional conditions relating the variables. One of these conditions is associated with the experimentally determined distribution parameter, which relates the quantities x and y in the solid solutions (4). It is conventional to express this parameter through the fraction of tetrahedral positions occupied by one of the cations, that is,

$$f_t = y/z. \quad (6)$$

It should be noted that one of the quantities (y or x) is determined experimentally [5–8, 11, 13–16], whereas the second quantity is calculated from the relationship $z = x + y$. In this case, the presence of defects is disregarded. As a result, the fraction f_t defined by formula (6) slightly differs from the exact fraction by a value depending on the defect concentration.

As a first approximation, the concentrations of $[Y^{3+}]$, $[A^d]$, and $[B^d]$ defects in the solid solutions can be evaluated by assuming their linear dependence on the content z of the $Y_3B_5O_{12}$ component in the solid solution (4), that is,

$$n_O = n_A + k_1 z, \quad \lambda_O = \lambda_A + k_2(5 - z), \quad \beta_O = \beta_A + k_3 z. \quad (7)$$

The coefficients of Eqs. (7) can be calculated, for example, from the defect concentrations in the solid solution components, i.e., from n_A and λ_A ($\beta_A = 0$) for $Y_3A_5O_{12}$ and from n_B and β_B ($\lambda_B = 0$) for $Y_3B_5O_{12}$.

In order to refine the approximate parameters obtained from Eqs. (6) and (7) for the crystal chemical model (4), it is expedient to use nonlinear optimization methods. First and foremost, let us introduce physically justified limitations on the range of permissible values of the variables n, λ, β, f_t, and a. We assume that the parameters n, λ, and β for the solid solution cannot be twice as large as the maximum parameters for the solution components, that is,

$$0 \le n \le 2n_{max}, \quad 0 \le \lambda \le 2\lambda_{max}, \quad 0 \le \beta \le 2\beta_{max}. \quad (8)$$

Furthermore, it is assumed that the deviations Δ_a and Δf_t of the parameters a and f_t [calculated with the use of relationships (5) and (6)] from the experimental values do not exceed the corresponding experimental errors Δa_{err} and Δf_{t_err}, that is,

$$\Delta a \le \Delta a_{err}, \quad \Delta f_t \le \Delta f_{t\_err}. \quad (9)$$

It is desirable to obtain the minimum sum of the deviations Δa and Δf_t and the deviations Δn, $\Delta\lambda$, and $\Delta\beta$ of the exact concentration parameters n, λ, β from their approximate values determined from relationships (7). In order for this condition to be satisfied, an additional target function relating the aforementioned parameters is introduced in the following form:

$$S = (\Delta a/\Delta a_{err})^2 + (\Delta f_t/\Delta_{t\_err})^2 + (\Delta n/n_O)^2 + (\Delta\lambda/\lambda_O)^2 + (\Delta\beta/\beta_O)^2. \quad (10)$$

The optimum set of the parameters n, λ, β, f_t, and a corresponds to a minimum of function (10). This minimum in the range satisfying conditions (8) and (9) was sought by numerical (gradient) methods of multidimensional nonlinear optimization [48].

RESULTS

The $Y_3Fe_{5-z}Al_zO_{12}$ system. Crystalline ordering in $Y_3Fe_{5-z}Al_zO_{12}$ garnets was determined using the experimental data on the parameters a_{exp} and f_t taken from [5, 6] for the samples synthesized by sintering of oxides. The coefficients in the linear equations (7) were determined from the defect concentrations in the solid solution components. For $\{Y_3\}[Fe^{3+}_{2-n-\lambda}Fe^{2+}_{\lambda}Y_n](Fe_3)O_{12-\delta}$ polycrystals, the concentration of yttrium ions in the octahedral positions $n = 0.003$ per formula unit was taken from [37], whereas the concentration of $[Fe^{2+}]$ ions $\lambda = 0.016$ per formula unit was calculated from relationship (5). For $\{Y_3\}[Al_{2-n}Y_n](Al_3)O_{12}$, the concentration of yttrium ions in the octahedral positions was calculated [see relationship (5)] to be $n = 0.035$ per formula unit, which is in agreement with the experimental data obtained in [20, 25].

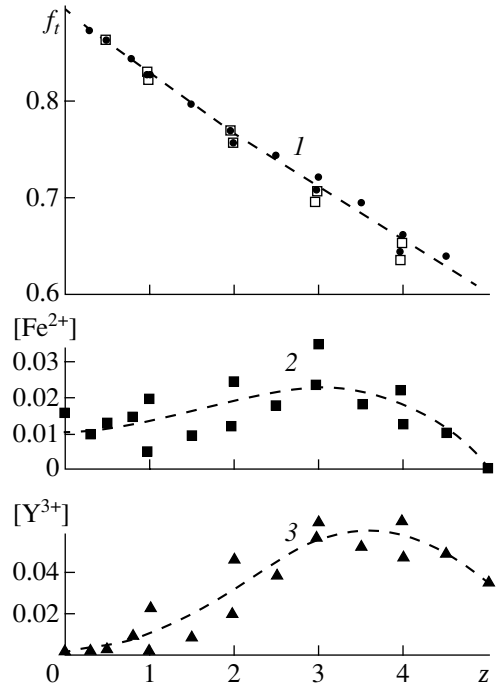

Fig. 1. Concentration dependences of the parameter f_t (closed circles) and the [Fe^{2+}] (closed squares) and [Y^{3+}] (closed triangles) concentrations calculated using formula (10) for $Y_3Fe_{5-z}Al_zO_{12}$ solid solutions. Open squares are the data taken from [5, 6]. Curve *1* shows the dependence evaluated by formula (11). Curves *2* and *3* represent the approximations of the calculated quantities.

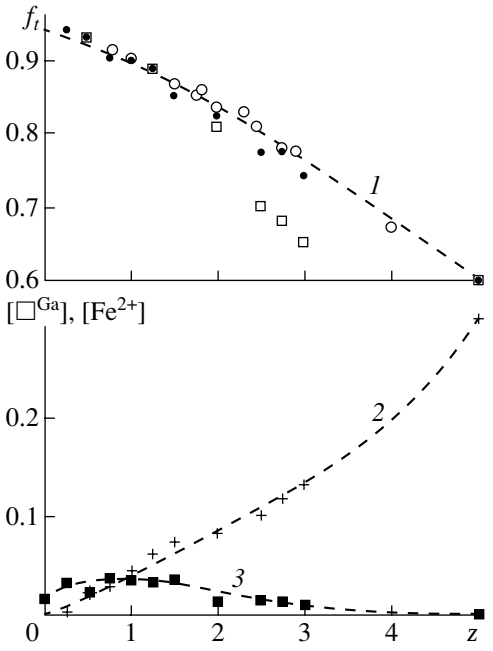

Fig. 2. Concentration dependences of the parameter f_t (closed circles) and the [$\square^{Ga}$] (crosses) and [Fe^{2+}] (closed squares) concentrations calculated using formula (10) for $Y_3Fe_{5-z}Ga_zO_{12}$ solid solutions (polycrystals). Open squares and open circles are the data taken from [7] and [8], respectively. Curve *1* shows the dependence evaluated by formula (11). Curves *2* and *3* represent the approximations of the calculated quantities.

Figure 1 depicts the concentration dependences of the parameters n, λ, and f_t calculated for yttrium aluminum ferrites [model (1)] at minimum values of the target function (10). It can be seen from this figure that the calculated and experimental [5, 6] parameters f_t are close to each other. These parameters correspond to the equilibrium attained at the temperature $T_e = 1200$ K and can be described (Fig. 1, curve *1*) by the relationship

$$f_t = \frac{3C - (C-1)y}{2 + 3C - (C-1)}. \qquad (11)$$

The equilibrium constant $C = (2-x)y/(3-y)x$ of the quasi-chemical cation-exchange reaction $(3-y)(A^{3+}) + x[B^{3+}] = (2-x)[A^{3+}] + y(B^{3+})$ for model (4) depends on the solid solution composition and was calculated from the equation [17]

$$kT_e \ln C = E_{\text{eff}} = E^0 - (x-y)(E^0 - E^5), \qquad (12)$$

where k is the Boltzmann constant, E_{eff} is the effective stabilization energy, and E^0 and E^5 are the stabilization energies at $z = 0$ ($Y_3A_5O_{12}$) and $z = 5$ ($Y_3B_5O_{12}$), respectively. According to [16], the stabilization energies for $Y_3Fe_{5-z}Al_zO_{12}$ are as follows: $E^0 = 0.178$ eV and $E^5 = 0.132$ eV.

In the concentration range $z = 3$–4, the calculated and experimental values of f_t somewhat differ from each other and the concentrations of [Fe^{2+}] and [Y^{3+}] defects reach a maximum (Fig. 1, curves *2*, *3*). It should be noted that YAG is sintered at higher temperatures as compared to those of YIG. Therefore, an increase in the sintering temperature, which is necessary for increasing the aluminum content in the solid solution, should lead not only to an increase in the concentration of [Fe^{2+}] defects but also to a partial evaporation of iron and filling of vacant octahedral positions with yttrium ions. However, the defect content decreases with a further decrease in the concentration of iron ions as the aluminum content in the solid solution increases (at $z > 4$).

The $Y_3Fe_{5-z}Ga_zO_{12}$ system. Crystalline ordering in the $Y_3Fe_{5-z}Ga_zO_{12}$ garnets was determined using the experimental data on the parameters a_{exp} and f_t for the polycrystalline samples synthesized by sintering of oxides [7, 8] and the single crystals grown from a solution in the melt [11]. According to [8, 16], the parameters f_t obtained in [7] from the data on the magnetization of solid solutions are characterized by a systematic error at $z > 2$. Therefore, at $z > 2$, the range of possible deviations of the parameter f_t was extended by a factor of 3; i.e., the boundary conditions (9) were changed. As for the aluminum ferrites, the defect concentrations in the extreme components of the solid solution were calculated from relationship (5). Then, these concentra-

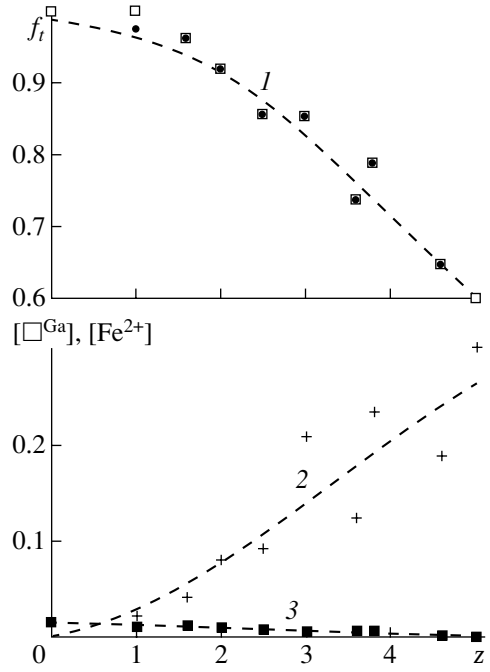

Fig. 3. Concentration dependences of the parameter f_t (closed circles) and the $[\square^{Ga}]$ (crosses) and $[Fe^{2+}]$ (closed squares) concentrations calculated using formula (10) for $Y_3Fe_{5-z}Ga_zO_{12}$ solid solutions (single crystals). Open squares are the data taken from [11]. Curve *1* shows the dependence evaluated by formula (11). Curves *2* and *3* represent the approximations of the calculated quantities.

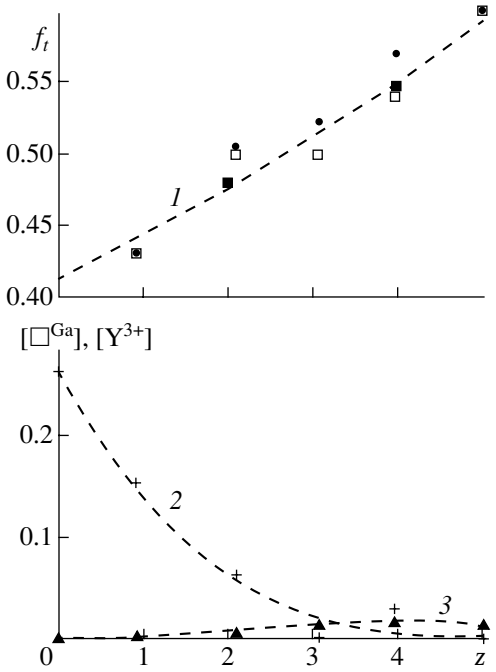

Fig. 4. Concentration dependences of the parameter f_t (closed circles) and the $[\square^{Ga}]$ (crosses) and $[Y^{3+}]$ (closed triangles) concentrations calculated using formula (10) for $Y_3Ga_{5-z}Al_zO_{12}$ solid solutions. Open squares and closed squares are the data taken from [13] and [14], respectively. Curve *1* shows the dependence evaluated by formula (11). Curves *2* and *3* represent the approximations of the calculated quantities.

tions were used for calculating the coefficients of the linear equations (7). The thermodynamic evaluation of f_t was performed according to Eqs. (11) and (12) at the stabilization energies $E^0 = 0.272$ eV and $E^5 = 0.230$ eV [16].

The calculated concentration dependences of the parameters λ, β, and f_t for yttrium gallium ferrite polycrystals [model (2)] are plotted in Fig. 2. The calculated values of f_t agree with the experimental data obtained in [8] and can be described by Eq. (11) for the equilibrium corresponding to the temperature $T_e = 1350$ K (Fig. 2, curve *1*). At $z > 2$, the parameters f_t given in [7] are somewhat less than the calculated parameters, which confirms the inference drawn in [8, 16] about the insufficient accuracy of the data presented in [7]. The calculated concentration dependence of the parameter f_t for the single crystals corresponds to a thermodynamically equilibrium state at the temperature $T_e = 823$ K (Fig. 3, curve *1*). It is evident that the low cooling rate (5 K/h) of the single crystals [11] favored the attainment of an equilibrium distribution at lower temperatures than those for the polycrystals [7, 8].

As follows from our calculations, the $Y_3Fe_{5-z}Ga_zO_{12}$ solid solutions contain $[Y^{3+}]$ defects. However, their concentration is very low (<0.005 per formula unit) and the corresponding data are not presented in Figs. 2 and 3. An increase in the gallium content results in an increase in the concentration of $[\square^{Ga}]$ vacancies and a decrease in the concentration of $[Fe^{2+}]$ ions both in the polycrystals (Fig. 2, curves *2*, *3*) and the single crystals (Fig. 3, curves *2*, *3*). At the same composition of the gas atmosphere, the $[Fe^{2+}]$ content in the garnets is predominantly determined by the temperature of the gas–solid high-temperature equilibrium. The quenching of the polycrystals [7, 8] made it possible to fix the equilibrium attained at temperatures higher than the temperatures of reaching the equilibrium in the single crystals [11]; therefore, the $[Fe^{2+}]$ concentration in the polycrystals is higher than that in the single crystals. An increase in the temperature and time of high-temperature treatment favors the transfer of gallium from the garnet to the gas phase, i.e., brings about the formation of $[\square^{Ga}]$ vacancies. Note that the quenching temperature is higher for the polycrystals, whereas the heat treatment time is longer for the single crystals. Apparently, this is the reason why the concentration dependence of the gallium vacancy content in the polycrystals (Fig. 2, curve *2*) is similar to that in the single crystals (Fig. 3, curve *2*).

The $Y_3Ga_{5-z}Al_zO_{12}$ system. The distributions of cations and defects in $Y_3Ga_{5-z}Al_zO_{12}$ solid solutions were calculated from the experimental values of a_{exp} and f_t for the single-crystal samples grown from a solution in the PbO melt (with B_2O_3) [13]. The concentra-

tions of [$\square^{Ga}$] vacancies and [Y^{3+}] defects in the YGG and YAG components of the solid solution were evaluated from relationship (5). These concentrations were used to calculate the coefficients of the linear equations (7) determining the initial approximations. As is known [49], lead ions can enter into the composition of garnets grown from PbO melts (with B_2O_3). Our calculations were performed under the assumption that the concentration of {Pb^{2+}} ions is equal to the concentration of [Pb^{4+}] ions and does not exceed the concentration of [Y^{3+}] defects.

The concentration dependences of the parameters f_t and λ determined at the minimum values of function (10) are represented in Fig. 4. The calculated values of f_t are in agreement with the experimental parameters obtained in [13, 14] and correspond to those evaluated from Eqs. (11) and (12) for the thermodynamically equilibrium state at the temperature T_e = 1300 K (Fig. 4, curve *1*). The results of calculations indicate that the Al^{3+} ions in the yttrium aluminum gallates predominantly occupy octahedral positions in the garnet and displace larger sized Ga^{3+} ions from these positions. This confirms the experimental findings [13, 14] that the size correlation is violated in the ion distribution in the $Y_3Ga_{5-z}Al_zO_{12}$ garnets. The calculated data on the defect content demonstrate that, as the fraction of aluminum in the solid solution increases, the [Y^{3+}] concentration increases almost linearly (Fig. 4, curve *2*) and the [$\square^{Ga}$] concentration decreases according to a nearly parabolic law (Fig. 4, curve *3*).

CONCLUSIONS

Thus, we constructed the crystal chemical models describing the regularities of the distributions of ions and point defects in $Y_3Fe_{5-z}Al_zO_{12}$, $Y_3Fe_{5-z}Ga_zO_{12}$, and $Y_3Ga_{5-z}Al_zO_{12}$ quasi-binary solid solutions.

A technique for quantitative evaluation of the crystalline ordering in solid solutions was proposed. This technique is based on the determination of the minimum of function (10), which is the sum of the relative deviations of the quantities a, f_t, n, λ, and β (calculated or experimental) from their exact values.

The concentration dependences of the distributions of ions and defects were calculated for solid solutions in the $Y_3Fe_{5-z}Al_zO_{12}$, $Y_3Fe_{5-z}Ga_zO_{12}$, and $Y_3Ga_{5-z}Al_zO_{12}$ systems. Moreover, the thermodynamic characteristics of the cation distribution were estimated for these systems.

The computational technique proposed in this work can be useful for evaluating the distributions of ions and defects (or for fitting the experimental data obtained by different methods) not only in garnets but also in other compounds.

REFERENCES

1. S. Geller, H. J. Williams, G. P. Espinosa, and R. C. Sherwood, Bell Syst. Tech. J. **43** (2), 565 (1964).
2. R. K. Watts and W. C. Holton, J. Appl. Phys. **45** (2), 873 (1974).
3. P. Hansen, P. Röschmann, and W. Tolksdorf, J. Appl. Phys. **45**, 2728 (1974).
4. T. Okuda, H. Ohsato, S. Nishida, and T. Makita, *Ferrites: Proceedings of the Sixth International Conference on Ferrites (ICF 6), Tokyo and Kyoto, Japan, 1992*, p. 1554.
5. E. R. Czerlinsky, Phys. Status Solidi **41**, 333 (1970).
6. P. Fisher, W. Halg, P. Roggwiller, and E. R. Czerlinsky, Solid State Commun. **16** (8), 987 (1975).
7. S. Geller, J. A. Cape, G. P. Espinosa, and D. H. Leslie, Phys. Rev. **148**, 522 (1966).
8. E. R. Czerlinsky, Phys. Status Solidi **34**, 483 (1969).
9. E. V. Zharikov, V. V. Laptev, A. A. Maĭer, and V. V. Osiko, Izv. Akad. Nauk SSSR, Neorg. Mater. **20** (6), 984 (1984).
10. R. Nitsche, G. Tippelt, and G. Amthauer, J. Mater. Sci. **29**, 2903 (1994).
11. A. Nakatsuka, A. Yoshiasa, and S. Takeno, Acta Crystallogr., Sect. B: Struct. Sci. **51**, 737 (1995).
12. A. S. Kamzin and Yu. N. Mal'tsev, Fiz. Tverd. Tela (St. Petersburg) **39** (7), 1248 (1997) [Phys. Solid State **39**, 1108 (1997)].
13. M. Marezio, J. P. Remeika, and P. D. Dernier, Acta Crystallogr., Sect. B: Struct. Crystallogr. Cryst. Chem. **24**, 1670 (1968).
14. N. Gautier, D. Massiot, I. Farnan, and J. P. Coutures, J. Chem. Phys. **92** (10), 1843 (1995).
15. N. Gautier, M. Gervais, C. Landron, *et al.*, Phys. Status Solidi A **165** (2), 329 (1998).
16. C. Borghese, J. Phys. Chem. Solids **28**, 2225 (1967).
17. W. van Erk, J. Cryst. Growth **46**, 539 (1979).
18. P. Röschman, J. Phys. Chem. Solids **41** (6), 569 (1980).
19. G. V. Bezrukov and V. M. Talanov, Zh. Fiz. Khim. **59** (1), 27 (1985).
20. Yu. K. Voron'ko and A. A. Sobol', Tr. Fiz. Inst. Akad. Nauk SSSR **98**, 41 (1977).
21. J. Dong and Kunquan Lu, Phys. Rev. B **43** (11), 8808 (1991).
22. Yu. V. Zorenko, M. V. Pashkovskiĭ, M. M. Batenchuk, *et al.*, Opt. Spektrosk. **80** (5), 776 (1996) [Opt. Spectrosc. **80**, 698 (1996)].
23. A. Lupei, C. Stoicescu, and V. Lupei, J. Cryst. Growth **177** (3/4), 207 (1997).
24. S. R. Rotman, H. L. Tandon, and H. L. Tuller, J. Appl. Phys. **57** (6), 1951 (1985).
25. Kh. S. Bagdasarov, E. A. Fedorov, V. I. Zhekov, *et al.*, Tr. Inst. Obshch. Fiz. Akad. Nauk SSSR **19**, 112 (1989).
26. Kh. S. Bagdasarov, A. I. Munchaev, and M. V. Remizov, Kristallografiya **36** (2), 463 (1991) [Sov. Phys. Crystallogr. **36**, 253 (1991)].
27. Kh. S. Bagdasarov, N. B. Bolotina, and V. I. Kalinin, Kristallografiya **36** (3), 715 (1991) [Sov. Phys. Crystallogr. **36**, 398 (1991)].

28. C. D. Brandle, D. C. Miller, and J. W. Nielsen, J. Cryst. Growth **12**, 195 (1972).
29. C. D. Brandle and R. L. Barns, J. Cryst. Growth **26**, 169 (1974).
30. G. M. Kuz'micheva, S. N. Kozlikin, E. V. Zharikov, *et al.*, Zh. Neorg. Khim. **33** (9), 2200 (1988).
31. Ya. O. Dovgiĭ, I. V. Kityk, A. O. Matkovskiĭ, *et al.*, Fiz. Tverd. Tela (St. Petersburg) **35** (2), 544 (1993) [Phys. Solid State **35**, 146 (1993)].
32. R. Metselaar and M. Hyberts, J. Solid State Chem. **22**, 309 (1977).
33. A. Ya. Neĭman, E. V. Tkachenko, and V. M. Zhukovskiĭ, Dokl. Akad. Nauk SSSR **240** (4), 876 (1978).
34. A. Ya. Neĭman, V. M. Zhukovskiĭ, I. P. Pazdnikov, *et al.*, in *Chemical Thermodynamics and Technology* (Nauka, Moscow, 1979), p. 145.
35. V. B. Fetisov, M. A. Dvinina, Yu. P. Vorob'ev, *et al.*, Izv. Akad. Nauk SSSR, Neorg. Mater. **19** (11), 1871 (1983).
36. G. V. Denisov, Author's Abstract of Candidate's Dissertation in Chemistry (Ural'skiĭ Gos. Univ., Sverdlovsk, 1986).
37. K. Wagner, H. Lütgemeier, W. Zinn, *et al.*, J. Magn. Magn. Mater. **140–144**, 2107 (1995).
38. P. Novak, J. Englich, H. Stepankova, *et al.*, Phys. Rev. Lett. **75** (3), 545 (1995).
39. M. S. Lataifeh and A.-F. D. Lehloof, Solid State Commun. **97** (9), 805 (1996).
40. H. Donnerberg and C. R. A. Catlow, J. Phys.: Condens. Matter **5** (18), 2947 (1993).
41. Yu. P. Vorob'ev and O. Yu. Goncharov, Neorg. Mater. **30** (12), 1576 (1994).
42. A. F. Konstantinova, G. N. Gorbenko, and L. A. Korostel', Kristallografiya **41** (2), 320 (1996) [Crystallogr. Rep. **41**, 302 (1996)].
43. Yu. P. Vorob'ev, Kristallografiya **34** (6), 1461 (1989) [Sov. Phys. Crystallogr. **34**, 876 (1989)].
44. I. I. Novikov, *Defects in Crystal Structure of Metals* (Metallurgiya, Moscow, 1975).
45. Yu. P. Vorob'ev, O. Yu. Goncharov, and V. B. Fetisov, Kristallografiya **45** (6), 1053 (2000) [Crystallogr. Rep. **45**, 971 (2000)].
46. B. Strocka, P. Holst, and W. Tolksdorf, Philips J. Res. **33** (3/4), 186 (1978).
47. R. D. Shannon and C. T. Prewitt, Acta Crystallogr., Sect. B: Struct. Crystallogr. Cryst. Chem. **25** (4), 925 (1969).
48. L. I. Turchak, *Principles of Numerical Methods* (Nauka, Moscow, 1987).
49. Duk Yong Choi and Su Jin Chung, J. Cryst. Growth **191**, 754 (1998).

Translated by O. Borovik-Romanova

Crystallography Reports, Vol. 48, No. 1, 2003, pp. 106–111. Translated from Kristallografiya, Vol. 48, No. 1, 2003, pp. 111–116.

LATTICE DYNAMICS AND PHASE TRANSITIONS

Phase Transformations in Titanium Oxycarbide $TiC_{0.545}O_{0.08}$

M. Yu. Tashmetov*, V. T. Em*, B. N. Savenko, and G. Batdemberel*****

** Institute of Nuclear Physics, Academy of Sciences of Uzbekistan, Tashkent, 702132 Uzbekistan*
e-mail: savenko@nfsun1.jinr.ru
*** Joint Institute for Nuclear Research, Dubna, Moscow oblast, 141980 Russia*
**** Institute of Physics and Technology, Mongolian Academy of Sciences, Ulan Bator, Mongolia*
Received February 17, 1999; in final form, April 18, 2002

Abstract—Phase transformations in titanium oxycarbide $TiC_{0.545}O_{0.08}$ have been studied by the methods of neutron diffraction and X-ray structure analysis. It was established that the ordered cubic structure δ' (sp. gr. *Fd*3*m*) of the oxycarbide sample is the low-temperature ordered phase existing up to 990 K. The order–disorder phase transition (990 K) results in the formation of an ordered trigonal structure (sp. gr. $R\bar{3}m$ or $P3_121$). The α-Ti-phase is separated at the temperature 1020 K. The order–disorder phase transition was found at T = 1040 K. © *2003 MAIK "Nauka/Interperiodica".*

INTRODUCTION

Ordering in interstitial phases occurs mainly because of the deformational interaction between the interstitial atoms [1]. It is also known that the interactions between the interstitial atoms in interstitial alloys determine, to a large extent, their crystal structure and properties [2]. Therefore, it is expedient to study the structure, phase transformations, and characteristics of phase transitions in the systems where the interstitial atoms belong to different groups of the Periodic Table. We studied titanium oxycarbide $TiC_{0.545}O_{0.08}$. The choice of the sample of this composition is explained by the fact that, up to now, the ordered structures were studied on titanium oxycarbides with a high oxygen content [3–5], although it is well known that a low content of the second metalloid strongly affects the structural characteristics of the compound [6] and the phase transformations in it [7]. Therefore, it is expedient to study ordering of interstitial atoms and the phase transformations in titanium oxycarbides with a low oxygen content and to compare the results of such study with the data obtained in nonstoichiometric titanium carbide $TiC_{0.63}$, whose ordered structures and phase transformations were studied in sufficient detail [8]. The study of ordered structures and phase transformations is also important for particles, because, in many instances, synthesis of titanium carbides takes place in the presence of oxygen, which can be hardly be removed (or, in some cases, cannot be removed) from nonstoichiometric titanium carbide. At the same time, it is also well known that oxygen influences many physical properties of carbides.

Thus, we decided to study the structure and phase transformations in titanium oxycarbide $TiC_{0.545}O_{0.08}$.

EXPERIMENTAL

A sample of titanium oxycarbide $TiC_{0.545}O_{0.08}$ was prepared by vacuum sintering. The starting components a PTVD-TS-1 titanium powder containing ~2 wt. % of oxygen and lamp black. A mixture of the starting materials the necessary proportion was briquetted and sintered for four hours under a pressure of 5×10^{-5} mm Hg at T = 1900 K. The additional grinding and briquetting were made after each two hours of annealing, and then the sample were selected for the X-ray phase analysis. The X-ray diffraction data from these samples showed how close was the sample to the equilibrium state. The titanium and carbon content in the samples were determined by the chemical method; the oxygen content was determined by the method of activation analysis [9]. The X-ray diffraction experiment was performed on a DRON-4 diffractometer (CuK_α-radiation). The point-by-point scanning was made with the exposure times of 30, 40, or 60 s at each point at a step of 0.01°, 0.02°, or 0.05°. Depending on the aim of the experiment, the angular ranges $2\theta_b$ were 100°–108°, 33°–43°, or 20°–130°. The neutron diffraction experiments were performed on a DN-500 diffractometer [10] and a high-resolution Fourier diffractometer (FDVR) [11]. A DN-500 diffractometer ($\Delta d/d$ ~ 1.6%) at a constant wavelength λ = 1.085 Å was equipped with a ten-detector ^{3}He-superpositional system of neutron recording. A monochromator was a copper single crystal (mosaicity β = 25′) with the reflecting (111) plane. The contribution of the neutrons of second-order reflection was ~1.5%. The effect/background ratio of the control nickel sample was $I_{111}/I_{back} \approx 22$. A powdered sample was placed into a cylindrical vanadium cell 6 mm in diameter with the 0.1-mm-thick and 80-mm-heig walls. The measurements were made at a scan step 0.1° and 0.2° over the angular ranges $2\theta_b$ = 10°–80° and $2\theta_b$ =

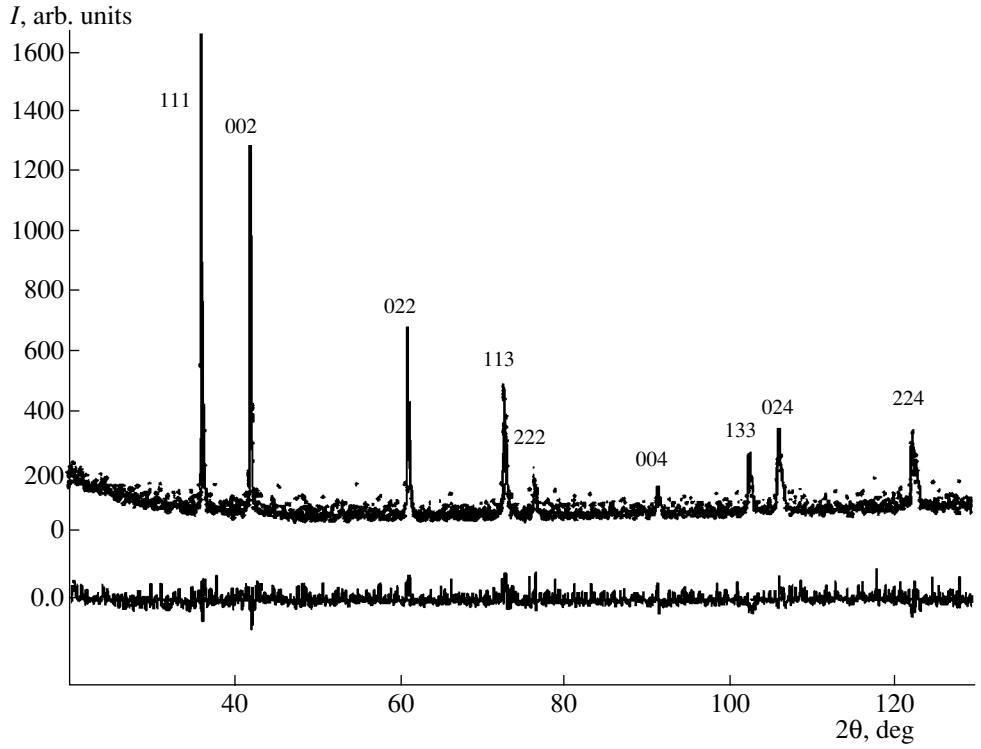

Fig. 1. X-ray diffraction pattern from the initial $TC_{0.545}O_{0.08}$ sample. Solid line and points show the calculated and experimental intensities of the diffraction peaks, respectively; the lower curve is the difference between the experimental and calculated data.

8°–70°. In a FDVR diffractometer, a sample was placed into a cylindrical cell 6 mm in diameter prepared from the TiZr alloy with a zero coherent-scattering length. In our calculations we used the coherent-scattering lengths of atoms taken from [12]. The d_{hkl} resolution of the FDVR diffractometer is defined by the rate of the interrupter rotation, which in our experiment was $\Delta d/d \sim 0.005$. The measurements were made at room temperature. The data were processed by the Rietveld method using the MRIA program [13] for the neutron diffraction data measured on a FDVR diffractometer and using the DDWS-3.2 program [14] for the neutron diffraction data measured on a DN-500 diffractometer and the X-ray diffraction data. Upon high-temperature annealing in evacuated and sealed ampoules in a Nabertherm furnace with a C19 + S19 programmed controller (maximum temperature 1670 K), the sample was quenched in water.

RESULTS AND DISCUSSION

The X-ray diffraction pattern (Fig. 1) of the initial sample had structural reflections corresponding to the face-centered cubic NaCl-type structure (a = 4.3158 Å). Like in [8], after sample annealing at 870 K (96 h), its X-ray diffraction pattern corresponded to the cubic structure (sp. gr. $Fm3m$), whereas the neutron diffraction pattern had some additional reflections (Fig. 2). The structure determination showed the formation of an ordered cubic structure (sp. gr. $Fd3m$) with a double unit-cell parameter in comparison with the initial one, $a_{\delta'} = 2a_\delta$ = 8.6371 Å. In this model of ordering, the metal atoms are located in the 32(e) position and the metalloid atoms are located in the octahedral interstitial positions 16(c) and 16(d). The atoms occupy mainly the 16(c) position, although not fully. The metal atoms are displaced from their ideal positions ($x_{\text{ideal}} = 0.250$) in the fcc metal lattice in the direction from the vacancies toward the metalloid atoms ($x_{\text{real}} = 0.246$). X-ray and neutron diffraction patterns measured from the samples annealed at evealed temperature (higher than 920 K) showed splitting of the (331) and (420) structural peaks on the X-ray diffraction pattern (indexed in the sp. gr. $Fm3m$) at the temperature 990 K (Fig. 3). The neutron diffraction pattern measured on a DN-500 [10] also showed the additional superstructural reflections (Fig. 4). The measurements on a high-resolution neutron diffractometer (FDVR) [11] showed splitting of the (311) and (331) structural reflections (indexed in the sp. gr. $Fm3m$) (Fig. 5). The (331) reflection is split into three peaks having different intensities, but the (002) and (004) reflections remained unsplit on both X-ray and neutron diffraction patterns. The interpretation of the spectra measured on the DRON-4, DN-500, and FDVR diffractometers showed the formation of the trigonal ordered structure. This structure can be described equally well within both the $P3_121$ and $R\bar{3}m$ space groups. In the sp. gr. $P3_121$ (the extinction condi-

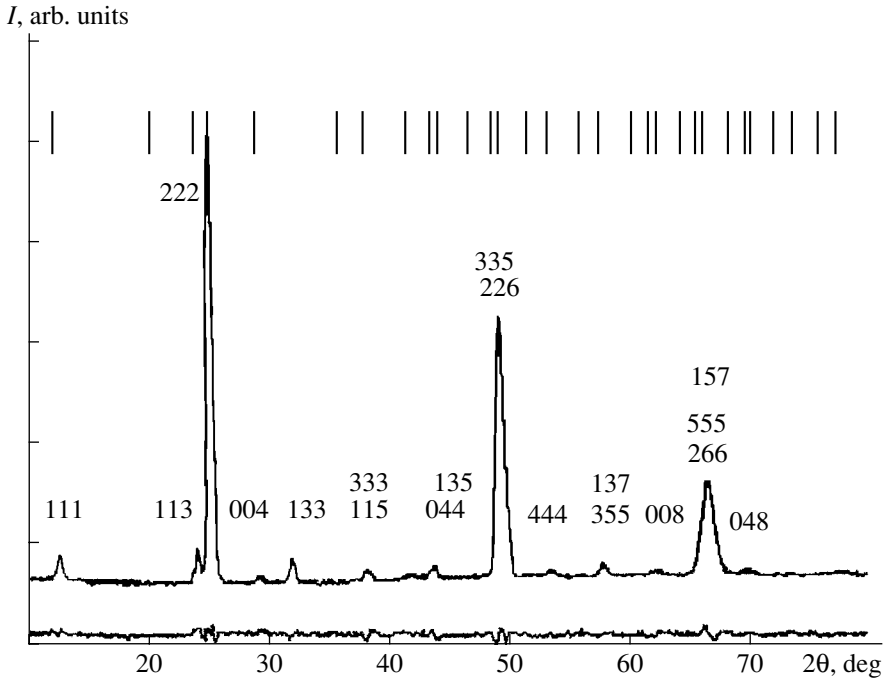

Fig. 2. X-ray diffraction pattern from the $TiC_{0.545}O_{0.08}$ sample annealed for 96 hours at 870 K and measured on a DN-500 diffractometer. Solid line shows the experimental intensities of diffraction peaks, the lower line shows the difference between the experimental and calculated data.

tion $l \neq 3n$ for the (00l reflections), the unit-cell parameters are $a \approx a_0/\sqrt{2} = 3.0604$ Å, $c \approx 2\sqrt{3}\,a_0 = 14.8628$ Å (a_0 is the unit-cell parameter of the initial structure). The metal atoms are located in the 6(c) position (0.6666, 0, 0.0861), the metalloid atoms occupy mainly the 3(b) (0.6666, 0, 0.8333) and 3(a) (0.6666, 0, 0.3333) interstitial positions. In the sp. gr. $R\bar{3}m$, the coordinates of the metal atoms are (0, 0, 0.2537), and of the metalloid atoms, (0, 0, 0) and (0, 0, 0.5). It is difficult to determine the space group of this ordered structure from powder neutron diffraction data from nonsoichiometric titanium oxycarbide.

With a further increase in temperature (from 990 K) at a step of 15 K, the X-ray diffraction pattern obtained at 1020 K (Fig. 6) showed two new reflections in addition to the split structural reflections. The neutron diffraction pattern also showed a new reflection with the interplanar distance $d/n = 2.2413$ Å, in addition to the superstructural reflections corresponding to the trigonal structure. The analysis of the X-ray and neutron diffraction patterns showed that the reflection with $d/n = 2.2413$ Å corresponds to the 101 reflection of the α-Ti phase (Fig. 6b) and the reflection with $d/n = 2.4256$ Å corresponds to the 002 reflection (CuK_β-radiation) (Fig. 6a).

Thus, a decomposition of nonstoichiometric titanium oxycarbide $TiC_{0.545}O_{0.08}$ into the trigonal phase and α-Ti phase is established at $T = 1020$ K. No splitting of the structural reflections was observed on the X-ray pattern at 1040 K, but the neutron diffraction pattern had structural reflections corresponding to the disordered NaCl-type cubic structure (sp. gr. $Fm3m$) and the α-Ti phase. This signifies that the phase transformations in titanium oxycarbide $TiC_{0.545}O_{0.08}$ and the transformations taking place in nonstoichiometric titanium carbide $TiC_{0.63}$ [8] occur not only at different transition temperatures but also proceed by different schemes. Earlier, the following scheme of the equilibrium phase transformations occurring in the nonstoichiometric tita-

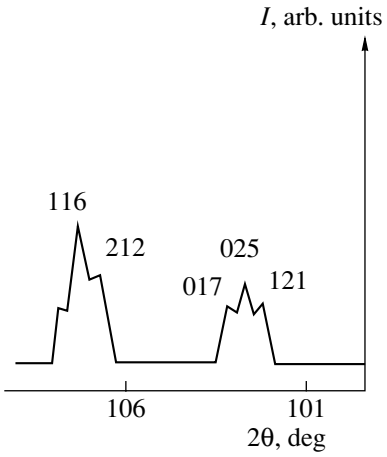

Fig. 3. Fragment of X-ray diffraction pattern from the sample annealed at 990 K (trigonal structure, sp. gr. $R\bar{3}m$; sp. gr. $P3_121$).

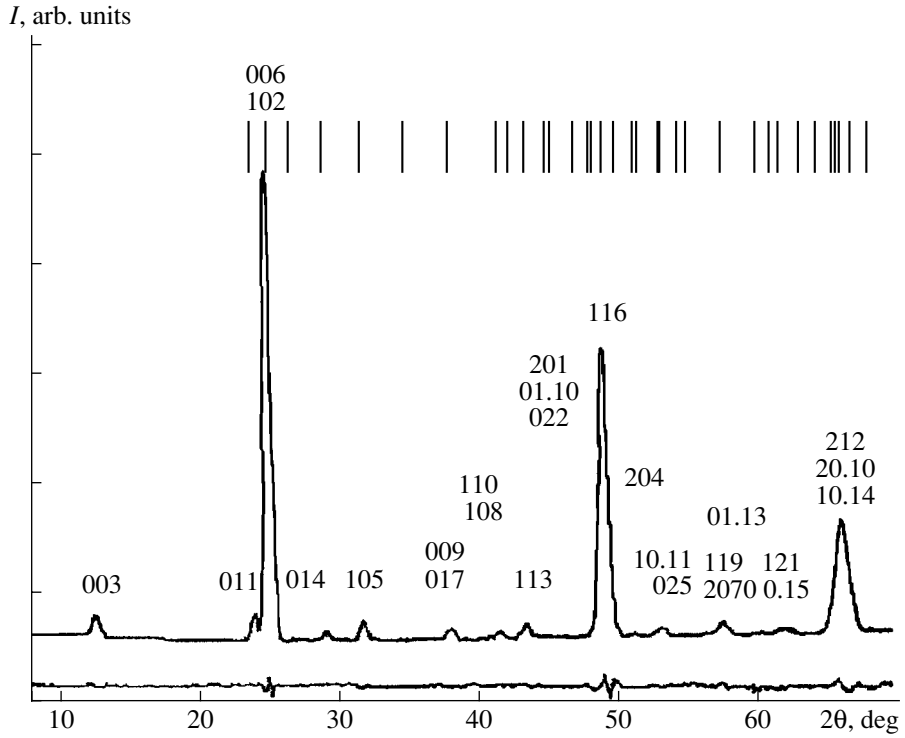

Fig. 4. Neutron diffraction pattern from trigonal ordered structure (sp. gr. $R\bar{3}m$; $P3_121$) measured on a DN-500 diffractometer. Solid line shows the experimental intensities of diffraction peaks, the lower line shows the difference between the experimental and calculated values.

nium carbide with the change in temperature was established from the X-ray and neutron diffraction data [8]:

$$\delta'' \text{ (sp. gr. } R\bar{3}m\text{)}$$

$$\xrightarrow{T_1 = 1053\ \mathrm{K}} \delta' \text{ (sp. gr. } Fd3m\text{)} \xrightarrow{T_2 = 1068\ \mathrm{K}} \delta \text{ (sp. gr. } Fm3m\text{).}$$

However, the ordered cubic structure δ' can be formed as a metastable phase at the temperature $T <$ 1053 K [8]. Both ordered structures are formed upon the replacement of some titanium atoms by tantalum, niobium [15], or molybdenum [16] atoms. The temperature of the order–order phase transition (δ'' ⟶ δ') was the same (1053 K) for all the samples studied in [15, 16], but the temperature of the order–disorder phase transition (δ' ⟶ δ) increased at higher contents of the second metal [17]. However, it is established that the phase-transition temperature (δ' ⟶ δ) is the same as in titanium carbide, which may be explained by the small amount of molybdenum in the complex titanium carbide [16]. X-ray and neutron diffraction studies showed only one ordered cubic structure (sp. gr. *Fd*3*m*) in $TiC_{0.62}H_{0.05}$, $TiC_{0.62}H_{0.14}$, and $TiC_{0.62}H_{0.18}$ titanium carbohydrides [7]. In [18], the decomposition of nonstoichiometric titanium carbide into the ordered cubic phase (sp. gr. *Fd*3*m*) and the α-Ti (C, O) phase was established. The formation in addition to the trigonal phase of the α-Ti phase (instead of a solid solution of oxygen and carbon, as in [18]) during decomposition of $TiC_{0.545}O_{0.08}$ may be explained by the relatively low oxygen content in the sample studied.

Earlier, it was established that long annealing of $TiC_{0.58}$ at the temperature T = 1000 K [19] results in the formation of the α-Ti phase. Later, the formation of the α-Ti phase was also found in titanium carbohydrides [6].

Thus, a small amount of oxygen, as well as of hydrogen, does not hinder the formation of the α-Ti phase in titanium carbide $TiC_{0.545}$.

A superstructure with the unit-cell parameter $a_1 = 2a$ (a and a_1 are the unit-cell parameters of the initial and ordered phases, respectively) was observed in the metallographic and electron-microscopy studies of the samples of titanium oxycarbides with the oxygen content lower than in $TiC_{0.14}O_{0.80}$ [4]. The cubic ordered structure (sp. gr. *Fd*3*m*), in which the metalloid sublattice is divided into the carbon and oxygen sublattices, was also established in titanium oxycarbide $TiC_{0.44}O_{0.57}$ by the neutron-diffraction method [3]. It seems that the oxygen-rich titanium oxycarbides were studied in [3, 4], and, therefore, only a cubic ordered structure (sp. gr. *Fd*3*m*) was found in these compounds. It is difficult to establish unambiguously a division of the metalloid sublattices into the carbon and oxygen ones from the X-ray diffraction data for the $TiC_{0.545}O_{0.08}$ sample because of the close values of the coherent-scattering

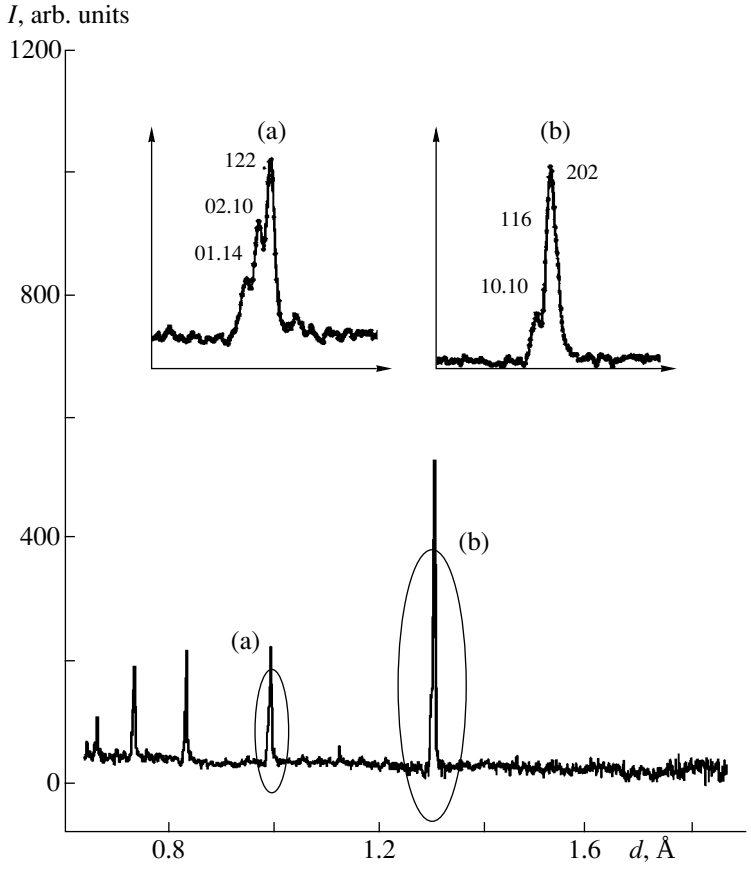

Fig. 5. Fragment of the neutron diffraction pattern from the sample annealed at 990 K measured on a high-resolution Fourier-diffractometer.

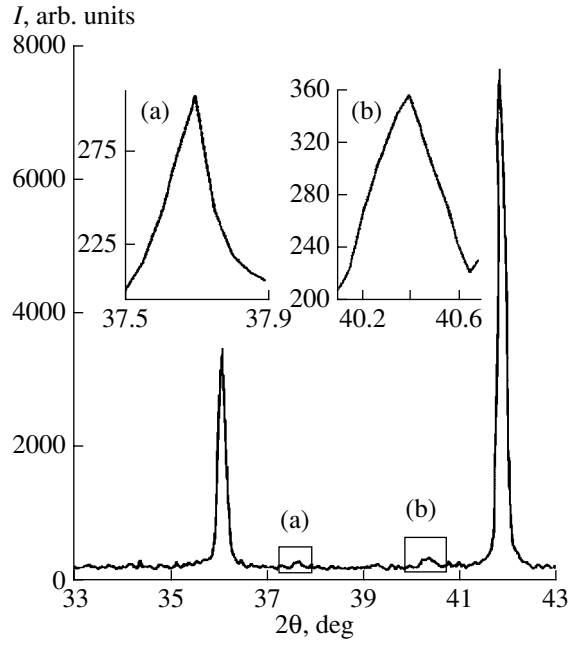

Fig. 6. Fragment of the X-ray diffraction pattern from the sample decomposed into the trigonal (sp. gr. $R\bar{3}m$ or $P3_121$) and α-Ti phases; (a) (002) structural reflection, (b) (101) reflection of the α-Ti phase.

amplitudes and pronouncedly different contents of oxygen and carbon in the sample studied. Thus, assuming that the 16(*c*) position is occupied only by carbon atoms and the 16(*d*) positions, by oxygen and remaining carbon atoms, then $R_b = 3.29\%$ (R_b is the total R factor over the profile with a subtracted background) and the occupancy of the 16(*c*) positions $P = 0.918$. If the 16(*c*) position is occupied with oxygen and carbon atoms and the 16(*d*) position is filled only with carbon atoms, then $R_b = 3.39\%$ and $P = 0.955$. If carbon and oxygen atoms are located in both interstitial octahedral positions, then $R_b = 3.49\%$ and $P = 0.945$.

CONCLUSIONS

Thus, the study of titanium oxycarbide $TiC_{0.545}O_{0.08}$ by neutron and X-ray diffraction methods allowed us to establish the existence of the ordered cubic (sp. gr. $Fd3m$) and trigonal (sp. gr. $R\bar{3}m$ or $P3_121$) structures.

The scheme of the phase transformations different from the scheme of phase transformations in nonstoichiometric titanium carbide and the decomposition

temperatures are established as

$$\delta'\,(Fd3m) \xrightarrow{T_1 = 990\ \mathrm{K}} \delta''\,(R\bar{3}m)$$

$$\xrightarrow{T_2 = 1020\ \mathrm{K}} \delta'\,(R\bar{3}m) + \alpha\text{-Ti} \xrightarrow{T_3 = 1040\ \mathrm{K}} \delta\,(Fm3m) + \alpha\text{-Ti}.$$

In both ordered structures, the metal atoms are displaced from vacancies toward the metalloid atoms.

The temperatures of the order–order (T_1 = 990 K) and order–disorder (T_3 = 1040 K) phase transitions in the sample studied are lower than in titanium carbide $TiC_{0.63}$ [8].

It is found that the α-Ti phase is formed in titanium oxycarbide $TiC_{0.545}O_{0.08}$ at the temperature T = 1020 K.

Thus, the rather strong influence of the relatively low oxygen content on the phase transformations and phase-transition temperatures in nonstoichiometric titanium carbide indicates that ordering is associated with deformational interaction in the complex systems caused by different energies of interaction between the interstitial atoms and their nearest neighbours.

ACKNOWLEDGMENTS

The authors are grateful to A.V. Pole for help in performing measurements on a FDVR diffractometer and V.V. Cherezov for making measurements on a DRON-4 diffractometer.

REFERENCES

1. A. G. Khachaturyan, *The Theory of Phase Transformations and the Structures of Solids Solutions* (Nauka, Moscow, 1974).
2. L. Toth, *Transition Metal Carbides and Nitrides* (Academic, New York, 1971; Mir, Moscow, 1974).
3. V. G. Zubkov, I. I. Matveenko, L. B. Dubrovskaya, *et al.*, Dokl. Akad. Nauk SSSR **1** (2), 323 (1970).
4. J. Vicens and J. L. Chermant, Phys. Status Solidi A **7** (1), 217 (1971).
5. Yu. G. Zaĭnulin, S. I. Alyamovskiĭ, E. I. Pavlov, and G. P. Shveĭkin, Izv. Akad. Nauk SSSR, Neorg. Mater. **13** (2), 381 (1977).
6. I. S. Latergaus, Author's Abstract of Candidate's Dissertation in Physics and Mathematics (Institut Yadernoĭ Fiziki Akad. Nauk UzSSR, Tashkent, 1986).
7. V. T. Em and M. Yu. Tashmetov, Phys. Status Solidi B **198**, 571 (1996).
8. M. Yu. Tashmetov, V. T. Ém, M. U. Kalanom, *et al.*, Metallofizika **13** (5), 100 (1991).
9. D. Taylor, *Neutron Irradiation and Activation Analysis* (Academic, London, 1964).
10. I. A. Karimov, V. T. Ém, V. F. Petrunin, *et al.*, Izv. Akad. Nauk Uz. SSR, Ser. Fiz.-Mat. Nauk, No. 6, 68 (1974).
11. V. L. Aksenov and A. M. Balagurov, Usp. Fiz. Nauk **166** (9), 955 (1996) [Phys. Usp. **39**, 897 (1996)].
12. V. F. Sears, Neutron News **3**, 26 (1992).
13. V. B. Zlokazov and V. V. Chernyshev, J. Appl. Crystallogr. **25**, 447 (1992).
14. A. Albinati and B. T. Willis, J. Appl. Crystallogr. **15** (4), 361 (1982).
15. V. T. Ém and M. Yu. Tashmetov, Fiz. Met. Metalloved., No. 3, 112 (1992).
16. M. Yu. Tashmetov, V. T. Ém, and N. N. Mukhtarova, Metallofiz. Noveĭshie Tekhnol. **17** (8), 51 (1995).
17. M. Yu. Tashmetov, V. T. Ém, and I. S. Latergaus, Fiz. Met. Metalloved., No. 12, 104 (1990).
18. S. I. Alyamovskiĭ, Yu. G. Zaĭnulin, and G. P. Shveĭkin, *Oxycarbides and Oxynitrides of the Metals of* IV *and* VA *Subgroups* (Nauka, Moscow, 1981).
19. V. Moisy-Maurice, N. Lorenzelli, C. H. de Novion, and P. Convert, Acta Metall. **30**, 1769 (1982).

Translated by T. Dmitrieva

Crystallography Reports, Vol. 48, No. 1, 2003, pp. 112–115. Translated from Kristallografiya, Vol. 48, No. 1, 2003, pp. 117–120.

PHYSICAL PROPERTIES OF CRYSTALS

Growth and Ionic Conductivity of $Li_{3+x}P_{1-x}Ge_xO_4$ ($x = 0.34$) Single Crystals

A. K. Ivanov-Shitz and V. V. Kireev

Shubnikov Institute of Crystallography, Russian Academy of Sciences, Leninskiĭ pr. 59, Moscow, 119333 Russia

e-mail: ivanov@ns.crys.ras.ru

Received February 6, 2002

Abstract—$Li_{3+x}P_{1-x}Ge_xO_4$ crystals ($x = 0.34$) with dimensions of about $3 \times 3 \times 5$ mm^3 were grown for the first time from flux. The conductivities of the crystals measured along three directions have close values and are equal to $\sigma \approx 1.8 \times 10^{-6}$ and 3.7×10^{-2} Sm/cm at the temperatures 40 and 400°C, respectively (similar to the case of pure lithium phosphate, somewhat lower values of electric conductivity were measure along the *b* axis). The activation energy of conductivity is equal to 0.54 eV. A considerable increase in the conductivity of the solid solution in comparison with the conductivity of pure lithium phosphate is explained by the specific features of the lithium sublattice in the crystal structure of the γ-Li_3PO_4 type. © *2003 MAIK "Nauka/Interperiodica".*

INTRODUCTION

Earlier [1–3], we described in detail the method of synthesis and the main electrophysical characteristics of γ-Li_3PO_4 single crystals. The interest in this compound is explained by the fact that solid electrolytes with the γ-Li_3PO_4-type structure can be considered as model objects for studying the influence of various factors on ionic conductivity. An increase in ionic conductivity was observed in the solid solutions with the γ-Li_3PO_4-type structure. Thus, the ionic conductivity of the nonstoichiometric phases in the Li_4GeO_4–Li_3VO_4 and Li_4GeO_4–Li_3PO_4 systems ranges within 10^{-4}–10^{-5} Sm/cm at room temperature [4–6], which makes these phases very promising for various practical purposes, e.g., as electrolytes in lithium-based current sources. However, the modern experimental investigations require large high-quality single crystals; therefore, the present article is dedicated to growth of bulky $Li_{3+x}P_{1-x}Ge_xO_4$ single crystals, the anisotropy of ionic conductivity, and the determination of the mechanism of ion transport.

EXPERIMENTAL

The starting materials for crystal growth were polycrystalline lithium orthophosphate and orthogermanate (Li_3PO_4 and Li_4GeO_4) obtained by the solid-phase synthesis. The reagents for the synthesis of lithium orthophosphate, LiH_2PO_4 and Li_2CO_3, were thoroughly mixed in equimolar quantities. The charge was annealed at 800°C. Lithium orthogermanate was synthesized from Li_2CO_3 and GeO_2 under the same conditions.

Single crystals in the Li_3PO_4–Li_4GeO_4 system were grown by crystallization from flux, with the solvent being the Li_2MoO_4–LiF mixture. To obtain the solid solution of the $Li_{3.5}P_{0.5}Ge_{0.5}O_4$ composition lithium orthophosphate and orthogermanate were taken in the equimolar quantities. The initial components in the weight ratio solute : solvent ~ 1 : 1 were loaded into a 60-ml-large platinum vessel. The seed was a platinum rod. Upon the complete dissolution of lithium orthophosphate and orthogermanate in the melt at 970°C, the system was rapidly cooled to 911°C, and the crystallization occurred via cooling the melt down to the temperature of 858°C at a rate of 0.1 K/h. The crystals grown were extracted from the melt and cooled to room temperature at a rate of 30 K/h.

Because of the orthorhombic symmetry of $Li_{3+x}P_{1-x}Ge_xO_4$ crystals, the ionic conductivity σ was measured along three directions coinciding with the crystallographic *a*, *b*, and *c* axes. In order to measure the electric conductivity by the method of impedance spectroscopy in the frequency range 100 Hz–500 kHz, silver electrodes were used (silver paste was applied to the preliminarily polished surfaces of the oriented $Li_{3+x}P_{1-x}Ge_xO_4$ crystals subsequently annealed at 200–250°C). The impedance spectra were processed using the EQUIVCRT computer program [7].

RESULTS AND DISCUSSION

As a result of the growth experiment, we synthesized a druse consisting of individual transparent crystals of irregular shapes. The individual crystals broken out from the druse were studied in a polarization microscope. It was established that, among the samples thus

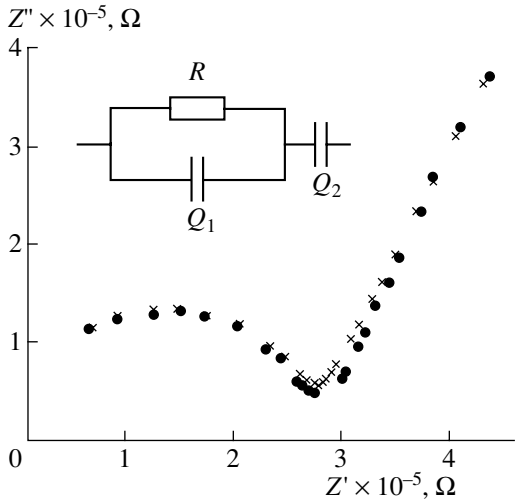

Fig. 1. Frequency dependences of the total complex resistance $Z = Z' + jZ''$ of a $Li_{3.34}P_{0.66}Ge_{0.34}O_4$ crystal at 89°C (measured along the *c* axis). Experimental data are indicated by filled circles, the calculated data, by crosses; *R* is the resistance and Q_1 and Q_2 are the frequency-dependent elements.

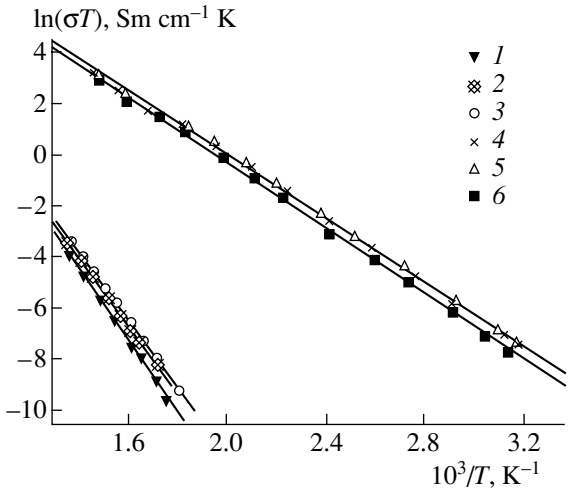

Fig. 2. Temperature dependences of conductivity of the $Li_{3.34}P_{0.66}Ge_{0.34}O_4$ and γ-Li_3PO_4 crystals. (*1*) γ-Li_3PO_4, parallel to the *b* axis, (*2*) γ-Li_3PO_4, parallel to the *c* axis, (*3*) γ-Li_3PO_4, parallel to the *a* axis, (*4*) $Li_{3.34}P_{0.66}Ge_{0.34}O_4$, parallel to the *c* axis, (*5*) $Li_{3.34}P_{0.66}Ge_{0.34}O_4$, parallel to the *a* axis, and (*6*) $Li_{3.34}P_{0.66}Ge_{0.34}O_4$, parallel to the *b* axis.

obtained, there were both single-domain and polydomain crystals. The electrophysical properties were studied on a specially chosen large crystal having no blocks. A rectangular parallelepiped was cut out from this crystal in such a way that its faces were perpendicular to the main crystallographic directions. The parallelepiped dimensions (upon polishing of its faces) were $2.00 \times 2.80 \times 3.35$ mm.

The X-ray phase analysis (Rigaku D maxIIIc diffractometer, CuK_α radiation) showed that the diffraction pattern of the material synthesized is close to the diffraction pattern of γ-Li_3PO_4 with the only difference being that the maxima are displaced toward larger interplanar spacings, which indicates the partial substitution of phosphorus ions by germanium ones in lithium orthophosphate. The unit-cell parameters are a = 6.178 Å, b = 10.656 Å, and c = 5.013 Å, whereas the lattice parameters of pure γ-Li_3PO_4 are a = 6.115 Å, b = 10.475 Å, c = 4.923 Å (ASTM-JCPDS card no. 15-0760). In order to establish the quantitative composition of the obtained solid solution, we constructed the calibration dependences of the unit-cell parameters (a, b, c) on the composition of the $Li_{3+x}P_{1-x}Ge_xO_4$ solid solution. With this aim we obtained the solid solutions of different compositions by the solid-phase synthesis and determined their unit-cell parameters. It is established that the composition of the grown and studied crystal corresponds to the $Li_{3.34}P_{0.66}Ge_{0.34}O_4$ solid solution with x = 0.34.

Figure 1 shows the hodographs of the total resistance of $Li_{3+x}P_{1-x}Ge_xO_4$ at 89°C (σ was measured along the *c*-axis) and also the equivalent electric circuit for which the parameters of this hodograph were determined. The resistance R of the equivalent electric circuit corresponds to the bulk resistance of the crystal. The impedance hodographs are the same for the conductivity measured along all the crystallographic axes. As is seen from Fig. 1, the impedance hodograph is a distorted semicircumference (at high frequencies) "conjugating" with a straight line at low frequencies. Depending on the temperature interval, various individual parts of the hodograph can play the key role. At high temperatures, the accuracy of the R determination decreases because of the strong effect of the electrode resistance.

As is seen from Fig. 2, the temperature dependence of ionic conductivity of $Li_{3+x}P_{1-x}Ge_xO_4$ single crystals obeys the Arrhenius equation in the whole temperature interval

$$\sigma T = \sigma_0 \exp(-E_{\sigma T}/kT), \quad (1)$$

which is consistent with the data from [4–6]. For comparison, Fig. 2 shows our data obtained earlier for a γ-Li_3PO_4 single crystal [1]. The conductivities of $Li_{3.34}P_{0.66}Ge_{0.34}O_4$ crystals measured along the *a* and *c* directions coincide and are $\sigma = 1.8 \times 10^{-6}$ and 3.7×10^{-2} Sm/cm at 40 and 400°C, respectively. As in the case of pure lithium phosphate, somewhat lower electric conductivities were measured along the *b* axis, $\sigma = 1.2 \times 10^{-6}$ and 3.1×10^{-2} Sm/cm at 40 and 400°C, respectively. The activation energy of conductivity is 0.54 eV. The conductivity of γ-Li_3PO_4 is lower by several orders of magnitude, and the activation energy of conductivity measured along different directions ranges within 1.14–1.23 eV [1]. The conductivity data obtained for pure and doped lithium phosphate indicate

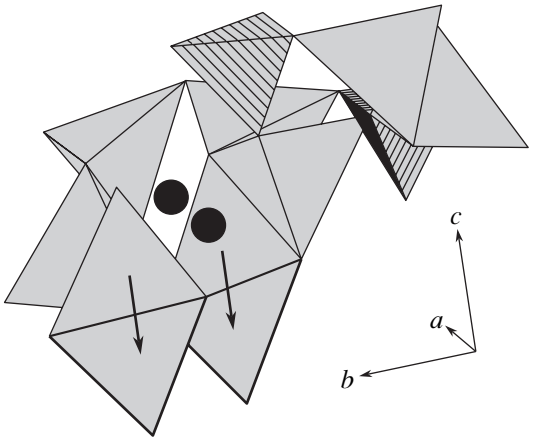

Fig. 3. Model of the crystal structure of the $Li_{3+x}P_{1-x}Ge_xO_4$ solid solution. Hatched figures correspond to the PO_4-tetrahedra, nonhatched ones, to the LiO_4-tetrahedra. The additional lithium ions are indicated by filled circles. Arrows indicate the displacements of the lithium ions during the formation of the solid solution. Tetrahedra into which the intrinsic lithium ions are incorporated are indicated by solid lines (in pure γ-Li_3PO_4, these tetrahedra are empty).

a dramatic increase in conductivity of the solid solution. Consider the microscopic aspects of ion transport in the $Li_{3+x}P_{1-x}Ge_xO_4$ solid solution and in nominally pure γ-Li_3PO_4. Lithium orthophosphate is a typical representative of the compounds with the framework structure. Lithium cations are located at two types of positions, Li1 and Li2, with all these positions being fully occupied. The γ-Li_3PO_4 structure is rather loose, i.e., the framework voids comprise a considerable fraction of the total volume and penetrate the structure along all the directions, thus providing favorable conditions for ionic conductivity. Nevertheless, the low values of ionic conductivity in γ-Li_3PO_4 could have been expected, because all the lithium cations are located in fully occupied positions and are rigidly bound to the framework. In this case, conductivity can be associated with the formation of thermal defects such as, e.g., Frenkel defects. The concentration of interstitial ions in this case is rather low, which results in a low conductivity of pure γ-Li_3PO_4. In order to increase the conductivity and, at the same time, preserve the structure, one has to introduce a considerable amount of lithium ions into the voids of the crystal framework, which really takes place in the $Li_{3.34}P_{0.66}Ge_{0.34}O_4$ solid solution. For definiteness, we call the lithium ions located in the rigid framework and rigidly bound to it "intrinsic ions" and ions statistically filling the framework voids, additional ions.

One has also to consider a decrease in the anisotropy of conductivity in $Li_{3.34}P_{0.66}Ge_{0.34}O_4$ in comparison with the anisotropy in γ-Li_3PO_4 (it is seen from Fig. 2 that the conductivity of the solid solution is almost isotropic, whereas the conductivity of pure lithium orthophosphate is slightly anisotropic). It was indicated in [1] that the lower conductivity along the *b* axis is associated with the zigzag shape of the conductivity channels along this direction, whereas the conductivity channels along the *a* and *b* axes are smoothed. In order to interpret the decrease in anisotropy of the solid solution, consider how the additional lithium ions fill the crystal framework. We invoke here the powder neutron diffraction data for the $Li_{3+x}P_{1-x}V_xO_4$ solid solution [8, 9] with the structure and properties similar to those of the $Li_{3+x}P_{1-x}Ge_xO_4$ solid solution considered in the present article. In accordance with the model suggested in [8], the voids of the crystal framework are filled and form a cluster (Fig. 3). The additional ions (black circles in Fig. 3) occupy the octahedral voids sharing the faces with tetrahedra filled with the intrinsic lithium ions. As a result of the electrostatic interaction with additional ions, some tetrahedrally coordinated intrinsic lithium ions are displaced from their positions to the neighboring tetrahedra (shown by solid edges in Fig. 3). Thus, some lithium positions occupied in γ-Li_3PO_4 are liberated during the formation of the $Li_{3+x}P_{1-x}Ge_xO_4$ solid solution. This results in disordering in the lithium sublattice not only along the conductivity channels, but also in the rigid framework. The number of positions accessible for lithium migration considerably increases, and the crystal structure becomes equally transparent for ion transport in all the directions, which decreases the anisotropy of conductivity in the $Li_{3+x}P_{1-x}Ge_xO_4$ solid solution in comparison with the conductivity in γ-Li_3PO_4.

The microscopic structure model of ion transport suggested here indicates the transport paths (conductivity channels) along all the three main crystallographic directions. Moreover, one can draw the conclusion that conductivities along all the three directions should be equal, because the concentration of the charge carriers (Li^+) and the hopping length (approximately equal distances between the neighboring partly filled crystallographic positions in the lithium sublattice) differ only insignificantly. Of course, in order to give an unambiguous answer to the question about the microscopic characteristics of the ion transport, one has to obtain more reliable data from precision structure experiments.

ACKNOWLEDGMENTS

This study was supported by the Russian Foundation for Basic Research, project no. 99-03-32726.

REFERENCES

1. A. K. Ivanov-Shitz, V. V. Kireev, O. K. Mel'nikov, and L. N. Dem'yanets, Kristallografiya **46** (5), 938 (2001) [Crystallogr. Rep. **46**, 864 (2001)].

2. A. K. Ivanov-Shitz and V. V. Kireev, in *Proceedings of the 12th Russian Conference on Physical Chemistry and Electrochemistry of Melted and Solid Electrolytes, Nal'chik, 2001*, p. 41.
3. A. K. Ivanov-Schitz and V. V. Kireev, in *Abstracts of 13th International Conference on Crystal Growth, Japan, 2001*, p. 552.
4. A. K. Ivanov-Shitz and I. V. Murin, *Ionics of Solid State* (St. Petersburg Gos. Univ., St. Petersburg, 2000), Vol. 1.
5. J. T. S. Irvine and A. R. West, in *High Conductivity Solid Ionic Conductors*, Ed. by T. Takahashi (World Scientific, Singapore, 1989), p. 201.
6. E. I. Burmakin, *Solid Electrolytes with Conductivity on Cations of Alkali Metals* (Nauka, Moscow, 1992).
7. B. A. Boukamp, Solid State Ionics **18/19**, 136 (1986).
8. P. G. Bruce and I. Abrahams, J. Solid State Chem. **95**, 74 (1991).
9. I. Abrahams and P. G. Bruce, Acta Crystallogr., Sect. B: Struct. Sci. **47**, 696 (1991).

Translated by L. Man

Crystallography Reports, Vol. 48, No. 1, 2003, pp. 116–123. Translated from Kristallografiya, Vol. 48, No. 1, 2003, pp. 121–129.

PHYSICAL PROPERTIES OF CRYSTALS

Transport Properties of $Y_3Fe_5O_{12}$ Garnet Crystals

I. D. Lomako*, V. I. Pavlov, and N. Ya. Shishkin*****

** Institute of Solid-State and Semiconductor Physics, National Academy of Sciences of Belarus, ul. Brovki 17, Minsk, 220072 Belarus*

e-mail: Lomako@iftt.bas-net.by

*** Belarussian State Technological University, ul. Sverdlova 13a, Minsk, 220050 Belarus*

**** Belarussian State Pedagogical University, ul. Sovetskaya 18, Minsk, 220809 Belarus*

Received March 28, 2002

Abstract—The temperature dependence of electrical resistivity ρ and thermopower θ is studied for a series of $Y_3Fe_5O_{12}$ (YIG) garnet single crystals with different levels of optical and structural quality. The effect of some technology-related impurities on the value of ρ is discussed. It is shown for the first time that the experimental data on the absorption coefficient and electrical resistivity can be interpreted based on a single physical parameter, namely, the intensity ratio of coherent and incoherent X-ray scattering (*K*/*nk*). This ratio characterizes the fraction of conduction electrons in a given sample. The results are discussed with due regard for the nonequivalence of the planes of the {110} and {111} types. The additional details of the charge-transfer mechanism are established for the (111)-oriented YIG samples. It is suggested that the θ values could be characterized in terms of *nk* or *nk*/*K*. *© 2003 MAIK "Nauka/Interperiodica".*

INTRODUCTION

Yttrium iron garnet (YIG) is a model object for research work and a promising material for various applications [1, 2]. In spite of the significant role of YIG single crystals for both theory and practical applications, questions concerning their properties are still open. In particular, the role of the orientation of crystal axes on the distribution of uncontrolled "technological impurities" (Ba, Mn) and the their effect on the transparency of the crystals in the infrared range remain unclear. As a rule, researchers use doped YIG samples of only one crystallographic orientation [3–5]. In [3], dedicated to the conductivity of *p*- and *n*-doped YIG samples, it was first assumed that the formation of oxygen vacancies V_O should occur. These vacancies act as natural donors whose number is unknown. The presence of these vacancies in the crystal facilitates and accelerates charge transfer. According to Iida and Miwa [6], the vacancies play the mediatory role in charge transfer, since the latter proceeds via the charge exchange between a cation and vacancies [6]. Different cation sublattices of the garnet crystals contain Fe, Mn, and Sm ions of different valences and various magnetic states. Therefore, even the lowest concentration of vacancies favors dynamic ordering of ion valences and the hopping conductivity. Ksengzov and his coworkers [5] studied the mobility of charge carriers in Si-doped *n*-type yttrium garnet.

It is well known that YIG crystals grown from flux exhibit a noncubic anisotropy [7]. Moreover, the EXAFS studies of the fine structure of garnets revealed that about 10% of Y ions in dodecahedral positions exchange places with 5% of Fe ions located in octahedral sublattice [8]. The Fe ions occupying the octahedral positions and along the [111] axis are substituted by Y ions. It is the exchange between the Y and Fe ions, as also the small displacements of the atomic positions, that are responsible for the noncubic symmetry $R\bar{3}$ in YIG, i.e., for symmetry lower than *IA*3*d*.

In the present paper, we study the temperature dependences of electrical resistivity ρ and thermopower θ for differently oriented YIG samples of different degrees of perfection. The electrical properties of magnetic semiconductors, in particular of YIG, are completely determined by the mechanism of scattering of charge carriers and their energy spectrum. The charge transfer in these crystals occurs mostly via defect centers; therefore, the analysis of the kinetic processes is equivalent to the study of the characteristics of the distribution of defect states in the (110)-, (111)-, and (100)-oriented plates.

The aim of the present paper is to establish the charge-transfer mechanism in the YIG samples and to explain the pronounced scatter in the values of electrical resistivity observed for both the differently oriented plates cut out from the same crystal and for the samples cut out from the crystals with different degrees of structural and optical perfection.

EXPERIMENTAL

Here, we continue the study of the YIG samples whose characteristics were studied in [9–11] and reported in [11]. The samples were $6 \times 7 \times (1.5–2.6)$-$mm^3$-large plates cut out parallel to the (110), (111), and (100) crystallographic planes.

1063-7745/03/4801-0116$24.00 © 2003 MAIK "Nauka/Interperiodica"

Electrical resistivity and thermopower for YIG crystals at different temperatures (°C)

Sample	lnρ	θ, μV/K	lnρ	θ, μV/K	lnρ	θ, μV/K	lnρ	θ, μV/K	lnρ	θ, μV/K
	200		250		300		350		410	
7(110)	15.28	560	13.23	600	11.10	490	10.0	510	9.26	520
41(110)	18.09	−276	16.97	−440	15.19	−470	13.6	−480	12.04	−460
52(110)	17.0	107	14.82	290	13.1	500	12.0	480	10.84	450
50(110)	17.38	−640	15.72	−790	13.59	−740	12.04	−700	10.0	−650
50"(110)	20.67	80	18.75	370	16.8	680	15.2	760	14.0	830
51(110)		340		60		4		20		15
42(111)	17.99	125	16.7	370	14.62	440	12.9	410	11.3	410
34(111)	17.73	390	15.57	760	13.29	810	11.8	830	11.27	820
46(111)	12.01	620	11.12	600	10.85	580	10.72	580	10.4	570
III-6(111)	10.12	710	9.71	650	9.32	610	8.9	590	8.13	580
32-HO	18.75		15.80		14.69		12.9		12.0	
40(100)	22.4	−130	21.4	122	20.4	450	19.38	580	18.15	780
3(100)	15.59		15.48		13.79		12.27		11.48	
VI-4(100)	10.22		9.75		9.21		8.61		8.06	

The study of the kinetic properties is quite a labor-consuming task; therefore, the resistivity was measured only for 14 samples from the total 19. The methods of crystal growth, the values of the absorption coefficient in the IR range, the weight ratio Y/Fe of the main cations, and the relative content of Mn and Fe ions, Mn/Fe, determined by the neutron activation analysis can be found elsewhere [10–12].

Now, we note the main statements and conclusions made in the earlier studies, which will be used in the present paper. The Ba ions are considered as an uncontrolled technological impurity substituting the Y ions in the dodecahedral sublattice. The Ba ions can suppress the formation of dislocations and thus somewhat reduce the optical transparency of YIG crystals [11]. Using the data of neutron activation analysis, we came to the conclusion that the quality criterion of YIG samples can be the ratio of the sum of the Y and Fe cations to the O anions expressed in wt %. In the samples characterized by different degrees of the structural and optical perfection [12], we revealed the nonequivalence of the {110} and {111} crystal planes, which results from the dependence of the density *d* of the YIG plates on the intensity ratio of the coherent and incoherent X-ray scattering (*K*/*nk*). As was shown in [12], the YIG samples can be divided into two groups according to the degree of their transparency (see the table in that paper). The first group consists of the plates having absorption coefficient α less than 7 cm^{-1} (at the wavelength λ = 1300 nm): the (110)-oriented samples (nos. 7, 41, and 52), the (111)-orientated ones (nos. 42 and 34), and the (100)-orientated ones (nos. 40 and 3). The second group includes the samples characterized by medium and low transparency ($\alpha > 7$ cm^{-1}); these are samples nos. 50", 51, and 50 ((110) orientation), nos. 46 and III-6 ((111) orientation), no. VI-4 ((100) orientation), and also the unoriented sample no. 32-NO. Thus, the (110)-, (111)-, and (100)-oriented samples are divided into two groups characterized by different characters of the variation of their physical properties. Below, in the analysis of the electrical resistivity of garnet crystals, we take into account the nonequivalence of the crystallographic planes, which makes it necessary to consider the reason of this nonequivalence. In our opinion, the nonequivalence of the crystallographic planes is caused by the distortions in the garnet structure arising in the course of crystal growth from flux, by the orthorhombic symmetry of the dodecahedral positions, and by the nonequivalence of two octahedral sublattices, which make a considerable contribution to the total noncubic anisotropy of the YIG crystals. Moreover, the nonequivalence of both {110} and {111} planes is observed for the samples cut out mainly from nonidentical parts of different crystals, which, during growth, were located differently with respect to the feeding concentration flows of the melt resulting in nonstoichiometry and significant fluctuations in the composition of microimpurities.

We believe that this effect passed unnoticed, because it can be observed only on a sufficient number of YIG samples (more than ten) of different quality and having at least two orientations.

The temperature dependences of electrical resistivity were measured in the mode of temperature stabilization of the samples. The contacts were prepared from a special silver paste. Prior to measurements, the samples were annealed for 3 h in air at 800°C. The thermopower θ was measured on a setup with the platinum electrodes fastened to the electrodes prepared for the gallium–

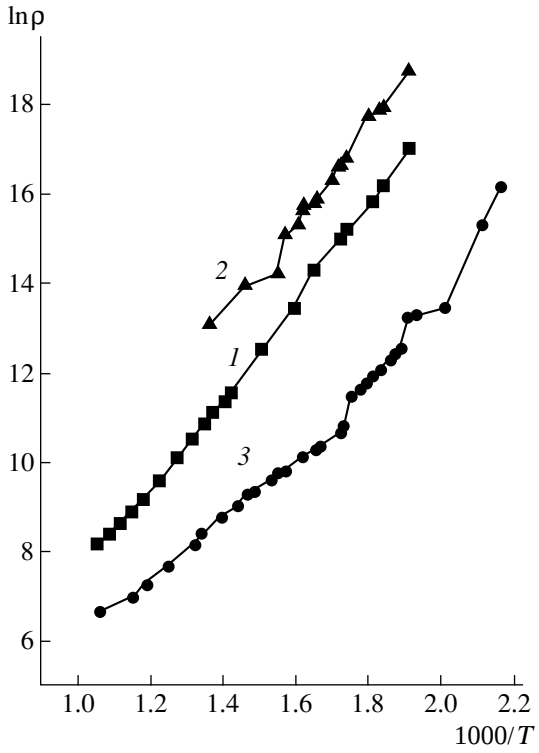

Fig. 1. Electrical resistivity ρ of (110)-oriented YIG samples versus temperature: (*1*) sample no. 41; (*2*) sample no. 50"; (*3*) sample no. 7.

indium alloy and deposited onto the sample using an ultrasonic soldiering iron. The e.m.f. was measured by an electrometer. The temperature gradient ranged within 5–15°C, the temperature was measured by chromel–alumel thermocouples. The heating rate was 10 K/min, whereas cooling was performed at a rate of about 5 K/min. The measuring cycles were repeated four times.

RESULTS AND DISCUSSION

Figure 1 shows the temperature dependence of resistivity ρ for (110)-oriented samples nos. 41, 50", and 7 (curves *1*, *2*, and *3*, respectively). Samples nos. 7 and 41 have the highest optical transparency in the IR range; i.e., they fall to group I (see Fig. 1 and the table in [12]). Sample no. 50" belongs to the samples of moderate optical quality ($\alpha = 6.9$ cm^{-1}), i.e., to group II in this case. Note that there are no rigorous boundaries between the two groups, especially for the samples of moderate optical quality. The additional factor, low value of *K*/*nk*, the YIG samples of moderate and even low optical quality (for example, samples nos. 50" and 51), can have a low conductivity (see table). The minimum values of lnρ are observed over the whole temperature range for sample no. 7 possessing the minimum absorption coefficient ($\alpha = 0.4$ cm^{-1}) among the whole batch of the YIG plates under study. It is a rather unusual situation, since it was expected *a priori* that the sample with the highest transparency should have had the highest resistivity. Probably, one of the most reliable explanations of this paradox is a relatively large number of Mn ions in the sample with the highest transparency, which favors an increase in the number of free charge carriers (conduction electrons) and, hence, a significant decrease in resistivity. Note that samples nos. 41 (curve *1*) and 50" (curve *2*) are characterized by similar behavior of ρ at high temperatures. At $t = 250$°C ($1000/T = 1.91$), the sample with the lowest transparency among those presented in Fig. 1 (sample no. 50") has the resistivity ρ exceeding by a factor of 250 the resistivity for sample no. 7 and by a factor of 5.8, the resistivity for sample no. 41. Among the (110)-oriented samples, sample no. 50 with a rather low transparency ($\alpha = 13.2$ cm^{-1}) has the ρ at $t = 250$°C exceeds by more than an order of magnitude (by a factor of 12) the resistivity of the sample no. 7 with the highest transparency (table). In this case, sample no. 7 (group I) has the highest conductivity because of a large number of active Mn ions incorporated into the crystal. Such a paradoxical situation explained by the absence of a correlation between the values of α and ρ in this batch of samples is observed only on the (110)-oriented YIG plates.

Figure 2 shows the $\rho(T^{-1})$ curves for the (111)-oriented samples: samples nos. 34 and 42 (group I, curves *1* and *2*) and sample no. 46 (group II, curve *3*). One can clearly see different shapes of these curves: as was expected, the peaks in curves *1* and *2* are much higher than the peak in curve *3*. In contrast to curves *1* and *2*, the values of lnρ corresponding to curve *3* vary only slightly over a wide temperature range (390–220°C). Sample no. 46 is characterized by the minimum content of Ba ions and minimum *K*/*nk* value among the (111)-oriented plates of groups I and II, which follows from the X-ray radiometric analysis data.

At $t = 200$°C ($1000/T = 2.11$), sample no. 42 with a high transparency has the maximum resistivity, exceeding the ρ value for sample no. 34 by a factor of 1.3 and for sample no. 46 by a factor of 400 (group II). As was expected, the ρ value for sample no. III-6 with the lowest transparency ($\alpha = 17.3$ cm^{-1}) is lower than ρ for sample no. 42 almost by a factor of 3000.

Periodic chains of bonds along 111 are normal to the (111) plane; these are *O*–3*A*–3*D*–3*A*–*O* chains, where *O* is a Fe ion at the octahedral site, *A* is an anion (oxygen), *D* is an Y ion at the dodecahedral site [13]. In the YIG crystals, the easy magnetization axes, domain boundaries, and dislocations are located along these directions. As follows from [14], the stepwise motion of dislocations, associated with the inhomogeneous distribution of impurities "picked up" by a dislocation in the course of its motion in a slip plane, is confirmed experimentally. In garnets, dislocations are located mainly along the crystallographic [111] directions. Blakemore [15] believes that dislocations are surrounded by space charges possessing cylindrical sym-

metry. The octahedral sublattices considerably distort the general noncubic anisotropy of a garnet [7]. Therefore, one can conclude that the periodic chains of bonds along [111] have a considerable number of defects. This facilitates charge transfer along the [111] directions and provides the minimum resistivity ($\ln\rho$ = 23.95) of sample no. 42 in comparison with the resistivity of (100)-oriented sample no. 40 ($\ln\rho$ = 26.05) at room temperature (t_{room}) [12]. We believe that the charge transfer in the (110)- and (100)-oriented plates takes place along the periodic chains of bonds along [001], i.e., the *T*–2*A*–*D*–2*A*–*T* chains where *T* is the tetrahedral site. The tetrahedral sites are occupied by Fe ions or by impurity ions with small ionic radii, which provide the minimum distortions in the garnet structure. The number of distortions along the periodic chains of bonds along [001] is much less than along the periodic chains of bonds along [111]. Therefore, the number of defects and conduction electrons is less along this direction, which explains the maximum resistivity of (111)-oriented YIG samples.

As was found earlier [11], Ba^{2+} ions are an inevitable technological impurity substituting the Y^{3+} ions in the dodecahedral positions. The Ba^{2+} ions have stable valence and are acceptor impurities in YIG samples. For the (110)- and (111)-oriented samples, the resistivity increases with the number of Ba ions, whereas, for the (100)-oriented samples, it decreases. In contrast to the Ba and Y ions, the valence of Mn ions can range from 2 to 4, whereas their magnetic moments have nonzero values. Thus, Mn ions can actively participate in the charge transfer.

In Fig. 3, we present the $\ln\rho = f(\mathrm{Mn/Fe})$ curves at t = 250°C. We can clearly see the influence of Mn ions on the resistivity of the YIG samples. Sample no. 7 (orientation (110)) with the maximum content of Mn ions in this series of the samples has the minimum resistivity among the samples of group I (curve *1*). It is rather unusual that the resistivity at t_{room} for sample no. 7 is lower than the resistivity of sample nos. 42 and 34 (group I) having an elevated concentration of defects along the [111] directions favorable for the charge transfer [12]. Small contents of Mn ions can hardly decrease the transparency in the IR range, because α = 0.4 cm^{-1} for sample no. 7. For the (110)-oriented YIG samples (curves *1* and *2*) and (100)-oriented ones (curve *5*), the ρ value increases with a decrease in the content of Mn ions. For samples nos. 50 and 50" (curve *2*), and also for (100)-oriented sample nos. 40, VI-4 and 32-HO (curve *5*), the $\rho(\mathrm{Mn/Fe})$ curves and the $\alpha = f(K/nk)$ curves are identical (see [12], Fig. 2). Curve *4* represents the (111)-oriented plates of group II. For these samples, the resistivity decreases with an increase in the content of Mn ions, similarly to curves *1*, *2*, and *5*.

Now, consider the $\ln\rho = f(K/nk)$ curves at $t > T_C$, e.g., at 410°C in the absence of magnetic ordering in the garnet crystals. As is seen from Fig. 4, for the YIG samples in the paramagnetic state, the experimental points

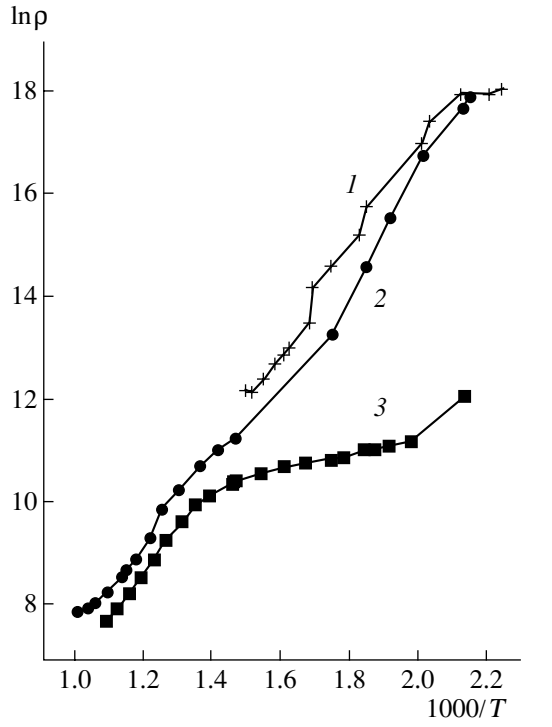

Fig. 2. Electrical resistivity ρ of (111)-oriented YIG samples versus temperature: (*1*) sample no. 42; (*2*) sample no. 34; (*3*) sample no. 46.

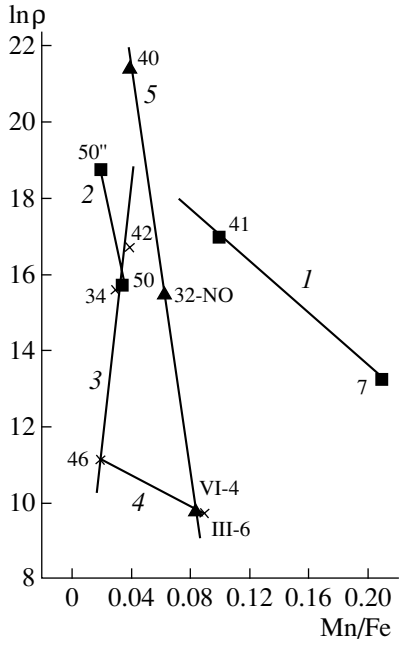

Fig. 3. Electrical resistivity ρ of YIG samples at t = 250°C versus relative Mn/Fe content with due regard for different crystallographic orientations: (*1* and *2*) (110) orientation; (*3* and *4*) (111) orientation; (*5*) (100) orientation and sample no. 32-NO.

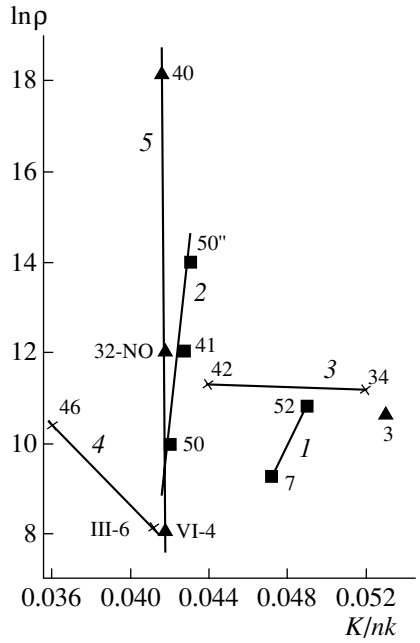

Fig. 4. Electrical resistivity ρ of YIG samples at t = 410°C versus K/nk ratio with due regard for different crystallographic orientations: (*1* and *2*) (110) orientation; (*3* and *4*) (111) orientation; (*5*) (100) orientation (triangles) and sample 32-NO.

(curves *1*, *2*, and *5*) corresponding to the samples from different groups are located at straight lines parallel (or almost parallel) to the vertical axis. The point is that among the same group, the (110)- and (100)-oriented plates of a rather high quality have close values of K/nk but different resistivities. This is the manifestation of the influence of the degree of the structural and optical perfection of the YIG samples on the K/nk values. The maximum resistivity values correspond to the (110)-oriented sample nos. 50", lnρ = 14, curve *2* and (100)-oriented sample no. 40, lnρ = 18, curve *5*. Sample no. 50" has the absorption coefficient $\alpha = 6.9$ cm^{-1} and the ρ value lower than sample no. 40. The latter has a high transparency ($\alpha = 0.8$ cm^{-1}). Therefore (100)-oriented sample no. 40 having the highest transparency also has the maximum resistivity. Sample no. 32-NO with a moderate optical quality ($\alpha = 7.2$ cm^{-1}) is characterized by the parameters $K/nk = 0.0418$ and lnρ = 12. The corresponding point in Fig. 4 fits curve *5* well. Sample no. VI-4 (lnρ = 8) has the minimum resistivity in spite on the low K/nk value. This is explained by its low structural and optical quality ($\alpha = 23.5$ cm^{-1}). Sample no. 3 (orientation (100)) has a high transparency ($\alpha = 2.3$ cm^{-1}) but also the maximum K/nk value ($K/nk = 0.053$) because of the incorporated Sm and Mn ions. Hence the ρ value is ratter low. Samples nos. 7 and 52 (group I) represented by curve *1* have the maximum content of such impurities as active Mn and Sm ions, respectively, high values of K/nk, and low values of ρ. The samples of good structural and optical quality (samples nos. 7 and 52) have the electrical resistivity ρ of the same order of magnitude as plate no. 50 (Fig. 4, curve *2*) from group II (according to its optical transparency, $\alpha = 13.2$ cm^{-1}) and containing Pt^{4+} ions as an inactive impurity. In our opinion, these factors (K/nk values, the degree of the structural and optical perfection, and the high content of both active (Mn, Sm) and inactive (Ba, Pt) ions, which become the dominant impurities) determine the value of ρ for a given sample.

The (111)-oriented YIG samples of group II with different values of K/nk but almost coinciding ρ values are represented by the straight line *3* almost parallel to the horizontal axis. For the (111)-oriented samples of group II characterized by a higher defect concentration and a lower transparency (curve *4*), the lnρ(K/nk) curves are similar to those for the samples of group I

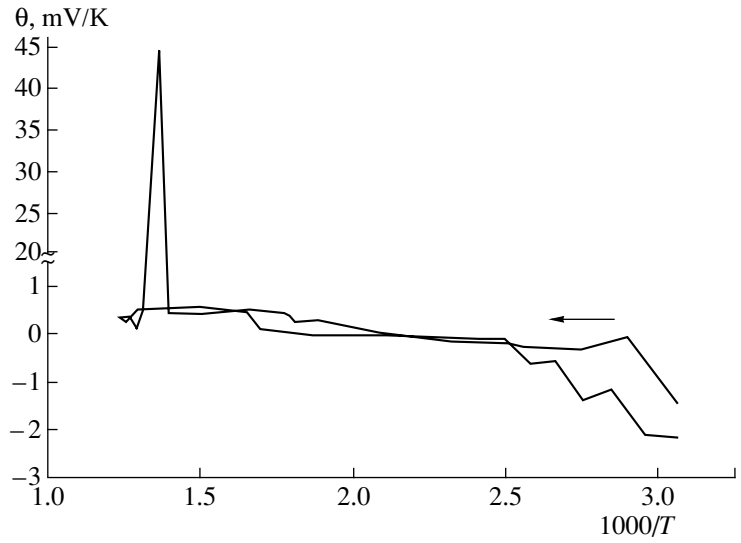

Fig. 5. Temperature dependence of thermopower θ for sample 52.

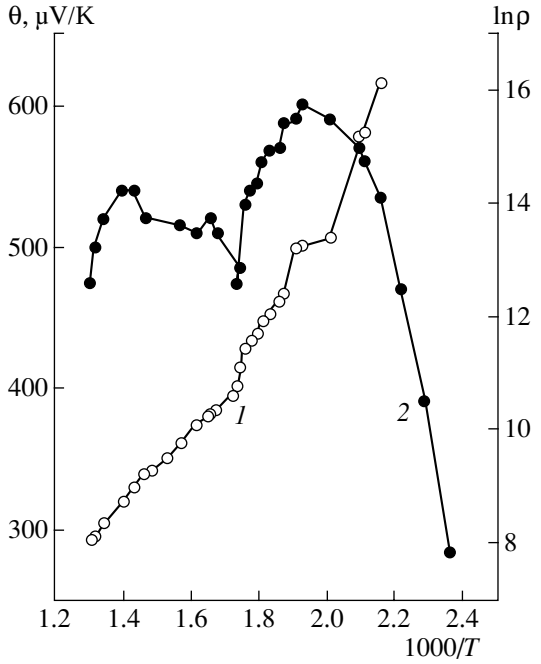

Fig. 6. (*1*) Electrical resistivity ρ and (*2*) thermopower θ versus temperature for (100)-oriented sample no. 7.

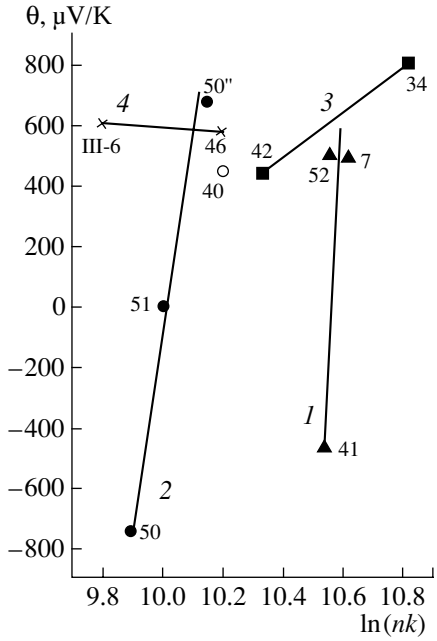

Fig. 7. Thermopower θ at t = 300°C versus the logarithm of the intensity of incoherent X-ray scattering for differently oriented YIG samples: (*1* and *2*) (110) orientation; (*3* and *4*) (111) orientation; open circle, (100)-oriented sample no. 40.

(curve *3*), whereas the samples of group II have the minimum ρ values. According to the percolation theory, the easy magnetization axis is an additional factor favoring charge transfer along the [111] direction.

To establish the conductivity type of YIG samples with different degrees of perfection, we analyzed the temperature dependence of thermopower θ for six (110)-oriented YIG samples, four (111)-oriented samples, and 40 (100)-oriented samples. Among the (110)-oriented samples, samples nos. 41 and 50 exhibit the *n*-type conductivity, whereas all other samples have the *p*-type conductivity (see table). Sample no. 50 has a low percentage of Ba ions, whereas the content of Pt^{4+} ions is significantly higher. This determines the presence of donors and the *n*-type conductivity. Currently there is no unambiguous explanation of the *n*-type conductivity in sample no. 41, because it contains many more Ba ions than sample no. 50, but there are also Sm and Mn ions with the valence ranging from 2 to 4. It is rather difficult to suggest the specific mechanism underlying the *n*-type conductivity in sample no. 41. In fact, the concentration of Sm ions in sample no. 52 exceeds that in sample no. 41 approximately by a factor of four; in addition, it also contains a lot of Ba and V ions but nevertheless exhibits *p*-type conductivity above 130°C (Fig. 5). At t < 130°C, sample no. 52 shows the *n*-type conductivity both on heating and cooling. Note that the maximum values of thermopower, θ ≈ 45 mV/K, are observed in the range of 450–460°C. These values are higher by two orders of magnitude than the value 450 μV/K characteristic of sample no. 52 at 410°C. A giant value of emf was also observed for SmS crystals within the same temperature range [16], which was interpreted as a consequence of a high conduction gradient of conductivity electrons because of the phase transition in the system of defect-forming Sm ions [16]. We observed a high concentration gradient of Sm ions in sample no. 52. In fact, according to the X-ray photoemission data, Sm ions are the only impurity and are located only on one side of the plate (l = 2.623 mm), whereas the other side has impurities of Pb, V, and Ba ions. This sample allows us to follow the evolution of the nonuniform distribution of both inactive impurities (Ba and V) and dominant active (Sm and Mn) impurities in a real YIG sample. As to sample no. 41, it probably contains, in addition to Pb and Bi ions (which can have different valence states), also oxygen vacancies V_0, which provides the *n*-type conductivity [3]. Another explanation of the presence of donors in sample no. 41 is based on the fact that Fe ions substituting Y ions at the sites of the dodecahedral sublattice with a large unit cell can have valence two, whereas in order to preserve the electroneutrality, some Fe ions occupying the tetrahedral sublattice should be tetravalent, whereas the majority of Fe ions are trivalent. According to Krupicka, the ferrites containing both di- and trivalent Fe ions exhibit the *n*-type conductivity [17]. It is just in sample no. 41 that the periodic chains of bonds along [001] include the dodecahedral and tetrahedral positions alternating with oxygen anions, which gives rise to the formation of donors. Note that (111)-oriented sample no. 42 cut out from the same garnet crystal as

sample no. 41 contains periodic chains of bonds along [111] with the octahedral and dodecahedral cation positions with only positive values of θ in the whole temperature range. For sample 40, the negative θ values are observed at $t < 220$°C, whereas, at temperatures exceeding 250°C, the thermopower is positive. Sample no. 7 with the highest Mn content among all the YIG samples under study has very low amounts of Pb and Bi ions. This sample has *p*-type conductivity in a wide temperature range (20–460°C). For sample no. 51, the θ values are close to zero at $t > 230$°C, whereas, in the ferromagnetic state, θ is positive.

In Fig. 6, we present the temperature dependence of resistivity (curve *1*) and thermopower (curve *2*) for sample no. 7. Note that behavior of lnρ and θ with an increase in temperature is quite different. Resistivity ρ has the maximum at 190°C. With an increase in the temperature ($1000/T = 2.2$–1.9), resistivity increases in an almost quasi-linear manner and shows stepwise anomalies and the changes in the slope. The thermopower θ is almost twice as low in the temperature range $1000/T = 2.35$–2.0 and has the first minimum at 150°C ($1000/T = 2.36$). The maximum thermopower is observed at $t = 230$°C ($1000/T = 1.99$). Within this temperature range, the values of lnρ are almost constant. At $t = 288$°C ($1000/T = 1.78$), both ρ and θ exhibit anomalous behavior (θ has a minimum) associated with the transition of sample no. 7 from the ferromagnetic to paramagnetic state. In Fig. 6, we can see that the extremum values of resistivity and thermopower in the whole temperature range under study are attained at the same temperatures. However, in most cases, the minimum in ρ corresponds to the maximum in θ (and vice versa). This means that the mechanisms underlying these kinetic properties are different. In [12], it was revealed that the resistivity and the absorption coefficient in the IR range depend on the *K*/*nk* ratio, i.e., on the fraction of conduction electrons in the sample. Consider the thermopower of the YIG samples with the intensities of incoherent X-ray scattering (*nk*). This makes sense, because the analysis of transport properties in the vicinity of magnetic critical points shows the important role of inelastic scattering of conduction electrons in the vicinity of critical fluctuations [18].

In Fig. 7, we present the dependence of thermopower on *nk* for eleven YIG samples at $t = 300$°C. Curves *1* and *2* correspond to the (110)-oriented samples of groups I and II, respectively. In the paramagnetic state of the (110)-oriented samples, curves *1* and *2* (each of them describes three samples) are almost parallel, whereas curves *3* and *4* (orientation (111)) form an acute angle.

In the garnet-type ferrite, the presence of cation sublattices, whose magnetic and electrical characteristics are not equivalent, and the interactions between the impurity ions (Mn–Ba and Sm–Ba) [11] compete and lead to the anomalous behavior of resistivity and thermopower not only in the vicinity of the Curie point but also in other sections of the temperature range under study (Figs. 1, 2, 5, and 6).

Comparing the θ values for differently oriented YIG plates (see table), we see that the thermopower of the (111)-oriented samples is positive and varies only slightly in the temperature range 300–460°C. As was mentioned earlier, the easy magnetization axes and dislocations surrounded by the space charge are located along the [111] direction. It is well known that the static dislocations (solitons) give rise to stress and strain fields in the crystal lattice. These fields determine the mechanical, magnetic, and optical properties of real crystals [19]. It should be noted that the θ values increase by a factor of 2–3 for samples of group I (nos. 42 and 34) in the temperature range 200–300°C, whereas, for the samples of group II (nos. 46 and III-6), the θ values decrease by 5–15% within the same temperature range. Among the (110)-oriented samples, a significant increase in θ (by about an order of magnitude) is observed only for sample no. 50" at 200–300°C. This sample is characterized by a moderate optical quality and the minimum *K*/*nk* value. A large increase in θ is also observed in sample nos. 52 and 41 of group I. Sample no. 51 exhibits unusual behavior of θ: at 250°C, the θ value decreases by about half an order of magnitude in comparison with the value at 200°C and almost vanishes at temperatures higher than 300°C (see table). According to Mott, only the half-filled impurity band should lead to a low or zero value of θ [20]. In addition, the simultaneous presence of Fe^{2+} and Fe^{3+} ions in the octahedral sites determines the constant θ value over a certain temperature range, since the formation of charge carriers requires low activation energies [17]. The change in the θ sign at low temperatures observed for sample no. 40, can be interpreted as the change in the mechanism of conductivity from the charge transfer by excited charge carriers to the band conductivity in a certain band provided by complexes of defects. The necessity of the compensation was first emphasized in the theoretical studies by Mott and Conwell as the main condition for the action of the mechanism of conductivity over impurities [20, 21]. The thermopower is determined mainly by the density of states; therefore, in the range of hopping conductivity, θ is positive, which corresponds to the hole conductivity at a rather low compensation. In real YIG samples, the one type of impurities and the complete absence of the compensation are impossible. If only one impurity is indicated in the text or in the table, e.g., only Ba ions, this signifies that the plate contains either Fe-ions of different valences or Sm, Mn, V, and B ions, or oxygen vacancies with such low (micro) concentrations, that they cannot be defected by the methods used. In general, the crystals contain a combination of various point defects, but only one of these defects dominates in a certain temperature range [22].

CONCLUSION

The (111)-oriented YIG samples have the minimum resistivities, because the charge transfer proceeds along the chains with the highest concentration of defects (Fe ions located in the octahedral lattice, oxygen anions, Y ions in the dodecahedral sites). The direction of these chains coincides with the easy magnetization axis. Among the samples cut out from one crystal (sample nos. 40, 41, and 42), the (111)-oriented sample no. 42 has the lowest and (100)-oriented sample no. 40 has the highest resistivity.

It was shown that the YIG resistivity is provided by the fraction of conduction electrons, which is determined by the *K*/*nk* ratio, the degree of the structural and optical perfection, and the type of the dominant impurity, which determines the conductivity type of the YIG sample considered.

The maximum resistivities were determined for the (110)- and (100)-oriented YIG plates with the lowest *K*/*nk* ratio (sample nos. 50" and 40), i.e., the least number of conduction electrons. In these samples, the charge transfer occurs along the periodic chains of bonds along [001], which contain Fe ions in the tetrahedral sites and give rise to insignificant distortions along the charge-transfer path. The anomalies in the form of kinks in the linear dependence $\ln\rho$ (T^{-1}) can be explained not only by the change in the magnetic state but also by the existence of several competing mechanisms of conductivity. In Figs. 1, 2, and 6, one can see, in addition to kinks, also various deviations from the linear dependence—the convex or concave portions at the temperatures not associated with the Curie temperature T_C. Usually, garnet crystals are multicomponent systems where, for the time being, only Mn and Sm ions are singled out as dominant active impurities.

The presence of Mn and Sm ions (possessing magnetic moments and having the valence ranging from 2 to 4) in plates nos. 7, 41, and 52 results in an increase in the number of conduction electrons and, hence, in a drastic decrease in the resistivity in these samples of group I (see table). For the (110)-oriented sample no. 52, a pronounced splash in θ is observed in the temperature range 450–460°C. This can be associated with the high concentration gradient for Sm ions and to their nonuniform distribution together with Ba and V ions. The presence of Pt^{4+} ions in (110)-oriented sample no. 50, the dominant impurities, leads to the formation of donors and the *n*-type conductivity.

We believe that the value of thermopower can be characterized by the intensity of incoherent X-ray scattering *nk* (see Fig. 7) or by the parameter *nk*/*K*.

REFERENCES

1. S. Geller and M. A. Gilleo, J. Phys. Chem. Solids **3**, 30 (1957).
2. D. L. Wood and J. P. Remeika, J. Appl. Phys. **38**, 1038 (1967).
3. R. Metselaar and P. K. Larsen, J. Phys. Chem. Solids **37**, 599 (1976).
4. R. Metselar and M. Hyberts, J. Solid State Chem. **22**, 309 (1977).
5. Ya. M. Ksendzov, A. Kotel'nikova, and V. V. Makarov, Fiz. Tverd. Tela (Leningrad) **15**, 2343 (1973) [Sov. Phys. Solid State **15**, 1563 (1973)].
6. S. Iida and H. Miwa, J. Phys. Soc. Jpn. **21**, 2505 (1966).
7. A. Rosencwaig and A. W. Tabor, J. Appl. Phys. **42**, 1643 (1971).
8. J. Dong and L. Kunquan, Phys. Rev. B **43**, 8808 (1991).
9. I. D. Lomako, T. V. Smirnova, A. N. Igumentsev, and A. A. Mel'nikov, Zh. Prikl. Spektrosk. **63**, 667 (1996).
10. I. D. Lomako, A. G. Dutov, and A. N. Igumentsev, Zh. Prikl. Spektrosk. **67**, 217 (2000).
11. I. D. Lomako and A. G. Dutov, Kristallografiya **47** (1), 128 (2002) [Crystallogr. Rep. **47**, 120 (2002)].
12. I. D. Lomako, Kristallografiya **47** (4), 724 (2002) [Crystallogr. Rep. **47**, 666 (2002)].
13. S. Sh. Gendelev and S. E. Semenov, Izv. Akad. Nauk SSSR, Ser. Fiz. **35**, 1220 (1971).
14. S. Sh. Gendelev, L. M. Dedukh, Yu. P. Kabanov, and V. I. Nikitenko, Dokl. Akad. Nauk SSSR **237**, 817 (1977) [Sov. Phys. Dokl. **22**, 747 (1977)].
15. J. S. Blakemore, *Semiconductor Statistics* (Pergamon, Oxford, 1962; Mir, Moscow, 1964).
16. V. V. Kaminskiĭ and S. M. Solov'ev, Fiz. Tverd. Tela (St. Petersburg) **43**, 423 (2001) [Phys. Solid State **43**, 439 (2001)].
17. S. Krupicka, *Physik der Ferrite und der verwandten magnetischen Oxide* (Academia, Prague, 1973; Mir, Moscow, 1976), Vol. 2.
18. P. P. Craiy and W. I. Goldburg, J. Appl. Phys. **40**, 964 (1969).
19. *Modern Crystallography*, Vol. 4: *Physical Properties of Crystals*, Ed. by B. K. Vainshtein, A. A. Chernov, and L. A. Shuvalov (Nauka, Moscow, 1981; Springer-Verlag, Berlin, 1988).
20. N. F. Mott and E. A. Davis, *Electronic Processes in Non-Crystalline Materials* (Clarendon, Oxford, 1971; Mir, Moscow, 1974).
21. E. M. Conwell, Phys. Rev. **103**, 51 (1956).
22. Yu. D. Tret'yakov, Vestn. Mosk. Univ., Ser. 2: Khim., No. 2, 216 (1970).

Translated by K. Kugel

Crystallography Reports, Vol. 48, No. 1, 2003, pp. 12–15. Translated from Kristallografiya, Vol. 48, No. 1, 2003, pp. 17–20.

STRUCTURE OF INORGANIC COMPOUNDS

Crystal Structure of β-Uranophane from the Transbaikal Region and Its Relation to the Structure of the α Modification

A. V. Barinova*, R. K. Rastsvetaeva, G. A. Sidorenko***, and I. A. Verin****

** Faculty of Geology, Moscow State University, Leninskie gory, Moscow, 119992 Russia*

e-mail: rast@ns.crys.ras.ru

*** Shubnikov Institute of Crystallography, Russian Academy of Sciences, Leninskiĭ pr. 59, Moscow, 119333 Russia*

**** Fedorov All-Russia Institute of Mineral Resources (VIMS), Staromonetnyĭ per. 29, Moscow, 109017 Russia*

Received August 1, 2002

Abstract—The crystal structure of β-uranophane was refined (R = 0.034, 4898 independent reflections), and its relation to the α modification was established. The modifications of uranophane differ primarily in the orientation of the silicon–oxygen tetrahedra with respect to the plane of the layer formed by Si-tetrahedra and U^{6+}-bipyramids and also in the arrangement of calcium cations between the layers. In the structure of β-uranophane, calcium cations are bound to three oxygen atoms of uranyl groups of the adjacent U–O-polyhedra, whereas Ca atoms in the α modification are bound only to two uranyl oxygen atoms. *© 2003 MAIK "Nauka/Interperiodica".*

Two polymorphs of calcium uranyl silicate (α-uranophane and β-uranophane) occur in nature. Both minerals have the stable elemental composition $Ca(UO_2)_2[SiO_3OH] \cdot 5H_2O$ and contain no isomorphous impurities. The paragenetic association was established for many natural specimens of this compound [1], which indicates that these modifications can be formed under similar conditions. This assumption was confirmed experimentally during decrystallization of the common gel [2]. However, the comparison of the solubility curves shows that the β modification is formed in a weakly acidic medium, whereas the α modification, over a wide range of neutral and alkaline solutions, which is reflected in the more widespread occurrence of the α modification in nature. Slight deviations from pH 7 (close to "neutral") can stimulate the formation of mixed-layered phases and inclusions of the α modification into β-uranophane resulting in crystal imperfection. The structure of α-uranophane was first solved in [3] and refined in [4] within the sp. gr. $P2_1$. Recently, we have refined the structure of α-uranophane within the centrosymmetric sp. gr. $P2_1/b$ [5] on a specimen from the hydrothermal deposit of the Strel'tsovskiĭ ore field (Transbaikal region). In the oxidation zone of this deposit, crystals of α-uranophane occur in association with the second modification (β-uranophane) existing as massive amber–honey-colored formations. From these formations, single-crystal chips were easily separated along perfect-cleavage planes. Although the structure of β-uranophane had already been established [6], we refined it starting from the atomic coordinates determined earlier. The refinement completely confirmed the structure motif described in [6]. However, we refined the structure to a lower R factor and obtained atomic coordinates with a higher accuracy.

The crystallographic parameters of the mineral and details of X-ray diffraction study are given in Table 1. The atomic coordinates and principal interatomic distances are listed in Table 2 and Table 3, respectively.

Like α-uranophane, the structure of β-uranophane contains U^{6+}-ions coordinated by seven O anions, which form typical pentagonal bipyramids. In these polyhedra, two O atoms, which either occupy lone vertices or are included into Ca-polyhedra, are located at short distances from the central cation and form uranyl groups UO_2. The five remaining O atoms are located in the equatorial plane. The U^{6+}-bipyramids share edges to form chains along the [100] direction. The adjacent uranium-containing chains are linked into layers parallel to the (001) plane via the Si-tetrahedra sharing the vertices and edges with the U^{6+}-bipyramids. Similar mixed layers of T-tetrahedra and UO_7-bipyramids were found in 16 structures (half of theses structures belong to minerals) [9], and these layers are topologically equivalent to the uranophane layers. In β-uranophane, the layers are linked by the Ca cations along the longest b axis and

1063-7745/03/4801-0012$24.00 © 2003 MAIK "Nauka/Interperiodica"

Table 1. Crystallographic parameters and characteristics of X-ray diffraction study

Characteristic	Data and conditions
Formula	$Ca(UO_2)_2[SiO_3OH]_2 \cdot 5H_2O$
Unit-cell parameters, Å	
a	13.947
b	15.465
c	6.626
β, deg	91.399
Unit-cell volume *V*, Å^3	1428.73
Sp. gr.; *Z*	$P2_1/b$; 4
$\rho_{exp}-\rho_{calcd}$, g/cm^3	3.96–4.08, 3.9
Absorption coefficient μ, cm^{-1}	3.384
Molecular weight	1712.68
Diffractometer	ENRAF–NONIUS
Radiation, wavelength	MoK_α, 0.709
Total number of reflections	9227
Number of reflections with, $\|F\| > 3\sigma(F)$	9069
Maximum $\sin\theta/\lambda$	0.806
Ranges of the indices of measured reflections	$-22 < h < 22$; $0 < k < 24$; $-10 < l < 10$
Number of reflections upon averaging equivalent reflections	4898
R-factor upon merging	0.052
Program for structure calculations	AREN [7]
Absorption correction	DIFABS [8]
R-factor upon anisotropic refinement	0.037
Extinction parameter *E*	0.0000015

Table 2. Atomic coordinates and equivalent thermal parameters

Atom	*x*/*a*	*y*/*b*	*z*/*c*	U_{eq}, Å^2
U(1)	0.0192(0)	0.2601(0)	0.2627(0)	1.09(1)
U(2)	0.2315(0)	0.7395(0)	0.4708(0)	0.96(1)
Ca	0.1902(1)	0.4856(1)	0.2826(2)	1.30(2)
Si(1)	0.0187(1)	0.2230(1)	0.7297(2)	0.73(3)
Si(2)	0.2670(1)	0.1945(1)	0.0636(2)	0.56(3)
O(1)	0.2652(3)	0.3523(3)	0.4927(9)	1.00(8)
O(2)	0.9920(5)	0.1491(4)	0.2347(10)	1.62(9)
O(3)	0.7321(4)	0.8741(3)	0.4401(8)	0.90(8)
O(4)	0.0441(5)	0.3724(4)	0.2893(10)	1.7(1)
O(5)	0.1794(4)	0.2234(4)	0.2114(7)	0.98(8)
O(6)	0.8923(4)	0.7639(5)	0.4197(8)	1.37(9)
O(7)	0.3579(4)	0.2045(4)	0.2200(8)	1.23(8)
O(8)	0.5684(4)	0.7492(4)	0.4260(8)	1.30(9)
O(9)	0.9795(4)	0.7189(4)	0.0718(7)	1.12(8)
O(10)	0.7271(4)	0.7468(4)	0.1343(8)	0.99(8)
OH(1)	0.9857(5)	0.8807(5)	0.2099(11)	1.7(1)
OH(2)	0.7414(5)	0.9074(5)	0.0016(11)	1.9(1)
$H_2O(1)$	0.5426(5)	0.9459(6)	0.1656(14)	2.3(1)
$H_2O(2)$	0.3609(8)	0.4906(7)	0.3296(17)	3.1(2)
$H_2O(3)$	0.8044(7)	0.5927(5)	0.0255(12)	2.5(2)
$H_2O(4)$	0.8770(6)	0.4992(5)	0.3770(11)	2.2(1)
$H_2O(5)$	0.1303(8)	0.0064(7)	0.2371(18)	3.5(1)

also by hydrogen bonds between the hydroxy groups and water molecules.

The essential difference between the two uranophane modifications is the orientations of the Si-tetrahedra relative to the layer planes. In the structure of α-uranophane (Fig. 1a), the free vertices of all the Si-tetrahedra located on one side of the uranium-containing chains deviate in the same directions with respect to the layer plane, whereas the free vertices of the Si-tetrahedra located on another side of the uranium-containing chains deviate in the opposite directions. By contrast, the free vertices of the Si-tetrahedra located on each side of the uranium-containing chains in the structure of β-uranophane alternate in their orientations relative to the layer plane (Fig. 1b), which results in doubling of the period along the chain axis (~7 Å × 2). These differences can also be described in the context of the symmetry approach [10, 11] with the aid of zero-dimensional modules. Each module consists of one bipyramid and one tetrahedron; the modules are related by the symmetry elements located on the shared edges of the pentagonal bipyramids and thus form chains. Unlike the structure of β-uranophane, in which the twofold axes alternate with inversion centers in the chains, in the structure of α-uranophane, the zero-dimensional modules are related by twofold axes.

The difference in the orientation of Si-tetrahedra in two polymorphs is also reflected in the arrangement of the Ca cations between the layers. Although the structure of α-uranophane is centrosymmetric, the Ca atoms statistically occupy only one of two positions related by a center of symmetry (Ca–Ca distance is ~4 Å). By contrast, the Ca atoms in the structure of β-uranophane occupy both positions separated by a distance exceed-

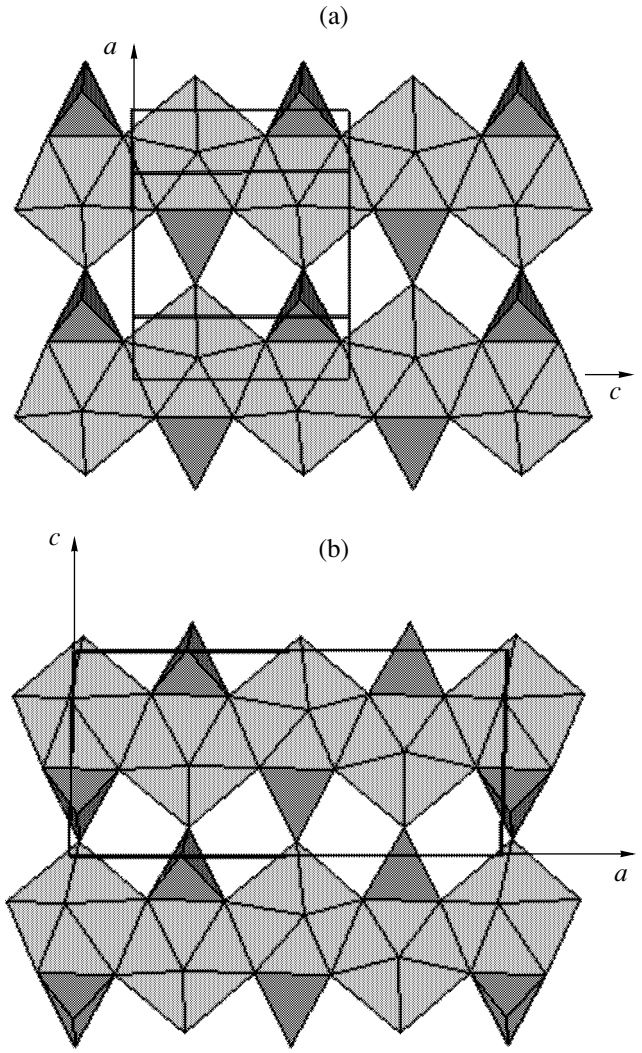

Fig. 1. Layers of UO_7- and SiO_4-polyhedra in the structures of (a) α-uranophane and (b) β-uranophane.

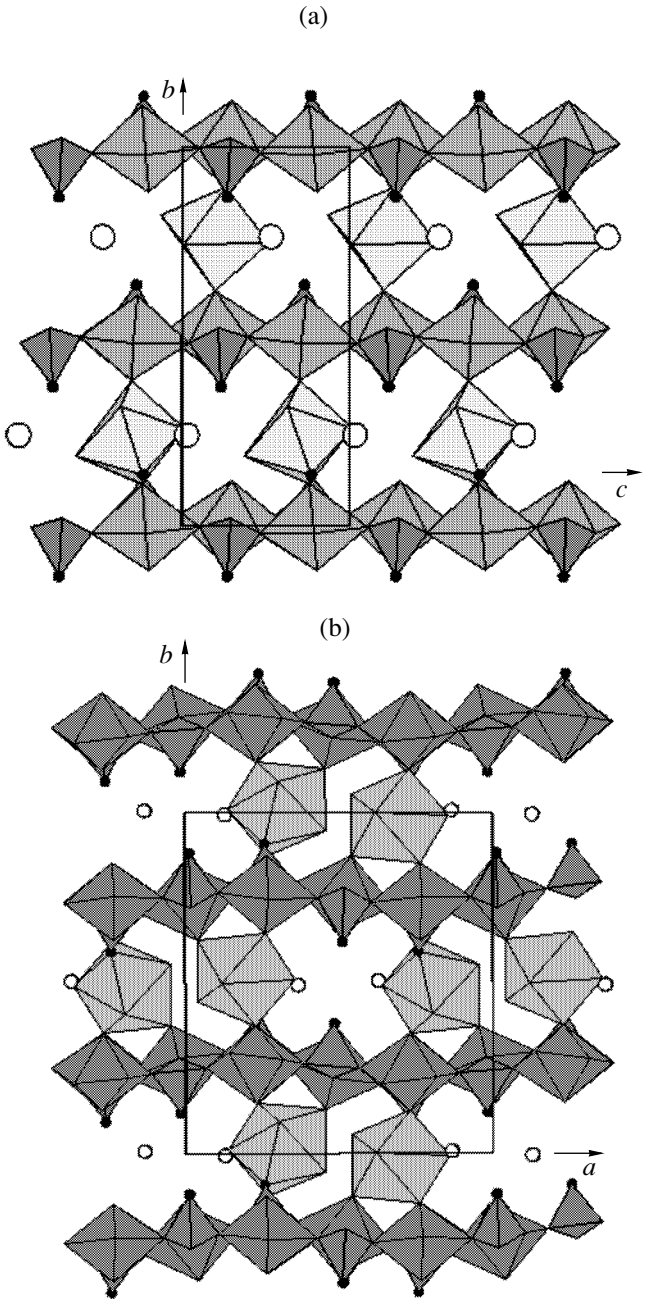

Fig. 2. Structures of (a) α-uranophane projected onto the (100) plane and (b) β-uranophane projected onto the (001) plane. OH groups and free water molecules are indicated by solid and empty circles, respectively.

ing 6 Å. Because of these displacements, the Ca cations in the structure of α-uranophane are bound to two oxygen atoms of the uranyl groups from two adjacent layers, whereas the calcium cations in the structure of β-uranophane are bound to three oxygen atoms of uranyl groups. Two of these oxygen atoms are involved in coordination of the uranium atoms of one layer, whereas the third oxygen atom is coordinated to the uranium atom from another layer (Figs. 2a and 2b). Correspondingly, the Ca-polyhedra differ in their coordination numbers. In the structures of the α- and β-modifications, the Ca atoms are located in the seven- and eight-vertex polyhedra, respectively. Therefore, it can be assumed that the β modification is characterized by stronger inter layer bonding.

It should be noted that the structure of β-uranophane has two types of OH groups, unlike the structure of α-uranophane containing OH groups of only one type statistically incorporated into the Ca-polyhedra. In the structure of β-uranophane, the OH(2) group is bound to the Ca atom, whereas the OH(1) group is not bound to the Ca atom.

The differences between the structures of the two polymorphs clearly manifest themselves in the IR and luminescence spectra. In the IR spectra of both modifications (Fig. 3) measured by N.V. Chukanov, the bands

Table 3. Interatomic distances, Å

U-seven-vertex polyhedra			
U(1)–O(2)	1.767(7)	U(2)–O(1)	1.761(5)
O(4)	1.778(7)	O(3)	1.769(5)
O(9)	2.240(5)	O(10)	2.238(5)
O(7)	2.325(5)	O(6)	2.276(6)
O(5)	2.337(5)	O(8)	2.292(6)
O(8)	2.429(6)	O(5)	2.432(5)
O(6)	2.442(6)	O(7)	2.483(5)
	⟨2.188⟩		⟨2.179⟩
Si-tetrahedra			
Si(1)–O(9)	1.593(6)	Si(2)–O(10)	1.599(6)
O(6)	1.620(6)	O(7)	1.625(5)
O(8)	1.626(6)	OH(2)	1.636(8)
OH(1)	1.653(8)	O(5)	1.646(6)
	⟨1.623⟩		⟨1.627⟩
Ca-eight-vertex polyhedron			
Ca–H_2O(3)	2.376(8)		
H_2O(2)	2.39(1)		
H_2O(1)	2.426(8)		
O(3)	2.471(6)		
H_2O(4)	2.475(8)		
OH(2)	2.603(8)		
O(1)	2.685(6)		
O(4)	2.688(8)		
	⟨2.514⟩		

at (3450, 3348), (986, 946), and (880, 845) cm^{-1} were attributed to the H_2O molecules, UO_2 groups, and SiO_4-tetrahedra, respectively. However, the ν(Si–O) and ν(UO_2) bands in the IR spectrum of the β modification are split, unlike analogous bands in the spectrum of the α modification. In addition, the ν(SiO–H) band in the spectrum of the β modification has a higher intensity than the analogous band in the spectrum of α-uranophane.

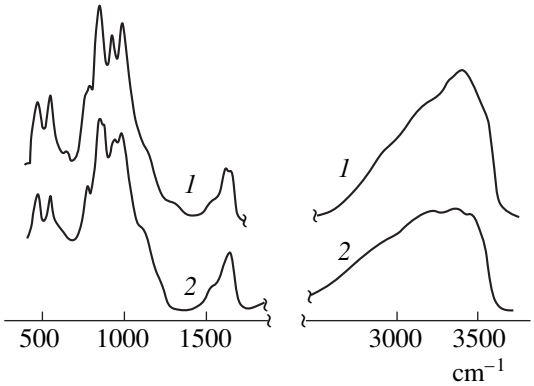

Fig. 3. IR spectra of (*1*) α-uranophane and (*2*) β-uranophane.

To summarize, the analysis of the structural relations between α- and β-uranophanes provided the interpretation of the difference in their unit-cell parameters, crystal morphology and properties (in particular, instability of optical characteristics), and the conditions of the formation of these polymorphs.

ACKNOWLEDGMENTS

This study was supported by the Russian Foundation for Basic Research, project no. 02-05-64080.

REFERENCES

1. I. Kh. Moroz, G. A. Sidorenko, and I. G. Zhil'tsova, Zap. Vses. Mineral. O–va **104** (5), 559 (1975).
2. V. I. Ludikov, I. G. Zhil'tsova, G. A. Sidorenko, and S. A. Perlina, Dokl. Akad. Nauk SSSR **245** (1), 212 (1979).
3. D. K. Smith, J. W. Gruner, and W. N. Lipscomb, Am. Mineral. **42**, 594 (1957).
4. P. D. Ginderow, Acta Crystallogr., Sect. C: Cryst. Struct. Commun. **44** (3), 421 (1988).
5. A. V. Barinova, R. K. Rastsvetaeva, G. A. Sidorenko, and D. Yu. Pushcharovskiĭ, Dokl. Akad. Nauk **378** (2), 201 (2001).
6. K. Viswanathan and O. Harneit, Am. Mineral. **71**, 1489 (1986).
7. V. I. Andrianov, Kristallografiya **32** (1), 228 (1987) [Sov. Phys. Crystallogr. **32**, 130 (1987)].
8. N. Walker and D. Stuart, Acta Crystallogr., Sect. A: Found. Crystallogr. **39** (2), 158 (1983).
9. P. C. Burns, M. L. Miller, and R. C. Ewing, Can. Mineral. **34** (4), 845 (1996).
10. R. K. Rastsvetaeva, A. V. Arakcheeva, and A. V. Barinova, Vestn. Nizhegorod. Univ., Fiz. Tverd. Tela **1** (4), 38 (2001).
11. A. V. Barinova, R. K. Rastsvetaeva, and A. V. Arakcheeva, in *Proceedings of the 2nd International Symposium "Phase Transitions in Solid Solutions and Alloys," Sochi, 2001*, p. 42.

Translated by T. Safonova

Crystallography Reports, Vol. 48, No. 1, 2003, pp. 124–140. Translated from Kristallografiya, Vol. 48, No. 1, 2003, pp. 130–147.

LIQUID CRYSTALS

Simulation of Electrooptical Effects and Dynamics of Ferroelectric Liquid Crystals

S. P. Palto

Shubnikov Institute of Crystallography, Russian Academy of Sciences, Leninskiĭ pr. 59, Moscow, 117333 Russia

e-mail: palto@online.ru

Received June 21, 2002

Abstract—The behavior of ferroelectric liquid crystals in an external electric field is simulated numerically. The equations that describe the dynamics of the director of a liquid crystal are derived within the continuum theory of elasticity with due regard for compressibility of smectic layers, finite anchoring energy, and dielectric properties of orienting coatings and external elements of a real electric circuit. These equations make the basis for simulation of the electrooptics of ferroelectric liquid crystals. The specific features and mechanisms of the surface-stabilized bistability and hysteresis-free electrooptical switching (the *V*-shape effect) are discussed.

INTRODUCTION

At present, the numerical simulation of physical processes occurring in liquid crystals (LCs) is of great importance. This is explained, first and foremost, by the complexity and diversity of the physical processes in LCs. The use of various simplified approaches that allow simple analytical solutions turned out to be insufficient for a deep understanding of the physics of the phenomena observed. In recent years, the methods of numerical simulation of electrooptics in nematic liquid crystals have become very popular. Now, there exist commercial programs that allow one to simulate rather reliably the dynamics and electrooptics of nematic liquid crystals [1, 2]. This process was stimulated to great extent by the development of the display technology. It is the numerical simulation that provides better understanding of many electrooptical effects and their use in the display technology.

The achievements in the field of smectic LCs are less impressive than in the field of nematic ones. When the author, already possessing some experience in the simulation of electrooptics of nematic LCs, started designing software for simulating the dynamics and electrooptics of ferroelectric liquid crystals, he encountered numerous physical problems in derivation of the equations that describe the dynamics of the director in smectic liquid crystals (smectics) and some other important aspects associated with the role of the constituent elements of external electric circuits in the presence of spontaneous polarization of LCs. The conventional forms of the equations that describe the dynamics of ferroelectric smectic liquid crystals turned out to be oversimplified because they ignored a number of the well-known experimentally observed effects.

In the present study, we derive these equations within the framework of the continuum theory of elasticity. I introduced an additional term into the traditional expression for the free energy of smectics, which takes into account the compressibility of smectic layers and, thus, makes the resulting equations of the dynamics more comprehensive. For example, at certain values of the elasticity modulus of the smectic layers, these equations describe the motion of the director over the cone (traditionally postulated in ferroelectrics). The electroclinic effect is also described by these equations (whereas, usually, this effect is interpreted within the framework of the Landau theory only in the vicinity of the smectic A^*–smectic C^* phase transition [3, 4]).

The problem considered in this article is a complex one and requires the solution of the equations not only in the bulk of a liquid crystal but also at its boundaries, where the LC interacts with the orienting surfaces. The important feature of the approach suggested here is the complement of the equations of the dynamics of a LC with the corresponding system of equations that describe the currents flowing in an external electric circuit. It is the consistent solution of all the equations mentioned above that provides the creation of the realistic picture of the processes occurring in ferroelectric LCs.

Since this article is intended not only for the people working with LCs but also for all those who are interested in problems of mathematical simulation of similar systems, I explain the physical meaning of some key terms conventionally used in the description of LCs.

Ferroelectric LCs considered in this article belong to the class of smectic LCs characterized by the orientational order of the molecules and, at the same time, possessing layer structures [3, 4]. Unlike nematic LCs

1063-7745/03/4801-0124$24.00

characterized only by orientational order, smectics also possess one-dimensional periodicity. The corresponding interlayer period is determined by the size and tilt of the molecules in the smectic layers. There is no long-range translational order in the plane of the layers, which makes smectics similar to liquids. However, like solid crystals, smectics possess translational periodicity along the normal to the layers. Along this direction, smectics are weakly compressible "rigid" systems. The latter property provides some specific electrooptical effects and allows one to make a number of simplifications, not always quite justified, in writing the equations of the dynamics of smectic LCs, and especially in the quantitative description of the system and some fine effects, which, in some instances, play the decisive role. These cases will also be discussed in the article.

In terms of symmetry, the condition necessary for the manifestation of the ferroelectric properties in smectics is the chirality and tilt of the molecules in the layers, which results in the absence of an inversion center and a symmetry plane normal to smectic layers. As a consequence, the polarization along the direction perpendicular to the layer normal and the director of a LC can arise. This effect was first indicated by Meyer *et al.* [5]. The corresponding phases that may possess ferroelectricity are related to chiral smectic phases denoted as *C**.

Ferroelectric LCs are still less used in the display technology than nematics. This is explained by the technological difficulties in obtaining homogeneous samples and also insufficient knowledge about the properties of smectics. However, smectics also have an important advantage in comparison with the nematic LCs—they are characterized by extremely short switching times (microseconds). Therefore, ferroelectric LCs are used, first and foremost, in high-speed light modulators and controllable phase plates and also in some devices that require the linear electrooptical response. Some new electrooptical effects such as, e.g., hysteresis-free switching, allow us to hope for the creation of the gray scale and the widespread use of ferroelectric LCs in the display technology. Up to now, despite the intense study by various scientific groups [6–8], hysteresis-free switching has not been interpreted reliably and is considered as a somewhat mysterious phenomenon. Our earlier studies [9] (which also include the solution of the equations described in the present article) allow one to clarify this mysterious effect. The comparison of the predictions based on the numerical solution of the equations given below and the experimental data show that the system of equations obtained is sufficiently comprehensive, and the approach suggested is rather efficient.

The article consists of two main parts. The first one is devoted to the detailed derivation of the equations that describe the dynamics of the director of a ferroelectric LC. I thought that it was also important to consider here numerous consequences despite the fact that many of them could be obtained by the reader himself, because some of the calculations are rather cumbersome, which considerably increases the number of possible errors. Moreover, my own experience shows that the statement completeness and detalization are always justified, especially if one uses the equations derived for numerical simulation. The second part of the article is dedicated to the results of simulation and discussion of two electrooptical effects–bistability in surface-stabilized ferroelectric LC (the well-known Clark–Lagerwall effect [10, 11]) and also the dynamic effect of hysteresis-free electrooptical response (the so-called *V*-shape effect). Although both effects are intensely studied (especially, the bistability effect), many of the important aspects of these effects have not been quite understood as yet.

Simulation of electrooptics also requires the solution of the corresponding Maxwell equations for one-dimensionally nonuniform anisotropic optic media. The basis for solving this problem was suggested by Berreman in his fundamental study [12]. The Berreman approach is now widely used for solving complex optical problems. Earlier, I described the corresponding generalized algorithm for the numerical solution of the optical problem in [13]. There are also some analytical solutions convenient for the uniaxial optical media [14]. Therefore, the optical problem is not considered in this article and I focus here attention only on the results obtained in simulation of electrooptics.

1. DYNAMIC EQUATIONS FOR THE DIRECTOR OF A FERROELECTRIC LIQUID CRYSTAL

We consider a layer of a ferroelectric liquid crystal (FLC) between two parallel surfaces–electrodes connected to a voltage source. The laboratory coordinate system is chosen in such a way that the *x* and *y* axes lie in the plane of the first surface, whereas the *z* axis is directed along the normal to the second one. This is a natural and very convenient choice for an experimentalist. Such a choice is also explained by the fact that the simulation is associated with the solution of an optical problem for which another choice of the coordinate system would be associated with many difficulties. Usually, FLC are described theoretically in the coordinate system in which the *z* axis is directed along the normal to the smectic layers. Therefore, the reader should be very careful when comparing the results obtained in the present article with the data published earlier.

The description of the dynamics of molecules in a LC is based on the notion of a director, $\mathbf{n} = (n_x, n_y, n_z)$, which is a pseudovector that represents two equivalent directions ($\mathbf{n} = -\mathbf{n}$) of the preferable orientation of long axes of the constituent molecules in a LC. Despite the fact that *n* is a mathematical abstraction, it is associated with the physical (although very small) volume of a LC. Therefore, when discussing the spatial distribution of molecules in an LC, it is convenient to use the notion of

a director distribution. In a similar way, it is convenient to describe the dynamics of molecules in an LC as the dynamics of its director. The general considerations make it clear that, in order to write the equations of the director motion, one has to define the torques that act on the director. In this article, we consider the orientational dynamics, i.e., changes in the angular coordinates of the director, and ignore the hydrodynamics of an LC, which seems to be the only essential simplification that should be considered separately.

A method adequate for the determination of a torque, is the variation of the director state and the determination of the virtual physical work necessary for changing this state. It is convenient to use as the function of the director state the density of the free energy F, which, in the general case, consists of two components—the density of the elastic-deformation energy and the density of the electric-field energy. To the equilibrium state there corresponds the minimum of the total free energy

$$\Phi = \int_V F dV, \tag{1}$$

which, in accordance with the well known theorem of the mathematical analysis, is obtained by solving the system of the Lagrange–Euler equations. We are interested here only in those liquid-crystal cells where the director distribution along the z direction is nonuniform and, therefore, the free-energy density is a function of seven variables $F = F(z, n_x, n_y, n_z, \partial n_x/\partial z, \partial n_y/\partial z, \partial n_z/\partial z)$. However, the requirements that the vector $\mathbf{n}$ should have the unit length reduces the number of the independent variables, and the corresponding system of the Lagrange–Euler equations takes the form

$$-\frac{\partial(F+g)}{\partial n_i} + \frac{d}{dz}\left(\frac{\partial(F+g)}{\partial n_i'}\right) = 0, \quad i \in \{x, y, z\}, \tag{2}$$

$$g \equiv \frac{1}{2}\lambda\left(1 - \sum_i n_i^2\right) = 0, \tag{3}$$

where $n_i' = \partial n_i/\partial z$.

Physically, the left-hand sides of the equations of system (2) represent the resulting torque, which, in the equilibrium state, is equal to zero (hereafter we consider the torque related to the unit volume). The first term is the consequence of the virtual physical work which should be done during the variation of the director state. This torque is balanced by the second term, which reflects the environmental reaction associated with the nonuniform director distribution. Expression (3) (where λ is the Lagrange multiplier) is the consequence of the additional normalization condition decreasing the number of the independent variables and modifying the function to be differentiated in the Lagrange–Euler equation, as can be seen from Eq. (2).

In order to pass to the equations of the director dynamics, we have to introduce into Eq. (2) the corresponding dynamic torques associated with the director rotation. These are the inertia and friction torques with the latter being responsible for the energy dissipation. Up to now, there are no experimental data that prove the importance of the inertia forces, and, therefore, we consider only the contribution from the friction torque determined by the rotational-viscosity tensor $\boldsymbol{\gamma}$. Thus, Eq. (2) is transformed into the following vector equation:

$$\boldsymbol{\gamma}\frac{d\mathbf{n}}{dt} = -\frac{\partial F}{\partial \mathbf{n}} + \frac{d}{dz}\left(\frac{\partial F}{\partial \mathbf{n}'}\right) + \lambda\mathbf{n}. \tag{4}$$

The left-hand side of Eq. (4) represents the total derivative of the director state with respect to time. Strictly speaking, this is only an approximation admissible in virtue of the simplification made above associated with the neglect of the hydrodynamics and allowance for the rotational viscosity alone. In the numerical solution, the last term in Eq. (4) containing the Lagrange multiplier is taken into account automatically if the director is normalized at each discrete time and space interval. As is seen from Eq. (4), the main problem in the derivation of the motion equations for the components of the vector $\mathbf{n}$ is associated with the determination of the form of the free-energy density $F = F(z, \mathbf{n}, \mathbf{n}')$ and its derivatives. The determination of the form of the rotational-viscosity tensor and the boundary conditions is also important.

The total density of the free energy of the FLC volume (at the moment without the allowance for the energy of anchoring with the boundary surfaces which will be considered later) can be represented as the sum of two terms

$$F = F_1 + F_2, \tag{5}$$

where F_1 represents the density of the elastic energy and F_2, the density of the electric-field energy.

1.1. Elastic Energy of a FLC and Corresponding Torques

For a nematic LC, the elastic-energy density is written in the form of the well-known Frank–Oseen expression [15, 16, 3],

$$F_1 = \frac{1}{2}[K_{11}(\mathrm{div}\,\mathbf{n})^2 + K_{22}(\mathbf{n}\,\mathrm{curl}\,\mathbf{n} + q_0)^2 + K_{33}(\mathbf{n} \times \mathrm{curl}\,\mathbf{n})^2]. \tag{6}$$

Here, K_{11}, K_{22}, and K_{33} are the elasticity constants of a LC and q_0 is the quantity characterizing the natural pitch, $P = 2\pi/q_0$ (where, in the case of chirality, q_0 has a nonzero value).

For a chiral smectic LC, Eq. (6) can have the contribution associated with the spontaneous bend deforma-

tion, and Eq. (6) is transformed into the well-known expression [4]

$$F_1 = \frac{1}{2}[K_{11}(\mathrm{div}\,\mathbf{n})^2 + K_{22}(\mathbf{n}\mathrm{curl}\mathbf{n} + q_0)^2 + K_{33}(\mathbf{n}\times\mathrm{curl}\mathbf{n} - \mathbf{b})^2], \quad (7)$$

where $\mathbf{b} = \beta\mathbf{k}\times\mathbf{n}$. Hereafter $\mathbf{k} = (k_x, k_y, k_z)$ is the unit vector of the normal to the smectic layers. Unlike in chiral nematics, the period of the director helix in chiral smectics is determined by both scalar quantity q_0 and vector of the spontaneous bend deformation, **b**.

Expression (7) is often used to consider ferroelectric LCs; however, this expression does not take into account a very important property of smectics—compressibility of smectic layers. The thickness of smectic layers is determined by the size of molecules l and their tilt angle with respect to the normal **n**. The variation of the smectic-layer thickness requires some additional work which, in the linear approximation, can be represented in the form

$$\delta A = K\delta^2/2, \quad (8)$$

where δ is the variation of the smectic-layer thickness and K is the corresponding elasticity coefficient. Excluding interlayer diffusion, we can express δ in terms of the natural tilt angle Ψ of molecules in a nondeformed smectic layer and the cosine determined by the scalar product **nk**. Then Eq. (8) can be represented in the form

$$\delta A = \frac{1}{2}K_4(\cos\Psi - \mathbf{nk})^2, \quad (9)$$

where below K_4 will refer to the elasticity modulus of smectic layers.[1]

Thus, with due regard for Eq. (9), the free-energy density of a smectic LC acquires the form

$$F_1 = \frac{1}{2}[K_{11}(\mathrm{div}\,\mathbf{n})^2 + K_{22}(\mathbf{n}\mathrm{curl}\mathbf{n} + q_0)^2 + K_{33}(\mathbf{n}\times\mathrm{curl}\mathbf{n} - \mathbf{b})^2 + K_4(\cos\Psi - \mathbf{nk})^2]. \quad (10)$$

We limit ourselves to the case where the director distribution is uniform in the *xy* plane, i.e., where the following relationships are valid for the corresponding terms in Eq. (10):

$$\mathrm{div}\,\mathbf{n} = \frac{\partial n_z}{\partial z}, \quad (11.0)$$

$$\mathbf{n}\mathrm{curl}\mathbf{n} = -n_x\frac{\partial n_y}{\partial z} + n_y\frac{\partial n_x}{\partial z}, \quad (11.1)$$

$$(\mathbf{n}\times\mathrm{curl}\mathbf{n})^2 = (\mathrm{curl}\mathbf{n})^2 - (\mathbf{n}\mathrm{curl}\mathbf{n})^2 = n_z^2\left[\left(\frac{\partial n_y}{\partial z}\right)^2 + \left(\frac{\partial n_x}{\partial z}\right)^2\right] + \left[n_x\frac{\partial n_x}{\partial z} + n_y\frac{\partial n_y}{\partial z}\right]^2, \quad (11.2)$$

$$(\mathbf{n}\times\mathrm{curl}\mathbf{n})\mathbf{b} = \beta\left\{\frac{\partial n_x}{\partial z}(k_z n_y n_z + k_x n_x n_y - k_y(n_x^2 + n_z^2)) + \frac{\partial n_y}{\partial z}(k_x(n_y^2 + n_z^2) - k_y n_x n_y - k_z n_x n_z)\right\}. \quad (11.3)$$

Using Eqs. (11) and the notation

$$\xi \equiv n_x, \quad \eta \equiv n_y, \quad \zeta \equiv n_z, \quad \frac{\partial n_x}{\partial z} \equiv \xi', \quad \frac{\partial n_y}{\partial z} \equiv \eta', \quad \frac{\partial n_z}{\partial z} \equiv \zeta' \quad (12)$$

(to abridge the form of the equations), we obtain from Eq. (10) the following expression for the elastic component of the free-energy density:

$$F_1 = \frac{1}{2}\{K_{11}\zeta'^2 + K_{22}(\eta\xi' - \xi\eta' + q_0)^2 + K_{33}[\zeta^2(\eta'^2 + \xi'^2) + (\xi\xi' + \eta\eta')^2]\} - \beta K_{33}[(k_z\eta\zeta + k_x\xi\eta - k_y(\xi^2 + \zeta^2))\xi' + (k_x(\eta^2 + \zeta^2) - k_y\xi\eta - k_z\xi\zeta)\eta'] + \frac{1}{2}K_4[\cos\Psi - \xi k_x - \eta k_y - \zeta k_z]^2. \quad (13)$$

In accordance with Eq. (2), the torques that arise due to elastic interactions are determined by the corresponding derivatives of the free-energy density F_1. Thus, differentiating Eq. (13), we arrive at the following expression for the torque associated with the *x* component of the director:

$$M_{1x} = -\frac{\partial F_1}{\partial\xi} + \frac{d}{dz}\left(\frac{\partial F_1}{\partial\xi'}\right) = [K_{22}\eta^2 + K_{33}(\xi^2 + \zeta^2)]\xi'' + [K_{33} - K_{22}]\xi\eta\eta'' + [K_{33} - 2K_{22}]\xi\eta'^2 + K_{33}\xi\xi'^2 + 2K_{33}\zeta\zeta'\xi' + 2K_{22}\eta\eta'\xi' + 2K_{22}q_0\eta' + \beta K_{33}[(2k_y\zeta - k_z\eta)\zeta' - (2k_z\zeta + k_x\xi + k_y\eta)\eta'] + K_4(\cos\Psi - k_x\xi - k_y\eta - k_z\zeta)k_x. \quad (14)$$

In a similar way, we also obtain the expression for the *y* and *z* components:

$$M_{1y} = [K_{22}\xi^2 + K_{33}(\eta^2 + \zeta^2)]\eta'' + [K_{33} - K_{22}]\eta\xi\xi''$$

[1] The elasticity coefficient can also be defined differently. For example, in the approximation of small variations of the director angle θ with respect to the layer normal (weak compressibility), one can introduce the elasticity coefficient α and write the contribution to the free-energy density as $\alpha(\theta - \Psi)^2/2$. Comparing the latter with Eq. (9) in the approximation of small deviations of θ from Ψ, one can readily obtain $\alpha = K_4(\sin\Psi)^2$. It should also be noted that, in the vicinity of the phase transition into the smectic phase A^*, the value of Ψ is close to zero and the term $\alpha(\theta - \Psi)^2/2 \cong \alpha\theta^2/2$ is equivalent to the first term in the expansion of the free-energy density in the framework of the Landau theory.

$$+ [K_{33} - 2K_{22}]\eta\xi'^2 + K_{33}\eta\eta'^2 + 2K_{33}\zeta\zeta'\eta' + 2K_{22}\xi\xi'\eta' - 2K_{22}q_0\xi' \quad (15)$$
$$+ \beta K_{33}[(k_z\xi - 2k_x\zeta)\zeta' + (2k_z\zeta + k_x\xi + k_y\eta)\xi'] + K_4(\cos\Psi - k_x\xi - k_y\eta - k_z\zeta)k_y,$$

$$M_{1z} = K_{11}\zeta'' - K_{33}(\xi'^2 + \eta'^2)\zeta + \beta K_{33}[(k_z\eta - 2k_y\zeta)\xi' + (2k_x\zeta - k_z\xi)\eta'] + K_4(\cos\Psi - k_x\xi - k_y\eta - k_z\zeta)k_z. \quad (16)$$

1.2. Electric-Field Energy in a FLC and the Corresponding Torques

In order to describe the contribution of the electric-field energy to the free-energy density, we use as the field variable the displacement and not the electric-field strength. In other words, we proceed from the assumption that it is the charge that is defined at the LC boundaries and not the potentials. This approach is more efficient for numerical solution. Since the z component of the displacement is constant inside the dielectric layer of an LC, we can consider only one variable of the electric displacement instead of the set of variables corresponding to the one-dimensional electric-field distribution. There is another important aspect associated with the choice of the displacement instead of the field strength. The point is that the choice of the field strength as a variable requires the allowance for the work done by the voltage source at the fixed potential difference at the LC layer. However, the fixation of the voltage at each moment in the solution of the dynamic problem is associated with certain difficulties because the voltage at the electric capacity cannot be changed instantaneously since this would require the infinite current. The situation is quite different if we consider the rate of the charge variation at the electric capacity (or the electric current) which is always limited either by the internal resistivity of the power source or the resistivity of the electrodes. In turn, the current flowing inside the dielectric can be considered as the rate of the variation of the displacement (the conductivity current is taken into account as an individual contribution, see below).

One can show that for a linear polar dielectric, the electric contribution into the free-energy density is given by the expression [17]

$$F_2 = \frac{\mathbf{D}_i\mathbf{E}}{2}, \quad (17)$$

where $\mathbf{D}_i$ is the vector corresponding to the field-induced contribution to the total displacement

$$\mathbf{D} = \mathbf{D}_0 + \mathbf{D}_i \equiv \mathbf{P}_s + \boldsymbol{\varepsilon}\mathbf{E}, \quad (18)$$

where $\boldsymbol{\varepsilon}$ is the permittivity tensor and $\mathbf{D}_0 = \mathbf{P}_s$ is the polarization of a dielectric in the zero electric field. We should like to emphasize that contribution (17) enters the total energy with the plus sign because we consider the system under the conditions, where the charge and not the voltage is set at the boundaries of an LC layer.[2]

With due regard for the geometry used for which $\mathbf{E} = (0, 0, E_z)$ and $\mathbf{D}_i = (D_{xi}, D_{yi}, D_{zi})$, Eq. (17) acquires the form

$$F_2 = \frac{D_{zi}E_z}{2} = \frac{(D_z - P_{sz})^2}{2\varepsilon_\perp\left(1 + \frac{\Delta\varepsilon}{\varepsilon_\perp}n_z^2\right)} \equiv \frac{(D_z - P_{sz})^2}{2\varepsilon_\perp\left(1 + \frac{\Delta\varepsilon}{\varepsilon_\perp}\zeta^2\right)}. \quad (19)$$

In Eq. (19), $\Delta\varepsilon = \varepsilon_\parallel - \varepsilon_\perp$ and $\varepsilon_\parallel$ and $\varepsilon_\perp$ are the principal values of the permittivity tensor (the components parallel and perpendicular to the director, respectively). It should also be noted that the allowance for only two components of the permittivity tensor is an approximation, because the symmetry of the chiral C^* phase admits three different principal values. If it is necessary to take into account biaxiality, one has to apply the similarity transformation to the tensor $\boldsymbol{\varepsilon}$ in the way analogous to that considered below for rotational viscosity.

The use of the relationships for the density of the electric-field energy for a linear dielectric should not be considered as an approximation, because the general character of the nonlinear behavior of an LC is taken into account by the elastic contributions. Indeed, since the free energy is a function of the state, its change in the transition to a new state in the isothermal quasistatic process is independent of the transition path. Thus, we can represent the real process of deformation in an electric field as a virtual two-stage process during which, first, the deformed state of the director is created (which corresponds to the finite state) and then an electric field is switched on at the fixed deformation. At the second stage, we deal with the linear dependence of displacement on an electric field, because the external fields are essentially less intense than the intramolecular fields. This approach is of the general character [18].

The quantity P_{sz} should be expressed in terms of the director state. Proceeding from the most general ideas on the symmetry of a ferroelectric C^* phase, we can write the following expression for P_{sz} [19, 20]:

$$P_{sz} = P_0[(\mathbf{kn})(\mathbf{k}\times\mathbf{n})]_z = P_0(k_xn_x + k_yn_y + k_zn_z)(k_xn_y - k_yn_x) \equiv P_0(k_x\xi + k_y\eta + k_z\zeta)(k_x\eta - k_y\xi), \quad (20)$$

where P_0 is the quantity that can be expressed in terms of the spontaneous polarization P_{s0} of the nondeformed layer of a ferroelectric

$$P_0 = P_{s0}/|(\mathbf{kn}_0)(\mathbf{k}\times\mathbf{n}_0)| = P_{s0}/\cos\Psi\sin\Psi. \quad (21)$$

[2] If we had considered the system at the fixed voltage at the LC layer, the contribution to the free energy would have had the "minus" sign and would have contained the well-known term – **PE** associated with allowance for the work of the voltage source.

It should be noted that P_0 is a more general characteristic than spontaneous polarization P_{s0}, which, in accordance with Eq. (21), should vanish in the absence of the natural tilt of the director in the smectic layers, where $\Psi = 0$.

Substituting Eq. (20) into Eq. (19) and differentiating the latter equation, we obtain the following expressions for the torque components:
for the *x*-component,

$$M_{2x} = -\frac{\partial F_2}{\partial \xi} = -\frac{D_{zi}P_0[(k_x\xi + k_y\eta + k_z\zeta)k_y - (k_x\eta - k_y\xi)k_x]}{\varepsilon_\perp\left(1 + \frac{\Delta\varepsilon}{\varepsilon_\perp}\zeta^2\right)}, \quad (22)$$

for the *y* component,

$$M_{2y} = -\frac{\partial F_2}{\partial \eta} = \frac{D_{zi}P_0[(k_x\xi + k_y\eta + k_z\zeta)k_x + (k_x\eta - k_y\xi)k_y]}{\varepsilon_\perp\left(1 + \frac{\Delta\varepsilon}{\varepsilon_\perp}\zeta^2\right)}, \quad (23)$$

and for the *z* component,

$$M_{2z} = -\frac{\partial F_2}{\partial \zeta} = \frac{D_{zi}^2\Delta\varepsilon\zeta}{\varepsilon_\perp^2\left(1 + \frac{\Delta\varepsilon}{\varepsilon_\perp}\zeta^2\right)^2} + \frac{D_{zi}P_0(k_x\eta - k_y\xi)k_z}{\varepsilon_\perp\left(1 + \frac{\Delta\varepsilon}{\varepsilon_\perp}\zeta^2\right)}. \quad (24)$$

It should be noted that Eqs. (22)–(24) include the electroclinic effect. Even if the polarization is parallel to the electric field, there is a nonzero torque which tends to change the smectic-layer thickness.[3] Moreover, as has already been noted, P_0 can have a nonzero value in a chiral smectic *A** phase. Then, the corresponding torques would determine the electroclinic effect in smectics *A**. This differs the equations considered here from the equations conventionally used to describe FLCs [3, 4].

In order to determine the total and field-induced displacements, one can use the following integral expressions

$$D_z = \frac{\varepsilon_\perp U_{LC} - P_0\int_z (k_x\xi + k_y\eta + k_z\zeta)(k_y\xi - k_x\eta)\left(1 + \frac{\Delta\varepsilon}{\varepsilon_\perp}\zeta^2\right)^{-1} dz}{\int_z \left(1 + \frac{\Delta\varepsilon}{\varepsilon_\perp}\zeta^2\right)^{-1} dz}, \quad (25)$$

$$D_{zi} = D_z - P_0(k_x\xi + k_y\eta + k_z\zeta)(k_x\eta - k_y\xi), \quad (26)$$

where U_{LC} is the potential difference at the liquid-crystal layer.

1.3. Anchoring Energy and Boundary Conditions

The director state at the boundary is determined by the balance of two torques—the elastic torque of a LC and the surface torque due to anchoring,

$$\int_z \frac{d}{dz}\left(\frac{\partial F}{\partial \mathbf{n}'}\right)dz = \frac{\partial W}{\partial \mathbf{n}}. \quad (27)$$

The above equation is the consequence of the application of Lagrange equation (2) to the surface layer of a LC. Obviously, Eq. (27) is equivalent to the equation

$$-\frac{\partial F}{\partial \mathbf{n}'} + \frac{\partial W}{\partial \mathbf{n}} = 0, \quad (28)$$

where *W* is the anchoring energy of a LC. The signs of the terms in Eq. (28) correspond to the first surface. For

[3] It is important to consider the particular case of a homogeneous layer of a LC with the vector $\mathbf{k} = (1, 0, 0)$ (the layers are normal to the substrate surfaces) in a static field *E*. With due regard for Eqs. (22)–(24) and Eqs. (14)–(16) at $\Delta\varepsilon = 0$, system (2) acquires the form

$$\begin{aligned} EP_0 n_y + \lambda n_x &= K_4(n_x - \cos\Psi), \\ EP_0 n_x + \lambda n_y &= 0, \\ \lambda n_z &= 0, \end{aligned} \quad (*)$$

where λ is the Lagrange multiplier [see (3)]. The solution of the system (*) yields $n_z = 0$ (the director lies in the *xy* plane) and

$$\Delta\phi \cong -\frac{EP_0}{K_4}\left(1 - \frac{n_x^2}{n_y^2}\right) = \frac{EP_0}{K_4}\left(\frac{\cos^2\phi}{\sin^2\phi} - 1\right), \quad (**)$$

where $\Delta\phi$ is the change in the angle ϕ of the director with respect to the *x* axis under the conditions that the polarization vector $\mathbf{P}_s$ is parallel to the electric-field vector $\mathbf{E}$. Expression (**) is written in the approximation of small changes in the angle $\phi \approx \Psi + \Delta\phi$ and is associated with the electroclinic effect. One can readily see that the electroclinic effect should vanish at $\Psi = \pi/4$ and change the sign at $\Psi > \pi/4$. With a decrease in Ψ, i.e., with an approach to the point of transition into the smectic phase *A**, expression (**) predicts a dramatic increase in the electroclinic effect at the normal behavior of K_4.

the second surface of a LC cell, the sign of one of the terms should be changed to the opposite one.

For the torque components, the following equations follow from Eq. (28).

For the x component,

$$-\frac{\partial F}{\partial \xi'} + \frac{\partial W}{\partial \xi} = 0. \quad (29)$$

Using Eq. (13), we obtain for the first surface ($z = 0$)

$$-\frac{\partial F}{\partial \xi'} = -[K_{22}\eta^2 + K_{33}(\xi^2 + \zeta^2)]\xi' + [K_{22} - K_{33}]\xi\eta\eta' - K_{22}q_0\eta - K_{33}\beta[k_x\xi\eta + k_z\eta\zeta - k_y(1-\eta^2)]. \quad (30)$$

Thus, substituting Eq. (30) into Eq. (29), we obtain the derivative of the x component at the boundary

$$\xi' = \left[\frac{\partial W}{\partial \xi} + (K_{22} - K_{33})\xi\eta\eta' - K_{22}q_0\eta - K_{33}\beta[k_x\xi\eta + k_z\eta\zeta - k_y(1-\eta^2)]\right] \times [K_{22}\eta^2 + K_{33}(\xi^2 + \zeta^2)]^{-1} \equiv G_x. \quad (31)$$

The expressions for the derivatives of the remaining components are obtained in a similar way.

For the y component, we have

$$\eta' = \left[\frac{\partial W}{\partial \eta} + (K_{22} - K_{33})\eta\xi\xi' + K_{22}q_0\xi - K_{33}\beta[k_x(1-\xi^2) - k_y\xi\eta - k_z\xi\zeta]\right] \times [K_{22}\xi^2 + K_{33}(\eta^2 + \zeta^2)]^{-1} \equiv G_y. \quad (32)$$

For the z component, we have

$$\zeta' = \frac{1}{K_{11}}\frac{\partial W}{\partial \zeta} \equiv G_z. \quad (33)$$

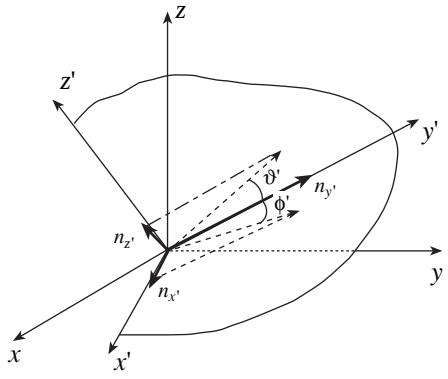

Fig. 1. To the interpretation of the azimuthal and zenithal contributions to the anchoring energy; xyz is the laboratory coordinate system, $x'y'z'$ is the local coordinate system, y' coincides with the easy axis, whereas the z axis lies in the $y'z'$ plane.

Using Eqs. (31)–(33), we determine the director state at the boundary $z = 0$ by solving the above equations simultaneously with the equations for the volume. For the second boundary ($z = d$), the sign of one of the terms on the left-hand side of Eq. (28) is changed, and one has also to change the signs of the corresponding terms in Eqs. (31)–(33).

It is very important to choose the form of the energy of anchoring of a LC with the surface appropriately. I have already discussed the problem of the representation of the anchoring energy in [21] and indicated the arguments in favor of the choice of the Fourier expansion. The Fourier expansion of the anchoring energy can conveniently be written in the local coordinate system $x'y'z'$ in which the y' axis coincides with the easy axis (Fig. 1). By definition, the easy axis in the laboratory coordinate system xyz is set by the pretilt angle ϑ_{s0} with respect to the xy plane and corresponds to the director orientation on the surface in the absence of elastic deformation in the bulk. If the director in the LC bulk is deformed, it deviates from the easy axis on the surface.[4] The restoring force arising on the side of the surface is determined by the form of the anchoring energy. In the local coordinate system, the director motion in two orthogonal planes $x'y'$ and $y'z'$ can be considered as two independent movements characterized by the amplitudes of their harmonics, defined here as those corresponding to the azimuthal and zenithal anchoring energies. Therefore, in the most general case, each of these energies can be represented as a Fourier series for the corresponding orthogonal direction (rotation by the angle ϕ' for the azimuthal energy and angle ϑ' for the zenithal energy)

$$W_{z'} = \sum_{m=0}^{\infty}(A_{zm}\cos(m\vartheta') + B_{zm}\sin(m\vartheta')), \quad (34.1)$$

$$W_{x'} = \sum_{m=0}^{\infty}(A_{xm}\cos(m\phi') + B_{xm}\sin(m\phi')), \quad (34.2)$$

where m is the harmonic number and A_{zm}, B_{zm}, A_{xm}, and B_{xm} are the corresponding harmonic amplitudes.

Assuming the existence of a certain symmetry, we can simplify expansion (34). For instance, the existence of the symmetry with respect to the easy axis requires an even energy function and, then, the Fourier series in both (34.1) and (34.2) expansions would consist only of cosines. The existence of an additional symmetry with

[4] The direction of the easy axis depends on the conditions of the surface treatment and does not necessarily lies in the xy plane of the laboratory coordinate system. In the general case of smectic LCs, the direction of the director on the surfaces does not coincide with the easy axis because of the elasticity of smectic layers. The structure of the layers at the surface is rather stressed because, on the one hand, the elasticity torques tend to preserve the thickness of the smectic layers, whereas the anchoring forces try to orient the director along the easy axis. The competition of these two torques can distort the smectic layers in the bulk.

respect to the $x'z'$ plane orthogonal to the easy axis results in the presence in the expansion of only even harmonics. In the latter case, the zeroth and second harmonics represent widely used Rapini's potential. Obviously, in the general case, there is no such symmetry, and the development of the methods for measuring Fourier coefficients would promote the creation of the method for the adequate characterization of the anchoring energy.

Below, we modify Rapini's potential with due regard for different azimuthal and zenithal contributions to the total anchoring energy. In other words, with due regard for only the zeroth and second harmonics of Fourier expansion (34), the total anchoring energy is expressed in terms of the director components as

$$W = W_{x'} + W_{z'} = \frac{1}{2}W_a n_{x'}^2 + \frac{1}{2}W_z n_{z'}^2, \tag{35}$$

where W_a and W_z are the amplitudes of the azimuthal and zenithal components of the anchoring energy and $n_{x'}$ and $n_{z'}$ are the director components in the local coordinate system (Fig. 1).

Equation (35) can also be interpreted in terms of a tensor. Indeed, by definition, the anchoring energy should reflect the physical work done during director deviation from the easy axis, i.e., should be determined by the integral

$$W = \int M\mathbf{n}d\mathbf{n} = \frac{1}{2}M\mathbf{n}^2. \tag{36}$$

Here, M is the torque amplitude independent of directions, which signifies that we do not account for the possible anisotropy of the torque amplitudes along different directions provided by different azimuthal and zenithal contributions. In order to take into account this anisotropy, one has to consider $\mathbf{M}$ as a matrix. Then Eq. (36) is transformed to

$$W = \frac{1}{2}(\mathbf{Mn})\mathbf{n}. \tag{37}$$

To represent Eq. (35) in the eigen coordinate system $x'y'z'$, we use

$$\mathbf{M} = \begin{pmatrix} W_a & 0 & 0 \\ 0 & 0 & 0 \\ 0 & 0 & W_z \end{pmatrix}. \tag{38}$$

Thus, in the terms discussed above, the anchoring energy can be characterized by a tensor.

To obtain the anchoring energy in the laboratory coordinate system, we have to perform the corresponding rotation operation. Then Eq. (35) acquires the form

$$\begin{aligned} W &= \frac{1}{2}W_a(n_x\sin\theta_a - n_y\cos\varphi_a)^2 \\ &+ \frac{1}{2}W_z(n_z\sin\theta_a - n_x\cos\varphi_a\cos\theta_a - n_y\sin\varphi_a\cos\theta_a)^2 \\ &\equiv \frac{1}{2}W_a(\xi\sin\varphi_a - \eta\cos\varphi_a)^2 \\ &+ \frac{1}{2}W_z(\zeta\sin\theta_a - \xi\cos\varphi_a\cos\theta_a - \eta\sin\varphi_a\cos\theta_a)^2, \end{aligned} \tag{39}$$

where φ_a and θ_a are the angles determining the easy axis with respect to the x and z axes of the laboratory coordinate system, respectively

To determine the director state at the boundaries in accordance with Eqs. (31)–(33), we have to take the partial derivatives of the interaction energy obtained from Eq. (39)

$$\begin{aligned} \frac{\partial W}{\partial \xi} &= W_a(\xi\sin\varphi_a - \eta\cos\varphi_a)\sin\varphi_a \\ &- W_z(\zeta\sin\theta_a - \xi\cos\varphi_a\cos\theta_a - \eta\sin\varphi_a\cos\theta_a) \\ &\times \cos\varphi_a\cos\theta_a, \end{aligned} \tag{40}$$

$$\begin{aligned} \frac{\partial W}{\partial \eta} &= -W_a(\xi\sin\varphi_a - \eta\cos\varphi_a)\cos\varphi_a \\ &- W_z(\zeta\sin\theta_a - \xi\cos\varphi_a\cos\theta_a - \eta\sin\varphi_a\cos\theta_a) \\ &\times \sin\varphi_a\cos\theta_a, \end{aligned} \tag{41}$$

$$\begin{aligned} \frac{\partial W}{\partial \zeta} &= W_z(\zeta\sin\theta_a - \xi\cos\varphi_a\cos\theta_a \\ &- \eta\sin\varphi_a\cos\theta_a)\sin\theta_a. \end{aligned} \tag{42}$$

Thus, we now possess the system of equations for solving the static problem on the spatial distribution of the director.

1.4. Friction Torques

The solution of the dynamic problem requires the allowance for viscosity. We ignore the substance transport in a LC cell and take into account only the rotational viscosity characterized by a second-rank tensor. Because of the low symmetry of the ferroelectric phase C^*, all the three principal values of the tensor can have different values.

To obtain the equation of motion, it is necessary to determine the components of the tensor $\boldsymbol{\gamma}$ in the laboratory coordinate system xyz related to the principal values of the tensor $\boldsymbol{\gamma}_L$ in the eigen coordinate system abc by the similarity transformation (one has to distinguish between this system and the local system related to the easy axis shown in Fig. 1)

$$\boldsymbol{\gamma} = \mathbf{R}\boldsymbol{\gamma}_L\mathbf{R}^{-1}. \tag{43}$$

Here, $\mathbf{R}$ is the rotation matrix relating the coordinates in the laboratory coordinate system to the coordinates in the eigen coordinate system.

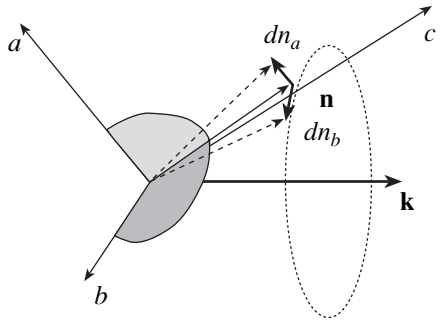

Fig. 2. Eigen coordinate system and the corresponding types of two orthogonal motions of the director that allow to understand the physical meaning of the components of the rotational-viscosity tensor.

The eigen coordinate system *abc* in which the tensor is in the diagonal form,

$$\boldsymbol{\gamma}_L = \begin{pmatrix} \gamma_1 & 0 & 0 \\ 0 & \gamma_2 & 0 \\ 0 & 0 & \gamma_3 \end{pmatrix} \tag{44}$$

is determined as follows:

—the *c* axis corresponding to the subscript 3 is chosen along the director **n**;

—the *b* axis corresponding to subscript 2 is chosen along the crystallographic C_2 axis, i.e., along the direction $\mathbf{k} \times \mathbf{n}$;

—the *a* axis corresponding to the subscript 1, i.e., chosen as the axis complementing the right-hand reference system, i.e., along the direction $(\mathbf{k} \times \mathbf{n}) \times \mathbf{n}$.

The components R_{ij} of the matrix are the directional cosines, which, by virtue of our choice of the eigen coordinate system, are determined as

$$\begin{aligned} (R_{13}, R_{23}, R_{33}) &= (n_x, n_y, n_z), \\ (R_{12}, R_{22}, R_{32}) &= (\mathbf{k} \times \mathbf{n})/|\mathbf{k} \times \mathbf{n}| \\ &= (k_y n_z - k_z n_y, k_z n_x - k_x n_z, k_x n_y - k_y n_x)/|\mathbf{k} \times \mathbf{n}|, \\ (R_{11}, R_{21}, R_{31}) &= ((\mathbf{k} \times \mathbf{n})/|\mathbf{k} \times \mathbf{n}|) \times \mathbf{n} \\ &= (R_{22} n_z - R_{32} n_y, R_{32} n_x - R_{12} n_z, R_{12} n_y - R_{22} n_x). \end{aligned} \tag{45}$$

Because the rotation and inverse matrices are orthogonal, the latter matrix is determined by transposition. Thus, substituting Eq. (45) into Eq. (43), we obtain the viscosity tensor in the laboratory coordinate system

$$\boldsymbol{\gamma} = \begin{pmatrix} R_{11}^2\gamma_1 + R_{12}^2\gamma_2 + R_{13}^2\gamma_3 & R_{11}R_{21}\gamma_1 + R_{12}R_{22}\gamma_2 + R_{13}R_{23}\gamma_3 & R_{11}R_{31}\gamma_1 + R_{12}R_{32}\gamma_2 + R_{13}R_{33}\gamma_3 \\ R_{11}R_{21}\gamma_1 + R_{12}R_{22}\gamma_2 + R_{13}R_{23}\gamma_3 & R_{21}^2\gamma_1 + R_{22}^2\gamma_2 + R_{23}^2\gamma_3 & R_{21}R_{31}\gamma_1 + R_{22}R_{32}\gamma_2 + R_{23}R_{33}\gamma_3 \\ R_{11}R_{31}\gamma_1 + R_{12}R_{32}\gamma_2 + R_{13}R_{33}\gamma_3 & R_{21}R_{31}\gamma_1 + R_{22}R_{32}\gamma_2 + R_{23}R_{33}\gamma_3 & R_{31}^2\gamma_1 + R_{32}^2\gamma_2 + R_{33}^2\gamma_3 \end{pmatrix}. \tag{46}$$

The corresponding torque provided by viscosity is

$$\mathbf{M}_\gamma = \begin{pmatrix} M_{x\gamma} \\ M_{y\gamma} \\ M_{z\gamma} \end{pmatrix} = \boldsymbol{\gamma}\frac{d\mathbf{n}}{dt} \tag{47}$$

$$= \begin{pmatrix} \gamma_{xx}\dot{n}_x + \gamma_{xy}\dot{n}_y + \gamma_{xz}\dot{n}_z \\ \gamma_{yx}\dot{n}_x + \gamma_{yy}\dot{n}_y + \gamma_{yz}\dot{n}_z \\ \gamma_{zx}\dot{n}_x + \gamma_{zy}\dot{n}_y + \gamma_{zz}\dot{n}_z \end{pmatrix} \equiv \begin{pmatrix} \gamma_{xx}\dot{\xi} + \gamma_{xy}\dot{\eta} + \gamma_{xz}\dot{\zeta} \\ \gamma_{yx}\dot{\xi} + \gamma_{yy}\dot{\eta} + \gamma_{yz}\dot{\zeta} \\ \gamma_{zx}\dot{\xi} + \gamma_{zy}\dot{\eta} + \gamma_{zz}\dot{\zeta} \end{pmatrix}.$$

It is important to clarify the physical meaning of the principal values of viscosity tensor (44). It is these values that are the characteristic quantities. Proceeding from the chosen eigen coordinate system, we obtain that the component γ_2 of the tensor corresponds to the change of the *b* component of the director, i.e., determines the friction along the direction normal to the plane in which the **k** and **n** vectors lie (Fig. 2). Thus, under certain conditions, this component determines the viscosity for director motion over the cone. In the absence of compressibility of the smectic layers, this component can be compared with quantity $\gamma_\varphi/\sin^2\Psi$ [3, 4]. The two remaining components γ_1, γ_3 correspond to the rotation in the **kn** plane, i.e., to the so-called "soft mode" of the director motion and viscosity, usually denoted as γ_θ. If the viscosity is invariant with respect to the operation of rotation of the eigen coordinate system about the *b* axis, then $\gamma_1 = \gamma_3 = \gamma_\theta$. The invariance is not the necessary condition, and, therefore, three different viscosity components are admissible.

1.5. Complete System of Equations with Due Regard for the Elements of Electric Circuit

In order to orient a FLC, one has to deposit onto it an additional film which prevents the direct contact of LC molecules with the electrodes. Thus, the electric circuit should have an additional element, which can be represented by an electric capacity *C* connected in parallel to the resistance *R*, which takes into account the capacity and the resistance of the orienting coatings. In addition, the resistance of electrodes, R_0, also has a nonzero value and should be taken into account as if it were connected in series with the voltage source (see the equivalent scheme in Fig. 3).

The current and the voltage in the circuit shown in Fig. 3 are described by the following system of differential equations:

$$\frac{dU_C}{dt} + \frac{1}{C}\left(\frac{1}{R} + \frac{1}{R_0}\right)U_C = \frac{1}{CR_0}(U - U_{LC}), \quad (48.1)$$

$$\frac{U_{LC}}{R_{LC}} + S\frac{dD_z}{dt} = I, \quad (48.2)$$

$$U_{LC} = U - IR_0 - U_C, \quad (48.3)$$

where S is the electrode area in the LC cell, U is the voltage provided by the power source, U_C is the voltage at the orienting layers, U_{LC} is the voltage at the liquid-crystal layer, R_0 is the resistance of the electrodes, C is the equivalent electrical capacity of the orienting layers, I is the resulting current of the source, D_z is the z component of the electric-displacement vector in an LC whose conductivity is taken into account with the aid of the resistance R_{LC} connected in parallel. Using R_{LC}, we take into account all the types of the conductivity of a LC in the linear approximation under the assumption that the conductivity is uniform over the whole thickness of the LC and is independent of the electric field.

Finally, the reduced additional system of equations necessary to describe the dynamics of the director of an LC in the notation accepted in this article are written as

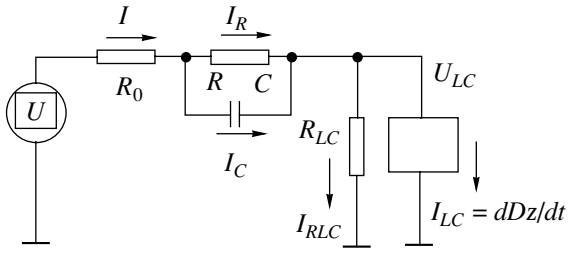

Fig. 3. Equivalent electric scheme of a LC cell.

$$n_x^2 + n_y^2 + n_z^2 = 1, \quad (49.1)$$

$$\gamma_{xx}\dot{n}_x = M_{1x} + M_{2x} + \lambda n_x - \gamma_{xy}\dot{n}_y - \gamma_{xz}\dot{n}_z, \quad (49.2)$$

$$\gamma_{yy}\dot{n}_y = M_{1y} + M_{2y} + \lambda n_y - \gamma_{yx}\dot{n}_x - \gamma_{yz}\dot{n}_z, \quad (49.3)$$

$$\gamma_{zz}\dot{n}_z = M_{1z} + M_{2z} + \lambda n_z - \gamma_{zx}\dot{n}_x - \gamma_{zy}\dot{n}_y, \quad (49.4)$$

$$\left.\frac{\partial n_x}{\partial z}\right|_{z=0,d} = G_x|_{z=0,d}, \quad (49.5)$$

$$\left.\frac{\partial n_y}{\partial z}\right|_{z=0,d} = G_y|_{z=0,d}, \quad (49.6)$$

$$\left.\frac{\partial n_z}{\partial z}\right|_{z=0,d} = G_z|_{z=0,d}, \quad (49.7)$$

$$D_z = \frac{\varepsilon_\perp U_{LC} - P_0\int_z (k_x n_x + k_y n_y + k_z n_z)(k_y n_x - k_x n_y)\left(1 + \frac{\Delta\varepsilon}{\varepsilon_\perp}n_z^2\right)^{-1} dz}{\int_z \left(1 + \frac{\Delta\varepsilon}{\varepsilon_\perp}n_z^2\right)^{-1} dz}. \quad (49.8)$$

The above system of equations together with system (48) form the complete system of equations valid not only for the ferroelectric LCs but also for other liquid-crystal phases of higher symmetries. Thus, assuming that spontaneous polarization P_{s0}, spontaneous bend β, and elasticity modulus of the smectic layers K_4 are zeroes and that the principal values of the viscosity tensor are equal, we automatically arrive at the system of equations for a nematic liquid crystal.

The solution of the complete system of equations is a very complicated problem, because it can be obtained only by the simultaneous and consistent solution of all the equations. The description of the algorithm of such a solution is beyond the scope of this article. Here, we would only like to note that this problem together with the optical problem is solved using the Ferroelectric Liquid Crystal Lab. (FLCL) program written by the author.

2. EFFECTS OF BISTABILITY AND HYSTERESIS-FREE ELECTROOPTICAL SWITCHING

Consider the results of the numerical solution of above systems of equations (48) and (49) and clarify the mechanisms of the two effects especially important for understanding the physical processes occurring in ferroelectric LCs and some of their applications. These are the effects of bistability and the hysteresis-free electrooptical switching. The first effect has been known and studied for quite a long time [10, 11], but some important aspects of the phenomenon have passed unnoticed. Despite the thorough study [9], the second effect is still somewhat mysterious. As will be shown later, these two effects reflect different manifestations of the same physical processes.

For simulation of these effects, define the following characteristics of a hypothetical LC cell:

—elasticity constants of an LC, $K_{11} = K_{22} = K_{33} = 5$ pN and K_4 is the parameter ranging within 5×10^5–10^6 pN/μm^2 (0.5–1.0 MPa);

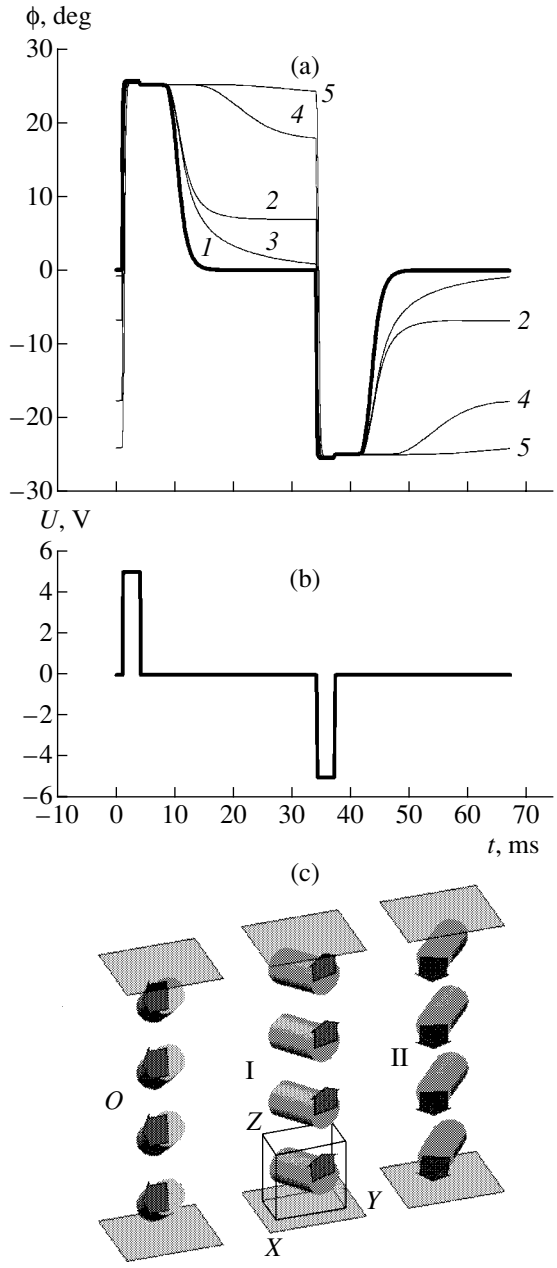

Fig. 4. (a) Dynamics of the director in the center of an LC cell depending on the anchoring energies W_z and W_a, the elasticity modulus K_4, electric capacity of the orienting layers C, and spontaneous polarization P_{s0}: (*1*) $W_z = W_a = 0.1$ mJ/m^2, $K_4 = 1$ MPa, $C = 50$ nF, and $P_{s0} = 30$ nC/cm^2; (*2*) $W_z = 1$ mJ/m^2, $W_a = 0.1$ mJ/m^2, $K_4 = 1$ MPa, $C = 50$ nF, $P_{s0} = 30$ nC/cm^2, (*3*) $W_z = 1$ mJ/m^2, $W_a = 0.1$ mJ/m^2, $K_4 = 0.5$ MPa, $C = 50$ nF, $P_{s0} = 30$ nC/cm^2; (*4*) $W_z = 1$ mJ/m^2, $W_a = 0.1$ mJ/m^2, $K_4 = 0.5$ MPa, $C = 50$ nF, $P_{s0} = 15$ nC/cm^2; (*5*) $W_z = 1$ mJ/m^2, $W_a = 0.1$ mJ/m^2, $K_4 = 1$ MPa, $C = 200$ nF, $P_{s0} = 15$ nC/cm^2; (b) the waveform of the applied voltage; and (c) different states of the director. The director of an LC is depicted in the shape of a cylinder, the arrow indicates the local direction of the polarization. The state *O* is observed in the absence of bistability and electric field. States I and II arise at the positive and negative applied voltages; these states are also preserved in the absence of the applied voltage if the bistability effect takes place.

—the components of the viscosity tensor of an LC $\gamma_1 = \gamma_2 = \gamma_3 = 0.5$ Pa s;

—moduli of spontaneous bend $\beta = 0.1$ μm^{-1} and the inverse pitch $q_0 = 0.1$ μm^{-1};

—natural tilt angle of molecules in smectic layers $\Psi = 25°$;

—thickness of the LC layer $d = 2$ μm;

—components of the permittivity tensor of a LC $\varepsilon_\parallel = \varepsilon_\perp = 3$;

—spontaneous polarization P_{s0} of a LC, the variable parameter ranging within 15–100 nC/cm^2;

—components of the anchoring-energy tensor $W_a = 0.1$ mJ/m^2 and W_z is the variable parameter ranging within 0.1–1.0 mJ/m^2;

—orientation of the easy axis on the cell surfaces $\varphi_a = 0°$ and $\theta_a = 86°$ (the pretilt equals 4°);

—orientation of the normal to smectic layers (k_x, k_y, k_z) = (1, 0, 0);

—electric resistance of an LC layer R at the electrode area $S = 1$ cm^2, the variable parameter ranging within 1–100 MΩ;

—electric resistance of electrodes $R_0 = 200$ Ω;

—electric capacity of the orienting layers of a LC cell, the variable parameter ranging within 25–200 nF.

The parameters indicated above as variables play the key part in the both effects.

2.1. Bistability Effect

At a high value of the compressibility modulus K_4, the external electric field influences the thicknesses of smectic layers only weakly and the molecules in the layers move around the layer normal over the cone determined by the natural angle Ψ. In this case, the vector of spontaneous polarization is normal to both the director **n** of the LC and the normal **k** to the smectic layers. One of the stable director distributions is the state in which the easy-orientation axes, the director **n**, and the vector of the normal **k** lie in the same plane (in our case, the *xz* plane). However, the experiment shows that two symmetric states for which the director deviates from the *xz* plane by a certain angle not exceeding the natural angle Ψ over the whole layer thickness can also be stable. The short application of an electric field of the corresponding sign parallel to the *z* axis results in switching of the director from one stable state to another, which fact underlies the bistability effect.

Consider the results of the effect simulation. Figure 4a shows the response of a LC to the application to the cell of short periodic voltage pulses of opposite signs (Fig. 4b). The ordinate axis shows the angle ϕ formed by the projection of the director **n** onto the *xy* plane and the *x* axis. Curve *1* corresponds to the situation, where no bistability effect is observed. Indeed, for the time of duration of a positive pulse, the director deviates for an

angle of $\phi = 26°$ slightly exceeding the natural angle (25°) because of the finite compressibility of the layer (the electroclinic effect). In this state, the director is almost parallel to the *xy* plane over the whole layer thickness (except of the subsurface regions), whereas the polarization is directed along the electric field (the *z* axis).This state is denoted as state I (Fig. 4c). Upon switching-off of the pulse, the director remains for some time in the state close to state I, but already 15 ms later, it relaxes to the zero state *O*, where $\phi = 0$. The pulse of the opposite sign brings the director to the symmetric state $\phi = -26°$ (state II), which also becomes unstable upon switching-off of the voltage. Thus, in this case, no bistability is observed.

Now, we change the properties of anchoring of a liquid crystal and the surface. As was shown in Sect. 1.3, anchoring is characterized by the tensor whose components are the amplitudes of the azimuthal and zenithal anchoring energy. Now, increase the anchoring energy W_z up to 1 mJ/m^2 without changing the azimuthal component (W_a = 0.1 mJ/m^2). The corresponding response is shown by curve *2* in Fig. 4a. It is seen that, upon the switching-off of the field, the system does not relax to the state *O* and the director still forms a certain angle with the *xz* plane ($\phi = 7°$ in the center of the LC layer). Applying a negative pulse, one can switch the director to the symmetric state ($\phi = -7°$). We see that the anisotropy of the anchoring energy $(W_z - W_a)/W_a$ gives rise to the bistability effect.

Nevertheless, being the necessary condition for the manifestation of bistability, the pronounced anisotropy of anchoring is not a sufficient condition for its manifestation. Curve *3* illustrates the situation in which no bistability is observed, with the anchoring being the same as in the previous example (curve *2*). In this example, we reduced twice the elasticity coefficient of the smectic layers K_4. The higher compressibility (the lower value of K_4) promoted a decrease in the energy barrier that separates the two bistable states and the state *O*. It will be obvious from the following example that two bistable states are preserved, but, for some reasons, the director "leaves" these states when the voltage pulse is switched off.

Curve *4* corresponds to a spontaneous polarization that is twice as low as in the previous example (curve *3*). As is seen, bistable states are also formed in this case. Moreover, the similar result can be achieved by increasing the electric capacity of the orienting layers. An increase in the capacity at a lower polarization results in a more pronounced effect: the absolute values of the angles corresponding to the two symmetric states become very close to the natural angle, $\Psi = 25°$ (curve *5*).

In order to understand why no bistable states are observed even in those instances where the anchoring energy is anisotropic, consider in more detail the current response and the dynamics of the change in the voltage at a LC layer, e.g., in the process of the application of a positive voltage pulse (Fig. 5). Current curve *1* in Fig. 5a corresponds to the absence of bistability (Fig. 4a, curve *1*). The current at the leading edge of the pulse reflects the process of charging the electric capacity of orienting layers and the capacity of a LC cell, including switching of the polarization vector in the LC layer. At the falling edge of the pulse, the capacities are partly discharged. The complete discharge is impossible because of the *z* component of the polarization and the absence of a considerable conductivity of the LC layer. Thus, the negative (reverse) voltage arises at the LC layer (curve *1** in the interval 4–10 ms in Fig. 5b). Because of the voltage of the opposite sign, the opposite torque is formed, which acts onto the director of the LC and brings it to the *O* state. The switching of the director is accompanied by the change of the orientation of the spontaneous-polarization vector and a formation of the characteristic current pulse in the circuit within the interval 10–15 ms (curve *1* in Fig. 5a). In the case of bistability, the reverse voltage upon switching-off of the external voltage pulse is considerably lower

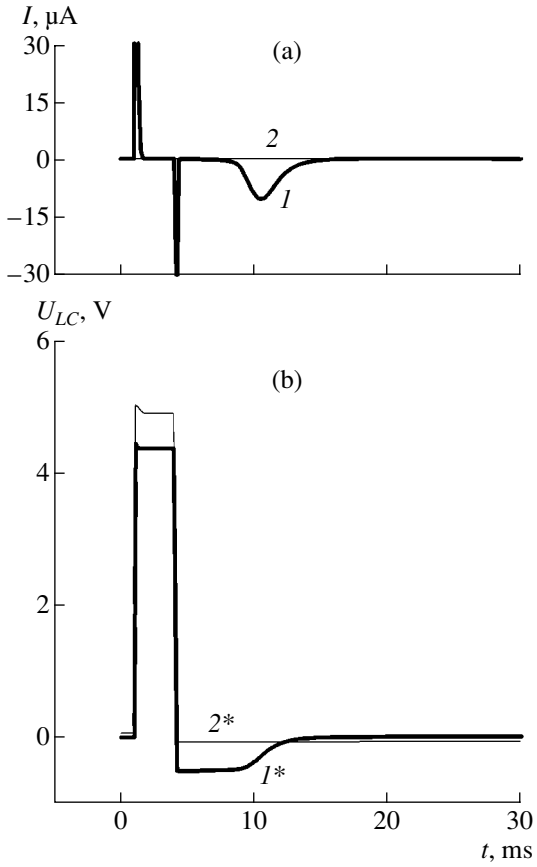

Fig. 5. (a) Kinetics of the electric current in the external circuit at the external voltage waveform shown in Fig. 4b. Curves *1* and *2* correspond to curves *1* and *5* in Fig. 4a. The choice of the ordinate scale limits the current pulses corresponding to the edges of the external voltage pulse. (b) Voltage at the liquid-crystal layer at the external voltage waveform shown in Fig. 4b.

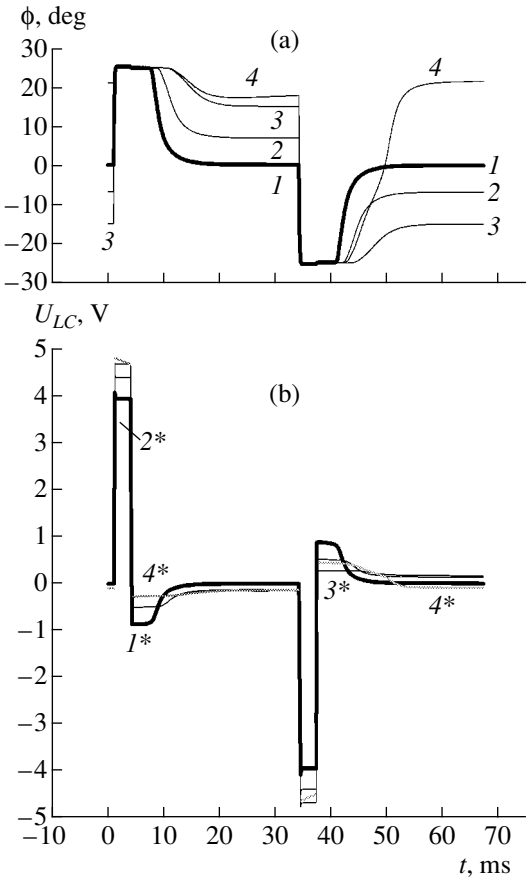

Fig. 6. (a) Dynamics of the director in the center of a LC cell depending on the capacity of the orienting layers and conductivity of a LC: (*1*) C = 25 nF, R = 100 MΩ; (*2*) C = 50 nF, R = 100 MΩ; (*3*) C = 100 nF, R = 100 MΩ; (*4*) C = 100 nF, R = 1 MΩ. All the curves are obtained at the anchoring energy W_z = 1 mJ/m^2 and W_a = 0.1 mJ/m^2, elasticity modulus K_4 = 1 MPa, and spontaneous polarization P_{s0} = 30 nC/cm^2. The voltage at the liquid-crystal layer at the external voltage waveform shown in Fig. 4b. Curves (*1**–*4**) correspond to curves (*1*–*4*) in Fig. 6a.

(curve *2**), so that it is insufficient for the director to overcome the potential barrier due to the anisotropy of the anchoring energy and high value of the elasticity coefficient K_4 (cf. curves *2* and *3* in Fig. 4).

Thus, along with the anisotropy of the anchoring energy, an important condition for the formation of bistable states is the minimization of the reverse voltage at the polar LC layer upon switching-off of the external voltage. There are two methods for reducing the reverse voltage. The first one is a decrease of spontaneous polarization of the LC. The second one is an increase of the electric capacity of the orienting layers (which can be attained either by decreasing the thickness of the orienting layers or by increasing their dielectric constant). Figure 6 illustrates the effect of electric capacity of orienting layers on the dynamics and bistability of the states of the director in a liquid crystal.

We should like to point out some other important aspects. As we saw, in the absence of bistability, the director relaxes to the *O* state. Then the spontaneous-polarization vector becomes normal to the *z* axis. Thus, the *z* component of the polarization becomes zero. The absence of the *z* component of the polarization is a very important fact. In the presence of dielectric orienting layers, the nonzero *z* component of the polarization inevitably generates an electric field inside the LC layer at the zero external voltage at the LC cell. This field increases the free energy of the LC layer, makes the state less favorable, and gives rise to electric currents (if the LC possesses certain conductivity). The competition between the torques associated with this field and elastic torques provided by anchoring and elasticity of the smectic layers results in the bistable states characterized by smaller angles than the natural tilt angle in smectic layers. All the above stated also relates to nonconducting and weakly conducting LCs ($\sigma < 10^{-12}$ Ω^{-1} cm^{-1}). Conductivity of an LC results in compensation of the electric field (at the zero external voltage) inside the LC layer via the additional charging the electric capacities of the orienting layers. This excessive free charge can introduce the asymmetry to the switching dynamics, which becomes dependent on the history of the LC state. This is illustrated by curve *4* in Fig. 6. It is seen that in this instance, the negative pulse does not bring the LC to symmetric state II. The point is that, first, a positive pulse is applied to the conducting LC in initial state I (where the field inside the LC layer is compensated with the free charge at the capacities of the orienting layers). As a result, the free charge stabilizing state I increases. For the time prior to the second negative pulse, the charge in the system cannot completely relax to the equilibrium value (at a low value of conductivity of the LC and a higher electric capacity of the orienting layers, the corresponding times can attain the values up to several tens of seconds). At the falling edge of a negative pulse, the reverse voltage (now positive) is somewhat enhanced and, therefore, the system cannot remain in state II and relaxes back to state I, thus giving rise to the "monostability" effect.

In conclusion, let us formulate the conditions necessary for the formation of bistable states. These are

—the anisotropy of the anchoring energy such that the zenithal component of the anchoring energy exceeds the azimuthal one. However, the existence of the polar contribution to the anchoring energy [11] is not the necessary condition for bistability;

—a high value of the elasticity modulus of the smectic layers (K_4 > 0.5 MPa) increases the stability of the symmetric states;

—a low spontaneous polarization P_{s0} decreases the reverse voltage at the LC layer upon switching-off of the external voltage, which increases the stability of the symmetric states. I recommend the value P_{s0} < 30 nC/cm^2;

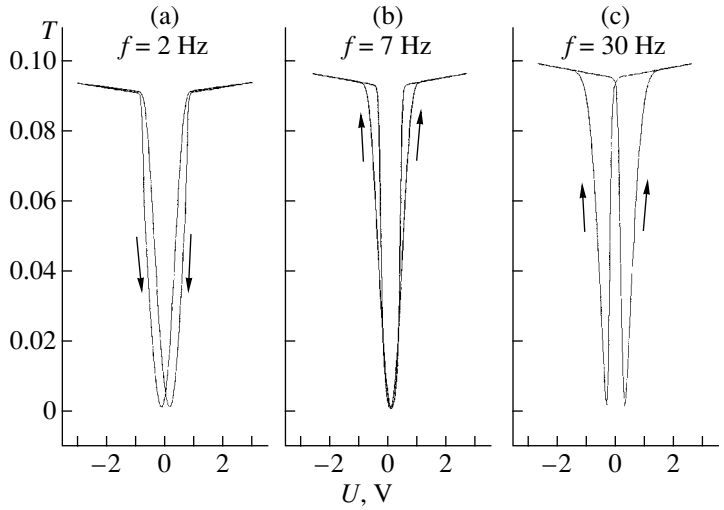

Fig. 7. Optical transmittance as a function of external voltage at the ferroelectric LC cell placed between the crossed polaroids. The curves in Fig. 7a, 7b, and 7c correspond to the frequencies of 2, 7, and 30 Hz of the external voltage of triangular waveform. The curves are obtained at the following parameters of the LC cell: spontaneous polarization of the liquid crystal P_{s0} = 50 nC/cm^2, capacity of the orienting layers C = 50 nF at the electrode area S = 1 cm^2. The axes of the first and second polaroids are parallel and perpendicular to the normal to smectic layers, respectively.

—as in the case of low spontaneous polarization, a higher electric capacity of the aligning layers decreases the reverse voltage arising at the LC layer upon switching-off the external voltage. This is the key aspect for attaining the bistable states. The recommended capacity value is C > 50 nF at S = 1 cm^2, which corresponds to the thickness of an orienting polyimide layer at each of the surfaces less than 30 nm;

—a low conductivity of the LC; otherwise, the effect of monostability can arise.

2.2. Effect of Hysteresis-Free Electrooptical Switching

As a rule, the electrooptical response and electric displacement in ferroelectric LCs demonstrate hysteresis behavior (Fig. 7c). However, it turned out that, at certain frequencies of the applied voltage of the triangular waveform, one can observe the hysteresis-free dependence of transmittance on voltage. The shape of this dependence looks like the letter *V,* which gave the name to the phenomenon—the *V*-shape effect. It was first observed in antiferroelectric LCs and interpreted as the manifestation of a new phenomenon —"hysteresis-free antiferroelectricity" [6]. The effect has attracted great attention, because it offers the possibility of the practical implementation of the gray scale necessary in the display technology. Later, a similar effect was also discovered in ferroelectric LCs. In recent years, various authors have tried to interpret this effect [6–8]. The effect was considered in association with the collective modes under the specified boundary conditions and also with the ionic processes occurring in LCs [7]. Only recent experiments showed that the effect of hysteresis-free switching is a seeming effect arising due to specific phase delays between the external voltage and the voltage at the LC layer [9]. Here, I should like to complement the conclusions drawn in [9] with new important results clarifying the mechanism of the above phenomenon.

Now, let us continue the simulation of our hypothetical cell with the parameters indicated above and also fix some new previously varying parameters, namely,

—spontaneous polarization P_{s0} = 50 nC/cm^2;

—components of the anchoring tensor $W_a = W_z$ = 0.1 mJ/m^2;

—electric resistance of a LC layer R = 10 MΩ at the electrode area S = 1 cm^2.

The characteristic features of the effect can be followed by varying the electric-field frequency and capacity of the orienting layers.

Figure 7 shows the results obtained for the external voltage of the triangular waveform by solving systems of equations (48) and (49) and the optical problem using the algorithm suggested in [13]. It can be seen that at low frequencies (less than 7 Hz), the optical transmittance is accompanied by a hysteresis. The specific feature of the hysteresis at very low frequencies is its anomalous nature: the switching of the director of a LC advances the external electric field (Fig. 7a). At a frequency of 7 Hz, there is almost no hysteresis (at low voltages the *V*-shape effect takes place) (Fig. 7b), whereas, at higher frequencies, e.g., 30 Hz (Fig. 7c), normal hysteresis is observed. In this instance, the value of 7 Hz is the frequency of the hysteresis inversion. Thus, the solution of the equations considered in this article allows us to simulate the specific features of the effect without the invocation of any particular model.

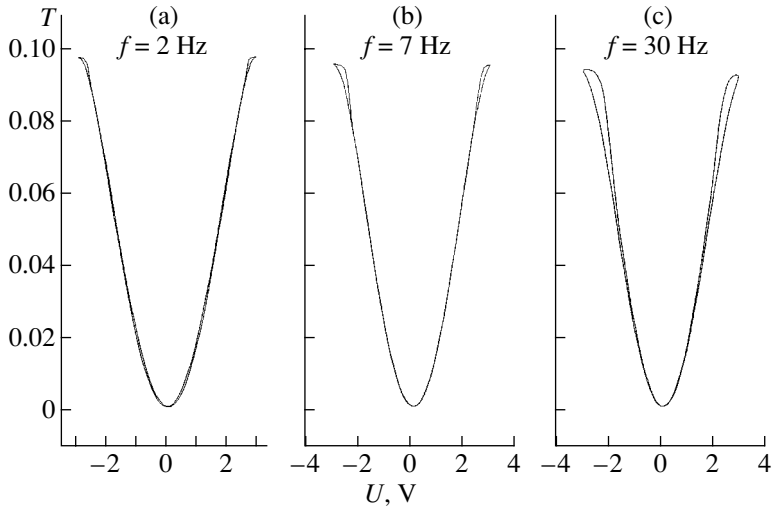

Fig. 8. Optical transmittance as a function of the external voltage at the ferroelectric LC cell placed between two crossed polaroids. The curves in Figs. 8a, 8b, and 8c correspond to the frequencies of 2, 7, and 30 Hz of the external voltage of triangular waveform. The curves are obtained at the following parameters of the LC cell: spontaneous polarization of the LC P_{s0} = 50 nC/cm^2, capacity of the orienting layers C = 13 nF at the electrode area S = 1 cm^2. The axes of the first and second polaroids are parallel and perpendicular to the normal to smectic layers, respectively.

In practice, it is important that the effect be observed at the highest frequency (the frequency of the hysteresis inversion usually observed experimentally is less than several hertz, which is insufficient for practical applications). Simulation shows that it is possible to control the inversion frequency by varying the conductivity of an LC [9]. With a decrease of the electric resistance of an LC, the inversion frequency increases; however, this is accompanied by one serious difficulty. The inversion frequency turns out to be dependent on the amplitude of the external voltage, and therefore this method can hardly be used in practice. Much better results can be obtained by using low-conductivity LCs (in our particular case, the resistivity should be not lower than 10 MΩ/cm^2), but it is important to decrease simultaneously the electric capacity of the orienting layers. This can be attained, e.g., by increasing the thickness of the orienting layers. The equivalent result can also be attained by using the capacitance of the given value connected in series with the cell [9]. Figure 8 illustrates the situation where the capacity of the orienting layers is reduced to 13 nF (which is equivalent to the polyimide-layer thickness of about 0.12 μm for each of the surfaces). As is seen, now the hysteresis-free switching is observed up to a frequency of 30 Hz. The frequency can be increased even more by using a LC with a pronounced spontaneous polarization. Thus, at P_{s0} = 100 nC/cm^2, the hysteresis-free switching takes place up to frequencies of 100 Hz.

The mechanism of the effect can be understood by considering the temporal dependences of the current in the circuit and the voltage at the LC layer (Fig. 9). Consider a normal hysteresis at a frequency of 200 Hz (Figs. 9a and 9c). In this case, the current response characteristic of ferroelectrics (solid curve in Fig. 9a) is observed, which is characterized by the pulses of the repolarization current. One can also see that at the moments when the pulses of the repolarization current are observed, the voltage at the LC layer (dash curve) decreases. At these moments, the director of a LC is in motion. The effective dielectric constant of the LC layer dramatically increases, because the spontaneous polarization rotating simultaneously with the director starts screening the electric field inside the LC layer, but has not enough time to screen it completely. When the director attains the end position corresponding to the polarization along the field, its motion becomes limited (only the electroclinic effect controlled by the elasticity modulus of the smectic layers is still observed). Now the polarization cannot screen the intensifying field. The voltage at the LC layer is now in phase with the external voltage of triangular waveform, whereas the current attains a certain low stationary value determined by the electric capacity in the circuit. For comparison, consider analogous dependences at the frequency of 30 Hz (Figs. 9b and 9d) with the *V*-shape effect being still observed. Now the current response becomes quite different. One has to single out three characteristic intervals during one period of the external field. The first interval corresponds to the situation where the voltage at the LC layer is in phase with the external voltage. At this time interval, the director is in the extreme position and cannot rotate over the cone. The second interval is a sharp current spike, the director becomes free and starts rotating. The electric capacity in the circuit is drastically changed and gives rise to a current spike. Then the third interval begins. Because of a lower frequency and capacity of the orienting layers, the rotation of the polarization practically screens the

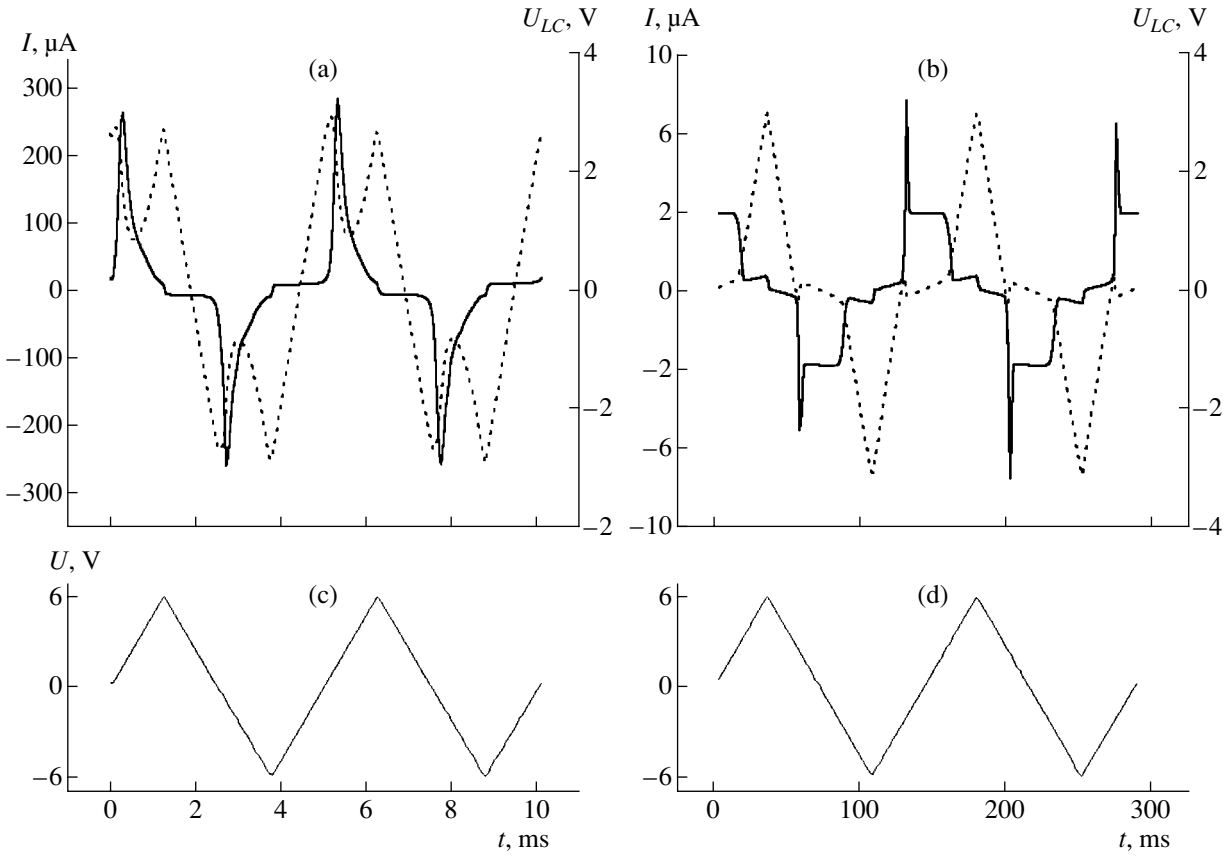

Fig. 9. (a, b) Time dependences of the current response (solid line) and voltage (dash lines) at the LC layer and (c, d) the same dependences obtained for the external voltage of triangular waveform. For notation see Fig. 8.

field inside the LC layer, and the voltage (dash line) becomes close to zero. The current has a constant value as if the circuit had only the capacity of the orienting layers.

Thus, the mechanism of the *V*-shape effect reduces to the fact that the presence of the electric capacity of the orienting layers results in the creation of the conditions such that the rotation of the polarization vector provides the field screening inside the FLC by the free charges at the electrodes of the LC cell. Under these conditions, the voltage at the LC layer tends to zero because of charging the electric capacity of the orienting layers, whereas the director motion is in phase with the changes in the external voltage, which results in the effect of hysteresis-free switching. Obviously, the lower the capacity of the orienting layers and the higher the spontaneous polarization of a LC, the faster the process of capacity charging and the higher the frequencies of the effect manifestation.

CONCLUSION

The article presents the complete system of equations providing the numerical solution of complex problems associated with the dynamics and electrooptics of ferroelectric liquid crystals. The mechanisms of the two most important effects observed in ferroelectric LCs—bistability and hysteresis-free electrooptics switching—are considered.

ACKNOWLEDGMENTS

The author is grateful to L.M. Blinov and S.A. Pikin (Institute of Crystallography) and W. Haase (Darmstadt University of Technology) for the formulation of the problem and numerous fruitful discussions. I would also like to thank M.I. Barnik, V.V. Lazarev, N.M. Shtykov, S.G. Yudin, N.N. Petukhova, and V. Petukhov for useful advice in the solution of the problem. Special thanks go to Ph. Martinot-Lagard (Université Paris Sud) for sharing with the author his rich experience in the numerical solution of the problems of dynamics in nematic liquid crystals.

The study was supported by the Russian Foundation for Basic Research, project no. 01-02-16287.

REFERENCES

1. http://autronic-melchers.com “Simulation software for LCDs.”

2. V. G. Chigrinov, D. A. Yakovlev, G. V. Simonenko, *et al.*, in *Proceedings of the 15th International Display Research Conference "Asia Display'95,"* 1995, p. 159.
3. L. M. Blinov and V. G. Chigrinov, in *Electrooptic Effects in Liquid Crystal Materials* (Springer-Verlag, New York, 1994), p. 69.
4. S. T. Lagerwall, in *Handbook of Liquid Crystals*, Ed. by D. Demus *et al.* (Wiley-VCH, Weinheim, 1998), Vol. 2B, p. 515.
5. R. B. Meyer, L. Liebert, L. Strzelrcki, *et al.*, J. Phys. Lett. **36**, L69 (1975).
6. A. Fukuda, S. S. Seomun, T. Takanishi, *et al.*, Mol. Cryst. Liq. Cryst. **303**, 379 (1997).
7. Yu. Panarin, V. Panov, O. E. Kalinovskaya, *et al.*, Ferroelectrics **246**, 35 (2000).
8. P. Rudquist, J. P. F. Lagerwall, M. Buivydas, *et al.*, J. Mater. Chem. **9**, 1257 (1999).
9. L. M. Blinov, E. P. Pozhidaev, F. V. Podgornov, *et al.*, Phys. Rev. E **66**, 021701 (2002).
10. N. A. Clark and S. T. Lagerwall, Appl. Phys. Lett. **36**, 899 (1980).
11. E. P. Pozhidaev, V. G. Chigrinov, Yu. P. Panarin, *et al.*, Mol. Mater. **2**, 255 (1993).
12. D. W. Berreman, J. Opt. Soc. Am. **62**, 502 (1972).
13. S. P. Palto, Zh. Éksp. Teor. Fiz. **119**, 638 (2001) [JETP **92**, 552 (2001)].
14. H. Wohler, G. Haas, M. Fritsch, *et al.*, J. Opt. Soc. Am. A **5**, 1554 (1988).
15. C. W. Oseen, Ark. Mat., Astron. Fys. A **19**, 1 (1925).
16. F. C. Frank, Discuss. Faraday Soc. **25**, 19 (1958).
17. L. D. Landau and E. M. Lifshitz, *Course of Theoretical Physics*, Vol. 8: *Electrodynamics of Continuous Media* (Nauka, Moscow, 1982; Pergamon, New York, 1984).
18. D. V. Sivukhin, *General Course of Physics* (Nauka, Moscow, 1996), Vol. III.
19. S. A. Pikin and V. L. Indenbom, Usp. Fiz. Nauk **125**, 251 (1978) [Sov. Phys. Usp. **21**, 487 (1978)].
20. S. A. Pikin, *Structural Transformations in Liquid Crystal* (Gordon and Breach, New York, 1991).
21. S. P. Palto, Zh. Éksp. Teor. Fiz. **121**, 308 (2002) [JETP **94**, 260 (2002)].

Translated by L. Man

Crystallography Reports, Vol. 48, No. 1, 2003, pp. 141–161. Translated from Kristallografiya, Vol. 48, No. 1, 2003, pp. 148–169.

CRYSTAL GROWTH REVIEW

Fluorite $M_{1-x}R_xF_{2+x}$ Phases (M = Ca, Sr, Ba; R = Rare Earth Elements) as Nanostructured Materials

B. P. Sobolev*, A. M. Golubev, and P. Herrero*****

** Shubnikov Institute of Crystallography, Russian Academy of Sciences, Leninskiĭ pr. 59, Moscow, 119333 Russia*

e-mail: sobolevb@crossovers.com

*** Moscow State Technical University, Moscow, Russia*

**** Instituto de Ciencia de Materiales, Madrid, Spain*

Received March 20, 2002

Abstract—The structural defects (M^{2+} and R^{3+} in the noncubic environment of F^-, interstitial F^-, and anion vacancies) in nonstoichiometric $M_{1-x}R_xF_{2+x}$ crystals with the CaF_2 structure form $\{M_8[R_6F_{68-69}]\}$ superclusters of nanometer linear dimensions. This fact allows one to classify the $M_{1-x}R_xF_{2+x}$ phases as nanostructured materials (NSM). The superclusters concentrate rare-earth ions (R^{3+} = RE). In a $M_{1-x}R_xF_{2+x}$ crystal with the fluorite cation motif, two chemically different parts can be separated: the R^{3+}-depleted matrix and the R^{3+}-enriched clusters. The $M_{1-x}R_xF_{2+x}$ phases are the first NSM among fluorides; they constitute a new type of these materials in which different chemical compositions of the matrix and nanoinclusions are combined with their isostructurality and coherent conjugation of the crystal lattices. Superclusters can also form associates with linear dimensions of tens or hundreds of angstroms. A model is suggested which describes the main characteristic of such NSMs. These materials behave as single crystals in X-ray, neutron, and electron diffraction experiments. The influence of microheterogeneity on some physical properties of the $M_{1-x}R_xF_{2+x}$ phases is also considered. © *2003 MAIK "Nauka/Interperiodica"*.

LIST OF CONTENTS

INTRODUCTION

In recent decades, the physics and chemistry of new objects—materials with at least one component characterized by the linear dimension ranging within 1–10 nm (10–100 Å)—have been intensely developed. This degree of dispersion lies at the boundary between the atomic (ionic) system of the solid solution and the two-phase system with grains of the second phase.

Below, we use the term "nanostructured material" (NSM) to refer to all the synonyms encountered in modern scientific literature such as nanophase, nanostructure, nanocrystal, etc. We should like to indicate that the term "nanophase" is inappropriate, because a high degree of dispersion of NSMs makes unjustified the relation of a nanoparticle to a phase in the classical sense of the word. Not discussing this problem here, we shall use here less dubious terms such as "nanoinclusion" and "nanoparticle."

The properties of single-phase NSMs (their classification is considered in Section 9) differ from the properties of materials with the same chemical composition but containing crystalline grains larger than a nanometer. This is explained by a considerable contribution of the boundary layer of nanoinclusions possessing a distorted structure.

A multiphase NSM with one or several phases of nanometer dimensions also have the properties different from the properties of the mechanical mixture of

large crystalline grains of the same composition. It is commonly accepted that a single crystal consists of only one phase. The formation of the second phase in a single crystal is usually accompanied by the deterioration or even complete loss of its optical transparency. There exist NSMs formed as a result of the decomposition of single crystals of solid solutions. The appearance of these materials differs from the appearance of single crystals. Therefore, there are grounds to believe that a single crystal having no visible interfaces cannot be a multiphase NSM (finely disperse mixture of phases).

However, there is a large family of $M_{1-x}R_xF_{2+x}$ phases that, being crystallized from melts, have the appearance of single crystals and behave as single crystals being studied by the X-ray, neutron, and electron diffraction methods but possess the microstructure characteristic of multiphase NSMs.

According to the distribution of RE elements R^{3+} in $M_{1-x}R_xF_{2+x}$ crystals, the latter can be considered as heterogeneous. The heterogeneity of the composition of these phases manifests itself at several levels. We consider here the minimum (linear) scale of inhomogeneities—the nanometer scale. The physical properties of the fluorite $M_{1-x}R_xF_{2+x}$ phases drastically differ from the properties of the MF_2 matrix and the second component RF_3. In the limit, the composition of a nanoinclusion tends to the composition of the second component of the $M_{1-x}R_xF_{2+x}$ systems (RF_3).

Numerous studies of the properties of $M_{1-x}R_xF_{2+x}$ phases are interpreted under the assumption that they are homogeneous crystalline media. We also have used this assumption for many years. However, the accumulated new data required the recognition of the microheterogeneity of $M_{1-x}R_xF_{2+x}$ phases. In recent years, the studies performed by various methods proved the existence of microinclusions of nanometer dimensions in these crystals. The microheterogeneity of $M_{1-x}R_xF_{2+x}$ crystals allows one to understand better their "anomalous" physical properties in terms of the conventional solid solutions.

Below, we consider the arguments that allow one to relate the fluorite $M_{1-x}R_xF_{2+x}$ phases to nanostructured materials, determine their position in the NSM classification, and discuss the specific features of their structural organization, which makes it possible to classify them as an independent type of NSMs, and consider some examples of the effect of microheterogeneity on their physical properties.

The defect crystal structure of the $M_{1-x}R_xF_{2+x}$ phase turned out to be very complicated. Although it has already been studied for more than thirty years, the work is still far from completion. In order to discuss the problem of nanostructured $M_{1-x}R_xF_{2+x}$ crystals, one has necessarily use some ideal notions of a fine atomic structure and its evolution in relation to the composition and conditions of synthesis of these crystals. The removal of the discrepancies and inconsistencies in the data on the defect structure of fluorite phases requires quite a long time, but the discussion of the related problems is beyond the scope of this article.

We believe that the general concepts of the specific (microheterogeneous) structure of fluorite $M_{1-x}R_xF_{2+x}$ phases are sufficient to draw the conclusion about their special place in the inorganic materials science as a new type of NSMs.

1. DEFECT (CLUSTER) STRUCTURE OF FLUORITE $M_{1-x}R_xF_{2+x}$ PHASES

This subject has been considered in hundreds of publications, so that even the most important of these publications cannot be discussed here. We limit ourselves to the conclusions related to the subject of our article. The structure was studied for the $Ca_{1-x}R_xF_{2+x}$ phases with all the RE elements, for $Sr_{1-x}R_xF_{2+x}$ with some RE elements of both subgroups, and for $Ba_{1-x}R_xF_{2+x}$ with RE elements of the Ce subgroup. There are no structural data for $Cd_{1-x}R_xF_{2+x}$, whereas for $Pb_{1-x}R_xF_{2+x}$, the structure was studied only for the high-pressure fluorite phase $Pb_{0.25}La_{0.75}F_{2.75}$.

The main result of the structural studies mentioned above is the establishment of the cluster structure for the $M_{1-x}R_xF_{2+x}$ phases by various methods, including X-ray and neutron diffraction, neutron and proton diffuse scattering, small-angle scattering, EXAFS, selective optical and laser spectroscopy, luminescence, conductometry, NMR and EPR, dielectric losses, ionic thermocurrent, Raman scattering, magnetic circular dichroism, etc.

It is usually accepted [1–5] that the $M_{1-x}R_xF_{2+x}$ crystals are solid solutions with the statistical distribution not of R^{3+} and M^{2+} ions (which can substitute each other) but of groupings having a specific shape or clusters. These clusters consist of concentrated structural defects such as highly charged R^{3+} cations (a defect of cation species), interstitial fluoride ions, and anionic vacancies of the main anionic motif. Hereafter, the clusters whose cationic composition consists mainly of RE elements are called rare earth clusters.

Since R^{3+} are concentrated in the cluster volume, the remaining part of the crystal (matrix) preserves the structure and the composition of initial MF_2. Thus, in a seemingly homogeneous $M_{1-x}R_xF_{2+x}$ crystal, two chemically different parts exist—the R^{3+}-depleted matrix and R^{3+}-enriched cluster. In the limit, the content of RE element in the cluster tends to 100%, i.e., to the pure RF_3 component of the MF_2–RF_3 system. This should be considered as anomalous behavior, because it does not correspond to the equilibrium phase diagrams, where some phases have a composition intermediate between the compositions of the main components, which should be separated during the decomposition of the fluorite solid solutions. Therefore, the formation of

clusters cannot uniquely be related to the decomposition processes. In the heterovalent $M_{1-x}R_xF_{2+x}$ solid solutions, the formation of RE clusters is observed at the R^{3+} content at a level of several tenths of the atomic percent [1–3]. In the isovalent solid solutions with such a content of impurity ions, one ignores the pair interactions between the ions, to say nothing of larger associates.

The structural studies of nonstoichiometric fluorite phases formed in the fluoride systems resulted in the construction of more than thirty cluster models for the description of the experimental data [4]. Summing up the structural studies performed for more than 20 years, Laval and Frit [5] write that the structures of various phases thoroughly investigated by theoretical calculations based on lattice simulation methods and various experimental techniques (ionic conductivity, dielectric relaxation, ionic thermocurrent, laser spectroscopy, EPR and ESR, NMR, Bragg and diffuse neutron scattering) still have not resulted in the creation of $M_{1-x}R_xF_{2+x}$ crystals. And now, almost twenty years later, this conclusion is still true.

This state of the knowledge on the defect structure of fluorite $M_{1-x}R_xF_{2+x}$ crystals reflects the difficulties in the choice of a concrete model from numerous energetically close ones. The examples of different interpretations of the experimental data for the crystals having the same composition are the interpretations of the $Ca_{0.9}Y_{0.1}F_{2.1}$ [6–9] and $Ca_{0.75}Y_{0.25}F_{2.25}$ [5, 6, 10] structures.

An important subjective factor is the selection of crystals appropriate for the structural studies. Recently, it has been shown [11] that as-grown $Ba_{1-x}R_xF_{2+x}$ crystals (i.e., crystals grown from melt and not subjected to any additional thermal treatment) have along with the cubic regions also the regions with low-symmetric distortions of the fluorite lattice. The dimensions of these regions exceed the dimensions of the crystals appropriate for X-ray studies. Thus, it is not clear which parts of heterogeneous crystalline $M_{1-x}R_xF_{2+x}$ rods were selected for the structural studies by different authors.

The interpretations of the structural data obtained by various research groups are often inconsistent. These inconsistencies can be explained by the complicated dependence of the defect structure of $M_{1-x}R_xF_{2+x}$ phases on some uncontrollable factors such as the thermal history of the crystals and the presence of oxygen impurity in fluorides. Oxygen impurity is formed because of the propensity of fluorides to react with water vapor at high temperatures (pyrohydrolysis). Oxygen contamination can hardly be controlled. This impurity strongly affects the properties and the defect structure of hydrolyzed fluorides. Sometimes, the deviation from the synthesis conditions providing the suppression of pyrohydrolysis results in the synthesis of oxyfluorides, such as, e.g., $Pb_8Y_6F_{32}O$.

The first experimental confirmation of the formation of the clusters of structural defects in the anionic motif of the nonstoichiometric $M_{1-x}R_xF_{2+x}$ fluorides was obtained in [6]. Earlier (1964), the anionic clusters were established by Willis in UO_{2+x} phases with the fluorite structure [12]. The F^{1-} (or O^{2-}) ions in the anionic clusters are displaced from the main positions of the fluorite structure. The interrelated anionic displacements prevent the formation of inadmissible short interatomic distances. They would be formed at the statistical distribution of the superstoichiometric X (F, O) ions (with respect to the MX_2 stoichiometry) over the centers of large cubic voids (1/2, 1/2, 1/2), the 4*b* position in the sp. gr. $Fm\bar{3}m$.

The general considerations and the computations performed in [13, 14] show that, in $M_{1-x}R_xF_{2+x}$, the local compensation of the R^{3+} charge by F^- ions is energetically advantageous. Thus, we passed from the anionic cluster to the anionic–cationic cluster of defects. Such a cluster concentrates the main species of structural defects: highly charged R^{3+}, fluorine incorporated into interstitials, and anionic vacancies.

A cluster of structural defects $[R_6F_{36}]$ for the nonstoichiometric fluorite $M_{1-x}R_xF_{2+x}$ phase was suggested in [15] based on the structural studies of the ordered phases. A $[R_4F_{26}]$ cluster was suggested as a possible structural subunit of fluorite phases [16] based on the structural studies of nonstoichiometric $M_{1-x}R_xF_{2+x}$ fluorites.

Figure 1 shows the idealized schemes of the formation of the above two rare earth clusters in $M_{1-x}R_xF_{2+x}$. In accordance with the arrangement of the cations at the vertices of polyhedra, they are called tetrahedral $[R_4F_{26}]$ (small) and octahedral $[R_6F_{36}]$ (large) clusters.

The structural data for disordered fluorite $M_{1-x}R_xF_{2+x}$ phases allow one to estimate the cationic composition of the clusters only approximately. A more reliable information is obtained from the studies of the ordered phases with the structure derived from the fluorite structure. These phases are formed in many of the MF_2–RF_3 systems (see Section 8.3). The clusters in these phases become the structural elements with the rigorously defined cationic composition. The study of the structures of ordered phases is limited by the difficulties associated with the synthesis of single crystals. Only some of these crystals are in equilibrium with the melt.

The nucleus of the octahedral rare earth cluster is a cuboctahedron $\{F_{12}\}$ formed by fluoride ions (Fig. 1). This anionic configuration is observed in the structure of the majority of the studied $M_{1-x}R_xF_{2+x}$ phases. The partial or complete compensation of the charge of the $\{F_{12}\}$ group is provided by highly charged R^{3+} ions.

The arrangement of the cations over an octahedron in clusters is set by the configuration of the anionic nucleus of the $\{F_{12}\}$ cluster. Hull and Wilson thor-

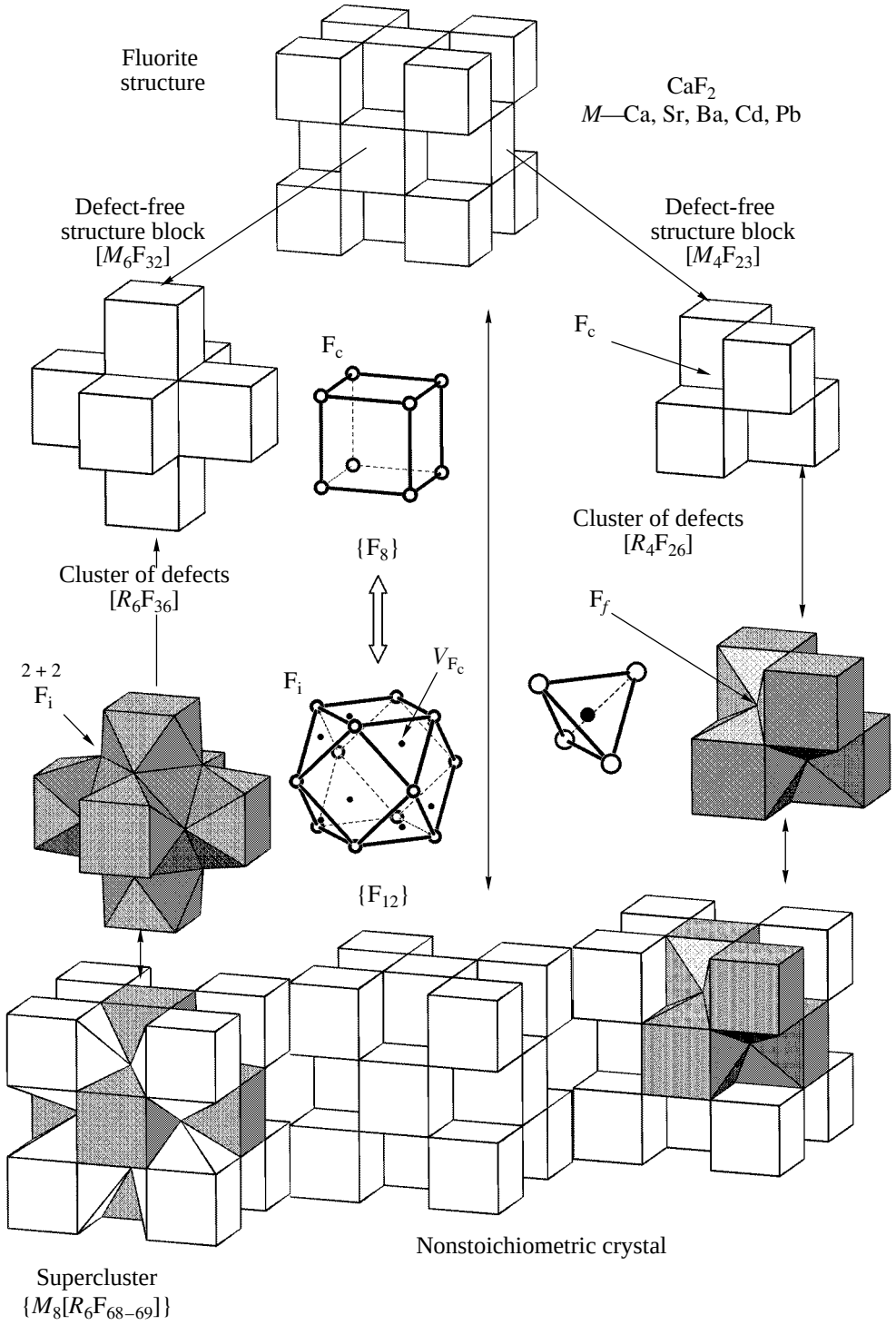

Fig. 1. Illustrating crystal chemistry of defects in the nonstoichiometric fluorite $M_{1-x}R_xF_{2+x}$ phases.

oughly analyzed the defect structure of the disordered $Ca_{0.94}Y_{0.006}F_{2.06}$ structure and came to the conclusion that the predominant defect species in disordered fluorite lattice comprises cuboctahedral anion clusters [17]. This anion configuration is one of a few configurations without anomalously short F–F distances.

The anion cluster $\{F_{12}\}$ is a universal structural defect in the phases with the cation fluorite motif (non-

stoichiometric fluorite phases, ordered phases with the structure derived from CaF_2, distorted fluorite phases without an increased lattice parameters). The universal character of this cluster is associated with the specific features of CaF_2-type structure.

The CaF_2 structure type is rather loose. Thus, in BaF_2, the ions (in the approximation of rigid spheres) fill only 52% of the space. The metal cations in the fluorite structure are surrounded with fluoride ions forming a cube. A cube is the less stable configuration of all the eight-vertex polyhedra (cube, square antiprism, dodecahedron).

The tendency of the CaF_2 structure type to form a stable configuration explains the diffuse high-temperature transition characteristic of all MX_2 (fluorites and antifluorites). Being heated to temperatures close to the melting point, some F^- occupy the interstitials, thus forming anion defects.

In the high-temperature modifications of MF_2, as well as in the fluorite phases $M_{1-x}R_xF_{2+x}$, the interstitial fluoride ions cannot be located at the center of the cubic void (1/2, 1/2, 1/2), because it is too small. This was shown experimentally by the *in situ* studies of thermostimulated defects of the anion motif in CaF_2 and PbF_2 by the method of diffuse neutron scattering [18]. According to the results of these studies, the centers of large cubic voids in the high-temperature phase are not occupied. The anion concentration in interstitials is estimated as 5 at. %.

It is reasonable to assume that the anion $\{F_{12}\}$ defects are as characteristic of the high-temperature MF_2 modification as for the fluorite $M_{1-x}R_xF_{2+x}$ phases.

The transformation of the $\{F_8\}$ cube into $\{F_{12}\}$ cuboctahedron reduces to the arrangement of four or five additional F^- (if the central cubic void is occupied). Without their location in the structure no broad homogeneity regions in the fluorite $M_{1-x}R_xF_{2+x}$ phase could be possible (see Section 8).

With a decrease in the temperature, the $\{F_{12}\}$ cluster in MF_2 is again transformed into the $\{F_8\}$ cube. It is not excluded that, in certain modes of cooling of the MF_2 crystals, the latter can partly preserve their high-temperature (disordered) modifications. Freezing of a large anionic $\{F_{12}\}$ cluster is more probable for a loose structure, especially for BaF_2.

In the $M_{1-x}R_xF_{2+x}$ phases, the grouping of $\{F_{12}\}$ is stabilized by R^{3+} ions, which provides the local compensation of the excessive charge and the formation of a more dense packing of the initially loose structure. In the limit, an octahedral rare earth $[R_6F_{37}]^{19-}$ cluster is formed.

The defect structure of the anion motif of the nonstoichiometric $M_{1-x}R_xF_{2+x}$ phases indicates that these phases are the stabilized high-temperature modifications of the fluorite MF_2 phases [19].

2. NANOSTRUCTURED $M_{1-x}R_xF_{2+x}$ PHASES AND BLOCK ISOMORPHISM

The association of structural defects into rare earth clusters and larger complexes (see Section 6) allows one to consider the formation of $M_{1-x}R_xF_{2+x}$ solid solutions as a result of the block isomorphism, which is provided not by individual ions but by large structural blocks (with the volume of several hundreds and thousands of cubic angstroms) having considerably different chemical (cation) compositions.

The typical sign of the block isomorphism in the form it manifests itself in the $M_{1-x}R_xF_{2+x}$ phases is the absence of any limitations on the dimensions of the structural blocks that can substitute each other (see Section 7). We assume that it is the block isomorphism that leads to the violation of stoichiometry. It allows one to reduce the size difference for lone M^{2+} and R^{3+} ions, which should limit the isomorphism in the absence of cluster formation.

In the isomorphism classification, the block isomorphism can be considered as a variety of the heterovalent isomorphism with the filling of the space [20]. The block isomorphism and the formation of nanostructured phases are the two forms of the manifestation of the general characteristic of the $M_{1-x}R_xF_{2+x}$ phases—their microheterogeneity. The block isomorphism will be considered in another publication.

3. HETEROGENEITY OF $M_{1-x}R_xF_{2+x}$ PHASES AND DIMENSIONS OF INHOMOGENEITIES

3.1. Superclusters $\{M_8[R_6F_{68-69}]\}$ as RE-containing Elementary Building Units of the $M_{1-x}R_xF_{2+x}$ Phases

The main feature that allows one to relate the $M_{1-x}R_xF_{2+x}$ phases to NSMs is the size of the associates of structural defects such as clusters and superclusters.

A rare earth $[R_6F_{37}]^{19-}$ cluster absorbs the major part of the structural defects (but not all of them) whose formation accompanies the heterovalent isomorphism of M^{2+} and R^{3+} in the CaF_2-type structure. The adjacent M^{2+} ions with the coordination polyhedra different from a cube are located outside the octahedral cluster. The polyhedron is a distorted sphenocrown—a ten-vertex polyhedron formed due to the substitution of one of the fluoride ions at the cube vertex per three such anions entering the coordination polyhedra of R^{3+} cations.

In the combination of clusters accompanied by the collectivization of M^{2+} ions, the anionic polyhedra of the latter are transformed from 10-vertex polyhedra into 12-, 14-, or 16-vertex ones. This occurs with the successive substitution of one of the vertices by three new ones. Figure 1 shows (below on the left) the

arrangement of light polyhedra with M^{2+} being located at the cube vertices and surrounding a rare earth cluster.

These M^{2+} polyhedra should also be considered as defect ones (in comparison with the fluorite matrix). It is reasonable to combine these polyhedra with a rare earth cluster $[R_6F_{37}]$ to obtain a larger structural unit—a supercluster $\{M_8[R_6F_{68-69}]\}$ (Fig. 1, below on the left).

The expediency of the introduction of superclusters is determined by at least three of its characteristics. First, a supercluster is the minimum volume of the crystal containing all the defect species, including the M^{2+} cations, which are characterized (as R^{3+}) by a nonideal "fluorite" (cubic) environment of fluorine. Second, the external (anionic) shell of the supercluster preserves the tetragonal motif MF_2, which facilitates the incorporation of superclusters into the initial fluorite matrix during the formation of $M_{1-x}R_xF_{2+x}$ phases. The third characteristic convenient for simulation of crystal structures is the simple form of this supercluster—a cube.

The notion of a supercluster was introduced in [21–27] to describe a set of several elementary clusters in concentrated fluorite solid solutions [10]; however, this term is rarely used in such a sense.

3.2. Volume Changes during Formation of $M_{1-x}R_xF_{2+x}$ Phases

Theoretically, several schemes of M^{2+} and R^{3+} isomorphism are possible in a CaF_2 structure. The existence of isomorphism with filling of the space [20] is proven by comparing the experimental densities of the $M_{1-x}R_xF_{2+x}$ phases with the densities calculated by various schemes (incorporation of anions and cation vacancies). To calculate the X-ray densities one has to know the lattice parameters.

The assumption that $M_{1-x}R_xF_{2+x}$ crystals consist of a matrix and rare earth clusters can be verified by comparing the calculated changes in the lattice parameters of the fluorite phases for various models. Two models are possible: a crystal structure consisting of the matrix and rare earth superclusters and the model in which the molar volume or the volume per formula unit of the $M_{1-x}R_xF_{2+x}$ solid solution is taken to be equal to the sum of the MF_2 and RF_3 volumes proportional to their molar fractions.

Let us determine the volumes of the matrix and rare earth superclusters.

Matrix superclusters $\{M_{14}F_{64}\}$ have volumes constant for each MF_2. They are calculated as the volume of a crystal containing 14 M^{2+} cations. The unit cell of the fluorite structure contains four MF_2 formula units. The volume of a matrix supercluster equals 14/4 = 3.5 of the unit-cell volume of the fluorite structure. During combination of the matrix clusters, the anions of the external shell are collectivized and the composition of the formula unit remains the same, MF_2.

Rare earth superclusters $\{M_8[R_6F_{68-69}]\}$ (RE_{sup}) have the volume V_{Rsup} dependent on the size of the R^{3+} and M^{2+} ions. It is inappropriate to use the ionic radii to calculate V_{Rsup} because of the relative nature of these quantities. The supercluster volume is calculated from the data on the lattice parameters of the ordered $M_9R_5F_{33}$ and $M_8R_6F_{34}$ phases. The unit-cell volume of the latter is divided into the number of the formula units. In this representation, it coincides with the number of superclusters per unit cell. For two series of the fluorite $Ca_{1-x}R_xF_{2+x}$ and $Sr_{1-x}R_xF_{2+x}$ phases, the cation composition of a supercluster is $\{M_9R_5\}$, whereas, for the series of the $Ba_{1-x}R_xF_{2+x}$ phases, it is $\{M_8R_6\}$. The volume V_{ss} of the structural fragment of the $M_{1-x}R_xF_{2+x}$ solid solution containing 14 cations was calculated as the sum of the molar fractions of the matrix (*Msup*) and rare earth (*Rsup*) superclusters

$$V_{ss} = (1-x)V_{M\text{sup}} + xV_{R\text{sup}}.$$

The fraction x of rare earth clusters was calculated from the molar fraction of $RF_3(y)$ by the ratio $x = 14y/N_R$, where N_R is the number of RE cations in the supercluster. The lattice parameter of the fluorite phase $M_{1-x}R_xF_{2+x}$ was calculated as a cubic root from $V_{ss}/3.5$.

4. LATTICE PARAMETERS OF $M_{1-x}R_xF_{2+x}$ PHASES OBTAINED BASED ON SUPERCLUSTER MODEL

Now consider the model of $M_{1-x}R_xF_{2+x}$ solid solutions consisting of matrix $\{M_{14}F_{64}\}$ and rare earth $\{M_8[R_6F_{68-69}]\}$ superclusters having the cubic shape of a cube and different dimensions and chemical compositions. The changes in the volume occurring during the formation of a solid solution depend on the volume of the rare earth supercluster which concentrates all the structural defects. The alternative model does not take into account the additional changes in the volume during the formation of clusters of defects.

Let us verify the appropriateness of the suggested procedure on isovalent $Sr_{1-x}Ba_xF_2$ and $La_{1-x}Nd_xF_3$ solid solutions. For the SrF_2–BaF_2 and LaF_3–NdF_3 systems, the complete mutual solubility of the components in the solid state and the linear dependences of the lattice parameters on concentration are established. The upper plots in Fig. 2 show the experimental lattice parameters of $Sr_{1-x}Ba_xF_2$ and $La_{1-x}Nd_xF_3$ and their values calculated from the molar volumes. The good agreement of these values for both systems confirms the fact that, during the formation of isovalent solid solutions, no changes in the volume associated with the interactions of defects and the cluster formation take place.

Figures 2c–2h compare the concentration dependences of the experimental values of the cubic lattice parameters (*1*) with those calculated for the fluorite $M_{1-x}R_xF_{2+x}$ phases based on the supercluster model (*2*) and the sum of the molar volumes of the components (*3*). The experimental lattice parameters coincide with those calculated based on the supercluster model of the $M_{1-x}R_xF_{2+x}$ solid solution. The possible reasons of the observed small deviations are not considered here.

The model of fluorite $M_{1-x}R_xF_{2+x}$ phases consisting of the matrix and rare earth superclusters in the shape of cubes describes the variation of the lattice parameters of these phases depending on their composition quite well. The considerably larger parameters obtained from the sum of the molar volumes of the MF_2 and RF_3 components indicate the "contraction" effect during the formation of heterovalent solid solutions.

5. CHANGE IN THE VOLUMES OF $\{M_8[R_6F_{68-69}]\}$ SUPERCLUSTERS ALONG THE ALKALI EARTH (M) AND RARE EARTH (R) SERIES

Consider the range of the dimension variations of the matrix and RE superclusters along the series of alkali earth and RE elements (Fig. 3). The rare earth superclusters $\{M_8[R_6F_{68-69}]\}$ also include M^{2+} cations and, therefore, for each fixed R^{3+}, their volumes increase in the transition from Ca to Sr and Ba. In the RE series, the volumes of RE superclusters decrease in the transition from La to Lu because of a decrease of the R^{3+} radius (lanthanide contraction).

It should be noted that the $V_{R\text{sup}}$ lines for different M^{2+} continue one another: the volume $V_{R\text{sup}}$ with Lu for the Ba series is practically equal to $V_{R\text{sup}}$ for La from the Sr series, whereas the $V_{R\text{sup}}$ for Lu from the Sr-series is close to $V_{R\text{sup}}$ for La from the Ca-series (dotted lines in Fig. 3). Thus, the volumes of $\{M_8[R_6F_{68-69}]$ superclusters continuously vary from the minimum value of 570 Å^3 (the matrix supercluster $\{Ca_{14}F_{64}\}$) to the value of 782 Å^3 (rare earth supercluster $\{Ba_8[La_6F_{69}]\}$).

The dependence of $V_{R\text{sup}}$ on the dimension of M^{2+} explains the widespread occurrence of nonstoichiometric fluorite phases in the MF_2–RF_3 systems. The formation of superclusters as the subunits that can be substituted smooths the differences in the dimensions of M^{2+} and R^{3+} and, thus, increases the regions of heterovalent isomorphism of these cations.

As is seen from Fig. 3, for the $Ba_{1-x}R_xF_{2+x}$ phases with all the RE elements, the inequality $V_{M\text{sup}} > V_{R\text{sup}}$ is fulfilled. For the $Sr_{1-x}R_xF_{2+x}$ phases, this inequality is fulfilled for the part of the RE series from (Pm)–Sm to Lu. At the part of the series from La to Nd, the volumes of RE clusters exceed the volume of a matrix supercluster, $V_{M\text{sup}} < V_{R\text{sup}}$. This inequality holds for the whole family of $Ca_{1-x}R_xF_{2+x}$ phases.

Thus, the dimensions of individual RE superclusters of the composition $\{M_8[R_6F_{68-69}]\}$ in the fluorite $M_{1-x}R_xF_{2+x}$ phases range approximately within 570–780 Å^3, whereas the matrix supercluster $\{Ba_{14}F_{64}\}$ attains the volume of 834 Å^3, which corresponds to the linear dimensions of the subunits of the order of 8–10 Å.

Thus, the minimum linear dimensions of rare earth superclusters of defects are close to a nanometer. They lie at the lower boundary of the linear dimensions of the particles that are considered as nanoinclusions characteristic of NSMs.

6. ASSOCIATION OF SUPERCLUSTERS IN $M_{1-x}R_xF_{2+x}$

The presence of defect-free regions (MF_2 matrix) in diluted $M_{1-x}R_xF_{2+x}$ solid solutions can be explained by the combination of RE ions into small formations (isolated rare earth superclusters). However, the concentrated $M_{1-x}R_xF_{2+x}$ solid solutions with several tens of mole percent of RF_3 also have some regions with the characteristics identical to those of the undistorted MF_2 matrix. The related data are scarce, but they indicate that the $M_{1-x}R_xF_{2+x}$ crystals are built by large associates of octahedral RE superclusters (nanoinclusions) dispersed over the undistorted fluorite matrix.

The studies of some physical properties of $M_{1-x}R_xF_{2+x}$ crystals that indicate the formation of large associates of clusters and $\{M_8[R_6F_{68-69}]\}$ superclusters are discussed in Section 10.

7. MODEL OF STRUCTURE OF FLUORITE $M_{1-x}R_xF_{2+x}$ PHASES WITH RARE EARTH NANOINCLUSIONS

In this section, we suggest an idealized model of fluorite nonstoichiometric $M_{1-x}R_xF_{2+x}$ phases based on the possible formation of nanoinclusions, individual superclusters, or their associates. In the bulk of these crystals, the substitution of M^{2+} by R^{3+} at the cationic sites of the fluorite structure and of the anionic cubes $\{F_8\}$ by the centered cuboctahedra $\{F_{13}\}$ occurs (the change of the qualitative and quantitative composition). As a result, the coordination of cations with anions, the density of the ion packing, and some other rearrangements take place, which are usually considered as structural changes. However, the general fluorite cationic motif of the structure is preserved.

The model does not take into account all the known features of the defect structure of these phases and thus should be considered only as the first approximation.

The following assumptions are made:

—for the sake of simplification, only the cationic motifs of the crystal (fluorite) matrix and rare earth superclusters are considered;

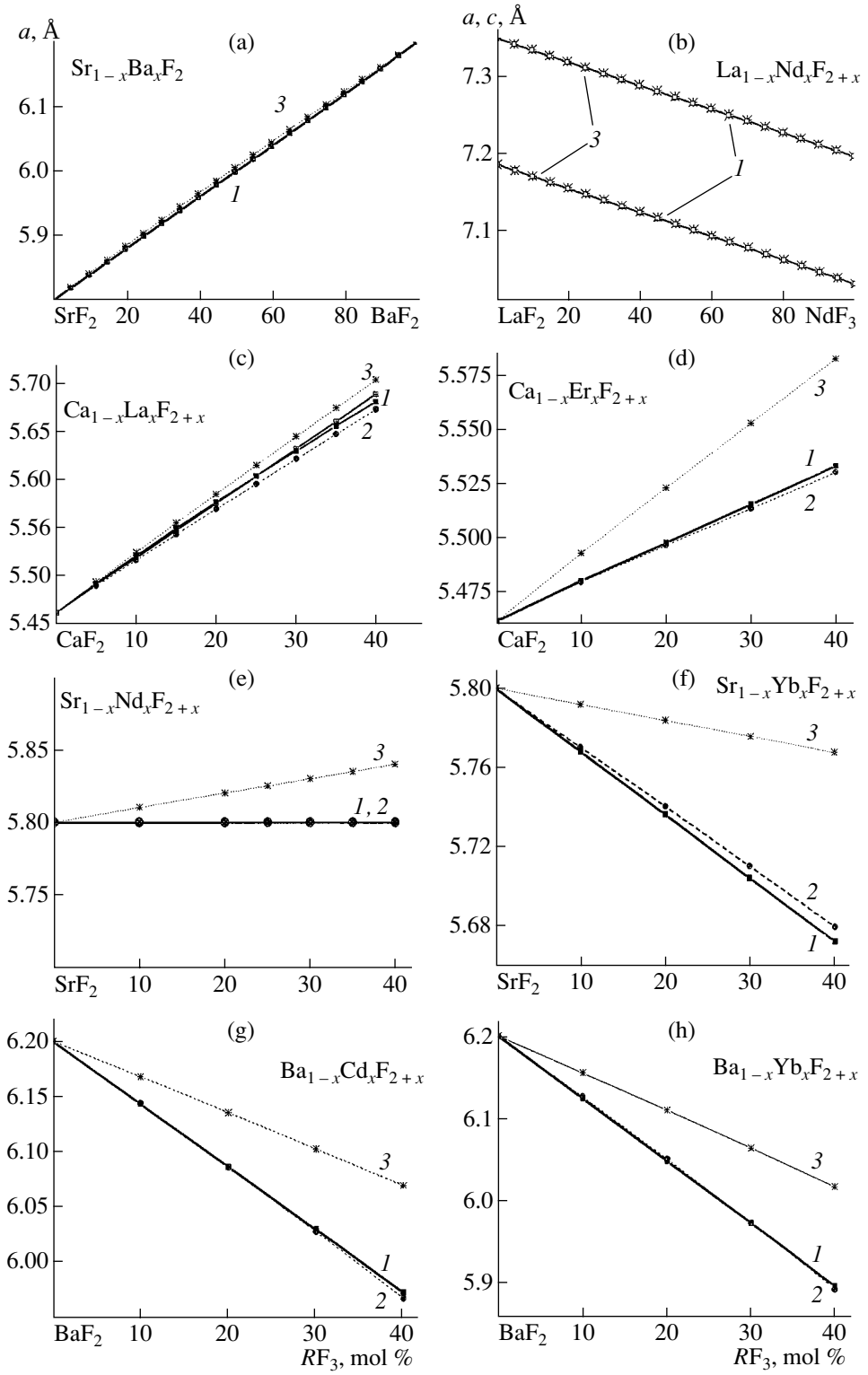

Fig. 2. Lattice parameters of the $M_{1-x}R_xF_{2+x}$ phases (*1*) obtained experimentally, (*2*) calculated based on the supercluster model, (*3*) calculated from the sum of molar volumes.

—small displacements of the cations from their ideal positions in the fluorite structure are ignored;

—the changes in the positions of anions during the formation of an RE supercluster are ignored;

—the model does not reflect the geometric differences between the matrix and rare earth superclusters. Such differences are characteristic of all the $M_{1-x}R_xF_{2+x}$ phases except of $Sr_{1-x}Nd_xF_{2+x}$. The max-

imum difference is observed between the matrix supercluster $\{Ba_{14}F_{64}\}$ and the supercluster $\{Ba_8[Lu_6F_{69}]\}$ and amounts to 5.4%;

—the model suggests the association of superclusters into larger nanoparticles (nanoinclusions). No size restrictions are imposed on such associates. This signifies that the model covers the whole interval of the degree of dispersion of such a NSM from several nanometers up to the separation of micronuclei of a new phase.

Under the above assumptions, the model reflects the main characteristic features of the defect structure of the fluorite $M_{1-x}R_xF_{2+x}$ phases as NSMs, namely:

—microheterogeneity at the level of nanoinclusions;

—single-crystal appearance of the heterogeneous system;

—the behavior of a NSM as a single crystal in the X-ray, neutron, and electron diffraction experiments;

—possible observation of undistorted matrix component by some physical methods (NMR, EPR, Raman scattering, etc., see Section 10) in the concentrated (with respect to RE ions) $M_{1-x}R_xF_{2+x}$ solid solutions up to the content of several tens of molar percent of RF_3;

—extremely high RF_3 solubilities in fluorite MF_2 and the weak dependence of these values on the geometric factor (difference in the size of isolated M^{2+} and R^{3+} ions).

Figure 4 shows the 2D sections of several hypothetical variants of the formation of nonstoichiometric $M_{1-x}R_xF_{2+x}$ crystals and ordered phases (with the structure derived from the fluorite structure) consisting of the matrix and rare earth superclusters. Filled circles indicate M^{2+} cations, light ones, R^{3+} cations. To simplify the drawing, no anions are indicated.

In the chosen projection of only one cationic layer, an isolated rare earth supercluster is represented by four R^{3+} ions arranged over the square. The remaining cations of the supercluster ($8M^{2+}$ and $2R^{3+}$) are located in the neighboring cationic layers. A single supercluster is shown in Fig. 4a (top left).

Figure 4 shows two pairs of models corresponding to the same or close concentration of RE elements but possessing (Figs. 4b, 4d) or not possessing (Figs. 4a and 4c) the long-range order in the arrangement of RE superclusters. The common feature of the 2D sections (Figs. 4a and 4c) is the fact that the crystallographic planes occupied by different species (M^{2+} and R^{3+}) of the matrix and the aggregate of superclusters (nanoinclusions) continuously pass into one another (coherent conjugation). This is one of the characteristic features of the $M_{1-x}R_xF_{2+x}$ phases as NSMs. Figure 4a shows the $M_{1-x}R_xF_{2+x}$ phase with ~15 mol % RF_3 (from the ratio of the areas). It is seen that, despite the formation of RE nanoinclusions, there is still a large fraction of undistorted matrix structure.

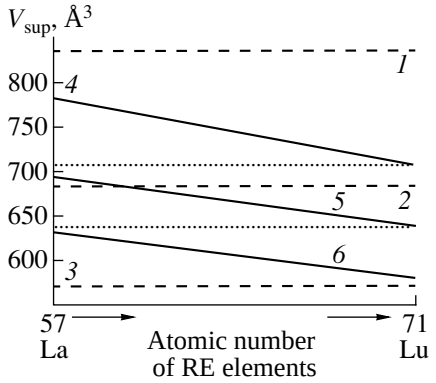

Fig. 3. The change in the supercluster volume obtained (*1–3*) from the volumes of matrix $\{M_{14}F_{64}\}$ superclusters ($V_{M\text{sup}}$) for M = Ba, Sr, and Ca, respectively, and (*4–6*) the change of the volume of RE $\{M_8[R_6F_{68-69}]\}$ superclusters ($V_{R\text{sup}}$) with the change of the atomic number along the RE series for M = Ba, Sr, and Ca, respectively.

Figure 4b shows the hypothetical ordered tetragonal phase with 15.38% of rare earth elements projected onto the (001) plane [26]. The ordered arrangement of superclusters results in disappearance of extended regions of undistorted matrix structure.

Figure 4c shows the nonstoichiometric $M_{1-x}R_xF_{2+x}$ phase with about 40 at. % of rare earth ions. This concentration considerably exceeds the percolation threshold for single octahedral superclusters. The associates of rare earth superclusters have different dimensions and the orientations in the crystalline matrix. The coherence condition for their crystallographic planes is preserved. It is seen that the formation of large associates results in the fact that, despite the high RE concentration, there are the regions of undistorted MF_2 matrix. The enlargement of the associates of the superclusters do not change the initial fluorite motif of the crystal, which is the necessary condition for the formation of the single-crystal diffraction pattern from such an object.

The model considered does not limit the associate dimensions. It can describe the whole dispersion range of rare earth elements in $M_{1-x}R_xF_{2+x}$ crystals from isolated R^{3+} ions to isolated superclusters to supercluster associates up to the formation of an individual RE-containing phase. Because of lowering of the symmetry of the associates of superclusters, they can be differently oriented with respect to the matrix lattice (Figs. 4a and 4c). These features of the nanostructure of the $M_{1-x}R_xF_{2+x}$ phases result in considerable diversity of the shape, dimensions, and spatial orientations of nanoinclusions. If the associates are oriented randomly, the NSMs show no essential changes in their diffraction patterns.

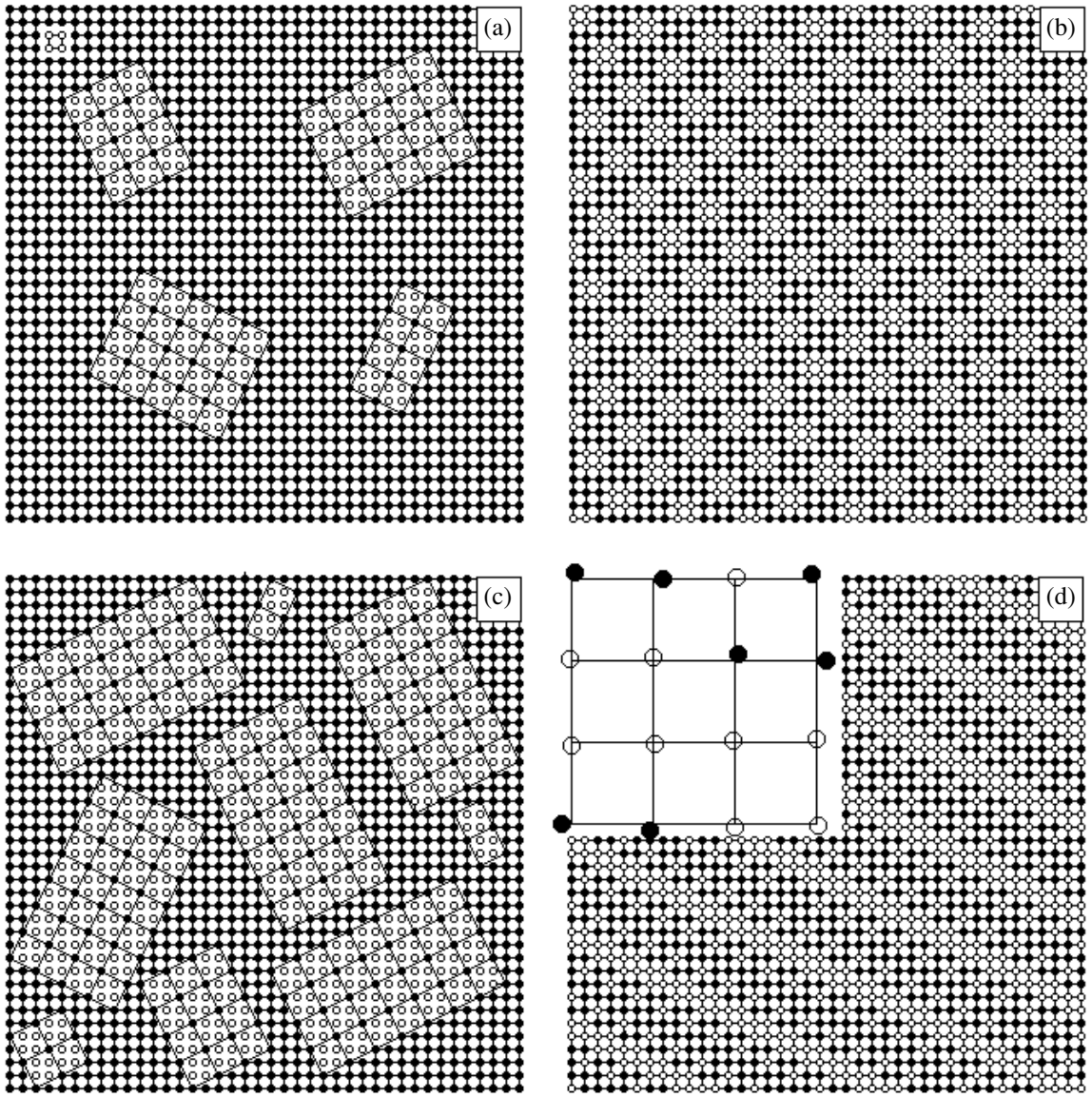

Fig. 4. The models of (a, c) nonstoichiometric $M_{1-x}R_xF_{2+x}$ crystals with 15 and 40 at. % R^{3+}, respectively, and (b, d) ordered phases with 15.38 and 42.86 at. % ($Ba_4Yb_3F_{17}$) [28]. Notation: light circles denote R^{3+}, black ones, M^{2+}.

The ordered arrangement of superclusters at the RE ion concentration 42.86 at. % is shown in Fig. 4d demonstrating an idealized $(\bar{1}\bar{2}4)$ section of the crystal structure of the ordered rhombohedral $Ba_4Yb_3F_{17}$ phase studied in [28]. The transition to the fluorite-like cell in this phase results in the isometric triclinic unit cell with the parameters $a = b = c = 5.869$ Å and $\alpha = \beta = \gamma = 90.2°$, which, in the first approximation, can be considered as a cubic one. Small displacements of the cations from the fluorite positions are seen on an enlarged part of the structure in the upper left corner in Fig. 4d.

Comparison of Figs. 4c and 4d representing the cationic nets of the crystals with almost the same RF_3 content demonstrates the effect of ordering. It is seen that the ordered arrangement of RE superclusters results in disappearance of undistorted matrix regions. This should be reflected by differences in some physical characteristics of nonstoichiometric phases and ordered phases with the structure derived from fluorite. The model of nanostructured nonstoichiometric fluorite phase suggested here should be further improved.

Now consider the data on the formation of $M_{1-x}R_xF_{2+x}$ phases, their position on the phase diagrams of the MF_2–RF_3 systems, and their relation to the ordered phases. All these problems are directly associated with the synthesis of new NSMs.

8. BASIC DATA ON FLUORITE $M_{1-x}R_xF_{2+x}$ PHASES AND ORDERED PHASES WITH THE STRUCTURE DERIVED FROM CaF_2 IN THE MF_2–RF_3 SYSTEMS

8.1. History of the Studies of Fluorite Phases $M_{1-x}R_xF_{2+x}$

The synthesis and the study of the $M_{1-x}R_xF_{2+x}$ phases (M = Ca, Sr, Ba, Cd, Pb; R = RE) with the defect CaF_2 structure have almost a century-long history. These phases were first discovered in 1911 [29] as minerals—yttrofluorite and fluorocerite (the solid solution of RE elements of the Y- and Ce-subgroups in CaF_2). For the first time, crystals of artificial $Ca_{1-x}YF_{2+x}$ and $Ca_{1-x}Ce_xF_{2+x}$ minerals were grown from melt in [30] and were considered as an example of isomorphism with the filling of the space [20]. The experimental study of the defect structure of the $M_{1-x}R_xF_{2+x}$ crystals was started much more later [6, 31].

Fluorite phases of the general formula $M_{(1-x)m}R_{xn}F_{(1-x)m+nx}$ are formed in the MF_m–RF_n systems ($m \neq n$) whose components are fluorides of more than thirty metals. There are no structural data for fluorite phases with R = Al, Sc, Ti, V, Cr, Fe, Ga, In, Sb, Tl, and Bi experimentally discovered in the corresponding systems [32]. We limit ourselves to the consideration of the fluorite phases $M_{1-x}R_xF_{2+x}$ formed in the MF_2–RF_3 systems structurally studied in sufficient detail. The consideration of the phase diagrams of the MF_2–RF_3 systems [33–35] showed that the $M_{1-x}R_xF_{2+x}$ phases are the basic products of high-temperature chemical interactions of fluorides of alkali earth and rare earth metals of different valence. The grossly nonstoichiometric fluorite phases $M_{1-x}R_xF_{2+x}$ comprise about 50% of all the nonstoichiometric phases discovered in the MF_m–RF_n systems ($m < n \leq 4$). The limit solubilities of RF_3 in $M_{1-x}R_xF_{2+x}$ attain 50 ± 2 mol % under atmospheric pressure. The structural defects in crystals with pronounced deviations from stoichiometry termed grossly nonstoichiometric phases [36] cannot be described in the approximation of point (noninteracting) defects.

Most of grossly nonstoichiometric $M_{1-x}R_xF_{2+x}$ phases are characterized by the pronounced propensity for preservation of disordered (defect) structure in cooling. Therefore, the crystals of the $M_{1-x}R_xF_{2+x}$ solid solutions grown from melt are important as stable materials (not decomposing during cooling, storage, and exploitation). They do not decompose even under thermal cycling from low to high temperatures. There are $M_{1-x}R_xF_{2+x}$ crystals that have shown no signs of decomposition for almost forty years.

8.2. Position of Nonstoichiometric $M_{1-x}R_xF_{2+x}$ Phases on Phase Diagrams and Their Relation to Ordered Phases

The information on the thermodynamic behavior of the $M_{1-x}R_xF_{2+x}$ phases can be obtained from the phase diagrams of the condensed state of the MF_2–RF_3 systems studied in our earlier work [33] for almost all the combinations of the cations considered in the present article. Let us illustrate the position of the $M_{1-x}R_xF_{2+x}$ phases on the phase diagrams and their relation to the ordered phase by several examples.

The $M_{1-x}R_xF_{2+x}$ phases show a different propensity to decomposition and ordering with a decrease in the temperature. This is reflected on the phase diagrams. Figure 5 shows the transformation of the phase diagrams of six MF_2–RF_3 systems (in the region 0–60 mol % RF_3) as a function of the volume difference ΔV of the matrix $\{M_{14}F_{64}\}$ and rare earth $\{M_8[R_6F_{68-69}]\}$ superclusters (in percent of the volume of a matrix supercluster). Figure 5 also shows Δr (the difference in the sizes of M^{2+} and R^{3+} in percent of the radius of M^{2+}). The coordination number for both cations is taken to be eight, the radii are used on the scale of the effective ionic radii [37].

The temperature scale is reduced to the melting point (T_m, °C) of the corresponding MF_2 component. In the interval of the reduced temperature 0.5–1.1, all the reactions with the participation of nonstoichiometric and ordered phases of interest occur.

Figure 5a shows that the fluorite solid solution $Ca_{1-x}Lu_xF_{2+x}$ in the CaF_2–LuF_3 system is formed at Δr = 13%. The constituent matrix and rare earth superclusters (see below) have practically the same volumes ($V_{M\text{sup}}$ and $V_{R\text{sup}}$, respectively). The ordered 2 : 1 and 8 : 5 phases are formed in the solid state. The ordered phase $Ca_{14-\delta}Y_{5+\delta}F_{43+\delta}$ (26.37–31.56 mol % YF_3) with the structure of the mineral tweitite in the CaF_2–YF_3 system decomposes in a "deep" subsolidus (670°C). Therefore, the $Ca_{14-\delta}Lu_{5+\delta}F_{43+\delta}$ phase analogous to tweitite is not represented in the phase diagram. Figure 4b shows the section of the model of this ordered phase.

The phase relationships between the fluorite and the ordered phases in the SrF_2–GdF_3 system are shown in Fig. 5b. Three ordered phases (T, R', and S) are transformed upon heating into the nonstoichiometric $Sr_{1-x}Gd_xF_{2+x}$ phase. The fourth one (R) is at the solubility limit of GdF_3 in SrF_2 at the eutectic temperature. The nonstoichiometric $Sr_{1-x}Gd_xF_{2+x}$ phase has an anomaly (the maximum) on the melting curves. These maxima are the characteristic feature of the heterovalent solid solutions with the varying number of atoms in the unit cell (nonstoichiometric phases) [38].

With a further increase in Δr and ΔV, the stability of the ordered $M_4R_3F_{17}$ phases also increases. In the PbF_2–LuF_3 system, such a phase is in equilibrium with the melt from which crystals can be grown. The melting

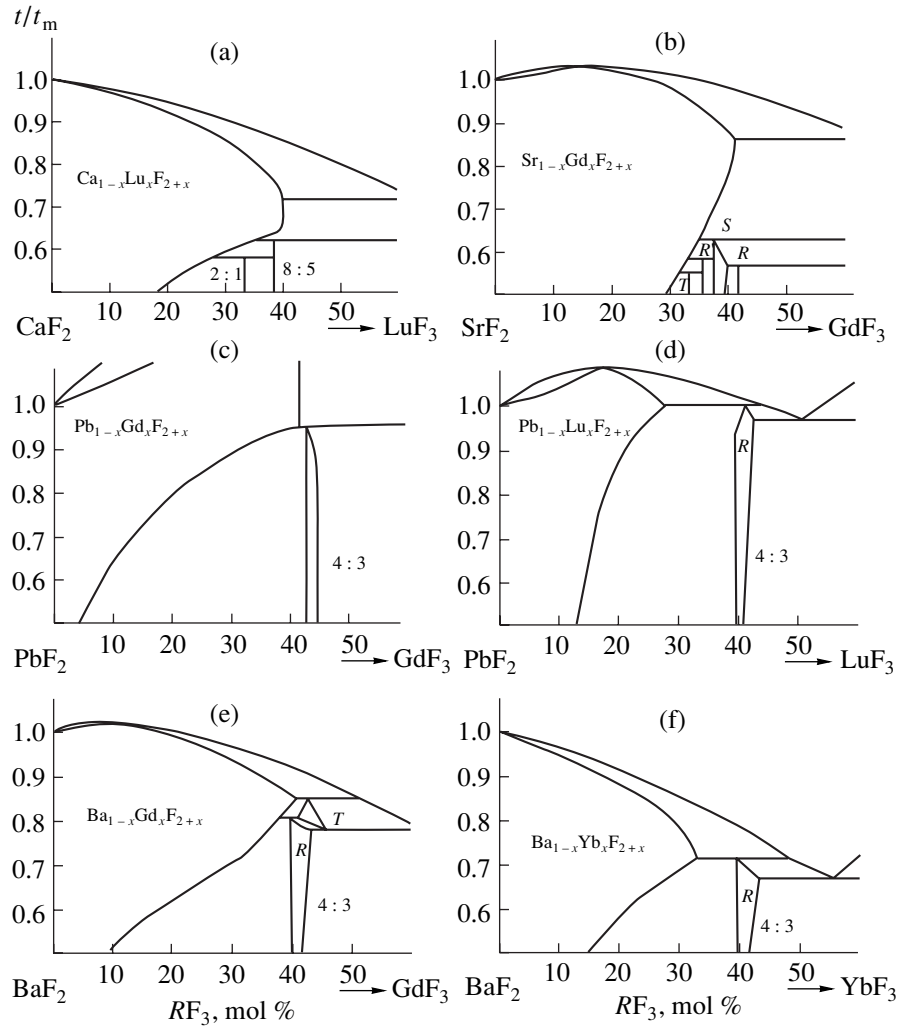

Fig. 5. Location of the nonstoichiometric fluorite $M_{1-x}R_xF_{2+x}$ phases and the phases with the structure derived from the fluorite one on the phase diagrams of the MF_2–RF_3 systems. The difference between the volumes of the RE and matrix superclusters (ΔV) is (a) 1, (b) 2, (c) 6, (d) 10, (e) 12, (f) 15%. The difference in the size of the M^{2+} and R^{3+} ions is (a)13, (b) 16, (c) 18, (d) 24, (e) 26, (f) 31%.

point of $Pb_4Lu_3F_{17}$ almost coincides with the melting point of the component PbF_2. The melting curves of the fluorite phase have a well developed maximum. Such a maximum in the PbF_2–GdF_3 system (Fig. 5c) corresponds to a higher melting point which is outside the chosen interval of the reduced temperatures. With a further increase in ΔV_{sup} (Figs. 5e and 5f), the thermal stability of the $M_4R_3F_{17}$ phases decreases. Their compositions either are outside the homogeneity region or lie at the limit of the solubility of RF_3 in MF_2. As a result, they acquire the characteristics of independent compounds with the structure derived from CaF_2. These compounds cannot be obtained as fluorite $M_{1-x}R_xF_{2+x}$ phases during heating up to the melting point. Because of the incongruent melting of the 4 : 3 phases, we managed to grow their single crystals appropriate for structural studies [28].

8.3. Ordered Phases with Structures Derived from CaF_2 *Type*

In the interval 0–50 mol % RF_3 in the MF_2–RF_3 systems, several tens of ordered phases with the structure derived from the CaF_2 type are formed [33]. They are related to five types of the distorted cubic face-centered lattice CaF_2—two tetragonal, two rhombohedral, and one cubic. The monoclinic $SrYbF_5$ phase was obtained in the decomposition of tysonite solid solutions with more than 50 mol % RF_3. The equilibrium nature of this phase has not been proven as yet.

Most of the ordered phases are formed as a result of solid phase reactions, and, therefore, the synthesis of their single crystals is difficult or even impossible. Crystal structures are determined only for the representatives of three structure types. One tetragonal type is represented by Ca_2YbF_7 [39, 40]. One rhombohedral

type is represented by $Ba_4R_3F_{17}$ (R = Y, Yb) [28] and is close to the $Pb_8Y_6F_{32}O$ phase [12]. Another rhombohedral type is represented by the mineral tweitite $Ca_{0.7}Y_{0.25}R_{0.05}(F, O)_{2.25-2.30}$ [41].

The ordered phases are characterized by long-range order in the arrangement of RE superclusters, with the cubic motif of the cationic packing being preserved. Their unit-cell parameters are larger than the parameter of the fluorite lattice. First, the structure of the ordered phases based on $[R_6F_{37}]$ clusters [15] was suggested, and then the associates of defects of larger dimensions—$\{M_8[R_6F_{68-69}]\}$ superclusters [21].

The superstructural phases are formed with the aid of six types of combinations of $\{M_8[R_6F_{68-69}]\}$ superclusters [26], which correspond to six families of the vectors of the initial CaF_2-type lattice. The combination of these vectors yields all the basis vectors of all the known superstructural fluorite phases built by $\{M_8[R_6F_{68-69}]\}$ clusters. The analysis of possible ways of combination of superclusters [27] provided the establishment of the correlations between the composition and the structure. It became possible to model crystal structure of the ordered and disordered fluorite-like phases in the MF_2–RF_3 system over the wide range of RF_3 content (0.1–75.0 mol %). The ordered phases with the superstructure are related not only to the MF_2–RF_3 but also to the MF–RF_3 and MF–RF_4 systems and some chloride, oxychloride, oxyfluoride, oxide, and carbide systems.

The clusters (superclusters) statistically distributed in a crystal of the disordered fluorite phase are transformed into the structural elements in the ordered phase. This allows one to determine the shape and the chemical composition of these elements by studying the structure of ordered phases. Such studies yield the arguments in favor of microheterogeneity of the fluorite $M_{1-x}R_xF_{2+x}$ phases.

Figure 6 shows the fragment of the structure of the ordered $Ba_4Yb_3F_{17}$ phase and the Yb^{3+} ions [28], which occupy the octahedron vertices. It is also established that the octahedral groupings have the purely cationic rare earth composition. For the first time, the following isomorphism scheme suggested in [42] was experimentally confirmed:

$$[M_6F_{32}]^{20-} + 6F^- \longrightarrow [R_6F_{37}]^{19-} + F^-.$$

As follows from Fig. 3, for all the combinations except of those with Sr^{2+} and Nd^{3+}, one observes the geometric mismatch of the matrix and rare earth superclusters. As a result, the combination of these subunits gives rise to elastic displacements of atoms resulting in internal stresses. There is an analogy between the microstructure of $M_{1-x}R_xF_{2+x}$ crystals (at the level of clusters) and the solid solutions in the systems with metals, which decompose with the formation of two isostructural phases (isostructural decomposition [43]).

No tetrahedral groupings $[R_4F_{26}]$ (small clusters) (Fig. 1, on the right) was observed in the ordered fluoride structures. Such groupings are the structural elements of the fluorite-like structures of the intermetallic compounds Ca_8In_3 ($[In_4Ca_{26}]$ cluster) and Mg_5Ga_2 ($[Ga_4Mg_{26}]$ cluster) [22].

At present, the octahedral rare earth $[R_6F_{37}]^{19-}$ cluster and the rare earth $\{M_8[R_6F_{68-69}]\}$ supercluster derived from it are the only building subunits of the $M_{1-x}R_xF_{2+x}$ phases whose possible formation in a disordered nonstoichiometric crystal is confirmed by its existence in the structures of the ordered phases.

According to [17, 45], the propensity of defect to associating into clusters only slightly depends on temperature. The estimates of the energy of cluster formation lead to the conclusion that they are stable to temperature increase [46, 47]. This allows one to assume that the main form of the existence of rare earth elements in the nonstoichiometric $M_{1-x}R_xF_{2+x}$ and numerous ordered phases with the structure derived from fluorite are their associates—clusters and superclusters. The cation composition (M/R ratio) of the cluster can change, but the octahedral configuration of RE cations is preserved.

9. $M_{1-x}R_xF_{2+x}$ PHASES IN THE CLASSIFICATION OF NANOSTRUCTURED MATERIALS

9.1. $M_{1-x}R_xF_{2+x}$ Phases in the Classification of Nanostructured Materials According to the Chemical and Phase Compositions of Nanoinclusions

According to the general three-category classification of the known NSMs suggested in [48], the $M_{1-x}R_xF_{2+x}$ phase should be related to the category of bulk solids with the microstructure of nanometer dimensions. This category includes two classes of NSMs—those with the continuous variation in the chemical composition on the atomic scale (glasses, gels, etc.) and the class of materials built by blocks (nanoinclusions) with the crystal structure, crystallographic orientation, and chemical composition different from the structure, orientation, and composition of the crystalline matrix, i.e., having different phase composition.

The $M_{1-x}R_xF_{2+x}$ phases obtained by directional crystallization of melts do not possess the complete set of the characteristics of any of the above classes of NSMs. This gives grounds to suggest the third class of NSMs consisting of bulk formations in which the microheterogeneity is provided by the blocks of nanometer dimensions with the compositions different from the composition of the matrix but having the same (or related) crystal structure.

The phases with the defect CaF_2 structure in the fluoride and oxide systems are still the only known representatives of the third class of NSMs. The number of fluorite nonstoichiometric phases is quite large [33–

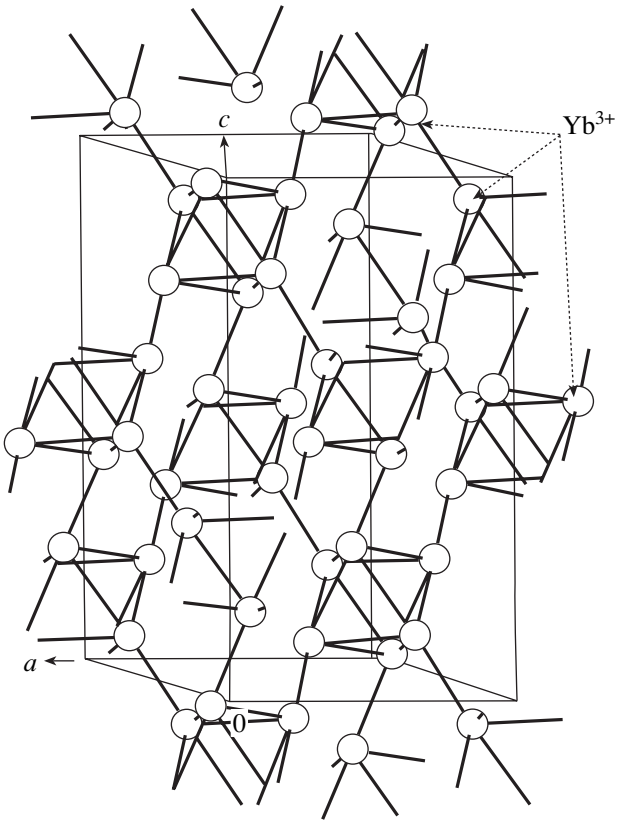

Fig. 6. Octahedral grouping of Yb^{3+} in the structure of the ordered $Ba_4Yb_3F_{17}$ phase [28].

35]. It seems that the new class of NSMs has the maximum number of the representatives of all the NSM of the third category.

9.2. $M_{1-x}R_xF_{2+x}$ Phases in the Classification of NSMs According to the Shape and the Composition of Nanoinclusions.

Depending on the shape of nanoinclusions, there are three categories of NSMs [48]: (1) layer, (2) rod, and (3) isometric ones. In turn, within each category, there are four families determined by the chemical compositions of the matrix and nanoinclusions. Family (1) in which both phases have the same composition, family (2) in which different nanoinclusions have different compositions, family (3) in which the boundaries and the bulk of nanoinclusions have different compositions, and family (4) where the nanoinclusions in the bulk and the matrix have different compositions. In all the cases it is assumed that the structures of the matrix and the inclusions are different. Thus, in accordance with the shape and the composition, we have altogether 12 types of NSMs. The shape and the composition of the $M_{1-x}R_xF_{2+x}$ phases make them closest to category (3) of isometric NSMs and family (4) of crystallites of nanoinclusions dispersed in the matrix with the structure and composition different from the structure and composition of the nanoinclusion.

The above classification ignores the two most important features of the fluorite $M_{1-x}R_xF_{2+x}$ phases—the same structures and the same crystallographic orientations of the matrix and the nanoinclusion. This difference is shown schematically in Fig. 7. On the left, the relation between the nanoinclusions and the matrix for the variant closest to our one (category 3, family 4) is shown according to [48], and on the right, the same is shown for the $M_{1-x}R_xF_{2+x}$ phases. The $M_{1-x}R_xF_{2+x}$ phases form an independent type not encountered among the known NSMs and characterized by the coherence of the symmetry elements of nanoinclusions and the matrix caused by their isostructurality despite the pronounced (qualitative) difference in their chemical compositions.

9.3. $M_{1-x}R_xF_{2+x}$ Phases in the Thermodynamic Classification of NSMs

Under the standard conditions, the nonstoichiometric fluorite $M_{1-x}R_xF_{2+x}$ phases in the NSM classification [48] are related to nonequilibrium ones. However, the problem of the state of these phases in the temperature interval from the beginning of volume diffusion to melting has not been studied as yet. It is probable that in as-grown crystals (crystals grown from melt and not subjected to any thermal treatment), the matrix and nanoinclusions are in an elastically stressed state, which is a nonequilibrium state, so that the stresses can be removed by annealing. The phase transformation of as-grown $Ba_{0.75}R_{0.25}F_{2.25}$ (R = Gd–Lu) phases with the distorted fluorite structure into the cubic fluorite phases upon 14-day-annealing at 900°C is also associated with the removal of elastic stresses.

The majority of the properties of the $M_{1-x}R_xF_{2+x}$ phases were studied on nonequilibrium samples, which hinders the interpretation of the results obtained. The nonequilibrium state indicates its dependence on usually noncontrollable conditions of crystal synthesis. As a result, the data obtained are often inconsistent because of some objective reasons.

9.4. Relation of the Matrix and Nanoinclusion Structures in the $M_{1-x}R_xF_{2+x}$ Phases.

This has no analogues in the classification of modern NSMs. The crystal structures of the nanoinclusions and the matrix in $M_{1-x}R_xF_{2+x}$ have the same cationic motif—the centers of gravity of the cations of different species (M^{2+} and R^{3+}) in the nanoinclusions and the matrix either coincide with or are close to the regular point system 4*a* in the sp. gr. $Fm\bar{3}m$. As a result, the cationic motif is the same for the whole crystal irrespectively of different chemical compositions of nanoinclusions and the matrix.

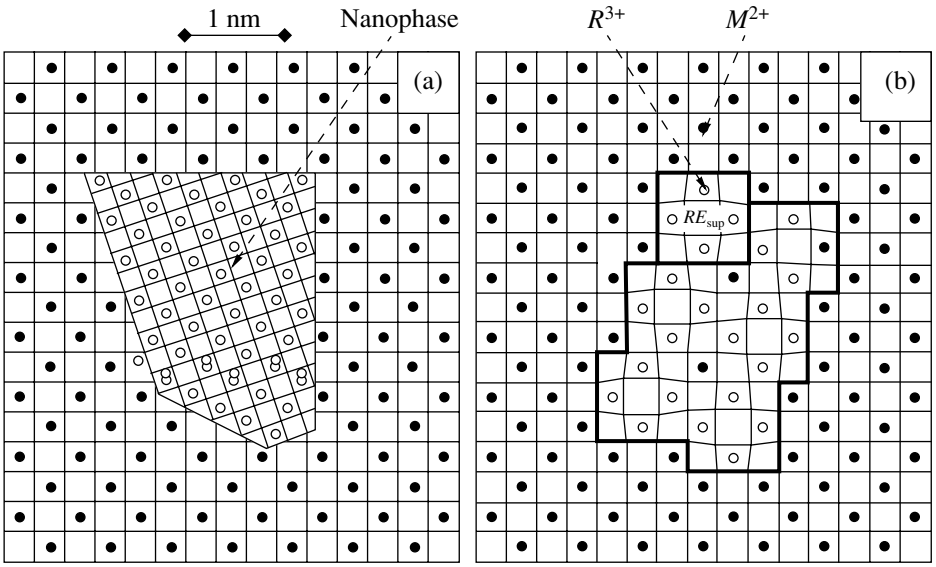

Fig. 7. Nanophase composite (a) consisting of blocks with the structure, crystallographic orientation, and the composition (light circles) different from those of the matrix (black circles) [48]; (b) aggregates of RE superclusters (RE_{sup}, R are indicated by light circles) of different compositions but with the coherent conjugation with the crystalline MF_2 matrix (M are indicated by black circles).

We believe that the identical structures (close relation) of the matrix and nanoinclusions are one of the main characteristics of the $M_{1-x}R_xF_{2+x}$ phases as NSMs. The suggested model of the nanophase composite $M_{1-x}R_xF_{2+x}$ (Fig. 4) does not take into account the displacements in the anionic sublattice. This model does not take into account the displacements of the cations of various species. Under these assumptions, the nanoinclusion and matrix structures can be considered to be identical. One can state that the crystalline fluorite matrix forms the fluorite structure of the rare earth component in the $M_{1-x}R_xF_{2+x}$ crystal. In the 2D variant, the fluorite layer consisting only of RE cations was established experimentally in the structure of the ordered KR_3F_{10} phases.

In the limit, nanoinclusions can be considered as high-pressure fluorite RF_3 phases dispersed in MF_2. The synthesis of high-pressure $Pb_{0.3}La_{0.7}F_{2.7}$ phase of the composition close to the composition of LaF_3 was reported in [49].

9.5. Single-Crystal Appearance of the $M_{1-x}R_xF_{2+x}$ Phases and Their Microheterogeneity

The most bright manifestation of the double nature of the $M_{1-x}R_xF_{2+x}$ phases as NSMs, which distinguishes these phases from all the known NSMs, is their appearance—they look like single crystals. It is this appearance that does not allow one to guess that they are microheterogeneous.

Despite the justified qualification of the $M_{1-x}R_xF_{2+x}$ phases as NSMs (which are heterogeneous by definition), some objective characteristics of these phases demand their relation to macroscopically homogeneous single crystals. This reflects the double nature of the $M_{1-x}R_xF_{2+x}$ phases showing the signs of both single crystals and specific two-phase systems with nanophase coherent inclusions isostructural to the matrix but having different composition. Figure 8 shows some crystals of the $M_{1-x}R_xF_{2+x}$ phases together with other multicomponent fluoride crystals. The NSMs such as $M_{1-x}R_xF_{2+x}$ not only have the appearance of single crystals but also behave like single crystals in the electron, neutron and X-ray diffraction experiments. Larger formations (conglomerates of RE clusters) can manifest themselves on the powder diffraction patterns as independent phases with the fluorite structure and the lattice parameter different from that of the matrix. However, in this case as well (which will be considered later), the material has the appearance of a single crystal.

In other words, the chemically heterogeneous system with large second-phase inclusions behaves as a single crystal in the diffraction experiments at the wavelength of about 1–10 Å. This differs the nonstoichiometric $M_{1-x}R_xF_{2+x}$ phases from the known NSMs in which (at their sufficient concentration) the presence of nanoinclusions was established by the diffraction method because their crystal structures differ from the structure of the matrix.

10. SOME PHYSICAL CHARACTERISTIC OF NANOSTRUCTURED $M_{1-x}R_xF_{2+x}$ CRYSTALS

10.1. Spectroscopy of RE ions in $M_{1-x}R_xF_{2+x}$ Crystals

Historically, the first observed anomaly was an inhomogeneous broadening of the absorption and lumi-

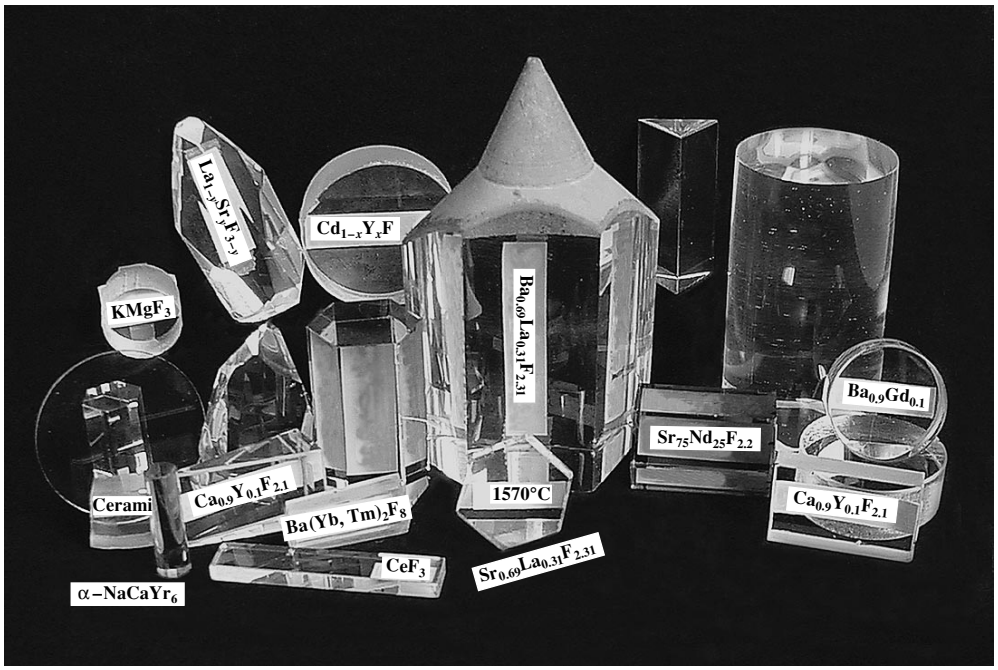

Fig. 8. Crystals of nonstoichiometric fluorite $M_{1-x}R_xF_{2+x}$ phases and some other multicomponent fluoride materials synthesized at the Shubnikov Institute of Crystallography of the Russian Academy of Sciences.

nescence spectra of Nd^{3+} in $Ca_{1-x}Y_xF_{2+x}$ crystals reported in [50]. The subsequent numerous studies of the spectral characteristics of $M_{1-x}R_xF_{2+x}$ crystals activated with RE ions confirmed that they are partly disordered optical media, which can have optical centers R^{3+} in different anionic environment. As a result, one observes the inhomogeneous broadening on the absorption and luminescence spectra of R^{3+}. The inhomogeneous broadening of the spectra of $M_{1-x}R_xF_{2+x}$ crystals can exceed broadening observed for fluoride glasses [51, 52] despite the fact that glasses are believed to be the most structurally disordered media.

The use of this feature of the RE ion spectroscopy in $M_{1-x}R_xF_{2+x}$ crystals provided the creation of a new class of active lasing media with partly disordered structures and better spectral characteristics [53]. The assumption on the association of (R^{3+}–F_{int}) dipoles into di- and tetramers was suggested in order to interpret the complicated character of the optical spectra of R^{3+} in CaF_2 [54] (F_{int} are interstitial fluoride ions). The concept of large defect complexes was suggested in [55] in order to explain an increase in the number of cubic centers (nonlocal charge compensation) with an increase in the R^{3+} concentration. The "clots" of RE ions in a crystal schematically shown in Figs. 1 and 4 explain the depletion of the remaining volume of R^{3+} ions. These facts were the first indication of the formation of defect complexes in $M_{1-x}R_xF_{2+x}$ prior to the structural studies. The first structure determinations were made on $Ca_{0.61}Ce_{0.39}F_{2.39}$ [31] and $Ca_{0.9}Y_{0.1}F_{2.1}$ [6] crystals. Since the structural determinations were made considerably later than the spectroscopic studies, there was no necessary grounds to interpret the experiments on optic spectroscopy of RE ions in the nonstoichiometric $M_{1-x}R_xF_{2+x}$ phases. A large volume of the experimental data accumulated in this field still need to be generalized on the basis of numerous but often inconsistent structural data.

10.2. Diffuse Neutron Scattering and Associates of Superclusters of Defects

The experiments on diffuse neutron scattering from $Ba_{1-x}La_xF_{2+x}$ crystals are interpreted in [56] as a result of formation of defect regions of connected rare earth clusters extended for five to seven unit-cell periods. The degree of association decreases with an increase of the temperature in the range 600–1000°C. Below 600°C, most of the clusters are in the associated state. The study of inelastic diffuse scattering of neutrons on $Ba_{0.84}La_{0.16}F_{2.16}$ and $Ba_{0.69}La_{0.31}F_{2.31}$ crystals [57] showed that, with an increase of the LaF_3 content, the clusters interact more intensely.

10.3. Heterogeneity of $M_{1-x}R_xF_{2+x}$ Phases in EPR

The EPR method was widely used for studying the local symmetry of paramagnetic RE ions in $M_{1-x}R_xF_{2+x}$ crystals [58–61]. The analysis of the related results is hindered because of the inconsistency of the data on the symmetry of the optical centers R^{3+}.

One of the objective reasons of these discrepancies is the dependence of the defect structure on the noncontrollable conditions of the synthesis and thermal treatment of the crystals.

The study of the $Ca_{1-x-y}R_xR'_yF_{2+x+y}$ ($0 < x < 0.02$; $0.001 < y < 0.38$; R = Er, Tm, Yb; R' = Y, Lu), $Sr_{0.969}Lu_{0.03}R_{0.001}F_{2.031}$, and $Ba_{0.969}Lu_{0.03}R_{0.001}F_{2.031}$ (R = Er, Tm) crystals synthesized under equivalent conditions provided the establishment of some tendencies in their behavior [1–3]. One of the most important conclusions is that at the RE content less than 0.2%, the RE clusters cannot exist in a crystal separately but accumulate into "grains" of the rare earth phase. The average RE concentration in these grains is not lower than 20–30%, i.e., is close to the limit solubility of RF_3 in CaF_2. The grain size is small, and, according to indirect estimates, ranges within 30–100 Å for the $Ca_{1-x-y}R_xR'_yF_{2+x+y}$ phases. Up to now, no grains have been revealed by direct methods. Among numerous publications on the properties of the fluorite $M_{1-x}R_xF_{2+x}$ phases, the conclusion drawn in [1] seems to be the best formulated indication to the heterogeneity of the crystals in which R^{3+} are combined into "microphases."

10.4. Heterogeneity of the $Ca_{1-x}R_xF_{2+x}$ *Phases in the Cathodoluminescence Method*

The use of the cathodoluminescence method in an electron microscope [62] allowed one to observe the regions with an elevated RE concentration in $Ca_{1-x-y}Gd_xEu_yF_{2+x}$ and $Ca_{1-x-y}Eu_xMn_yF_2$ crystals, the so-called "microphases" [62]. These regions were formed prior to the attainment of the solubility limits of the impurity components in CaF_2 and were observed because of the cathodoluminescence color varying with the changes in the composition. The dimensions of the activator-enriched regions were estimated as several tens of microns. Despite such large dimensions of inhomogeneities, neither X-ray phase analysis nor light scattering reveal any signs of the second phase.

10.5. Electron Diffraction and Heterogeneity of $Ca_{1-x}R_xF_{2+x}$ *Phases*

Electron diffraction was widely used to study the processes of decomposition of nonstoichiometric fluorite phases and to determine the lattice geometry of the forming ordered phases [63]. The microheterogeneity of $Ca_{1-x}R_xF_{2+x}$ is indicated by the nonequilibrium mixture of the fluorite and two ordered phases observed in $Ca_{0.95}Yb_{0.05}F_{2.05}$ [64]. Even if one assumes that this observation is the result of the partial decomposition of the crystal under an electron beam, the ordered phase in equilibrium with fluorite should have been a trigonally distorted phase ($rh\gamma$—$Ca_{13+\delta}Y_{6-\delta}F_{44-\delta}$; $\delta < 0.5$) and not the really observed mixture of this phase with the tetragonally distorted one t-Ca_2YbF_7.

The formation of ordered phases at the concentration of the impurity component less than 1% was indicated in [43] as the characteristic feature of interstitial solid solutions in the systems formed by metals. This can be explained by the much higher (by an order of magnitude) coefficients of the variation of the lattice parameters (a measure of static distortions) in the interstitial solid solutions (including $M_{1-x}R_xF_{2+x}$) in comparison with the substitutional solid solutions.

10.6. Heterogeneity of the $M_{1-x}R_xF_{2+x}$ *Phases in the NMR Method*

The valuable information on the defect structure of concentrated solid solutions $M_{1-x}R_xF_{2+x}$ is given by the NMR studies at ^{19}F nuclei. Since RE ions are concentrated in microvolumes of $M_{1-x}R_xF_{2+x}$ crystals, some regions of either pure MF_2 matrix or a solid solution less concentrated than the grains of the rare earth phase are formed. One of the most reliable proofs of the existence of the regions containing no RE ions was obtained on $Sr_{0.75}Nd_{0.25}F_{2.25}$ and $Ba_{1-x}Nd_xF_{2+x}$ crystals [65, 66]. At high concentration of Nd^{3+} and their statistical distribution, each F^- ion should have a Nd^{3+} ion as a nearest neighbor. However, the ^{19}F NMR spectrum of the $Sr_{0.75}Nd_{0.25}F_{2.25}$ crystal has an intense component whose chemical shift corresponds to practically pure SrF_2. This component does not obey the Curie–Weiss law and its intensity is in dependent of orientation. These characteristics can be inherent only in the regions of the crystal having no paramagnetic ions, i.e., in the regions of pure SrF_2.

The spectrum also has some satellites whose behavior in a magnetic field corresponds to F^- ions bound to Nd^{3+}. In this case, one of the components corresponds to fluorine bound to two Nd^{3+} ions. This spectrum can be explained by the microheterogeneity of the crystals at the level of the formation of microphases having pronouncedly different chemical compositions and enriched with RE ions. Their dimensions considerably exceed the dimensions of individual RE superclusters. Similar observations were also made for a concentration series of $Ba_{1-x}Nd_xF_{2+x}$ crystals (x = 0.15, 0.22, 0.32). The presence of the component with the chemical shift close to that of pure BaF_2 is also observed for the crystals of the composition $Ba_{0.68}Nd_{0.32}F_{2.32}$.

10.7. Heterogeneity of $Ba_{1-x}R_xF_{2+x}$ *Phases in Raman Scattering*

Raman scattering from $Ba_{1-x}La_xF_{2+x}$ crystals with x = 0.005, 0.01, 0.05, 0.10, 0.15, 0.25, 0.31 [67] and $Ba_{1-x}R_xF_{2+x}$ crystals with R = Ce, Pr, Gd, Tb, $0.10 \le x \le 0.30$ [68, 69] showed that the Ba^{2+} and R^{3+} ions in microvolumes of the crystals are differentiated. The

spectra change with an increase of RE content, but at high RE concentrations (tens of mol % of RF_3), the pure BaF_2 component is observed. This can be explained by a dramatic increase of RE ion content in some volumes of the crystal (Fig. 4).

10.8. Heterogeneity of the $M_{1-x}R_xF_{2+x}$ Phases and Their Mechanical Characteristics

The influence of small RE concentrations (up to 0.1 mol % RF_3) on the plastic deformation of $Ca_{1-x}R_xF_{2+x}$ crystals was first observed in [70] and was then studied in [71]. The effect becomes extremely pronounced at high RE concentrations. Thus, according to [35, 72], the $Ca_{1-x}La_xF_{2+x}$ crystals at $x = 0.25$ show an almost fivefold increase of hardness in comparison with the hardness of CaF_2. The hardness of $Ca_{0.75}La_{0.25}F_{2.25}$ becomes close to the hardness of rutile (TiO_2), one of the hardest oxide materials. At the same time, the cleavage of the crystal either deteriorates or completely disappears. All the fluorite MF_2 phases have perfect cleavage, which hinders the mechanical treatment of the crystals and the exploitation of the products manufactured based on these crystals. Thus, this effect is of great practical importance.

Strengthening of $Ba_{1-x}R_xF_{2+x}$ crystals was studied in [73] at a low content of RE elements and in [35, 72, 74] at their high content. The best studied crystals are $Ba_{0.69}La_{0.31}F_{2.31}$ [74]. The strain–stress curves in the temperature range (0.5–0.7) T_m the repeating jumplike changes of stress. One of the possible explanations of this fact is the heterogeneity (two phases) of the sample. At the same time, such a conclusion was not drawn, because it was inadmissible for crystals that show no light scattering, the typical sign of the formation of the second phase. Now, these jumps are explained by the nanostructured nature of the $Ba_{0.69}La_{0.31}F_{2.31}$ crystals.

As was expected, the mechanical characteristics of the fluorite $M_{1-x}R_xF_{2+x}$ phases are essentially different from the corresponding characteristics of MF_2. This fact can be understood if one considers these crystals as a NSM.

10.9. Heterogeneity of the $M_{1-x}R_xF_{2+x}$ Phases and Processes of Ion Transport

The ionic conductivity of the $M_{1-x}R_xF_{2+x}$ phases is higher by a factor of 8–10 orders of magnitude than of MF_2. This is the strongest dependence of the property of the nonstoichiometric fluorite crystals on the defect structure and the related microheterogeneity. Despite such a considerable increase in conductivity of the $M_{1-x}R_xF_{2+x}$ crystals, the number of charge carriers in these crystals is lower by about an order of magnitude than the number of the structural anion defects usually responsible for conductivity (interstitial fluoride ions and anion vacancies). In order to explain this phenomenon, it was assumed that the fluoride ions in rare earth superclusters are in the bound state in the process of charge transport. The mobile fluoride ions are located at the periphery of the so-called defect regions of the structure [75].

A defect region is a rare earth cluster with the surrounding region of the distorted matrix. This definition includes a $\{M_8[R_6F_{68-69}]\}$ supercluster with the structurally distorted periphery. The presence of the mobile fluoride ions is associated with the necessity to compensate the positive charge of the defect region with one or two additional fluoride ions (per one RE supercluster). These ions are located outside the supercluster and their number is lower by about an order of magnitude than the number of excessive anions in the supercluster. Thus, the cluster model and the close model of defect regions allow one to interpret the discrepancy between the observed number of charge carriers in the superionic $M_{1-x}R_xF_{2+x}$ crystals and the number of anionic defects.

The volumes of the defect regions in the BaF_2-based fluorite phases obtained from the data on the superionic conductivity range within 3000–4000 Å^3. The calculations based on the supercluster model yield values consistent with these estimates. The minimum volume of the defect region can be estimated by adding at least one (peripheral) layer of polyhedra to a RE supercluster with the cube edge $a_{sup} = 1.5a_{fl}$, where a_{fl} is the period of the fluorite lattice. The linear dimension of such a defect region is $a_{def} = 2.5a_{fl}$, and its volume is $V_{def} = (2.5a_{fl})^3$. For the $Ba_{1-x}R_xF_{2+x}$ phases, the interval of the changes of the defect region is determined by the minimum parameter of the cubic $Ba_{1-x}Lu_xF_{2+x}$ lattice (~5.9 Å) and the BaF_2 parameter (6.2 Å). Then, the minimum and maximum volumes of the defect regions are $V_{min} = 3209$ and $V_{max} = 3724$ Å^3.

The above values are close to the estimates based on the conductivity data. Thus, the dimensions of the defect regions which describe the superionic conductivity of $Ba_{1-x}R_xF_{2+x}$ crystals correlate with the dimensions of the associated superclusters.

10.10. High-Resolution Electron Microscopy, Electron Diffraction, and Heterogeneity of $Ba_{1-x}R_xF_{2+x}$ Crystals (R = Yb and Lu)

Heterogeneity of $M_{1-x}R_xF_{2+x}$ crystals manifests itself at the nanometer level and can be revealed by high-resolution electron microscopy and electron diffraction. Figure 9 shows the diffraction patterns from crystallites of the rod having the nominal composition $Ba_{0.8}Lu_{0.2}F_{2.2}$ (with respect to the charge) (Figs. 9a–9c) and the crystal images obtained on a JEOL 200 FX II electron microscope (200 kV) (Figs. 9d and 9e) [76].

Electron diffraction from as-grown $Ba_{1-x}R_xF_{2+x}$ crystals (R = Yb and Lu) [76, 77] showed that they are inhomogeneous at the level of crystallites that provided

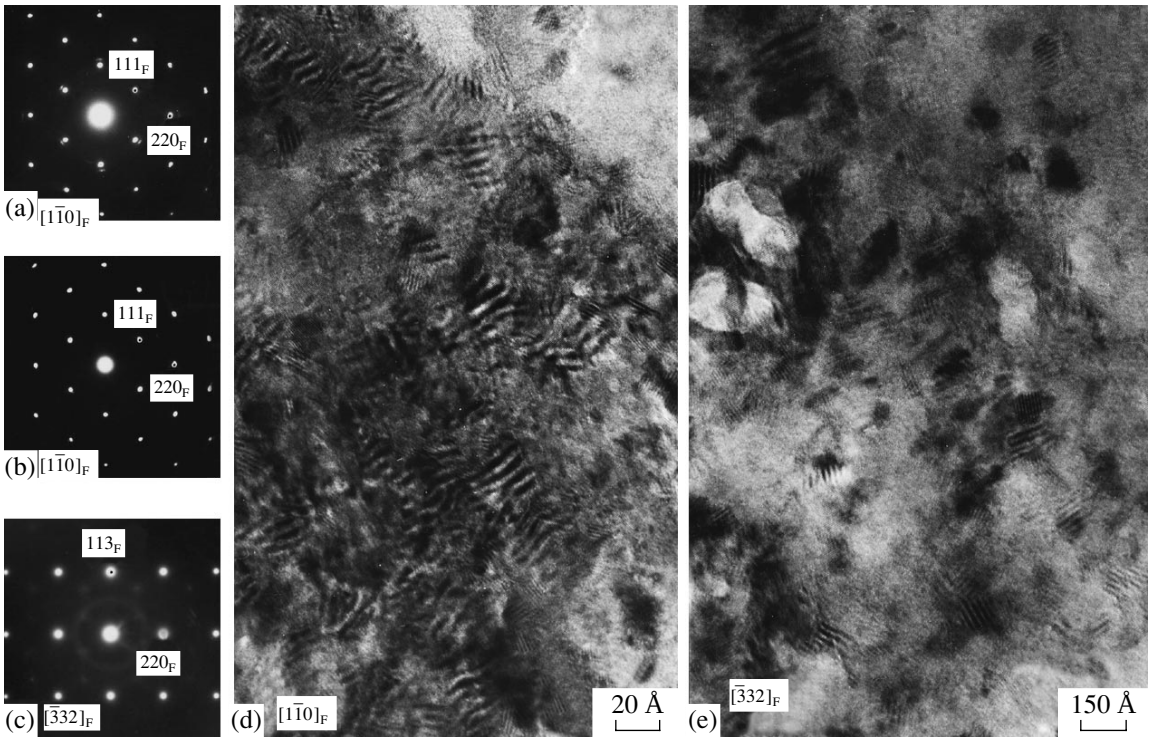

Fig. 9. Nonstoihiometric $Ba_{0.8}Lu_{0.2}F_{2.2}$ crystals; (a–c) electron diffraction patterns, (d, e) electron microscopy images [76, 77].

electron diffraction (with a diameter of tens or hundreds of nanometers). Some crystallites yielded electron diffraction patterns characteristic of the fluorite phase (Fig. 9b), whereas some other gave the diffraction patterns with satellite reflections (Fig. 9a). At some orientations, diffuse scattering was also observed (Fig. 9a).

As was shown by some additional investigations, different diffraction patterns are not associated with the crystal degradation under an electron beam. They seem to be caused by different structures in different microregions of the crystal. To interpret these observations, one has to treat thoroughly the already obtained electron images and also to study new crystals with different thermal history. One of the possible assumptions is that the crystal consists of the mixture of coherent intergrowths of microinclusions with different compositions and lattice parameters (Fig. 4).

Earlier [11], we observed the presence in the $Ba_{0.75}Lu_{0.25}F_{2.25}$ sample of at least two fluorite phases with somewhat different lattice parameters, which resulted in the formation of moire patterns. The corresponding studies are under way.

Concluding the review, we should consider inhomogeneities of the fluorite phases exceeding the nanometer level. Earlier, we grew from melt the metastable $Ba_{0.75}R_{0.25}F_{2.25}$ (R = Ge–Lu) phases [11]. The crystalline rods contained along with the isotropic regions also optically anisotropic ones with the total area of several squared millimeters. The powder X-ray diffraction patterns from these crystalline rods showed low-symmetric distortions of the fluorite lattice. The $Ba_{0.75}R_{0.25}F_{2.25}$ phases represent a large number of objects whose defect structures require a new interpretation at various levels.

The study of the heterogeneity of the $Ba_{1-x}R_xF_{2+x}$ phases and, in particular, of the whole family of the fluorite $M_{1-x}R_xF_{2+x}$ phases, by high-resolution electron microscopy and electron diffraction are at the very beginning. However, even the data that are already in our possession lead to the conclusion that, having the single-crystal appearance, these phases are inhomogeneous at the nanometer level and, therefore, the $M_{1-x}R_xF_{2+x}$ phases should be related to NSMs.

CONCLUSIONS

The present article aimed to draw the attention of the researchers to the microinhomogeneity of the fluorite $M_{1-x}R_xF_{2+x}$ phases at the nanometer scale. These phases can be considered as a new class of NSMs, which differs from the already known materials in isostructurality and, generally, in coherence of the matrix and nanoinclusions with essentially different chemical compositions. The investigation of this class of NSMs is only at the very beginning.

The study of such NSMs is of great interest for practice, because single crystals of the $M_{1-x}R_xF_{2+x}$ phases crystallized from melts are promising multicomponent fluoride materials. They should replace single crystals

of traditional one-component fluorides (CaF_2, BaF_2, etc.) in many fields. The number of the latter fluorides manufactured industrially is rather small and does not exceed ten compounds. The small set of the known characteristics of these materials is insufficient for the needs of new fields of the application of inorganic fluorides. We see no alternative to moving from one-component to multicomponent fluoride materials, of which the most important are $M_{1-x}R_xF_{2+x}$ crystals. We believe that deepening our knowledge about the $M_{1-x}R_xF_{2+x}$ phases as NSMs would give a new impetus to the development of this direction of materials science.

The $M_{1-x}R_xF_{2+x}$ crystals are the most characteristic and practically important representatives of grossly nonstoichiometric fluorides. However, they are not the only crystals having the fluorite structure and characterized by an extremely high concentration of structural defects. These phases enter the vast family of nonstoichiometric fluorite phases described by the general formula $M_{(1-x)m}R_{xn}F_{(1-x)m+nx}$. For the MF_m–RF_n system with $m < n \le 4$ and the cations of 34 metals, this family includes more than 300 phases with qualitatively different compositions [32–35]. The study of the microheterogeneity in this family of phases should answer the question about the relation between the nanostructured crystals of the fluorite phases and the pronounced nonstoichiometry observed for the CaF_2 structure type.

ACKNOWLEDGMENTS

The authors are grateful to the editor in chief of *Kristallografiya*, L.A. Shuvalov, for his invitation to write this review, A.P. Levanyuk for the discussion of some problems, and R.M. Zakalyukin for his help with the computer graphics. This study was supported by the International Association for the Promotion of Cooperation with Scientists from the New Independent States of the Former Soviet Union (INTAS), project no. 97-32045 "Nonstoichiometry in Inorganic Fluorides," Russian Foundation for Basic Research, project no. 01-03-33000.

REFERENCES

1. S. A. Kazanskiĭ, *Spectroscopy of Crystals* (Nauka, Leningrad, 1989), p. 110.
2. S. A. Kazanskiĭ, Zh. Éksp. Teor. Fiz. **89** (4), 1252 (1985) [Sov. Phys. JETP **62**, 727 (1985)].
3. S. A. Kazanskiĭ, Pis'ma Zh. Éksp. Teor. Fiz. **38** (9), 430 (1983) [JETP Lett. **38**, 521 (1983)].
4. P. P. Fedorov, Butll. Soc. Catalana Cienc. Fis., Quim. Mat. **12** (2), 349 (1991).
5. J. P. Laval and B. Frit, J. Solid State Chem. **49**, 237 (1983).
6. A. K. Cheetham, B. E. F. Fender, D. Steele, *et al.*, Solid State Commun. **8** (3), 171 (1970).
7. P. J. Bendall, C. R. A. Catlow, J. Corish, *et al.*, J. Solid State Chem. **51** (2), 159 (1984).
8. L. A. Muradyan, B. A. Maksimov, and V. I. Simonov, Koord. Khim. **12** (10), 1398 (1986).
9. L. P. Otroshchenko, V. B. Aleksandrov, N. N. Bydanov, *et al.*, Kristallografiya **33** (3), 764 (1988) [Sov. Phys. Crystallogr. **33**, 449 (1988)].
10. A. K. Cheetham, B. E. F. Fender, and M. J. Cooper, J. Phys. C **4** (18), 3107 (1971).
11. B. P. Sobolev, A. M. Golubev, E. A. Krivandina, *et al.*, Kristallografiya **47** (2), 237 (2002) [Crystallogr. Rep. **47**, 201 (2002)].
12. B. T. M. Willis, J. Phys. (Paris) **25** (5), 431 (1964).
13. V. V. Ovsyankin and P. P. Feofilov, Pis'ma Zh. Éksp. Teor. Fiz. **3**, 431 (1964) [JETP Lett. **3**, 322 (1966)].
14. C. R. A. Catlow, J. Phys. C **6** (4), L64 (1973).
15. D. J. M. Bevan, O. Greis, and J. Strahle, Acta Crystallogr., Section A: Cryst. Phys., Diffr., Theor. Gen. Crystallogr. **36** (6), 889 (1980).
16. B. A. Maksimov, L. A. Muradyan, and V. I. Simonov, *Crystallography and Crystal Chemistry* (Nauka, Moscow, 1986), p. 212.
17. S. Hull and C. C. Wilson, J. Solid State Chem. **100** (1), 101 (1992).
18. M. T. Hutchings, K. Clausen, M. H. Dickens, *et al.*, J. Phys. C **17**, 3903 (1984).
19. P. P. Fedorov and B. P. Sobolev, J. Less-Common Met. **63** (1), 31 (1979).
20. V. M. Goldschmidt, T. Barth, G. Lunde, *et al.*, Skr. Nor. Vidensk.-Akad., Kl. 1: Mat.-Naturvidensk **1** (2), 1 (1926).
21. A. M. Golubev and V. I. Simonov, Kristallografiya **31** (3), 478 (1986) [Sov. Phys. Crystallogr. **31**, 281 (1986)].
22. A. M. Golubev, Kristallografiya **34** (6), 1457 (1989) [Sov. Phys. Crystallogr. **34**, 874 (1989)].
23. A. M. Golubev, Koord. Khim. **16** (4), 461 (1990).
24. A. M. Golubev, Koord. Khim. **18** (12), 1232 (1991).
25. A. M. Golubev, Koord. Khim. **18** (9), 1001 (1992).
26. A. M. Golubev, Neorg. Mater. **30** (9), 1142 (1994).
27. A. M. Golubev, Zh. Neorg. Khim. **41** (3), 505 (1996).
28. B. A. Maksimov, Kh. Solans, A. P. Dudka, *et al.*, Kristallografiya **41** (1), 51 (1996) [Crystallogr. Rep. **41**, 50 (1996)].
29. T. Vogt, Z. Mineral. **15**, 373 (1911).
30. T. Vogt, Neues Jahrb. Mineral. **2** (1), 9 (1914).
31. V. B. Aleksandrov and L. S. Garashina, Dokl. Akad. Nauk SSSR **189** (2), 307 (1969) [Sov. Phys. Dokl. **14**, 1040 (1970)].
32. B. P. Sobolev, *The Rare Earth Trifluorides*, Part 2: *Introduction to Materials Science of Multicomponent Metal Fluoride Crystals* (Institut d'Estudis Catalans, Barcelona, 2001).
33. B. P. Sobolev, *The Rare Earth Trifluorides*, Part 1: *The High Temperature Chemistry of Rare Earth Trifluorides* (Institut d'Estudis Catalans, Barcelona, 2000).
34. B. P. Sobolev, Zh. Vses. Khim. O–va. **36** (6), 726 (1991).
35. B. P. Sobolev, Buttl. Soc. Catalana Cienc. Fis., Quim. Mat. **12** (2), 275 (1991).

36. J. S. Anderson, *Problems of Nonstoichiometry*, Ed. by A. Rabenau (North-Holland, Amsterdam, 1970).
37. R. D. Shannon, Acta Crystallogr., Section A: Cryst. Phys., Diffr., Theor. Gen. Crystallogr. **32** (5), 751 (1976).
38. P. P. Fedorov and B. P. Sobolev, Zh. Neorg. Khim. **24** (4), 1038 (1979).
39. D. J. M. Bevan, M. J. McCall, S. E. Ness, *et al.*, Eur. J. Solid State Inorg. Chem. **25** (5–6), 517 (1988).
40. D. J. M. Bevan, S. E. Ness, and M. R. Taylor, Eur. J. Solid State Inorg. Chem. **25** (5–6), 527 (1988).
41. S. Bergstol and B. Jensen, Lithos **10**, 81 (1977).
42. O. Greis, Rev. Inorg. Chem. **4** (2), 87 (1982).
43. A. G. Khachaturyan, *The Theory of Phase Transformations and the Structure of Solids Solutions* (Nauka, Moscow, 1974).
44. J. P. Laval, A. Abaouz, B. Frit, *et al.*, J. Solid State Chem. **85** (1), 133 (1990).
45. M. Hofmann, S. Hull, G. J. McIntyre, *et al.*, J. Phys.: Condens. Matter **9** (4), 845 (1997).
46. J. Corish, C. R. A. Catlow, P. W. M. Jacobs, *et al.*, Phys. Rev. B **25** (10), 6425 (1982).
47. P. J. Bendall, C. R. A. Catlow, J. Corish, *et al.*, J. Solid State Chem. **51** (2), 159 (1984).
48. H. Gleiter, Acta Mater. **48** (1), 1 (2000).
49. L. P. Otroshchenko, V. B. Aleksandrov, N. A. Bendeliani, *et al.*, Kristallografiya **37** (2), 405 (1992) [Sov. Phys. Crystallogr. **37**, 208 (1992)].
50. Kh. S. Bagdasarov, Yu. K. Voronko, A. A. Kaminskii, *et al.*, Phys. Status Solidi **12** (2), 905 (1965).
51. M. Yu. Sharonov, Z. I. Zhmurova, E. A. Krivandina, *et al.*, Opt. Commun. **124**, 595 (1996).
52. M. Yu. Sharonov, Z. I. Zhmurova, E. A. Krivandina, *et al.*, Opt. Commun. **124**, 558 (1996).
53. A. A. Kaminski, *Laser Crystals, Their Physics and Properties* (Springer-Verlag, Berlin, 1991).
54. V. V. Osiko, Fiz. Tverd. Tela (Leningrad) **7** (5), 1294 (1965) [Sov. Phys. Solid State **7**, 1047 (1965)].
55. Yu. K. Voron'ko, V. V. Osiko, and I. A. Shcherbakov, Zh. Éksp. Teor. Fiz. **56** (1), 151 (1969) [Sov. Phys. JETP **29**, 86 (1969)].
56. F. Kadlec, F. Moussa, P. Simon, *et al.*, Mater. Sci. Eng. **57** (3), 234 (1999).
57. F. Kadlec, F. Moussa, P. Simon, *et al.*, Solid State Ionics **119** (1–4), 131 (1999).
58. E. Fridman and W. Low, J. Chem. Phys. **33** (4), 1275 (1960).
59. A. A. Antipin, Uch. Zap. Kazan. Gos. Univ. **129** (1), 74 (1969).
60. F. Z. Gil'fanov, R. K. Luks, and M. S. Stolov, Fiz. Tverd. Tela (Leningrad) **11** (9), 2502 (1969) [Sov. Phys. Solid State **11**, 1779 (1970)].
61. F. Z. Gil'fanov, R. K. Luks, and M. S. Stolov, Fiz. Tverd. Tela (Leningrad) **11** (9), 2502 (1969) [Sov. Phys. Solid State **11**, 2020 (1970)].
62. Yu. N. Orlov, V. E. Bozevol'nov, L. N. Ivanov, *et al.*, J. Cryst. Growth **49** (1), 109 (1980).
63. O. Greis and J. M. Haschke, *Handbook on the Physics and Chemistry of Rare Earths*, Ed. by K. A. Gscheidner and Le Roy Eyring (North-Holland, Amsterdam, 1982), Vol. 5, Chap. 45, p. 387.
64. O. Greis, *Ein Beitrag zur Kristallchemie Schneller Ionenliter: Einkristall. Elektronen-Diffraction an Yttrofluoriten, Rysoniten und Natrium-Beta-Alumina*, Habilitation Thesis (University of Heidelberg, West Germany, 1980).
65. A. I. Livshits, V. M. Buznik, V. A. Vopilov, *et al.*, Preprint No. 244F, Inst. Fiziki Sib. Otd. Akad. Nauk SSSR (Institute of Physics, Siberian Division, Academy of Sciences of USSR, Krasnoyarsk, 1983), p. 48.
66. A. N. Matsulev, V. M. Buznik, A. I. Livshits, *et al.*, Fiz. Tverd. Tela (Leningrad) **29** (11), 3247 (1987) [Sov. Phys. Solid State **29**, 1864 (1987)].
67. M. Kolesik, D. Tuneda, and B. P. Sobolev, Phys. Status Solidi B **160** (1), 375 (1990).
68. M. Kolesik and B. P. Sobolev, Phys. Status Solidi A **166** (1), K113 (1991).
69. M. Kolesik and B. P. Sobolev, Solid State Ionics **47**, 325 (1991).
70. A. A. Urusovskaya and V. G. Govorkov, Kristallografiya **10** (4), 525 (1965) [Sov. Phys. Crystallogr. **10**, 437 (1965)].
71. A. R. Patel and C. C. Desai, J. Phys. D **3** (11), 1645 (1970).
72. B. P. Sobolev, Author's Abstract Doctoral Dissertation in Chemical Sciences (Inst. Kristallografii Ross. Akad. Nauk, Moscow, 1978).
73. S. N. Val'kovskiĭ, É. M. Nadgornyĭ, and E. A. Simun, Fiz. Tverd. Tela (Leningrad) **15** (2), 570 (1973) [Sov. Phys. Solid State **15**, 395 (1973)].
74. A. M. Aronova, G. V. Berezhkova, V. B. Aleksandrov, *et al.*, *Physical Crystallography* (Nauka, Moscow, 1992), p. 151.
75. A. K. Ivanov-Shitz, N. I. Sorokin, B. P. Sobolev, *et al.*, Fiz. Tverd. Tela (Leningrad) **28** (8), 2552 (1986) [Sov. Phys. Solid State **28**, 1431 (1986)].
76. R. Múñoz, R. Rojas, B. P. Sobolev, *et al.*, in *Proceedings of the 29th Reunión Bienal Sociedad Española de Microscopia, Murcia, Spain, 1999*, Ed. by M. A. Sanchez-Pina *et al.*, p. 317.
77. L. Pascual, R. Munoz, R. Roper, *et al.*, in *Proceedings of the 12th European Congress on Electron Microscopy, Brno. 2001*, Vol. IV, Supplement (in press).

Translated by L. Man

Crystallography Reports, Vol. 48, No. 1, 2003, pp. 16–23. Translated from Kristallografiya, Vol. 48, No. 1, 2003, pp. 21–28.

STRUCTURE OF INORGANIC COMPOUNDS

Crystal Structure of Magnesioferrikatophorite

D. Yu. Pushcharovskiĭ*, Yu. S. Lebedeva*, I. V. Pekov*, G. Ferraris, A. A. Novakova*, and G. Ivaldi****

** Moscow State University, Leninskie gory, Moscow, 119992 Russia*

*** Department of Mineralogy and Petrology, University of Turin, Via Valperga Caluso 35, Turin, 10125 Italy*

Received May 20, 2002

Abstract—The crystal structure of the Na,Ca-amphibole magnesioferrikatophorite found in carbonatites from the Turiy Cape (Kola Peninsula) was refined (Siemens P4 diffractometer, λMoK_α radiation, 1481 independent reflections with $|F| > 4\sigma(F)$, anisotropic refinement, $R(F) = 0.039$). The parameters of the monoclinic unit cell are $a = 9.875(5)$ Å, $b = 18.010(8)$ Å, $c = 5.309(3)$ Å, $\beta = 104.39(5)°$, sp. gr. $C2/m$, $Z = 2$. The distribution of the cations over the crystallographically nonequivalent M(1–4)-positions was revealed by Mössbauer spectroscopy and X-ray diffraction analysis. The character of splitting of the A-position correlates with the characteristic features of the magnesioferrikatophorite composition. The resulting structural formula $(Na_{0.87}K_{0.13})_{\Sigma=1} \cdot (Na_{1.18}Ca_{0.82})_{\Sigma=2}(Mg_{1.41}Fe^{3+}_{0.42}Ti^{4+}_{0.17})_{\Sigma=2}$ $(Fe^{3+}_{1.31}Mg_{0.69})_{\Sigma=2}$ $(Mg_{0.60}Fe^{2+}_{0.38}Mn_{0.02})_{\Sigma=1}(Si_{3.16}Al_{0.84})_{\Sigma=4} \cdot Si_4O_{22}(O_{1.05}OH_{0.66}F_{0.29})_{\Sigma=2}$ agrees well with the electron microprobe analysis data. Based on the zonal character of the crystal and high Fe^{3+} content, the conditions of crystallogenesis are defined as oxidative against the background of a decrease in the Na potential in the course of the evolution of a mineral-forming system. © *2003 MAIK "Nauka/Interperiodica".*

INTRODUCTION

Amphiboles are characterized by pronounced variations in the structure and chemical composition. The number of the mineral species that belong to this group approaches 100. The compositions of amphiboles can be described by the general formula $A_{0-1}B_2C_5^{[6]}T_8^{[4]}O_{22}(OH,F,Cl)_2$, where A is Na or K (coordination number ranges within 6–12), B is Ca, Na, Mn^{2+}, Fe^{2+}, Mg, or Li (coordination number ranges within 6–8, the M(4)-position), C is Mg, Mn^{2+}, Fe^{2+}, Fe^{3+}, Al, or Ti^{4+} (coordination number is 6, the M(1–3)-positions), T is Si or Al (coordination number is 4, the T(1)- and T(2)-positions). The monoclinic amphibole under consideration with the idealized formula $Na_2CaMg_3Fe^{2+}Fe^{3+}Si_7AlO_{22}(OH)_2$, sp. gr. $C2/m$, belongs to the *sodium–calcium subgroup*. For this subgroup, the contents of the chemical elements (the numbers of atoms per formula unit, apfu) vary in the following ranges: $(Ca + Na)_B \geq 1.00$, $0.50 < Na_B < 1.50$, $6.50 < Si < 7.50$, $(Na + K)_A > 0.50$. According to the modern amphiboles nomenclature [1], this mineral should be named magnesioferrikatophorite.

Although the structures of amphiboles of different compositions were refined in numerous studies, the crystal chemistry of the series of katophorites has been investigated insufficiently. In a number of earlier structure studies [2, 3], the specimens were described as katophorites, which they are not. According to the IMA-97 nomenclature, these compounds belong to other series of monoclinic amphiboles. In particular, the "katophorite varieties" (A1, A6, and A7) treated in [2] are riebeckite (A1) with the number of Al atoms per formula unit smaller than 0.5, arfvedsonite (A6) with three Na atoms per formula unit, and richterite (A7) containing two Na atoms, one Ca atom, and eight Si atoms per formula unit. The katophorite specimens A7 and A8, which were studied recently [3], contained two Al atoms per formula unit and, in fact, should be considered as magnesiotaramite.

Therefore, our study was stimulated by the lack of information on the crystallochemical features of katophorite species by a discovery of a new occurrence of the mineral of this series in carbonatites from the Turiy Cape (the Kola Peninsula, the North Shore of the Kandalaksha Bay of the White Sea), and also the possibility of analyzing the character of the cation distribution by modern methods of the Mössbauer spectroscopy and X-ray diffraction analysis.

EXPERIMENTAL

Chemical composition and the zonal character of the crystal (electron microprobe data). The mineral was discovered in a drill core. In this deposit, massive calcite carbonatite in some places is enriched with apatite, phlogopite, amphibole, and pyrrhotite. Amphibole occurs as black prismatic crystals (up to 7 × 1.5 × 1 mm) formed predominantly by the {110} and {100}

faces with poorly formed vertices. Its content in the rock reaches 3–5%.

Chemical analysis of the crystals was performed on a CAMEBAX SX 50 instrument (CAMECA); the accelerating voltage was 15 kV; the current intensity was 30 nA (analyst N.N. Korotaeva).

The formula coefficients were calculated for 46 negative charges, i.e., formally, for the anhydrous anionic basis [23(O)]. Then, the formula was converted to the calculated basis 23(O) + Σ(*T* + *C*) = 13, where *T* and *C* are the cations in the tetrahedral and octahedral positions of the amphibole structure. The empirical formula was determined by averaging the results of chemical analyses at 10 points performed for two grains. The Fe^{3+} content in the formula was determined from the requirement of its electroneutrality. The resulting formula can be written as $(Na_{0.75}K_{0.13})_{\Sigma 0.88}(Na_{1.45}Ca_{0.55})_{\Sigma 2.00} \cdot (Mg_{2.72}Fe^{2+}_{1.07}Fe^{3+}_{1.02}Ti^{4+}_{0.17}Mn_{0.02})_{\Sigma 5.00}(Si_{7.21}Al_{0.76} \cdot Fe^{3+}_{0.03})_{\Sigma 8.00}O_{22}(OH_{1.71}F_{0.29})_{\Sigma 2.00}$.

Chemical analysis revealed the zonal character of the crystals. For one of the crystals, the composition was determined at eight points along the elongation axis. The Ca : Na ratio changes substantially in moving from the specimen center to its periphery. In the central portion, the grain is enriched with Na (the Na content is higher than 1.5 apfu and the Ca content is lower than 0.5 apfu) and its composition corresponds to ferric-nyböite (idealized formula $Na_3Mg_3Fe^{3+}_2Si_7AlO_{22}(OH)_2$). At the specimen periphery, where the Ca content is higher (Na < 1.5 apfu, and Ca > 0.50 apfu), the composition corresponds to magnesioferrikatophorite. The volume of the ferric-nyböite core is less than the volume of the peripheral zone of the magnesioferrikatophorite crystal.

Analysis of the Mössbauer spectra of magnesioferrikatophorite performed at the preliminary stage of the investigation allowed us to distinguish between divalent and trivalent iron ions and showed that Fe^{3+} ions substantially dominate over Fe^{2+}. The refined empirical formula of the magnesioferrikatophorite specimen (Table 1) can be written as follows:

$$(Na_{0.74}K_{0.12})_{\Sigma 0.86}(Na_{1.45}Ca_{0.55})_{\Sigma 2.00} \cdot (Mg_{2.71}Fe^{3+}_{1.34}Fe^{2+}_{0.76}Ti^{4+}_{0.17}Mn_{0.02})_{\Sigma 5.00} \cdot (Si_{7.15}Al_{0.76}Fe^{3+}_{0.09})_{\Sigma 8.00}O_{22}(OH_{1.47}F_{0.29}O_{0.24})_{\Sigma 2.00}.$$

Evidently, the compositional characteristics of this amphibole are directly associated with the characteristic chemical features of the host rocks, which is indicative of a high oxidizing potential of the mineral-forming medium and a slight decrease in the activity of Na in the course of the evolution of crystallogenesis. In addition, it was demonstrated [4] that the composition of amphiboles serves as a certain indicator that allows one to estimate the silica content in magma. Amphiboles, which are relatively depleted of silica (Si < ~7.00 apfu), are formed in silicon-undersaturated rocks, whereas amphiboles formed in silicon-saturated and silicon-oversaturated rocks are characterized by a higher Si content (~7.00 < Si < 8.00 apfu). Based on the silica content in the specimen under study, the latter can be related to high-silica amphiboles. Taking into account the characteristic geochemical features of the carbonatite systems, it would be more correct to consider the medium as deficient in aluminum but rather as enriched with silica.

Table 1. Average chemical composition of magnesioferrikatophorite

Component	wt %
Na_2O	7.76
K_2O	0.67
CaO	3.50
MgO	12.53
MnO	0.19
FeO*	6.23
$Fe_2O_3^*$	12.32
Al_2O_3	4.42
TiO_2	1.51
SiO_2	49.23
F	0.62
$–O=F_2$	–0.26
Sum	98.72

* Divalent and trivalent iron ions are distinguished based on the Mössbauer spectroscopic data.

Mössbauer spectroscopy. The Mössbauer spectra were recorded on an instrument of the electrodynamic type using a Co^{57} (Rh) source at 300, 80, and 10 K. The experimental spectra were processed using the UNIVEM program [5]. The isomer shifts are given relative to α-Fe (main standard).

The mathematical processing of the spectrum measured at 300 K at a rate of ±8 mm/s allowed us to single out three doublets (Fig. 1), with two of them being unambiguously attributed to Fe^{2+} and Fe^{3+}, respectively (characteristic isomer shifts), with the third one being attributed to Fe^{4+} (isomer shift δ_3 = –0.10 mm/s, quadrupole splitting δ_3 = 0.25 mm/s) [6]. According to experimental data [7], similar parameters of the Mössbauer spectrum correspond to Fe^{3+} located in the vicinity of Ti^{4+}. The assignment of the Mössbauer-spectrum doublets to the structural positions in magnesioferrikatophorite was made with due regard for the known crystal chemistry data for amphiboles [6, 8] and the results of our X-ray diffraction study. The parameters of the spectrum are given in Table 2. The experiment was performed at a high rate (±8 mm/s) and confirmed

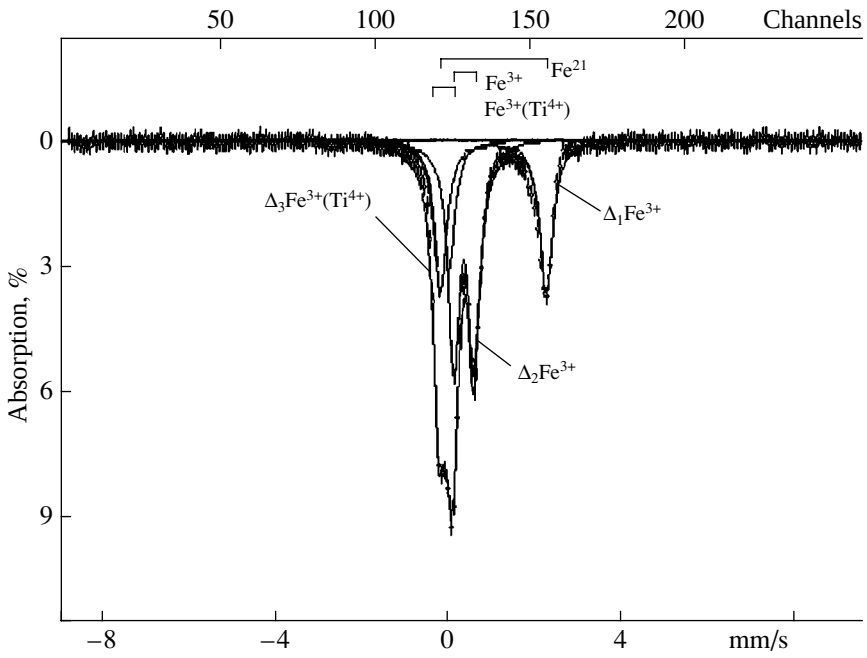

Fig. 1. Mössbauer spectrum of magnesioferrikatophorite.

the absence of magnetic splitting in the Mössbauer spectrum.

X-ray diffraction study. The crystallographic characteristics, the principal parameters of the X-ray diffraction study, and the details of the structure refinement are given in Table 3. The unit-cell parameters were determined by the least-squares refinement with the use of the angular characteristics of 22 reflections in the range $20° \le 2\theta \le 32°$. The empirical absorption correction was applied using the ψ-scan.

The crystal structure was refined starting from the atomic coordinates of K-edenite [9] within the sp. gr. *C*2/*m* using 1481 independent reflections with $I_0 > 2\sigma(I_0)$ by the SHELX97 program package [10]. The refinement was performed with the anisotropic thermal parameters up to $R(F) = 0.039$. At the first stage, the occupancies of five cation positions, namely, *M*(1), *M*(2), *M*(3), *M*(4), and *A*, were refined.

The subsequent determination of the distribution of isomorphous cations over the crystallographically nonequivalent positions was based on the following: (1) the refinement of the electron contents of the cation positions, (2) the correspondence between the structural formula and the data from electron microprobe analysis, (3) the electroneutrality of the chemical formula, (4) the requirements of the valence balance, and (5) the approximate equality of the average interatomic distances to the sums of the ionic radii of the cation and anion in the corresponding polyhedra. However, there are some limitations in the refinement of the mixed occupancies of the nonequivalent cation positions. Since the scattering abilities of Fe^{3+}, Fe^{2+}, and Mn, on the one hand, and Al and Mg, on the other hand, are virtually indistinguishable, the mutual replacement of cations that belong to the same group has almost no effect on the reflection intensities. This fact made it expedient to refine the distribution of the Fe^{3+} and Fe^{2+} ions over the nonequivalent positions using the Mössbauer spectroscopy data.

Table 2. Parameters of the doublets in the Mössbauer spectrum of magnesioferrikatophorite (T = 300 K and $V = \pm 8$ mm/s)

Cations	Isomer shift δ (mm/s)	Quadrupole splitting Δ (mm/s)	Relative area (%)
Fe^{3+} (Ti^{4+})	–0.1000	0.2500	20.09
Fe^{3+}	0.3789	0.5010	43.93
Fe^{2+}	1.0409	2.4690	35.98

The final coordinates and atomic-displacement parameters are listed in Table 4. The distribution of the cations over the positions is presented in Table 5. The local valence balance calculated in [13] is indicated in Table 6. The average interatomic distances in the coordination polyhedra have standard values ($\langle M(1)–O\rangle$ = 2.083 Å, $\langle M(2)–O\rangle$ = 2.061 Å, $\langle M(3)–O\rangle$ = 2.088 Å, $\langle M(4)–O\rangle$ = 2.539 Å, $\langle T(1)–O\rangle$ = 1.644 Å, $\langle T(2)–O\rangle$ = 1.635 Å, $\langle A(m)–O\rangle$ = 2.765 Å, and $\langle A(2)–O\rangle$ = 2.713 Å).

The overall view of the structure drawn using the ATOMS program [14] is shown in Fig. 2.

DESCRIPTION AND DISCUSSION OF THE STRUCTURE

Tetrahedral *T*(1)- and *T*(2)-positions. According to the electron microprobe analysis data, there are approximately eight Si + Al atoms per formula unit, which supports the conclusion about the tetrahedral coordination of aluminum in the structure. The structures of monoclinic amphiboles have two nonequivalent positions, namely, *T*(1) and *T*(2), characterized by a distorted tetrahedral coordination and the point symmetry 1.

A comparison of the average distances $\langle T(1)\text{–O}\rangle$ = 1.644 Å and $\langle T(2)\text{–O}\rangle$ = 1.635 Å shows that aluminum is located only in the *T*(1) position. The Si : Al ratio in this position (3.16 and 0.84 apfu for Si and Al, respectively) was determined based on the correlation between the average $\langle T(1)\text{–O}\rangle$ bond length and the Al content [15]

$$^{T(1)}\text{Al (apfu)} = [\langle T(1)\text{–O}\rangle - 1.6187] \times 33.2055.$$

A somewhat larger average distance $\langle T(2)\text{–O}\rangle$ = 1.635 Å falls within the range 1.628–1.635 Å typical of these tetrahedra and is consistent with the corresponding distances in the Ca-containing amphiboles studied earlier.

Octahedral positions. In addition to the tetrahedral cations, the octahedral cations are also of importance in the formation of the amphibole structure type. These polyhedra are linked to form the ribbons containing three nonequivalent cation positions, namely, *M*(1), *M*(2), and *M*(3), characterized by different point symmetry groups (2, 2, and 2/*m*, respectively). The cations located in these positions have a pseudooctahedral coordination. The *M*(4) position characterized by the point symmetry 2 and surrounded by eight anions holds a special place in the structure. However, not all these anions form bonds with the central cation.

The total scattering power of the *M*(1), *M*(2), and *M*(3) positions is provided by the sum of electrons of the cations located in these positions or, to put it differently, the sum of the average atomic numbers per position. Analogous calculations can be performed based on the chemical analysis data for one formula unit. A correlation between these two estimates can be considered as a correctness criterion for the structure-refinement data [2]. Figure 3 shows the plot characterizing the consistency of the electron contents of the *M*(1), *M*(2), and *M*(3) positions determined from the X-ray diffraction and chemical analysis data for amphiboles studied earlier [2]. The position of the point corresponding to magnesioferrikatophorite in this plot confirms the correctness of the proposed model of the cation distribution over the *M*(1), *M*(2), and *M*(3) positions.

Octahedral *M*(1) and *M*(3) positions. The atoms in the *M*(1) and *M*(3) positions are coordinated by four O atoms and two OH^- anions [O(3)]. In the *M*(1) octahedra, the O(3) anions are in the *cis* positions, whereas O(3) anions in the *M*(3) octahedra are in the *trans* positions. An *M*(1) octahedron shares five edges with the surrounding octahedra and only one edge with a *M*(4) polyhedron, whereas an *M*(3) octahedron shares all the six edges with the adjacent octahedra; i.e., it is the central polyhedron of the octahedral ribbon.

The results of the structure refinement of approximately 550 monoclinic amphibole specimens demonstrated that an increase in the electron content in the *M*(1) position is accompanied by an increase in the electron content in the *M*(2) position [2]. A slight deviation from this correlation was observed only for Li-containing amphiboles, in whose structures the light Li atoms are located, primarily, in the *M*(3) octahedra. The cation distribution found in the magnesioferrikatophorite structure is in good agreement with the above-

Table 3. Crystallographic characteristics and details of the X-ray diffraction study

Unit-cell parameters, Å, deg	a = 9.875(5), b = 18.010(8), c = 5.309(3), β = 104.39(5)
Sp. gr.; Z	$C2/m$; 2
V, Å^3	914.6
ρ_{calcd}, g/cm^3	3.211
μ (mm^{-1})	2.81
Molecular weight	1768.82
Crystal dimensions (mm)	0.15 × 0.10 × 0.06
F_{000}	872
Diffractometer	Siemens P4
Wavelength, Å	0.71069
$2\theta_{max}$, deg	70.08
otal number of reflections	4014
Total number of independent reflections	2072
Number of independent reflections with $I_0 > 2\sigma(I_0)$	1481
R_{int}, %	6.87
Method of refinement	Least-squares procedure based on F^2
Number of parameters in the refinement	145
Final $R(F)$ for reflections with $I_0 > 2\sigma(I_0)$	0.039
$R(F)$ for all independent reflections	0.064
wR (F^2)	0.102
$S = GOF$	1.047
$\Delta\rho_{max}$, e/Å^3	0.8
$\Delta\rho_{min}$, e/Å^3	–0.93

Table 4. Final atomic coordinates and atomic-displacement parameters in the magnesioferrikatophorite structure

Position	*x*/*a*	*y*/*b*	*z*/*c*	U^*_{eq}, Å^2
M(1)	0	0.08874(6)	0.5	87(2)
M(2)	0	0.18063(4)	0	96(2)
M(3)	0	0	0	70(2)
M(4)	0	0.27810(7)	0.5	150(2)
A(*m*)**	0.5	0	0	1004(55)
A(2)**	0.44870(3)	0	0.88028(4)	339(9)
T(1)	0.28009(8)	0.08562(4)	0.2968(2)	75(2)
T(2)	0.28894(7)	0.17158(4)	0.8049(1)	68(1)
O(1)	0.1098(2)	0.0882(1)	0.2144(4)	95(3)
O(2)	0.1194(2)	0.1711(1)	0.7313(4)	106(4)
O(3)=OH	0.1084(3)	0	0.7108(5)	101(5)
O(4)	0.3640(2)	0.2495(1)	0.7948(4)	124(4)
O(5)	0.3494(2)	0.1323(1)	0.0927(4)	153(4)
O(6)	0.3427(2)	0.1176(1)	0.5932(4)	137(4)
O(7)	0.3384(3)	0	0.2867(6)	149(6)

* $U_{eq} \times 10^4$.
** The nomenclature of the *A*-positions in amphiboles with the symmetry *C*2/*m* [11]: *A*(*m*), *x*, 1/2, *z*; *A*(2), 0, *y*, 0; *A*(2/*m*), 0, 1/2, 0.

mentioned correlation between the electron contents of the *M*(1) and *M*(3) positions. In Fig. 4, the point corresponding to magnesioferrikatophorite lies in the lenticular region, which also includes the electron contents of the *M*(1) and *M*(3) positions of most of the known amphiboles. In these structures, the Fe^{2+} ($r^{[6]}Fe^{2+}$ = 0.78 Å) and Mg^{2+} ($r^{[6]}Mg^{2+}$ = 0.72 Å) cations with large ionic radii occupy the largest *M*(3) octahedra.

Location of Ti^{4+} in the octahedral *M*(1) position. Electron microprobe analysis showed that the Ti^{4+} content in the specimen is ~0.17 apfu. In accordance with the earlier studies of amphiboles [16, 17], the Ti^{4+} ion was always placed into the *M*(2) octahedron of a relatively small volume. This was explained by the fact that $^{[6]}Ti^{4+}$ is a small-size cation with high valence ($r^{[6]}Ti^{4+}$ = 0.605 Å). Its role in the amphibole structures is analogous to the role played by other cations of the *C* group (Fe^{3+}, Mn, Mg, Al, etc.). In a more recent study of the structure of $^{[6]}$Ti-containing richterite [18], Ti^{4+} was found to occupy the *M*(1) position, which fact was attributed to the heterovalent substitution according to the following scheme:

$$^{[M(1)]}(Ti^{4+}) + 2^{[O(3)]}O^{2-} \Leftrightarrow {}^{[M(1)]}(Mg,Fe) + 2^{[O(3)]}OH^{-}.$$

Later on, the Ti^{4+} ion was found both in the *M*(1) and *M*(2) positions in the structures of amphiboles of various compositions.

Table 5. Distribution of the cations over the positions in the magnesioferrikatophorite structure

Position	Electron content	Occupancy of the position	Electron content with due regard for the real occupancy	Sum of ionic radii* of the cation and anion	Average cation–anion distance
M(1)	31.27	1.41Mg + 0.42Fe^{3+} + 0.17Ti^{4+}	31.59	2.075	2.083
M(2)	39.83	1.31Fe^{3+} + 0.69Mg	42.39	2.051	2.061
M(3)	16.95	0.60Mg + 0.37Fe^{2+} + 0.02Mn	17.06	2.118	2.088
M(4)	29.29	1.18Na + 0.82Ca	29.38	2.535	2.539
A(*m*)	11.58	0.56Na + 0.13K	8.58	2.448	2.765
A(2)		0.31Na	3.41	2.380	2.713

* The ionic radii were taken from [12].

Table 6. Local valence balance at the anions in the magnesioferrikatophorite structure

	M(1)	*M*(2)	*M*(3)	*M*(4)	*A*(*m*)	*A*(2)	*T*(1)	*T*(2)	Σ
O(1)	0.38	0.33	0.35				0.99		2.05
O(2)	0.37	0.40		0.23				1.01	2.01
O(3)=OH	0.37		0.37						0.74
O(4)		0.55		0.28				1.08	1.91
O(5)				0.08	0.05	0.01	0.95	0.92	2.01
O(6)				0.16		0.02	0.95	0.88	2.01
O(7)					0.16	0.04 + 0.02	0.94 × 2		2.10

In the magnesioferrikatophorite structure, the O(3) position is occupied by O^{2-} by more than 50%. Hence, it is reasonable to assume that the Ti^{4+} ion occupies the *M*(1) position together with Fe^{3+}, which is confirmed by the Mössbauer spectroscopy data. This distribution leads to an improvement of the valence balance, and the average interatomic distance $\langle M(1)\text{–}O\rangle$ = 2.083 Å becomes approximately equal to the sum of the ionic radii of the cation and anion (2.075 Å). The involvement of Ti^{4+} in the *M*(1) octahedra is also consistent with the estimate of the electron content in this position.

Octahedral *M*(2) position. In the amphibole structures, the atoms in the *M*(2) position with the point symmetry 2 are coordinated by six O atoms. The *M*(2) octahedron is generally occupied by cations with rather small radii. This octahedron shares three edges with the adjacent *M*(1) and *M*(3) octahedra and one edge with the *M*(4) polyhedron. In the magnesioferrikatophorite structure, the *M*(2) octahedron is also characterized by the smallest average bond length $\langle M(2)\text{–}O\rangle$ = 2.061 Å as compared to the *M*(1) and *M*(3) octahedral positions. The *M*(2) octahedra are occupied by more than 50% by the Fe^{3+} cations ($r^{[6]}Fe^{3+}$ = 0.645 Å), which is confirmed by the Mössbauer spectroscopy data. In addition, Mg atoms are also located in the *M*(2) octahedra.

The relatively low symmetry of the *M*(2) octahedron is attributed to the fact that four of the total six O atoms involved in this octahedron (O(4) and O(2)) are simultaneously bound to the large cations in the *M*(4) position. According to [8], the effect of these cations is seen from a decrease in the corresponding bond lengths in the *M*(2) octahedra. As a result, the average distances $\langle M(2)\text{–}O(4)\rangle$ = 1.961 Å and $\langle M(2)\text{–}O(2)\rangle$ = 2.072 Å in the magnesioferrikatophorite structure are substantially shorter than $\langle M(2)\text{–}O(1)\rangle$ = 2.151 Å.

The *M*(4) position. Taking into account eight neighboring anions, the coordination polyhedron about the *M*(4) position is either a distorted cube or a tetragonal antiprism sharing seven edges with the adjacent polyhedra, namely, four edges with the SiO_4 tetrahedra and three edges with the *M*(2) octahedra.

The *M*(4) position holds a special place in the amphibole structures. Since this position is occupied by different cations, it influences the isomorphism in the amphibole series and plays an important role for choosing the name of a mineral species. It is the change in the Ca : Na ratio in the *M*(4) position that is responsible for the zonal nature of the crystal studied. Thus, the com-

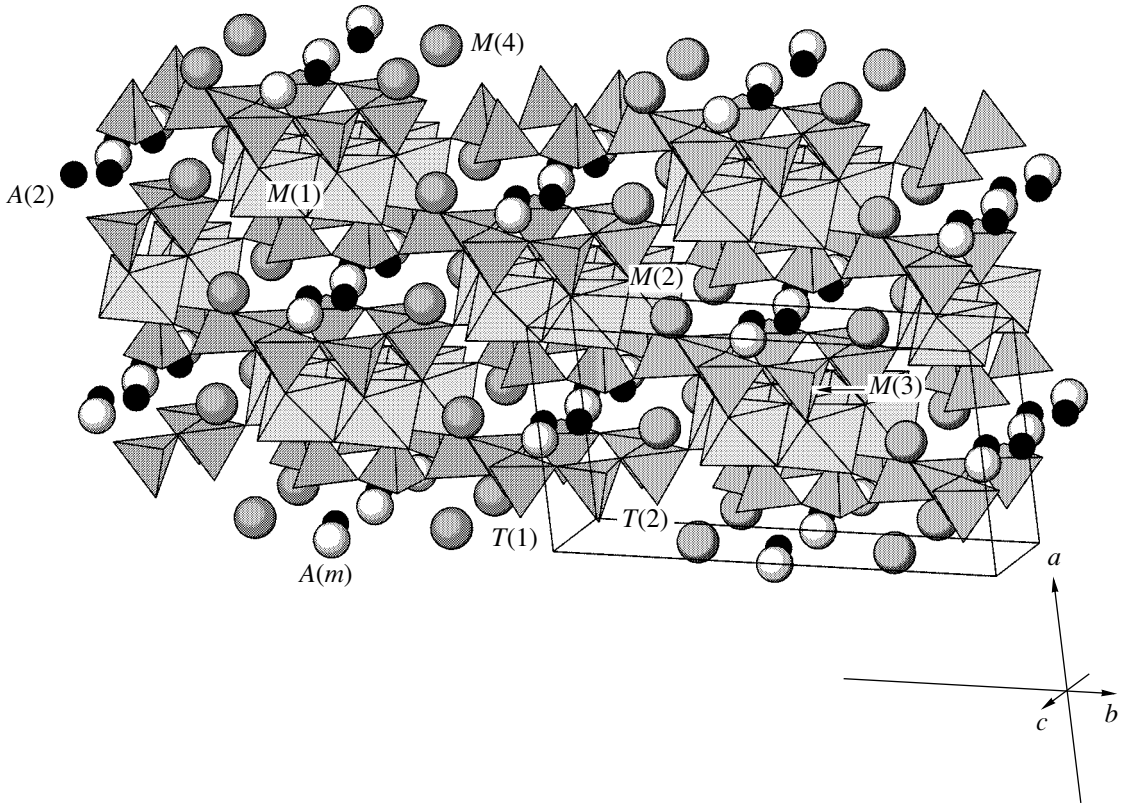

Fig. 2. Overall view of the magnesioferrikatophorite structure; the *A*(2), *A*(*m*), *M*(4) positions are indicated by solid, empty, and shaded circles, respectively.

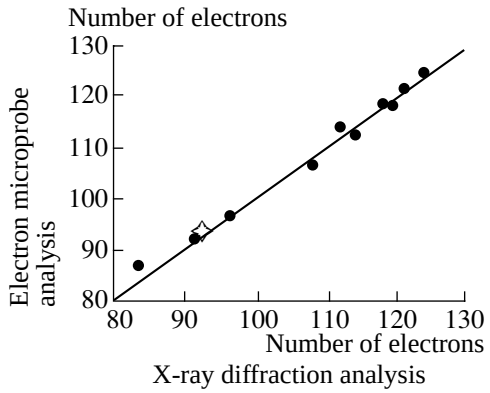

Fig. 3. Total electron content of the *M*(1), *M*(2), and *M*(3) positions in the magnesioferrikatophorite structure (white cross) according to the electron microprobe and X-ray diffraction analysis data in comparison with various amphiboles studied earlier [2].

positions of its core and the periphery correspond to different mineral species, namely, to ferric-nyböite and magnesioferrikatophorite, respectively.

According to [8], the size of the *M*(4) position depends on the sizes of the cations located in other octahedral positions. Thus, an increase in the ⟨*M*(1,2,3)–O⟩ distances averaged over three octahedra is accompanied by an increase in the average ⟨*M*(4)–O⟩ distance. In the magnesioferrikatophorite structure, the average interatomic distances ⟨*M*(4)–O⟩ = 2.539 Å and ⟨*M*(1,2,3)–O⟩ = 2.077 Å agree with the correlation reported in [8].

The *M*(4) position is very "elastic" as to the sizes and coordination of the cations entering this position. In monoclinic amphiboles with the symmetry group *C*2/*m*, this position is occupied by the cations of the *B* group, namely, by Ca ($r^{[8]}Ca^{2+}$ = 1.12 Å) and Na ($r^{[8]}Na^{+}$ = 1.18 Å).

Structural position *A*. The largest polyhedra occupied by the *A* cations are located between the adjacent silicon–oxygen ribbons along the *a* axis. These polyhedra are formed by 12 oxygen anions. The bridging anions between the SiO_4 tetrahedra form two ditrigonal rings at the opposite bases of the *A* polyhedra.

The *A* position is generally occupied by large K and Na cations. In monoclinic amphiboles with the symmetry group *C*2/*m*, this position is often split with respect to this position in an inversion center (0.5, 0, 0) because, first of all, of the larger size of the *A* cavity. The structural features associated with splitting of the *A* positions were considered in a number of studies. In [19], it was indicated that alkali cations occupy the *A*(2) or *A*(*m*) positions if the O(3) positions are occupied by OH groups or F^- anions, respectively. In terms of the valence balance [8], splitting of the *A* position led to the conclusion that the location of potassium in the *A*(2/*m*) position gives rise to an excessive sum of valence forces at this cation, whereas a deficiency of valence forces takes place if this position is occupied by Na.

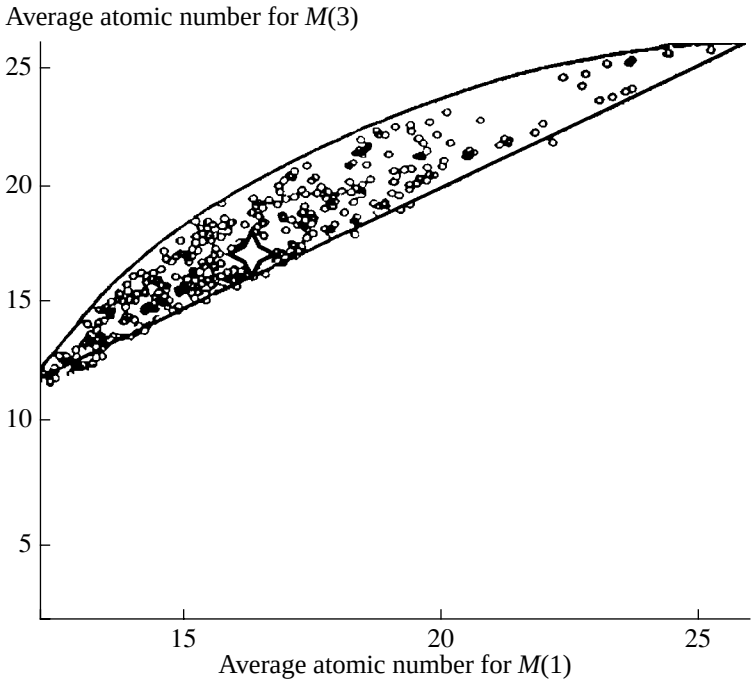

Fig. 4. Average atomic numbers in the *M*(1) and *M*(3) positions in the magnesioferrikatophorite structure (white cross within the lenticular region) in comparison with the electron contents of the same positions for different amphiboles studied earlier [2].

In the magnesioferrikatophorite structure, the *A* position is also split into two subpositions, namely, *A*(2) and *A*(*m*). This effect can be associated with the following facts:

(1) the presence of small amounts of K (~0.12 apfu) in the structure, which was confirmed by the electron microprobe analysis data; the large potassium cation ($r^{[12]}K^+$ = 1.64 Å) is located in the *A*(*m*) subposition together with Na ($r^{[12]}Na^+$ = 1.27 Å), whereas sodium can simultaneously occupy both subpositions [20], which is quite reasonable, because the average bond length $\langle A(m)–O\rangle$ = 2.765 Å is larger than $\langle A(2)–O\rangle$ = 2.713 Å;

(2) the presence of three types of cations (OH^-, F^-, and O^{2-}) in the O(3) position responsible for the redistribution of ^{A}Na over the *A*(2) and *A*(*m*) subpositions [3];

(3) the involvement along with Si also of aluminum in the tetrahedral *T*(1) position (Al content is 0.84 apfu); the positional disorder was attributed [21, 22] to the necessity of preservation of the valence balance at the anions involved in the bonds with the *T*(1) and *A* cations. In the presence of Al in the *T*(1) tetrahedra, Na atoms occupy the *A*(2) subposition, whereas, because of the larger size, the K atoms are located in the *A*(*m*) subposition.

Therefore, in the magnesioferrikatophorite structure, the Na atoms are located in both split subpositions, whereas the K atoms occupy only the *A*(*m*) subposition. The compositions of the cation positions in the structure are reflected by the refined crystallochemical formula of magnesioferrikatophorite $(Na_{0.87}K_{0.13})_{\Sigma A = 1} \cdot (Na_{1.18}Ca_{0.82})_{\Sigma M(4) = 2}(Mg_{1.41}Fe^{3+}_{0.42}Ti^{4+}_{0.17})_{\Sigma M(1) = 2}(Mg_{0.69} \cdot Fe^{3+}_{1.31})_{\Sigma M(2) = 2}(Mg_{0.60}Fe^{2+}_{0.38}Mn_{0.02})_{\Sigma M(3) = 1}(Si_{3.16} \cdot Al_{0.84})_{\Sigma T(1) = 4}Si_4O_{22}(O_{1.05}OH_{0.66}F_{0.29})_{\Sigma 2}$.

ACKNOWLEDGMENTS

We are grateful to R.K. Rastsvetaeva for helpful discussion and valuable advice.

This study was supported by the Russian Foundation for Basic Research (project nos. 00-05-65399 and 00-15-96633) and the Program "Russian Universities." D.Yu. Pushcharovskiĭ acknowledges the support of the program within the framework of Russian–Italian scientific cooperation (project no. 62).

REFERENCES

1. B. E. Leake, A. R. Woolley, C. E. S. Arps, *et al.*, Can. Mineral. **35**, 219 (1997).
2. F. C. Hawthorne, L. Ungaretti, R. Oberti, and P. Bottazzi, Am. Mineral. **78**, 733 (1993).
3. F. C. Hawthorne, R. Oberti, L. Ungaretti, and N. Sardone, Can. Mineral. **34**, 577 (1996).
4. A. Giret, B. Bonin, and J.-M. Leger, Can. Mineral. **18**, 481 (1980).
5. A. A. Novakova and T. Yu. Kiseleva, *Mössbauer Practical Work* (Mosk. Gos. Univ., Moscow, 2000).
6. F. Menil, J. Phys. Chem. Solids **46** (7), 763 (1985).
7. A. A. Novakova, O. V. Agladzeo, S. V. Sveshnikov, and B. P. Tarasov, Nanostruct. Mater. **10**, 365 (1998).
8. F. C. Hawthorne, Can. Mineral. **21**, 173 (1983).
9. R. K. Rastsvetaeva, D. Yu. Pushcharovskiĭ, and B. E. Borutskiĭ, Kristallografiya **40** (2), 33 (1995) [Crystallogr. Rep. **40**, 27 (1995)].
10. G. M. Sheldrick, *SHELX97: Program for the Solution and Refinement of Crystal Structures* (Siemens Energy and Automation Inc., Madison, 1997).
11. F. C. Hawthorne and H. D. Grundy, Can. Mineral. **16**, 53 (1978).
12. R. D. Shannon, Acta Crystallogr., Sect. A: Cryst. Phys., Diffr., Theor. Gen. Crystallogr. **32**, 751 (1976).
13. I. D. Brown and D. Altermatt, Acta Crystallogr., Sect. B: Struct. Sci. **41**, 244 (1985).
14. E. Dowty, *Atoms 3.2.: A Computer Program for Displaying Atomic Structures* (Kingsport, 1995).
15. R. Oberti, L. Ungaretti, E. Cannillo, *et al.*, Eur. J. Mineral. **7**, 1049 (1995).
16. K. Robinson, G. V. Gibbs, P. H. Ribbe, and M. R. Hall, Am. J. Sci. **273**, 522 (1973).
17. M. Kitamura, M. Tokonami, and N. Morimoto, Contrib. Mineral. Petrol. **51**, 167 (1975).
18. R. Oberti, L. Ungaretti, E. Cannillo, and F. C. Hawthorne, Eur. J. Mineral. **4**, 425 (1992).
19. G. V. Gibbs, in *AGI Short Course Lecture Notes on Chain Silicates, 1966*, p. 1.
20. L. Ungaretti, D. C. Smith, and G. Rossi, Bull. Mineral. **104**, 400 (1981).
21. P. B. Moore, Mineral. Soc. Am., Spec. Pap. **2**, 111 (1969).
22. J. J. Papike, K. L. Cameron, and K. Baldwin, Mineral. Soc. Am., Spec. Pap. **2**, 117 (1969).

Translated by T. Safonova

Crystallography Reports, Vol. 48, No. 1, 2003, pp. 162–164. Translated from Kristallografiya, Vol. 48, No. 1, 2003, pp. 171–174.

INFORMATION

Guidelines for Authors

These notes are intended as a guide for authors preparing the presentation of their manuscripts. These guidelines, if adhered to, save the author, publisher, and printer much labor and will ease the passage of an article through the production process.

Only original articles, review articles, and short communications on all aspects of crystallography can be submitted. An original article should describe new unpublished results not sent for publication anywhere else.

The sequence of the materials presented is as follows:

1. Title of the article
2. Names of all the authors with the initials before their names
3. Affiliations of all the authors
4. Addresses of all the authors (including the city and country and their zip/post codes, telephone and fax numbers) and e-mail
5. Abstract
6. List of Contents (for review articles only)
7. Text
8. List of References
9. Tables
10. List of Figure Captions
11. Figures

ABSTRACTS

The article should be preceded by the title of the Section in which the article is suggested to be published (the List of Sections is given at the end of the Guidelines) and a short abstract containing not more than 100 words (on a separate sheet) in which the author(s) should formulate the aim of the study and describe the results obtained. Be aware that the abstract and the conclusion(s) section should not repeat one another.

TYPESCRIPTS

Copy, to be submitted in duplicate, should be typed 1.5 spaced on one side of standard (A4) good-quality sheets with a wide left margin (3 cm), 1.5-cm right margin, and 2.0-cm top and bottom margins. The article should not exceed 10 pages in 14-point font.

The author(s) should briefly and clearly describe their work. One should avoid reporting the same data both in the text and tables or figures and figure captions. Neither should one present the same data simultaneously in the tabulated and graphical form.

It is desirable to divide the text into sections with appropriate headings. This should necessarily be done in the review articles. One should avoid paragraphs that are too long. A review article should be preceded by a list of contents.

One should avoid the use of nonstandard abbreviations. Consistency in the use of abbreviations is also very important. The number of abbreviations used should not be large, and they should all be identified when they first occur in the text.

All the pages of the typescript should be consecutively numbered (including the abstract, text, list of references, tables, and figure captions).

Along with the typed text of the articles and figures, the article should also be presented as a Word file on an IBM compatible 3.5″ diskette.

Articles dedicated to structure determinations should be supplied with a "standard" crystallographic information file (CIF), which should preliminarily be checked by the author(s) against the A, B, and C alerts automatically at the e-mail address **chekcif@iucr.org** or with the aid of the PLATON Internet program at the address http:**//www.chem.gla.ac.uk/~louis**.

The editorial board reserves the right to check the CIF and to return the articles to the author(s) for the correction of unreliable information (alert A). The presence of alerts B and C should be supplied with the author(s)'s comments.

Upon the acceptance of the article for publication, the author(s) should deposit the crystallographic data file (CIF) in

(a) Inorganic Crystal Structure Database ICSD (Karlsruhe, Germany) at the e-mail address **crysdata@fiz-karlsruhe.de** (for inorganic structures). The deposited article should be submitted with the corresponding reference number in the form ICSD no. …;

(b) Cambridge Structural Database CSD at the Cambridge Crystallographic Data Center (CCDC) (Cambridge, United Kingdom) at the e-mail address **deposit@ccdc.cam.ac.uk** (for crystal structures containing at least one "organic" carbon atom. The deposited article should be submitted with the corresponding reference number in the form CCDC no. …. The form for submitting CIF can be obtained automatically at the e-mail address **deposit@ccdc.cam.ac.uk** with the **sendme depform** command or via the Internet at the address http:**//www.ccdc.cam.ac.uk**.

1063-7745/03/4801-0162$24.00

The data submitted will be included in the corresponding databases only upon the publication of the corresponding articles.

In addition to the preliminary deposit of the CIF in the above data bases, the authors should also send these CIFs to the regional representative of the CCDC to the Nesmeyanov Institute of Organoelement Compounds, Russian Academy of Sciences, at the e-mail address **star@xray.ineos.ac.ru**.

The article should be signed by all the authors.

REFERENCES

The references are indicated in the text by consecutive arabic numbers in square brackets. The full list of references should be collected and typed at the end of the paper in numerical order (on separate sheets). Listed references should be complete in all details excluding article titles in journals. Authors' initials are placed before their names. The journal title abbreviations should conform to *Physical Abstracts*. Examples:

1. D. L. Wood and J. P. Remeika, J. Appl. Phys. **38**, 1038 (1976).
2. P. Mauerberger, H. J. Haupt, and F. Huber, Acta Crystallogr., Sect. B: Struct. Crystallogr. Cryst. Chem. **35** (2), 295 (1975).
3. G. E. Bacon, *Neutron Diffraction* (Clarendon, Oxford, 1955; Inostrannaya Literatura, Moscow, 1967).
4. S. A. Pikin, *Structural Transformations in Liquid Crystals* (Nauka, Moscow, 1981; Gordon and Breach, New York, 1991).
5. J. J. Conway and N. J. A. Sloane, *Sphere Packings, Lattices, and Groups* (Springer-Verlag, New York, 1988), Vols. 1, 2.
6. N. N. Vorontsov, *Principles of Synthesis of Intermediate Products and Dyes* (Goskhimizdat, Moscow, 1955).
7. M. L. Meilman, I. D. Ryabov, A. I. Mottchanui, and P. P. Chvanski in *Proceedings of the 3rd European Workshop on Piezoelectric Materials: Crystal Growth, Properties and Prospects, Montpellier, France, 2000*, p. 213.
8. G. M. Sheldrick, *SHELXTL97: Program for the Solution and Refinement of Crystal Structures* (University of Göttingen, Göttingen, 1997).

All the references given in the List of References should necessarily be mentioned in the text.

TABLES

Data collected in tables should be presented in a clear and concise form to help both typesetter and reader. Indicate clearly where in the typescript you would like the tables to be placed. Your instructions will be followed as far as technically possible. Number the tables consecutively with arabic numerals (Table 1, Table 2, etc.), and put a clear descriptive caption at the top of each table.

ILLUSTRATIONS

All the figures should be presented in a clear form in the format as close as possible to a square shape. All the details should be clearly resolved (this is especially important for photographs). Illustrations should be presented on separate sheets and should not be glued to the typescript. The figure captions should also be typed on a separate sheet, numbered by consecutive arabic numbers (Fig. 1, Fig. 2, etc.), and mentioned in sequential order in the text. Keep illustrations separate from the text, but indicate clearly an approximate position for each in the margin. One should indicate the name of the first author and the figure number on the front side of each figure. One should avoid any text in the figures by replacing the necessary text with a letter or a number symbol either in the corresponding figure caption or in the text of the article.

Two copies of each photograph should be presented on white glossy photographic paper. One of the copies should not have any writing on the front side. For micrographs, one has to indicate the scale of imaging (and not the magnification) in the lower right-hand corner.

EQUATIONS AND FORMULAS

Whenever possible, mathematical equations should be typewritten in large and distinct letters. One should avoid notation that is too cumbersome to facilitate setting. One should avoid unnecessary multiplication signs. The subscripts and superscripts should be clearly shown (by pencil marks $\cup$ and $\cap$). It is useful to identify unusual or ambiguous symbols in the margin when they first occur. To simplify typesetting, please use (1) the "exp" form of complex exponential functions; (2) fractional exponents instead of root signs; (3) a solidus (/) to simplify fractions, e.g.,

$$\frac{(a/b)+(c/d)}{(e/f)+(g/h)}, \qquad \frac{(a/b)+\exp(E/kT)}{(e/f)+\sin(w/w_0)}.$$

MARKING

The printer will set mathematical symbols in italics, except for obvious groups like sin and log. Any symbols which are to be left in roman (plain) type should be underlined with a square bracket in pencil in the typescript; bold symbols should be underlined with a blue pencil, Greek letters should be underlined with a red pencil. The super- and subscript should be indicated in pencil by signs $\cup$ and $\cap$.

One should underline with two lines uppercase letters $\underline{\underline{C}}$, $\underline{\underline{K}}$, $\underline{\underline{O}}$, $\underline{\underline{U}}$, $\underline{\underline{V}}$, $\underline{\underline{W}}$, and $\underline{\underline{\Psi}}$ and supply with two bars the low-case letters $\overline{\overline{c}}$, $\overline{\overline{k}}$, $\overline{\overline{o}}$, $\overline{\overline{u}}$, $\overline{\overline{v}}$, $\overline{\overline{w}}$, and $\overline{\overline{\psi}}$; the symbol 0 (zero) is indicated by a square bracket under it ($\underline{0}$).

Only the first copy of the article (including all the formulas, tables, figures, and figure captions) should be marked in accordance with the above guidelines.

One should indicate on a separate sheet the data necessary for correspondence: the author's name, his address, the telephone and fax numbers, and the e-mail address.

All the articles are sent to a referee and then can be sent back to the author(s) for necessary revision and introduction of corrections. This work should be done within four months, otherwise a new date of the acceptance of the manuscript will be indicated in the final publication.

The Editorial Board reserves the right to make necessary abridgements and to introduce some necessary stylistic corrections in the manuscript.

If the article is rejected, only one copy is sent back to the author(s).

The Editorial Board will send the authors the reprints of their articles in both Russian and English.

LIST OF SECTIONS

1. Crystallographic Symmetry
2. Theory of Crystal Structures
3. Crystal Chemistry
4. Diffraction and Scattering of Ionizing Radiations
5. Structure of Inorganic Compounds
6. Structure of Organic Compounds
7. Structure of Macromolecular Compounds
8. Real Structure of Crystals
9. Lattice Dynamics and Phase Transitions
10. Physical Properties of Crystals
11. Liquid Crystals
12. Surface, Thin Films
13. Nanomaterials
14. Ceramics
15. Crystal Growth
16. Apparatus
17. Crystallographic Software
18. History of Crystallography
19. Jubilees
20. Memorial Data
21. Obituaries
22. Information

Translated by L. Man

Crystallography Reports, Vol. 48, No. 1, 2003, p. 165.

ERRATA

Errata: "Statistical Characteristics of Inhomogeneities of Dislocation Networks" Published in *Crystallography Reports*, 2002, vol. 47, no. 3, pp. 475–479.

E. I. Gutorov

1. Abstract: the third line should read "by the functions of the type $f_k(x) = n(nx)^{n-1}e^{-nx}/(n-1)$...".
2. The heading of column 12 of Table 2 should read CdS(19).
3. Line 2 in the right-hand column on page 477 should read "...and in zinc [17] ...".
4. Expressions (2) and (3) should read

$$F(x) = \frac{5^5}{4!}x^4e^{-5x} \quad (2)$$

and

$$F_n(x) = \frac{n(nx)^{n-1}}{(n-1)!}e^{-nx}, \quad (3)$$

respectively.

1063-7745/03/4801-0165$24.00

Crystallography Reports, Vol. 48, No. 1, 2003, pp. 24–28. Translated from Kristallografiya, Vol. 48, No. 1, 2003, pp. 29–33.

STRUCTURE OF INORGANIC COMPOUNDS

Refinement of the Crystal Structure of $Na_2Ti_3O_7$

O. V. Yakubovich* and V. V. Kireev**

** Faculty of Geology, Moscow State University, Leninskie gory, Moscow, 119992 Russia*
e-mail: yakubol@geol.msu.ru
*** Shubnikov Institute of Crystallography, Russian Academy of Sciences, Leninskiĭ pr. 59, Moscow, 119333 Russia*

Received February 26, 2002

Abstract—The crystals of $Na_2Ti_3O_7$ were obtained by crystallization from flux. The structure of the compound was refined from X-ray diffraction data collected on a four-circle diffractometer (2θ/θ scanning technique, λMoK_α radiation, graphite monochromator, $\theta_{max} = 40°$). The crystals are monoclinic $a = 9.133(2)$ Å, $b = 3.806(1)$ Å, $c = 8.566(2)$ Å, $\beta = 101.57(3)°$, sp. gr. $P2_1/m$, $Z = 2$, $\rho_{calcd} = 3.435$ g/cm^3, $R = 0.035$, 1241 reflections with $I \geq 2\sigma(I)$. The geometric characteristics of the Ti-polyhedra are analyzed as to their positions in the trioctahedral ribbon. The polymorphism of the $\{Ti_3O_7\}^{2-}$ anionic radical in the structures of $Na_2Ti_3O_7$ and $PbTi_3O_7$ is described. The topology and dimensionality of the $\{Ti_3O_7\}^{2-}$ anionic radical are demonstrated to depend on the type of the large cations located at the lattice points of the hexagonal close packing characteristic of both structures. © *2003 MAIK "Nauka/Interperiodica".*

INTRODUCTION

A variety of compounds are known for the Na–Ti–O system. The crystal structures of more than ten sodium titanates were established. The $Na_2Ti_3O_7$ phase was among the first to be synthesized and structurally studied [1]. Its crystal structure was solved in 1961 with the use of experimental data obtained by the photographic method (*h*0*l* and *h*1*l* layer-line scanning, $R = 14.9\%$). The accuracy of this structure determination was low by modern standards. In addition, the data on atomic thermal motion as well as on the standard deviations of the atomic parameters and interatomic distances were lacking. This gave impetus to the refinement of the crystal structure of this phase. Below, we report the results of this refinement.

EXPERIMENTAL AND STRUCTURE REFINEMENT

Colorless transparent flattened-prismatic crystals of $Na_2Ti_3O_7$ with the longest dimension varying from 0.1 to 0.3 mm (Fig. 1) were obtained by crystallization from the flux of sodium titanogermanate Na_2TiGeO_5 [2]. The initial blend was prepared from stoichiometric amounts of Na_2CO_3, TiO_2, and GeO_2 by mixing and grinding in an agate mortar. Cooling of the melt was started at 950°C. Cooling at a high rate (15–50 K/h) led to the formation of cavities in a solidified material, in which crystals of sodium titanate were found. By contrast, only sodium titanogermanate crystallized upon slow cooling of the melt.

An X-ray spectral analysis (CamScan 4DV) of the crystals showed the presence of Na and Ti atoms in the compound under study. The unit-cell parameters and monoclinic system, which were determined by the Laue and oscillation technique on a RKOP camera, in combination with the results of X-ray spectral analysis made it possible to identify the crystals with $Na_2Ti_3O_7$.

The X-ray diffraction data for the structure refinement were collected on a four-circle SYNTEX $P\bar{1}$ diffractometer (MoK_α radiation) using the 2θ/θ scanning technique. The intensities of the reflections were corrected for the Lorentz and polarization factors.

All calculations were carried out with the use of the SHELXL program package [3]. The atomic scattering curves and anomalous dispersion corrections were taken from the International Tables for Crystallography [4]. The structure was refined anisotropically by the full-matrix least-squares method with the inclusion of absorption and isotropic secondary extinction. The crystallographic parameters of the phase, details of the

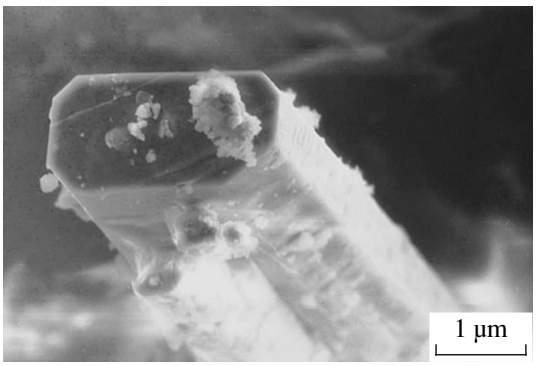

Fig. 1. Scanning electron microscope image of a crystal of $Na_2Ti_3O_7$.

X-ray diffraction study, and the characteristics of the structure refinement are given in Table 1. The coordinates of the base atoms and the equivalent thermal parameters are listed in Table 2. The interatomic distances are given in Table 3. The local valence balance on the anions [5] is presented in Table 4.

Table 1. Crystallographic data, characteristics of X-ray diffraction study, and details of structure refinement

Molecular formula	$Na_2Ti_3O_7$
Absorption μ, mm^{-1}	4.14
Space group	$P2_1/m$
Number of formula units Z	2
Unit-cell parameters, Å	
a	9.133(2)
b, β	3.806(1), 101.57(3)°
c	8.566(2)
Unit-cell volume V, $Å^3$	291.7(2)
Density ρ, g/cm^3	3.435
Diffractometer	SYNTEX $P\bar{1}$
Radiation	MoK_α (graphite monochromator)
T, K	293
θ_{max}, deg	40.00
Number of reflections: independent/observed with $I > 1.96\sigma(I)$	1244/1241
Mode of refinement	based on F^2
Number of parameters in the refinement	74
Absorption correction	DIFABS
T_{max}, T_{min}	1.000, 0.565
Extinction coefficient	0.006(1)
Reliability factors	
R (for observed reflections)	0.035
$wR2$ (for all independent reflections)	0.089
s	1.102
Residual electron density, $e/Å^3$:	
ρ_{max}	1.08 (1.29 Å from Ti(3))
ρ_{min}	–1.20 (0.59 Å from Ti(1))

RESULTS AND DISCUSSION

All atoms in the crystal structure of $Na_2Ti_3O_7$ occupy special positions on mirror planes in the space group $P2_1/m$. Three independent Ti atoms each have six anions in the nearest environment. The polyhedra around the Ti atoms can be interpreted as strongly distorted octahedra with the average Ti–O distances in the range of 1.98–1.99 Å. Three crystallographically independent edge-sharing octahedra are the building blocks of the structure. These blocks, related by symmetry elements, form ribbons with the thickness of three octahedra. The ribbons are extended approximately along the *b*-axis and can be considered a "section" of a close-packed layer with occupied octahedral cavities. The free oxygen vertices of the octahedra located at the edges of the ribbons are shared by the adjacent ribbons, giving rise to step-like layers parallel to the *ab*-plane. Translationally equivalent layered constructions of the Ti-octahedra are linked through the Na^+ cations along the *c*-axis (Fig. 2).

As mentioned in the monograph [6], the crystal structure of $Na_2Ti_3O_7$ is characterized by a very high degree of condensation of the polyhedra in the layers. Thus, four Ti-octahedra come together at each of two, out of a total of seven, oxygen vertices, namely, at the O(5) and O(7) vertices. The number of shared edges of the Ti-polyhedra reaches 6, i.e., one-half of all linear elements of the octahedron, which is in excess (from the viewpoint of the formal valence balance) of the allowable (according to Pauling) 25% limit of excessive valence on the oxygen atom. Hence, the crystal structure can be stabilized only at the expense of a strong distortion of the polyhedra. This construction cannot occur under the rather mild temperature and pressure conditions of Earth's crust. For this reason, crystal structures of minerals, in which four Ti-octahedra come together at a single oxygen vertex, are unknown [6].

The high degree of condensation of the Ti-octahedra in the $Na_2Ti_3O_7$ structure results from the ability of the Ti^{4+} cations to form essentially nonequivalent Ti–O bonds under special physicochemical conditions. The analysis of the deformation electron density distribution in the Ti-octahedra in titanite $CaTiSiO_5$ showed that the electron density peaks, which characterize the partial occupancy of the titanium *d* orbital, are shifted from the center of the coordination octahedron toward one of the oxygen vertices [7]. The redistribution of valence forces in the octahedron is manifested in a distortion of the polyhedra up to the formation of Ti-half-octahedra. This situation is also observed in the mineral natisite and its numerous structural analogues [8], as well as in sodium trititanate. In the structure of the latter compound, the above-mentioned distortion gives rise to the coordination polyhedra about the Ti(2) and Ti(3) atoms, which are more correctly interpreted as tetragonal pyramids than as octahedra.

Thus, the interatomic distances in the Ti(2)- and Ti(3)-polyhedra can be divided into three categories, namely, four distances, which vary from 1.958 to 2.089 Å for Ti(2) and from 1.953 to 2.026 Å for Ti(3), with one shortened distance characterizing the titanyl

Table 2. Coordinates of the basis atoms and equivalent thermal parameters (Å^2)

Atom	*x*/*a*	*y*/*b*	*z*/*c*	U_{eq}
Ti(1)	0.98502(7)	0.25	0.14606(7)	0.0043(1)
Ti(2)	0.67593(7)	0.25	0.24887(7)	0.0051(1)
Ti(3)	0.28030(7)	0.25	0.02857(7)	0.0046(1)
Na(1)	0.5929(3)	0.25	0.6830(2)	0.0253(5)
Na(2)	0.1553(2)	0.25	0.4999(2)	0.0167(4)
O(1)	0.1865(3)	0.25	0.2188(3)	0.0067(4)
O(2)	0.4612(3)	0.25	0.1465(3)	0.0088(5)
O(3)	0.6510(3)	0.25	0.4413(3)	0.0133(5)
O(4)	0.9081(3)	0.25	0.3246(3)	0.0068(4)
O(5)	0.7532(3)	0.25	0.0161(3)	0.0053(4)
O(6)	0.3182(3)	0.25	0.8035(3)	0.0066(4)
O(7)	0.0440(3)	0.25	0.9152(3)	0.0046(4)

Table 3. Interatomic distances (Å)

Atoms	Coordination polyhedron	Interatomic distances	
		ranges	average
Ti(1)–O	Octahedron	1.807(2)–2.186(2)	1.986
Ti(2)–O	Octahedron	1.709(3)–2.245(2)	1.990
Ti(3)–O	Octahedron	1.755(2)–2.181(3)	1.976
Na(1)–O	Nine-vertex polyhedron	2.238(3)–2.961(3)	2.729
Na(2)–O	Seven-vertex polyhedron	2.448(3)–2.725(3)	2.562

bond (1.709 and 1.755 Å for Ti(2) and Ti(3), respectively), and one elongated distance opposite to the titanyl bond (2.245 and 2.181 Å, respectively). The smaller Ti(2)–O(3) titanyl bond length (1.709 Å) as compared to the Ti(3)–O(2) bond length results from the fact that the O(3) vertex is pendant, i.e., it is not shared by other Ti-polyhedra in the layer. The O(2) vertex is shared by the Ti(2)- and Ti(3)-octahedra, due to which the Ti(3)–O(2) titanyl bond is elongated to 1.755 Å according to the requirement of the local valence balance on the O(2) atom (Table 4).

The character of distortion of the Ti(1)-polyhedron differs from the above-described distortions of the Ti(2)- and Ti(3)-octahedra. In the Ti(1)-polyhedron, the two Ti–O distances (1.979 Å) are close to the average distance in the polyhedron (Table 3). There are also two shortened (1.807 and 1.821 Å) and two rather long distances (2.148 and 2.186 Å). The redistribution of the valence forces responsible for this geometry of the Ti-polyhedra leads to the formation of a rather stable crystal structure, which is confirmed by the results of analysis of the local valence balance on the anions (Table 4).

The reasons for the difference in the character of the distortion of the Ti-octahedra in the structure of sodium trititanate can be revealed from the analysis of interactions between the polyhedra within the titanium–oxygen layers. As can be seen from Fig. 2, the polyhedron around the Ti(1) atom occupies the middle place in the ribbon with the thickness of three octahedra and has the maximum number of edges shared by other polyhedra of the ribbon. Since the Ti-ribbons are fragments of a closely packed octahedral layer, in which the distances between the centers of the edge-sharing octahedra are ~2.8 Å, the adjacent Ti atoms tend to be as far apart as possible due to Coulomb repulsions. Under the conditions of the octahedral close packing, this tendency is implemented via the displacement of the terminal Ti(2)

Table 4. Local valence balance on the anions

Atom	Ti(1)	Ti(2)	Ti(3)	Na(1)	Na(2)	Σ	δ
O(1)	0.952		0.607	0.113 × 2	0.154	1.939	0.061
O(2)		0.617	1.137	0.144 × 2		2.042	0.042
O(3)		1.290		0.192	0.140 × 2	1.952	0.048
				0.095 × 2			
O(4)	0.991	0.467			0.160	1.902	0.098
					0.142 × 2		
O(5)	0.381	0.318	0.663 × 2	0.098		2.123	0.123
O(6)		0.654 × 2	0.550	0.101	0.122	2.081	0.081
O(7)	0.629 × 2		0.379			2.056	0.056
	0.419						
							0.509

Note: $D = 0.509/14 \times 100\% = 3.6\%$.

and Ti(3) atoms in the ribbon from the centers of the octahedra toward the edges of the ribbon (shortened Ti(2)–O(3) and Ti(3)–O(2) interatomic distances, Table 3) to form pronounced titanyl bonds. The Ti(1) atoms occupying the middle positions in the trioctahedral ribbon tend to move away from the adjacent four Ti atoms. As a result, the Ti(1) atom is shifted to the O(1)–O(4) edge of the octahedron to form two shortened Ti(1)–O(1) and Ti(1)–O(4) bonds, as distinct from the Ti(2)- and Ti(3)-polyhedra, in which the titanium atoms are displaced to one of the vertices of the corresponding octahedra (Fig. 2).

The Na^+ cations located between the layers neutralize the anionic two-dimensional titanium–oxygen constructions. The Na(1) and Na(2) atoms are located in the centers of the nine- and seven-vertex oxygen polyhedra, respectively. The cation–oxygen interatomic distances in the Na(1)-polyhedron vary over a wider range (2.238–2.961 Å; the average value is 2.729 Å) than those in the Na(2)-polyhedron (2.448–2.725 Å; the average value is 2.562 Å).

The anionic titanium–oxygen radical in the crystal structure of $PbTi_3O_7$ (a = 10.718 Å, b = 3.812 Å, c = 6.577 Å, β = 98.27°, Z = 2) [9] is described by the same $\{Ti_3O_7\}$ formula as that in the structure of $Na_2Ti_3O_7$. The monoclinic structures of both titanates belong to the same space group $P2_1/m$, have close unit-cell volumes (266 and 292 $Å^3$, respectively), and have equal numbers of independent Ti and O atoms per unit cell. Like in the structure of sodium titanate, all atoms forming the crystal structure of lead titanate occupy mirror planes. Although these compounds differ substantially in the a and c parameters and the monoclinic angle, the b parameters of two titanates are equal to within 0.01 Å (Table 1).

Like the $Na_2Ti_3O_7$ structure, the crystal structure of $PbTi_3O_7$ is built from blocks consisting of three edge-sharing octahedra. However, each central octahedron of the triad in the structure of $Na_2Ti_3O_7$ shares two opposite edges with the adjacent octahedra to form linear trioctahedral fragments, whereas the central octahedron in the structure of $PbTi_3O_7$ shares two adjoining edges with the adjacent polyhedra to form angular constructions consisting of three octahedra (Fig. 3). The trioctahedral blocks adjacent along the b- and c-axes share edges to form layers with the thickness of two octahedra. Unlike the structure of the sodium titanate composed of the two-dimensional layered $\{Ti_3O_7\}_{\infty\infty}$ anionic radicals, the $PbTi_3O_7$ structure consists of the octahedral layers, which are linked through the vertices along the a-axis to form a three-dimensional framework. The cavities in the anionic framework, which is described by the same $\{Ti_3O_7\}_{\infty\infty\infty}$ formula, are occupied by large Pb^{2+} cations. The unit cell of $PbTi_3O_7$ contains half as many Pb^{2+} cations as the smaller lower-charged Na^+ cations located between the layers in the unit cell of $Na_2Ti_3O_7$.

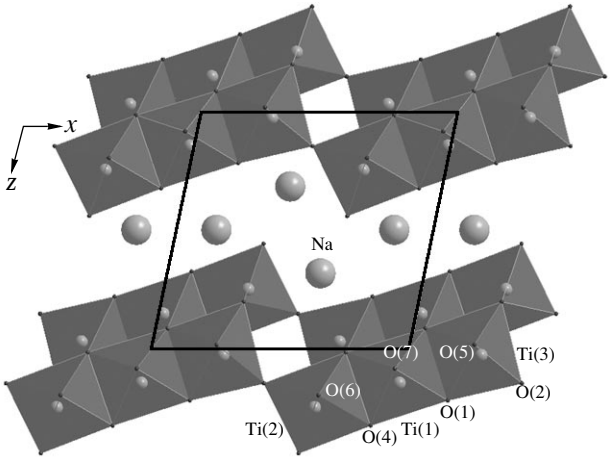

Fig. 2. Crystal structure of $Na_2Ti_3O_7$ projected onto the xz-plane.

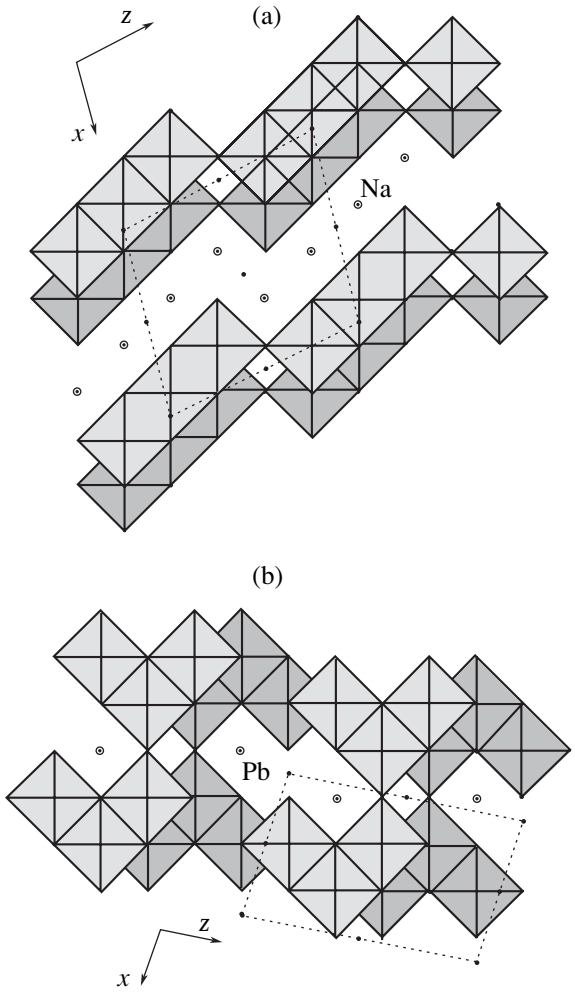

Fig. 3. Octahedral motifs of the Ti-octahedra in the idealized crystal structures of (a) $Na_2Ti_3O_7$ and (b) $PbTi_3O_7$ projected onto the square network. The O, Na, and Pb atoms occupy the lattice points of the hexagonal close packing. The unit cells are shown by dashed lines. The inversion centers are indicated by solid circles.

Polymorphism of the $\{Ti_3O_7\}^{2-}$ anionic radical, whose structure varies from two-dimensional (layered) to three-dimensional (framework), is determined by the type of cations neutralizing its charge. As demonstrated above, the replacement of two Na^+ cations in the unit cell by one Pb^{2+} cation leads to a change not only in the dimensionality of the anionic construction of octahedra but also to a change in its topology. When considering the arrangement of the oxygen atoms and large Na^+ and Pb^{2+} cations within the framework of a single system, one can see that they occupy the lattice points of the hexagonal close packing in both crystal structures. The close packing projected along the monoclinic axis (translation is 3.81 Å) appears as a square network (Fig. 3). The difference in the mode of occupancy of the octahedral cavities in the close packing by the Ti atoms is responsible for the difference in the crystal structures (layered sodium titanate $Na_2Ti_3O_7$ and framework lead titanate $PbTi_3O_7$).

ACKNOWLEDGMENTS

We are grateful to E.V. Guseva for performing X-ray spectral analysis.

This study was supported by the Russian Foundation for Basic Research, project nos. 00-05-64312 and 00-15-98582.

REFERENCES

1. S. Andersson and A. D. Wadsley, Acta Crystallogr. **14**, 1245 (1961).
2. V. V. Kireev, O. V. Yakubovich, A. K. Ivanov-Shits, *et al.*, Koord. Khim. **27** (1), 34 (2001).
3. G. M. Sheldrick, *SHELXL97: Program for the Refinement of Crystal Structures from Diffraction Data* (University of Göttingen, Göttingen, 1997).
4. *International Tables for Crystallography*, Ed. by T. Hahn (Kluwer, Dordrecht, 1995, 4th ed.), Vol. A.
5. Yu. A. Pyatenko, Kristallografiya **17** (4), 773 (1972) [Sov. Phys. Crystallogr. **17**, 677 (1972)].
6. Yu. A. Pyatenko, A. A. Voronkov, and Z. V. Pudovkina, *Mineralogical Crystal Chemistry of Titanium* (Nauka, Moscow, 1976).
7. V. S. Urusov, N. N. Eremin, and O. V. Yakubovich, Kristallografiya **40** (3), 485 (1995) [Crystallogr. Rep. **40**, 442 (1995)].
8. O. V. Yakubovich, V. V. Kireev, and O. K. Mel'nikov, Kristallografiya **45** (4), 635 (2000) [Crystallogr. Rep. **45**, 578 (2000)].
9. K. Kato, I. Kawada, and K. Muramatsu, Acta Crystallogr., Sect. B: Struct. Crystallogr. Cryst. Chem. **30**, 1634 (1974).

Translated by T. Safonova

Crystallography Reports, Vol. 48, No. 1, 2003, pp. 29–34. Translated from Kristallografiya, Vol. 48, No. 1, 2003, pp. 34–39.

STRUCTURE OF INORGANIC COMPOUNDS

Refinement of the Atomic Structure of Specimens Cut Out from Different Growth Pyramids of a $K(H_{0.052}D_{0.948})_2PO_4$ Single Crystal

L. F. Malakhova*, A. E. Voloshin*, C. C. Wilson, E. B. Rudneva*, N. G. Furmanova*, and V. I. Simonov***

** Shubnikov Institute of Crystallography, Russian Academy of Sciences, Leninskiĭ pr. 59, Moscow, 119333 Russia*

e-mail: malakhova@ns.crys.ras.ru

*** Rutherford Appleton Laboratory, Chilton, Didcot, UK*

Received September 9, 2002

Abstract—The structures of two crystalline specimens cut out from the pyramidal and prismatic growth sectors of a $K(H_{0.052}D_{0.948})_2PO_4$ single crystal have been studied by diffuse neutron scattering and precision diffuse X-ray scattering. Diffuse scattering is concentrated in the vicinity of the Bragg reflections and is practically the same in specimens cut out from different growth sectors of a single crystal. X-ray diffraction analysis using the extinction parameters provided the establishment of a higher perfection of the specimen cut out from the prismatic growth sector. The precision X-ray studies revealed different configurations of hydrogen bonds in the specimens. © *2003 MAIK "Nauka/Interperiodica".*

INTRODUCTION

Potassium dihydrophosphate KH_2PO_4 (KDP) and deuterated potassium dihydrophosphate (DKDP) crystals have attracted the attention of numerous researchers for more than 30 years. Deuterated single crystals with nonlinear optical characteristics are used in optical shutters and powerful laser systems for doubling their frequency. Thermonuclear reactions induced by laser irradiation require the use of perfect single crystals with a high deuteration degree and cross sections of 500×500 mm^2. High-quality single crystals of such dimensions are synthesized using the fast growth technology. It is well known that deuteration and high growth rates hinder the preparation of specimens possessing high optical quality. One has also to take into account the law of sectorial growth [1]. Different surfaces of single crystals grow at different rates. Different reticular densities of these faces lead to different mechanisms of impurity capture by growing faces and the formation of various defects in the crystal bulk which are different in different growth pyramids. Figure 1 shows a KDP crystal obtained by rapid growth technology and the corresponding X-ray topograph showing the boundaries between the pyramidal and prismatic growth sectors. In DKDP crystals, the degree of substitution of hydrogen by deuterium can also be different in different growth pyramids [2, 3]. The specimens cut out from different growth pyramids of a DKDP single crystal have considerably different optical and electrical characteristics [4, 5]. Detailed structural data on KDP and DKDP crystals and the corresponding bibliography can be found in [6].

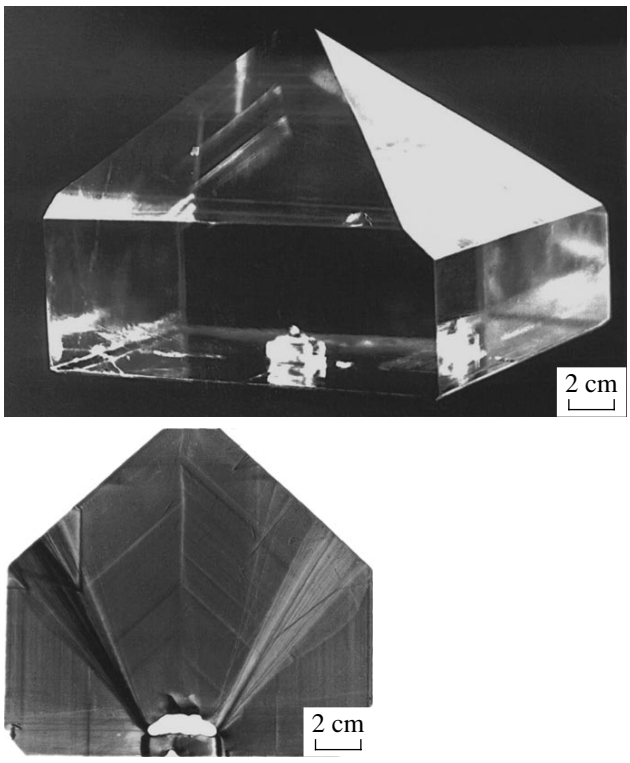

Fig. 1. KH_2PO_4 single crystal obtained by rapid-growth technology and the X-ray topograph of this crystal.

1063-7745/03/4801-0029$24.00 © 2003 MAIK "Nauka/Interperiodica"

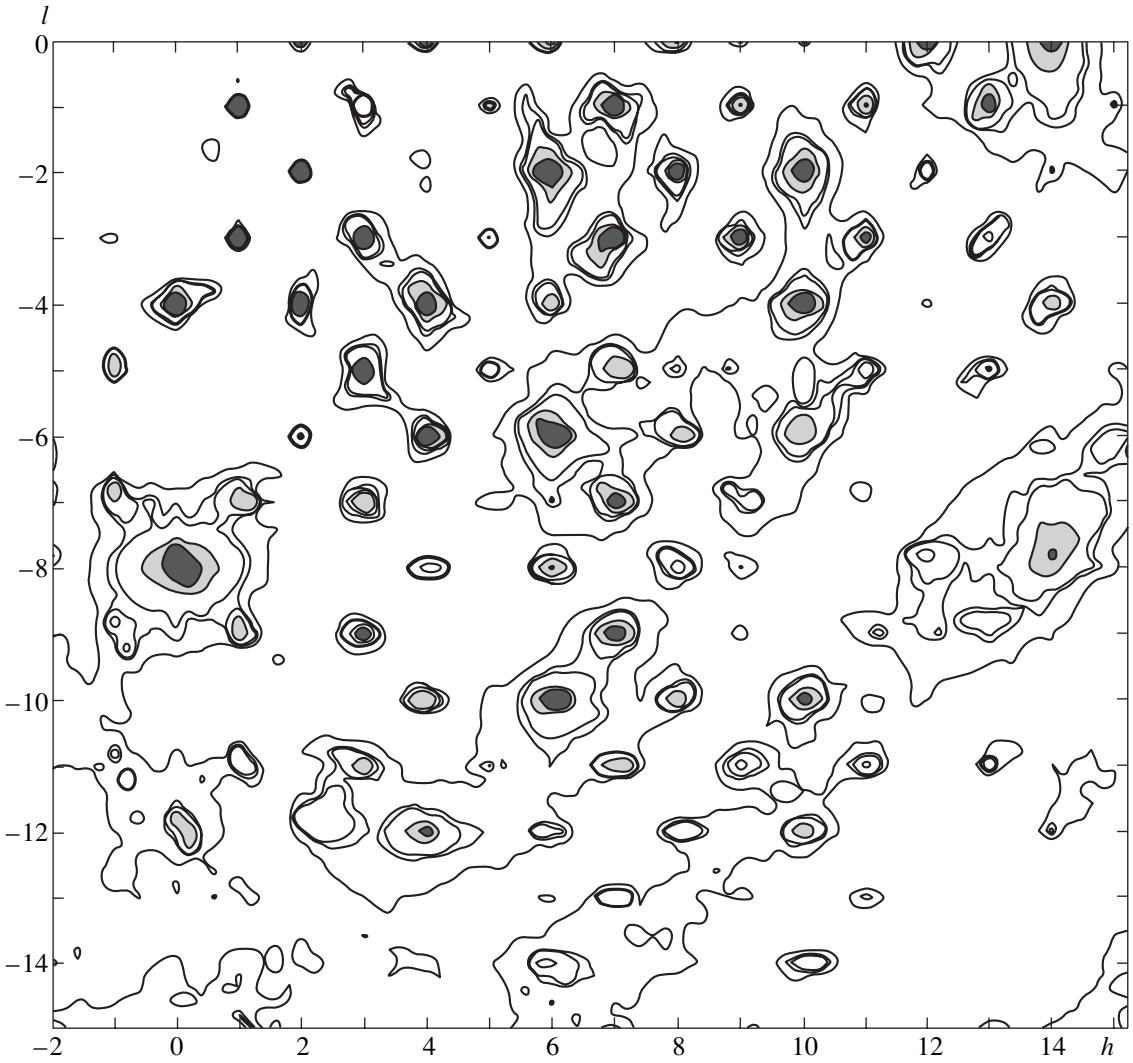

Fig. 2. Intensity distributions of the Bragg reflections and neutron diffuse scattering in the (*h*0*l*) plane of the reciprocal space of the specimen cut out from the pyramidal growth sector of a $K(H_{0.052}D_{0.948})_2PO_4$ single crystal.

The present article describes the precision structural studies of two specimens cut out from the pyramidal and prismatic growth sectors of one single crystal.

SPECIMENS

A large $K(H_{0.052}D_{0.948})_2PO_4$ single crystal was synthesized from solution in heavy water by rapid-growth technology. The average growth rate was 6.7 mm/day (24 h) along the [100] direction, 8.3 mm/day along the [010] direction, and 9 mm/day along the [001] direction. The studies were performed on the specimens cut out from the pyramidal and prismatic growth sectors as far as possible from the surface and the intersectorial boundaries. The specimen quality was checked by X-ray topography. The deuterium concentration was determined from the phase-transition temperature and was the same, within the accuracy of measurements (~0.1%), for the specimens cut out from both growth sectors.

The resistivities measured along the crystallographic *z* axis for the specimens from the prismatic and pyramidal growth sectors differed by a factor of 30, being 37 GΩ/cm and 1.3 GΩ/cm, respectively. The paraelectric tetragonal phase of the crystals was studied under atmospheric pressure at room temperature, sp. gr. $I\bar{4}2d$; the unit-cell parameters, $a = 7.470(3)$ Å and $c = 6.975(3)$ Å, were the same (within the measurement error) for both specimens.

DIFFUSE NEUTRON SCATTERING

Different properties of the specimens cut out from different growth pyramids of one single crystal indicate their different structures. Any distortions of the ideal periodic structure of the crystal result in the appearance

of the diffuse-scattering component on the corresponding diffraction patterns. For DKDP crystals, the distributions of hydrogen and deuterium can also be different in different growth sectors of the single crystal. Therefore, it was expedient to consider neutron diffuse scattering. The amplitudes of the neutron scattering from hydrogen and deuterium atoms have opposite signs. To analyze the distributions of hydrogen and deuterium atoms in different growth sectors, we prepared, in addition to the specimens cut out from a $K(H_{0.052}D_{0.948})_2PO_4$ single crystal, two similar specimens cut out from a single crystal with a lower deuterium content, $K(H_{0.327}D_{0.673})_2PO_4$. For neutron diffraction studies, we prepared the cylindrical specimens 10 mm in height and 8 mm in diameter. The long axis of the cylinders coincided with the *z* axis of the crystals.

The measurements were made on a SXD diffractometer with two-dimensional coordinate detector by the time-of-flight technique [7] at the pulse neutron source at the Rutherford Appleton Laboratory (UK). The scattered intensities were measured along the layer lines normal to the *y* axis of the crystal. The step along the reciprocal *h* and *l* axes was equal to 0.1. We measured the intensities along the layer lines $-6 \le k \le 6$. As an example, Fig. 2 shows the *h*0*l* line from the specimen cut out from the pyramidal growth sector of the single crystal containing 94.8% deuterium. The analysis of the diffuse-scattering intensities at all the measured points of the specimens cut out from different growth pyramids of a $K(H_{0.052}D_{0.948})_2PO_4$ single crystal showed their coincidence within the measurement error. A similar analysis for the specimens cut out from a single crystal with 67.3% deuterium was hindered because of the considerable background of incoherent neutron scattering from hydrogen atoms. However, in this case as well, we observed no considerable differences in the intensities of diffuse scattering from the specimens cut out from different growth pyramids of a $K(H_{0.327}D_{0.673})_2PO_4$ single crystal. In all the cases, diffuse scattering was observed in the vicinity of the Bragg maxima. The same neutron diffuse scattering from the specimens cut out from different growth sectors indicate that the defects in these DKDP specimens are of the same nature. The nature and the shape of such defects were studied in [8]. It is important that these defects in the specimens cut out from different growth pyramids are of the same nature and, thus, cannot be responsible for different physical properties of these specimens. The analysis of the intensities of the Bragg reflections on the neutron diffraction patterns showed their more pronounced difference for the specimens cut out from different growth sectors of a single crystal with 94.8% of deuterium. The precision structural studies of single crystals by the diffraction methods, should be made on a stationary source of radiation with fixed wavelength. Because of the pulsed source, different reflections are measured at different wavelengths, which requires the introduction of different individual corrections into the intensities of the primary radiation spectrum, extinction, and other experimental parameters. Therefore, further investigation was performed by the X-ray method.

Table 1. Parameters of the specimens and experiment

Characteristic	$K(H_{0.052}D_{0.948})_2PO_4$	
	prism	pyramid
a, Å	7.469	7.470
c, Å	6.974	6.975
V, Å^3	389.05	389.20
Number of reflections measured in two octants	1463	1445
R_{eq}, %	1.84	1.92
Number of independent reflections used in the refinement	525	504
Program	JANA 98	
Weighting scheme	$1/\sigma(F)^2$	
Number of the parameters to be refined	47	
Misorientation of the mosaics blocks $\times 10^{-4}$ rad	1.376	1.616
R/R_w,%	1.45/1.18	1.57/1.31

REFINEMENT OF STRUCTURAL MODEL

Using abrasive rolling, we obtained specimens of an almost spherical shape with the diameters of 0.16(1) and 0.15(1) mm for the specimens cut out from the

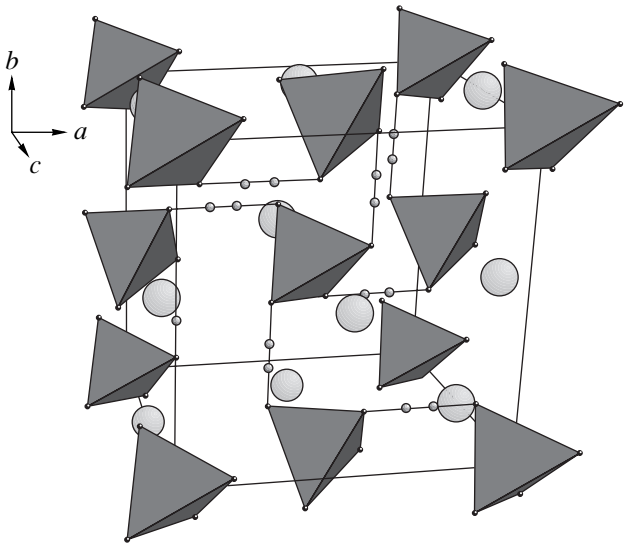

Fig. 3. KH_2PO_4 structure. One can see $[PO_4]$ tetrahedra, the positions of K atoms (large circles), and hydrogen bonds with (H,D) atoms (small circles).

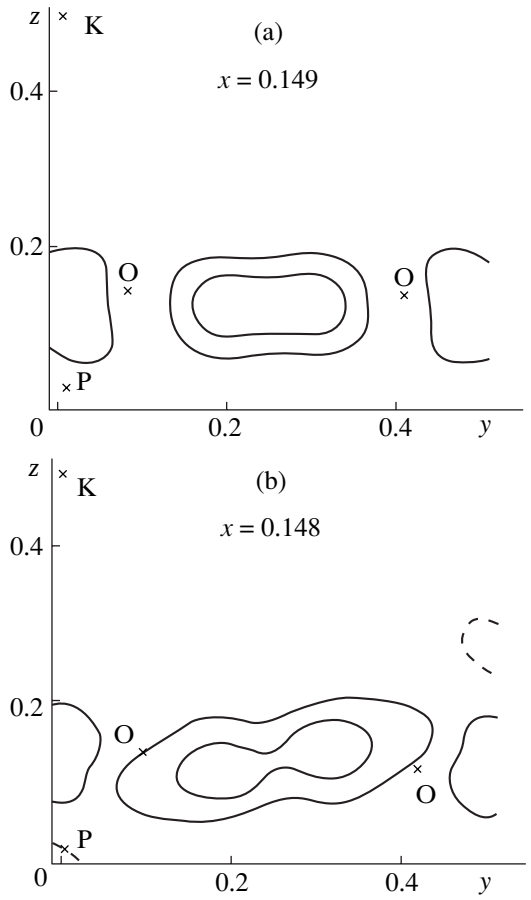

Fig. 4. Section of the difference electron-density distribution for the specimens cut out from the (a) prismatic and (b) pyramidal growth sectors of a $K(H_{0.052}D_{0.948})_2PO_4$ single crystal. Isolines are spaced by 0.1 e/Å^3.

pyramidal and prismatic growth sectors of a $K(H_{0.052}D_{0.948})_2PO_4$ single crystal, which allowed us to perform the precision X-ray analysis. The diffraction experiment was made on an Enraf-Nonius CAD-4f four-circle diffractometer (MoK_α radiation, graphite monochromator, $\omega/2\theta$ scan, $\sin\theta/\lambda \le 0.9$ Å^{-1}).

Stability of the diffractometer operation was controlled by regular measurements (once every hour) of the control reflection. All the stages of the measurements, processing of the experimental data, and the structural computations were performed in the same way for both specimens.

The experimental sets of integrated intensities of the reflections were corrected for the Lorentz and polarization factor and for absorption in a spherical specimen, $\mu = 1.635$ mm^{-1}. We also introduced corrections for the first- and the second-order thermal diffuse scattering [9] calculated with the elastic constants for KDP crystals [10]. The atomic factors and the corrections for anomalous scattering for neutral atoms were taken from the International Tables [11]. All the computations were performed by the JANA 98 complex of programs [12].

Table 1 lists the parameters of the specimens studied, the basic data concerning the experiment, and the characteristics of the models to be refined. The initial model for the refinement of the DKDP structure was taken from [6]. The KH_2PO_4 structure is based on rigid $[PO_4]$ tetrahedra forming an open three-dimensional framework connected by the net of hydrogen bonds, with potassium cations being located in the large cavities of this framework (Fig. 3).

At the first stage of the refinement, we used an abridged set of the experimental data in the range $0.5 \le \sin\theta/\lambda \le 0.9$ Å^{-1}. The corresponding amplitudes had almost no contributions from scattering by H and D atoms. Moreover, such a data set contains no reflections noticeably distorted by extinction. At this stage, we refined the coordinates of the basis O atom (the P and K atoms are located in the special positions having no parameters), the scale factor, the isotropic extinction parameter, and the atomic vibration parameter of the K, P, and O atoms. The thermal parameters were refined with due regard for anisotropy and the anharmonism of thermal vibrations. At this stage, we refined altogether 47 parameters using 239 and 433 independent structure factors for the specimens from the prismatic and pyramidal growth sectors of the $K(H_{0.052}D_{0.948})_2PO_4$ crystal, respectively. The concluding weighted reliability factors were 1.11 and 1.62% for the prismatic and the pyramidal growth sectors, respectively. At the next stage of the refinement, these structural parameters (except for the scale and extinction parameters) were fixed.

Thus, at the following stage, we refined only the scale and the extinction parameters over the whole set of reflections. Because of the strong correlation of these parameters, we used the method of step scanning [13] and excluded five reflections with the extinction parameter $y_{\min} \le 0.8$ from each set. The scale factor was varied and fixed at a step of 0.005. At each fixed value of the scale factor, the extinction parameter was refined. We selected as the solution the values corresponding to the minimum weighted reliability factor. At this stage, the minimum R_w values calculated over the whole set of reflections were 1.69 and 1.73% for the specimens cut out from the prismatic and pyramidal sectors, respectively.

For the reliable localization of H and D atoms, we constructed difference electron-density syntheses using the sets of the structure factors with $\sin\theta/\lambda \le 0.7$ Å^{-1}. The neglect of the high-angle reflections was justified by the practical absence of scattering from H and D atoms in these reflections. Figures 4a and 4b show the (yz) sections of these difference syntheses at the levels $x = 0.149$ and $x = 0.148$ for the specimens cut out from the prismatic and pyramidal growth sectors, respectively. It is in these sections that the maxima corresponding to (H,D) atoms lie. One can clearly see the split of the positions of these atoms into two potential wells with the equal (50%) occupancies.

The final refinement of the structure models was performed in the full matrix variant over the complete set of the experimental data, first, with the fixed position of (H,D) atoms. Then, the coordinates of the (H,D) atoms were refined at the fixed values of all the other parameters. The isotropic thermal parameter of the (H,D) atoms was refined separately at a step of 0.01 in the interval of the parameter values from 0.05 to 0.20. At this stage of the refinement, the conventional weighted reliability factors R/R_w for two specimens decreased to 1.45/1.18 and 1.57/1.31%, respectively. The results of the refinement are listed in Table 2.

DISCUSSION OF RESULTS

The diffraction quality of the specimen cut out from the prismatic growth sector of the single crystal was considerably higher than of the specimen cut out from the pyramidal growth sector, which is reflected in the reliability factors R_{eq} obtained upon averaging of the intensities of the symmetrically related reflections (Table 1). This also agrees with the well-known optical characteristics of such specimens [4]. When designing the experiments on neutron diffuse scattering, we expected to reveal a considerable difference in scattering from the specimens cut out from different growth pyramids. However, the most detailed analysis of the neutron scattering patterns practically in the whole three-dimensional reciprocal space showed that all the differences recorded at the points of measurements were within $3\sigma(I)$. In other words, diffuse scattering of neutrons is almost insensitive to the difference in the structures of the specimens studied. The recorded diffuse scattering is concentrated only in the vicinity of the Bragg maxima, which is associated with the disordered (statistical) distribution of H and D atoms over two positions with the same probabilities.

The X-ray diffraction studies of the specimens showed a noticeable difference in their extinction parameters. We considered various models allowance for extinction. The best results were obtained by allowance for extinction by the Becker–Coppens formalism, the model of type 1 with the approximation of the distribution of the blocks of the mosaics in accordance with the Lorentz function [14]. The extinction for the type-1model is determined by the parameter reflecting the characteristic of the real specimen associated with the misorientation of the mosaics blocks in the single crystal and not with their size distribution. For highly perfect DKDP crystals, including the specimens studied, the extinction parameter can be caused by distortion or bending of the planes due to elastic stresses in the crystal. Elastic stresses arise because of the nonuniform distribution of impurities or point defects formed during growth [15]. The refined extinction parameters of the specimens differed by 16%, with the minimum extinction being obtained for the specimen cut out from the prismatic growth sector, which indicated the lower degree of misorientation of the crystallographic planes.

Table 2. Results of the refinement of the structural parameters of the specimens cut out from a $K(H_{0.052}D_{0.948})_2PO_4$ single crystal

Atom	Characteristic	$K(H_{0.052}D_{0.948})_2PO_4$	
		prism	pyramid
O	x	.14888(7)	.14929(9)
	y	.08050(7)	.08036(8)
	z	.12504(9)	.12608(10)
	U_{11}	.01784(11)	.01772(12)
	U_{22}	.01840(11)	.01778(12)
	U_{33}	.02236(11)	.02214(12)
	U_{12}	.00179(10)	.00195(11)
	U_{13}	–.00577(12)	–.00600(13)
	U_{23}	–.00423(11)	–.00409(12)
H, D	x	.1485(22)	.1480(27)
	y	.2026(20)	.1896(18)
	z	.1284(35)	.1116(27)
	U_0	.13	.09
P	U_{11}	.01569(7)	.01472(8)
	U_{33}	.01835(20)	.01864(22)
K	U_{11}	.02401(7)	.02386(8)
	U_{33}	.01715(16)	.01675(19)
Interatomic distances, Å			
P–O		1.5359(6) × 4	1.5419(7) × 4
O–O in tetrahedron		2.4979(9) × 4	2.5103(10) × 4
		2.5323(8) × 2	2.5345(9) × 2
K–O		2.9049(6) × 4	2.8993(7) × 4
		2.8286(6) × 4	2.8233(7) × 4
O–(H, D)		0.9127(6)	0.8228(6)
O– – – – – –(H, D)		1.6201(6)	1.7200(6)
O–(H, D)–O		2.5286(8)	2.5330(10)
(H, D)–(H, D)		0.7092(0)	0.9204(0)
∠O H(D) O, deg		179.1	157.72

This agrees with the data on higher homogeneity of the specimens cut out from the prismatic growth sector than of those cut out from the pyramidal sectors of single crystals obtained by rapid-growth technology [3].

As is seen from Table 2, the P tetrahedra and K polyhedra in two specimens have almost the same geometries and dimensions. The only difference is observed in the configurations of their hydrogen bonds. The distances between the oxygen atoms bound by hydrogen bonds are rather close, 2.531 and 2.534 Å, respectively, but the ∠O(H,D)O angles (179.1° and 157.7°) and the O–H(D) distances are considerably different. The dif-

ference in the positions of (H,D) atoms is seen from Figs. 4a and 4b. The O(H,D)O angle in the specimen cut out from the prismatic growth sector is close to 180°. In the specimen cut out from the pyramidal growth sector, bending of hydrogen bonds is observed.

The amplitude ratio of the residual peak and the refined thermal parameters of hydrogen atoms for both specimens lead to the assumption that the occupancy of hydrogen positions in the prismatic growth sector can be slightly higher than in the pyramidal sector. Taking into account the real accuracy of our data, it is desirable to confirm this conclusion by neutron diffraction data for these single crystals, which should be obtained on a stationary reactor. Moreover, such data may also clarify the main cause of different electrical conductivities of the specimens.

ACKNOWLEDGMENTS

The authors are grateful to V.A. Kirikov for providing us with the data on the electric resistivity of the specimens. The study was supported by the Russian Foundation for Basic Research, project no. 00-02-17557, and the Federal Program on Support of Prominent Scientists and Leading Scientific Schools, project no. 00-15-96633.

REFERENCES

1. G. G. Lemmleĭn, *Sectorial Structure of Crystals* (Akad. Nauk SSSR, Moscow, 1948), p. 40.
2. A. S. Vasilevskaya, S. S. Gorbach, M. F. Koldobskaya, *et al.*, Kristallografiya **12**, 361 (1967) [Sov. Phys. Crystallogr. **12**, 308 (1967)].
3. A. É. Voloshin, E. B. Rudneva, I. L. Smol'skiĭ, *et al.*, in *To Centenary of G. G. Lemmleĭn: Physics of Crystallization, 2001*, p. 15.
4. É. P. Lokshin, Kristallografiya **41** (6), 1125 (1996) [Crystallogr. Rep. **41**, 1070 (1996)].
5. N. Zaitseva, L. Carman, I. Smolsky, *et al.*, J. Cryst. Growth **204**, 512 (1999).
6. R. J. Nelmes, Z. Tun, and W. F. Kuhs, Ferroelectrics **71**, 125 (1987).
7. C. C. Wilson, in *Workshop on Neutron Scattering Data Analysis, 1990*, Ed. by M. W. Johnson (Adam Hilger, Bristol, 1990), Inst. Phys. Conf. Ser., No. 107, p. 145.
8. N. M. Andrushevskiĭ, B. M. Shchedrin, L. F. Malakhova, and V. I. Simonov, Kristallografiya **47** (3), 518 (2002) [Crystallogr. Rep. **47**, 471 (2002)].
9. A. P. Dudka, M. Kh. Rabadanov, and A. A. Loshmanov, Kristallografiya **34** (4), 818 (1989) [Sov. Phys. Crystallogr. **34**, 490 (1989)].
10. E. M. Voronkova, B. N. Grechushnikov, G. I. Distler, and I. P. Petrov, *Optical Materials for Infrared Technology* (Nauka, Moscow, 1965).
11. *International Tables for Crystallography*, Ed. by A. J. C. Wilson (Kluwer, Dordrecht, 1992), Vol. C.
12. V. Petrichek and M. Duchek, *JANA 98: Crystallographic Computing System* (Institute of Physics, Academy of Sciences of the Czech Republic, Prague, 2000).
13. L. A. Muradyan, S. F. Radaev, and V. I. Simonov, *Methods of Structural Analysis* (Nauka, Moscow, 1989), p. 5.
14. P. J. Becker and P. Coppens, Acta Crystallogr., Sect. A: Cryst. Phys., Diffr., Theor. Gen. Crystallogr. **30**, 129 (1974); **30**, 148 (1974).
15. E. I. Suvorova and V. V. Klechkovskaya, Ferroelectrics **144**, 245 (1993).

Translated by L. Man

Crystallography Reports, Vol. 48, No. 1, 2003, pp. 35–38. Translated from Kristallografiya, Vol. 48, No. 1, 2003, pp. 40–43.

STRUCTURE OF INORGANIC COMPOUNDS

Crystal Structure of β'-$Zn_2V_2O_7$

T. I. Krasnenko, V. G. Zubkov, A. P. Tyutyunnik, L. V. Zolotukhina, and E. F. Vasyutinskaya

Institute of Solid State Chemistry, Ural Division, Russian Academy of Sciences, ul. Pervomaĭskaya 91, Yekaterinburg, 620219 Russia

e-mail: zolotukhina@ihim.uran.ru

Received June 30, 2000; in final form, February 2, 2001

Abstract—The crystal structure of the high-temperature modification of zinc pyrovanadate, namely, β'-$Zn_2V_2O_7$, is refined by the full-profile Rietveld method (GSAS) using the high-temperature X-ray diffraction data. The crystals are monoclinic (space group *C*2/*m*, *Z* = 2); the unit cell parameters are as follows: *a* = 6.9324(2) Å, *b* = 8.4394(2) Å, *c* = 5.0326(1) Å, and β = 108.272(2)°. Comparative analysis of the crystal structures of β'-$Zn_2V_2O_7$, β-$Mn_2V_2O_7$, and $Cd_2V_2O_7$ is performed. © *2003 MAIK "Nauka/Interperiodica".*

INTRODUCTION

It is known that zinc pyrovanadate crystallizes in two polymorphic modifications with a transition temperature in the range 608–620°C [1]. The low-temperature modification α-$Zn_2V_2O_7$ crystallizes in the monoclinic crystal system with the following unit-cell parameters: *a* = 7.429 Å, *b* = 8.340 Å, *c* = 10.098 Å, β = 111.37°, *Z* = 4, and space group *C*2/*c* [2]. Based on the melting behavior of zinc pyrovanadate, it was assumed that the high-temperature β modification crystallizes in the structural type of thortveitite. However, its complete crystal chemical identification is unavailable in the literature (in [3], only the interplanar spacings are reported).

We undertook this study in order to determine the crystal chemical parameters of the high-temperature modification of $Zn_2V_2O_7$.

EXPERIMENTAL

The high-temperature X-ray diffraction data were collected in air on a STADI-P instrument (STOE, Germany) in the Debye–Scherrer geometry using Cu$K_{\alpha 1}$ radiation. A polycrystalline sample, whose particles were 3–5 μm in size, was filled into a quartz capillary 0.3 mm in diameter. The temperature control was performed with an Eurotherm thermoregulator within ±0.1°. The diffraction data were collected with a PSD position-sensitive detector (the 2θ angle coverage is 43.5°, and the angular increment is 0.015°) in the 2θ range 12.34°–90°. The whole angular range was divided into the following four ranges: 12.34°–60°, 25°–75°, 45°–86°, and 58°–90°. In the calculations, the four diffraction files were used as sets of independent experimental data. The files were not merged into a common file because of the problems with the consideration for the effective sensibility from separate PSD parts. The profile-fitting program for the refinement of structural parameters using the full-profile Rietveld method (GSAS) operates simultaneously with several independent data sets [4]. The absorption μ*R* = 0.1 at a small distance *R* was obtained as a variable parameter in the refinement. This value corresponds to a sample density of approximately 0.08 g/cm^3.

RESULTS AND DISCUSSION

The X-ray diffraction data for the high-temperature modification of zinc pyrovanadate were obtained at 650°C. A comparison of our diffraction patterns with those obtained in [3] revealed that they are essentially

Table 1. Structural parameters of β'-$Zn_2V_2O_7$

Atom	Position	*x*/*a*	*y*/*b*	*z*/*c*	*N*	$U_{iso} \times 10^2$, Å^2
Zn	4*a*	0	0.31577(19)	1/2	1.0	3.89(7)
V	4*i*	0.21736(29)	0	0.9049(4)	1.0	2.50(9)
O(1)	2*a*	0	0	0	1.0	4.97(12)
O(2)	8*j*	0.2151(7)	0.1519(6)	0.7085(10)	1.0	4.97(12)
O(3)	4*i*	0.4091(11)	0	0.2050(16)	1.0	4.97(12)

Note: Space group *C*2/*m*; *a* = 6.9324(2) Å, *b* = 8.4394(2) Å, *c* = 5.0326(1) Å, β = 108.272(2)°, *V* = 279.59(1) Å^3.

1063-7745/03/4801-0035$24.00 © 2003 MAIK "Nauka/Interperiodica"

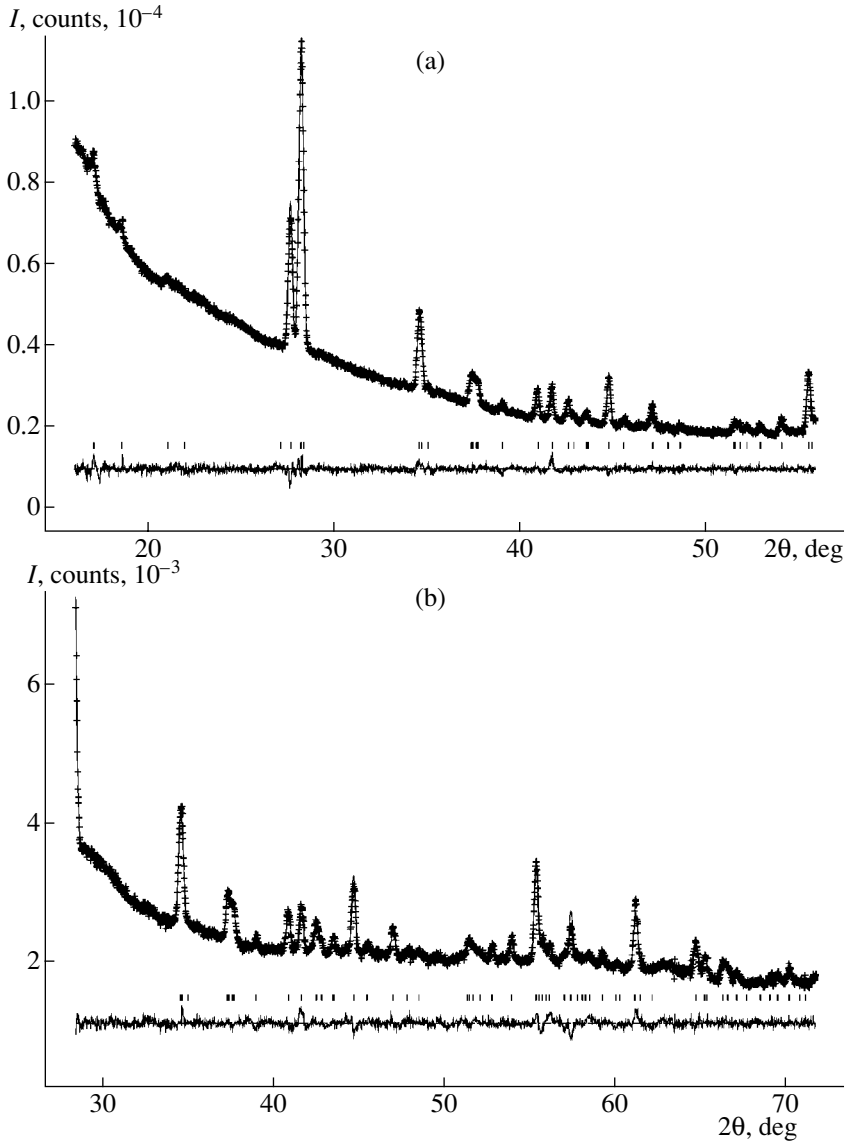

Fig. 1. Observed (crosses), calculated (solid line), and difference (at the bottom) diffraction patterns obtained in the refinement of the crystal structure of β'-$Zn_2V_2O_7$ in different angle ranges: (a) 12.34°–60°, (b) 25°–75°, (c) 45°–86°, and (d) 58°–90°.

different. For this reason, the $Zn_2V_2O_7$ high-temperature modification studied in the present work was designated as β'. The data on the crystal structure of β-$Mn_2V_2O_7$ (space group *C*2/*m*, *Z* = 2) [5, 6] were used as the starting model. For simplicity, we assumed that the individual isotropic thermal parameters of the three independent oxygen atoms were identical. The refinement converged at wR_p = 1.64, R_p = 1.22%, *DWd* = 0.561, $R(F^2)$ = 4.49%, and χ^2 = 0.8908.

The observed, calculated, and difference curves obtained in the structure refinement are shown in Fig. 1. The results of the full-profile refinement of the crystal structure of β'-$Zn_2V_2O_7$ are given in Table 1. Note that the thermal parameters U_{iso} have elevated values. For most of oxide compounds, $U_{iso} \le 0.012$ Å^2. The U_{iso} values obtained in this study at 650°C lie between 0.025 and 0.05 Å^2. These values indicate that the lattice of β'-$Zn_2V_2O_7$ approaches the limit of its stability and that, with further heating, it should either transform into another modification or melt.

Figure 2 shows the projections of the crystal structure of β'-$Zn_2V_2O_7$ onto the *ac* and *ab* planes. The zinc atoms have a sixfold coordination, and the vanadium atoms are coordinated by the four nearest oxygen atoms. The structure consists of double vanadium–oxygen tetrahedra, which are linked into the centrosymmetric [V_2O_7] diortho groups, and infinite columns of zinc–oxygen edge-shared polyhedra. The central fragment of the diortho group is linear [the V–O(1)–V angle is 180°], and the distances between the vanadium atom and the bridging oxygen atom [V–O(1)] are the longest in the structure. The flat V–O(1)–V angles are

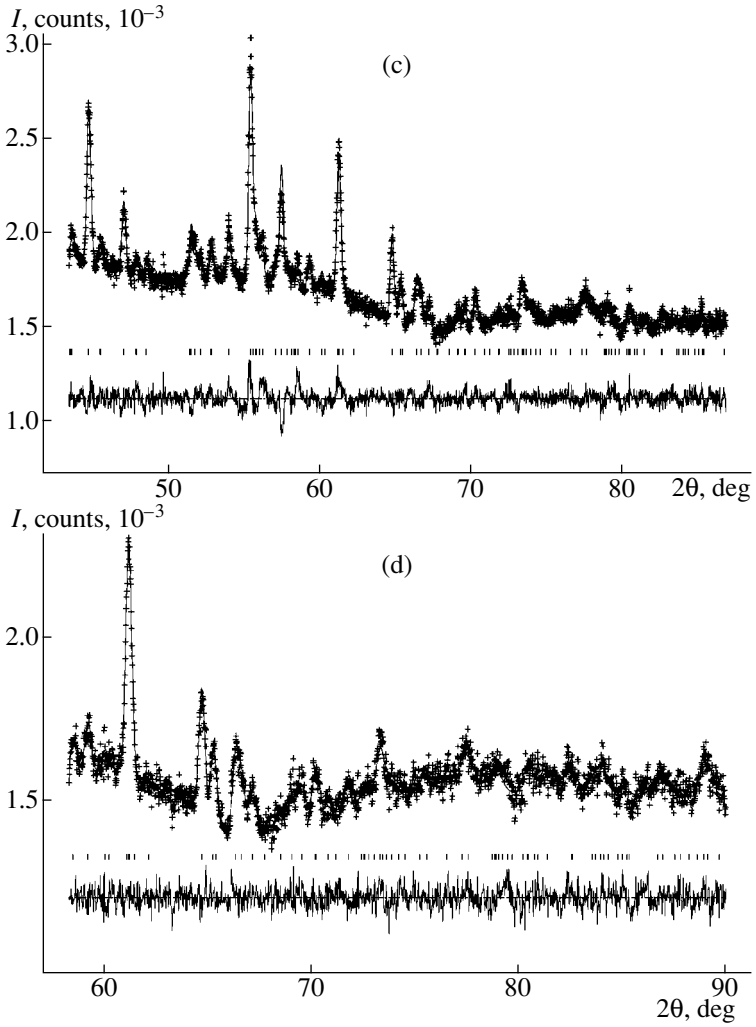

Fig. 1. (Contd.)

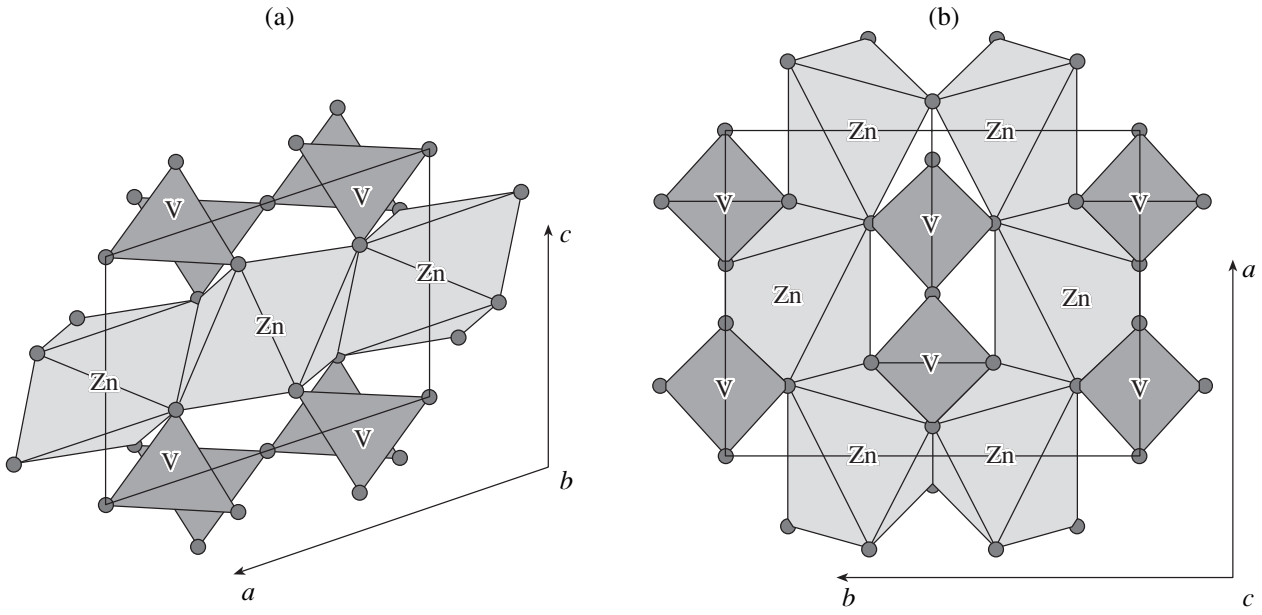

Fig. 2. Projection of the crystal structure of β'-$Zn_2V_2O_7$ onto the (a) *ac* and (b) *ab* planes.

Table 2. Interatomic distances (Å) in β'-$Zn_2V_2O_7$, β-$Mn_2V_2O_7$, and $Cd_2V_2O_7$

β'-$Zn_2V_2O_7$		β-$Mn_2V_2O_7$ [5]		$Cd_2V_2O_7$ [8]	
Zn polyhedron		Mn polyhedron		Cd polyhedron	
Zn–O(2)	2.063(5) × 2	Mn–O(2)	2.125 × 2	Cd–O(2)	2.236(4) × 2
Zn–O(2')	2.525(5) × 2	Mn–O(2')	2.304 × 2	Cd–O(2')	2.398(4) × 2
Zn–O(3)	2.105(5) × 2	Mn–O(3)	2.217 × 2	Cd–O(3)	2.278(3) × 2
Mean	2.231	Mean	2.215	Mean	2.304
V polyhedra					
V–O(1)	1.7182(19)	V–O(1)	1.759	V–O(1)	1.757(1)
V–O(2)	1.616(5) × 2	V–O(2)	1.680 × 2	V–O(2)	1.694(4) × 2
V–O(3)	1.670(7)	V–O(3)	1.703	V–O(3)	1.704(5)
Mean	1.655	Mean	1.706	Mean	1.712

characteristic of the compounds isostructural with the $Sc_2Si_2O_7$ thortveitite [7], among which are the β-$Mn_2V_2O_7$ [5] and $Cd_2V_2O_7$ [8] pyrovanadates.

The main interatomic distances in β'-$Zn_2V_2O_7$ were calculated using the data presented in Table 1 (Table 2). The interatomic distances in β-$Mn_2V_2O_7$, which were calculated based on the coordinates reported in [5] and our results obtained earlier for $Cd_2V_2O_7$ [8], are also included in this table.

In all the pyrovanadates under discussion, two of the six oxygen atoms are located at much longer distances from the bivalent metal than the other oxygen atoms. The degree of distortion of the metal–oxygen polyhedra (Δ_{Me}) was evaluated as the relative difference between the longest and shortest bonds and amounted to 8.4% for β-$Mn_2V_2O_7$, 22.4% for β'-$Zn_2V_2O_7$, and 27.4% for $Cd_2V_2O_7$. The Δ_{Me} value is directly proportional to the mean values of interatomic distances, which, in turn, determine the volumes of "soft" metal–oxygen polyhedra. The degrees of distortion of the vanadium–oxygen polyhedra (Δ_V) in the above series are 4.7, 6.3, and 3.7%, respectively. The absence of correlation between the degrees of distortion of the metal–oxygen and vanadium–oxygen polyhedra can be associated with the necessity of compensating the bond valence at the oxygen atoms, which is achieved through the variation in the V–O bond lengths.

Moreover, we believe that the crystallometric characteristics of the "soft" polyhedra determine the melting temperatures of these compounds: the longer the maximal metal–oxygen bond in the compounds, the lower the melting temperature (890°C for β'-$Zn_2V_2O_7$, 1020°C for $Cd_2V_2O_7$, and 1080°C for β-$Mn_2V_2O_7$ [9]).

ACKNOWLEDGMENTS

This study was supported by the Russian Foundation for Basic Research, project no. 98-03-32542A.

REFERENCES

1. V. A. Makarov, A. A. Fotiev, and L. N. Serebryakova, Zh. Neorg. Khim. **16** (10), 2849 (1971).
2. R. Gopal and C. Calvo, Can. J. Chem. **51** (7), 1004 (1973).
3. J. J. Brown and F. A. Hummel, Trans. Br. Ceram. Soc. **64** (8), 419 (1965).
4. A. C. Larson and R. B. von Dreele, "GSAS" LANSCE, MS-H805 (Los-Alamos National Laboratory, Los Alamos).
5. E. Dorm and B. O. Marinder, Acta Chem. Scand. **21**, 590 (1967).
6. A. G. Nord, Neues Jahrb. Mineral., 283 (1984).
7. D. W. I. Cruickshank, H. Zynton, and G. A. Barclay, Acta Crystallogr. **15**, 491 (1962).
8. E. V. Sokolova, Yu. K. Egorov-Tismenko, M. A. Simonov, and T. I. Krasnenko, Kristallografiya **31** (6), 1222 (1986) [Sov. Phys. Crystallogr. **31**, 722 (1986)].
9. A. A. Fotiev, B. V. Slobodin, and M. Ya. Khodos, *Vanadates* (Nauka, Moscow, 1988).

Translated by I. Polyakova

Crystallography Reports, Vol. 48, No. 1, 2003, pp. 39–43. Translated from Kristallografiya, Vol. 48, No. 1, 2003, pp. 44–48.

STRUCTURE OF INORGANIC COMPOUNDS

Crystal Structure of Li_2MgSiO_4

L. D. Iskhakova* and V. B. Rybakov**

** Fiber Optics Research Center, Institute of General Physics, Vavilova ul. 38, Moscow, 119992 Russia*

e-mail: ldisk@fo.gpi.ru

*** Department of Chemistry, Moscow State University, Vorob'evy gory, Moscow, 119992 Russia*

Received March 21, 2002

Abstract—The crystal structure of Li_2MgSiO_4 was established by single-crystal X-ray diffraction analysis. The crystals are monoclinic, a = 4.9924(7) Å, b = 10.681(2) Å, c = 6.2889(5) Å, β = 90.46(1)°, Z = 4, sp. gr. $P2_1/n$, V = 335.54 Å^3, R = 0.062. In a Li_2MgSiO_4 crystal, four types of independent T(1–4) tetrahedra share vertices to form a three-dimensional framework. Three of these tetrahedra are occupied simultaneously by Li and Mg cations, which corresponds to the crystallochemical formula $(Li_{0.98}Mg_{0.02})(Li_{0.80}Mg_{0.20}) \cdot (Li_{0.22}Mg_{0.78})SiO_4$. In slightly distorted SiO_4 tetrahedra denoted as T(1), the average Si–O distance is 1.635(2) Å. The distortions of other tetrahedra and the average (Li_xMg_{1-x})–O distances increase with an increase in lithium content. These distances in the T(2), T(3), and T(4) tetrahedra are 1.955(2), 1.971(4), and 2.019(6) Å, respectively. The structure of the new compound is compared with the crystal structures of other $Li_2M^{2+}SiO_4$ compounds and the luminescence spectra of $Cr^{4+} : Li_2MgSiO_4$. © *2003 MAIK "Nauka/Interperiodica".*

INTRODUCTION

Among chromium-activated materials for solid-state lasers tunable in the near-IR range, the $Cr^{4+} : Li_2MgSiO_4$ single crystals are of particular interest, because they are characterized by the maximum luminescence lifetime (100 and 400 μs at 300 and 50 K, respectively [1]). The luminescence lifetimes of other $Cr^{4+} : Li_2M^{2+}XO_4$ compounds (X = Si or Ge) are also pronounced (70, 45, and 40 μs for $Cr^{4+} : Li_2MgGeO_4$, $Cr^{4+} : Li_2ZnSiO_4$, and $Cr^{4+} : Li_2ZnGeO_4$, respectively [2]). Today, no single crystals of optical quality of this promising material are available, because all the attempts to determine the conditions for growth of bulk crystals have failed. Moreover, the crystallization process is hindered by a reversible polymorphic transformation (at 871 K) of Li_2MgSiO_4 from the monoclinic to the high-temperature orthorhombic modification [3] isostructural to Li_2MgGeO_4 [4]. This explains the insufficient study of the spectral-luminescence and laser characteristics of Li_2MgSiO_4 crystals. As was mentioned in [5], it is difficult to interpret the spectroscopic characteristics of $Cr^{4+} : Li_2MgSiO_4$ because of the lack of information on its structure. Therefore, the present study was aimed at the establishment of the crystal structure of Li_2MgGeO_4.

EXPERIMENTAL

In the X-ray diffraction study, we used a fragment of a Li_2MgSiO_4 single crystal grown from flux [3] and ground to a pseudospherical shape with a diameter of 0.3 mm. The parameters of the monoclinic unit cell were refined based on 25 high-angle reflections using the standard software for a CAD4 diffractometer [6] (Table 1). The X-ray data were collected on the same diffractometer (λMoK_α, graphite monochromator, $\omega/2\theta$ scan). A total of 2191 nonzero independent reflections were recorded in the range $0° \le \theta \le 40°$ ($-9 \le h \le 9$, $-7 \le k \le 19$, $0 \le l \le 11$). The preliminary processing of the X-ray data was performed using the WinGX98 program package [7].

Since the unit-cell metrics of Li_2MgSiO_4 is analogous to that of $Zn(Zn_{0.1}Li_{0.6}Si_{0.3})SiO_4$ [8] (Table 1), we used the coordinates of the Si atom of this lithium zinc silicate to solve the structure of Li_2MgSiO_4. The coordinates of all the oxygen atoms were determined from a series of successive difference Fourier syntheses. After the refinement of the oxygen–silicon motif, the positions of the Li^+ and Mg^{2+} cations in the T(2–4) tetrahedra were localized. The positional and thermal parameters of all the atoms and the occupancies of the T(2–4) positions by lithium and magnesium cations were refined anisotropically by the full-matrix least-squares method using the SHELX97 program package [9] (spherical absorption correction, μ = 0.73 mm^{-1}, 1773 reflections with $I > 2\sigma(I)$, R = 0.062, wR = 0.071, s = 1.070).

The atomic coordinates are given in Table 2. The principal interatomic distances and bond angles are listed in Table 3.

Table 1. Unit-cell parameters of Li_2MXO_4 and M_2XO_4 crystals

Compound	Unit-cell parameters				Sp. gr.
	a, Å	*b*, Å	*c*, Å	β, deg	
Li_2MgSiO_4*	4.9924(7)	10.681(2)	6.2889(5)	90.46(1)	$P2_1/n$
Li_2MgSiO_4 [3]	4.9946(7)	10.688(2)	6.2915(5)	90.479(9)	$P2_1/n$
Li_2MgSiO_4**	5.0042(2)	10.6847(8)	6.3171(2)	90.40(2)	$P2_1/n$
$Zn(Li_{0.6}Zn_{0.1}Si_{0.3})SiO_4$ [8]	5.011(1)	10.516(2)	5.011(1)	90.50(2)	$P2_1/n$
Mg_2SiO_4**	4.7553(4)	10.1960(9)	5.9820(4)		*Pbnm*
$CaMgSiO_4$ [10]	4.816(1)	10.987(3)	6.7773(7)		*Pbnm*
Li_2MgGeO_4 [4]	5.123(3)	10.796(3)	6.224(3)		*Pbnm*
Ca_2GeO_4**	5.2420(5)	11.4002(9)	6.7773(7)		*Pbnm*

* This study ($Z = 4$, $V = 335.34$ Å^3, $\rho_{calcd} = 2.58$ g/cm^3).
** Our experimental data obtained in the X-ray diffraction study of the single crystals grown at the Fiber Optics Research Center of the Institute of General Physics.

RESULTS AND DISCUSSION

In a Li_2MgSiO_4 crystal, four types of independent $T(1–4)O_4$ tetrahedra share vertices to form a three-dimensional framework (figure). All the oxygen atoms have a coordination number of four and are shared by four types of the *T*(1–4) tetrahedra. A slightly distorted *T*(1) tetrahedron is formed about the silicon atom. Its average geometric characteristics are identical to those of the SiO_4^{4-} tetrahedron in the forsterite structure Mg_2SiO_4 [11]. Three other tetrahedra, namely, *T*(2–4), are occupied by lithium and magnesium atoms in accordance with the crystallochemical formula $(Li_{0.98}Mg_{0.02})(Li_{0.80}Mg_{0.20})(Li_{0.22}Mg_{0.78})SiO_4$. The average *T*(2–4)–O distances increase with the lithium content in the tetrahedron, and the tetrahedra become more distorted, as is seen from the difference in the interatomic distances and bond angles (Table 3). The *T*(*i*)–*T*(*j*) contacts between cations vary from 2.671 to 3.092 Å. In the Li_2MgSiO_4 structure, the shortest Si–Si distances (4.093 and 4.098 Å) are much longer than those in the structure of the lasing material forsterite (3.631×2 Å).

Table 2. Atomic coordinates ($\times 10^4$) and equivalent isotropic thermal parameters U_{eq}, Å^2 ($\times 10^3$)

Atom	*x*	*y*	*z*	U_{eq}
T(1) (Si)	1857(2)	4131(1)	2584(1)	8(1)
T(2) $(Li_{0.22}Mg_{0.78})$*	1917(3)	1646(1)	14(2)	6(1)
T(3) $(Li_{0.80}Mg_{0.20})$*	1927(8)	1639(4)	4990(6)	13(1)
T(4) $(Li_{0.98}Mg_{0.02})$*	2917(14)	4253(6)	7596(10)	19(2)
O(1)	8586(4)	4087(2)	2549(3)	8(1)
O(2)	2112(5)	577(2)	2514(3)	10(1)
O(3)	2947(4)	3408(2)	4666(3)	8(1)
O(4)	2921(4)	3398(2)	421(3)	9(1)

* The occupancies of the positions were determined within an accuracy of ±0.01.

The Li_2MgSiO_4 structure can be described as a monoclinically distorted motif of its orthorhombic modification isostructural to Li_2MgGeO_4 [4]. One position with multiplicity 8 in the orthorhombic structure of lithium magnesium germanate corresponds to two different positions, *T*(2) and *T*(3), with multiplicities 4 in the monoclinic silicate structure. It has been mentioned [4] that the tetrahedral positions in Li_2MgGeO_4 can simultaneously be occupied by lithium and magnesium cations. Since the occupancies of the positions were not refined, and both (Li,Mg)–O distances [1.94(4) and 1.96(4) Å] are virtually equal within the experimental error, one cannot conclude that lithium cations predominantly occupy one of these positions. The Li_2MgSiO_4 structure differs from the structure of lithium zinc silicate [8] because of different distributions of cations over the tetrahedral *T*(2), *T*(3), and *T*(4) positions, with the SiO_4 tetrahedral motif being the same in both structures. In the structure of lithium zinc silicate, the *T*(2) tetrahedron is occupied by zinc cations alone, the *T*(3) tetrahedron is occupied by all the three types of cations [0.1Zn + 0.6Li + 0.3Si], whereas the *T*(4) position remains vacant. The occupancies of the positions were not refined, and the formula was written in accordance with the electron-probe microanalysis and emission-spectroscopy data. However, the calculation of the valence balance for the $Zn(Zn_{0.1}Li_{0.6}Si_{0.3})SiO_4$ structure according to a valence-force model [12] showed that the proposed composition and the distribution of cations in the structure lead to a deficiency of the valence forces at oxygen atoms ($\sum S_{ij}$ from 1.69 to 1.90 valence units). A much better correspondence was

Table 3. Principal interatomic distances and bond angles

T(1) tetrahedron		*T*(2) tetrahedron		*T*(3) tetrahedron		*T*(4) tetrahedron	
Bond	*d*, Å	Bond	*d*, Å	Bond	*d*, Å	Bond	*d*, Å
Si–O(1)	1.635(2)	*T*(2)–O(1)	1.931(2)	*T*(3)–O(1)	1.964(4)	*T*(4)–O(1)	1.927(7)
Si–O(2)	1.628(2)	*T*(2)–O(2)	1.945(2)	*T*(3)–O(2)	1.929(4)	*T*(4)–O(2)	2.103(8)
Si–O(3)	1.646(2)	*T*(2)–O(3)	1.993(2)	*T*(3)–O(3)	1.968(4)	*T*(4)–O(3)	2.052(7)
Si–O(4)	1.630(2)	*T*(2)–O(4)	1.953(2)	*T*(3)–O(4)	2.020(5)	*T*(4)–O(4)	1.992(7)
$[Si–O]_{av}$	1.635	$[T(1)–O]_{av}$	1.956	$[T(3)–O]_{av}$	1.970	$[T(4)–O]_{av}$	2.018
Angle	ω, deg	Angle	ω, deg	Angle	ω, deg	Angle	ω, deg
O(1)–Si–O(2)	110.1(1)	O(1)–*T*(2)–O(2)	113.1(1)	O(2)–*T*(3)–O(1)	114.0(2)	O(1)–*T*(4)–O(2)	107.9(3)
O(1)–Si–O(3)	107.4(1)	O(1)–*T*(2)–O(3)	109.6(1)	O(1)–*T*(3)–O(3)	110.9(2)	O(1)–*T*(4)–O(3)	111.6(3)
O(1)–Si–O(4)	109.2(1)	O(1)–*T*(2)–O(4)	112.3(1)	O(1)–*T*(3)–O(4)	107.2(2)	O(1)–*T*(4)–O(4)	117.5(3)
O(2)–Si–O(3)	110.6(1)	O(2)–*T*(2)–O(3)	96.6(1)	O(2)–*T*(3)–O(3)	117.9(2)	O(3)–*T*(4)–O(2)	90.1(3)
O(2)–Si–O(4)	109.9(1)	O(2)–*T*(2)–O(4)	116.6(1)	O(2)–*T*(3)–O(4)	98.5(2)	O(4)–*T*(4)–O(2)	93.9(3)
O(4)–Si–O(3)	109.5(1)	O(4)–*T*(2)–O(3)	107.2(1)	O(3)–*T*(3)–O(4)	106.8(2)	O(4)–*T*(4)–O(3)	126.6(3)
$[O(i)–Si–O(j)]_{av}$	109.4	$[O(i)–T(2)–O(j)]_{av}$	109.2	$[O(i)–T(3)–O(j)]_{av}$	109.2	$[O(i)–T(4)–O(j)]_{av}$	107.9

achieved under the assumption that the lithium content in the *T*(3) position is higher and, correspondingly, the silicon content is lower, so that the formula can be written as $(Li_{1.4}Zn_{0.1}Si_{0.1})ZnSiO_4$. The relatively high inaccuracy of the analytical determination of lithium content allowed us to conclude that the lithium content in the compound was higher than was reported in [8] and that this silicate was a representative of a series of double silicates $Li_{2+2x}Zn_{1-x}SiO_4$ (occurring in the range $-0.5 < x < +0.5$) studied by West [13] and did not belong to substituted zinc silicates. In most of the studies of $Li_2M^{2+}XO_4$ (see, e.g., [14, 15]), it was assumed that the compounds of this class could not be nonstoichiometric with respect to X^{4+}-cations. However, the smaller distortion of a *T*(3) tetrahedron compared to the distortion of the *T*(2) tetrahedron and, in particular, lower angular distortions in the $Zn(Zn_{0.1}Li_{0.6}Si_{0.3})SiO_4$ structure [7], can be explained only by the presence of the Si^{4+} cations in this position and their stabilizing effect on the geometric parameters of the tetrahedron. Hence, the structures of this class of compounds can be nonstoichiometric with respect to quadruply charged cations.

According to West [13], the $Li_{2+2x}Mg_{1-x}SiO_4$ compounds with $x = 0.2$, 0.4, and 0.6 exist. The differences in the unit-cell parameters of the Li_2MgSiO_4 single crystals, grown from flux using various solvents and lithium oxide concentrations exceeds the thrice error in their values (Table 1). Taking into account that lithium and magnesium cations have close ionic radii, the above-mentioned fact does not exclude the possibility of the deviation of the composition of lithium magnesium silicate from the Li_2MgSiO_4 stoichiometry.

Our study allows us to establish a certain correlation between the structural characteristics of Li_2MgSiO_4 and the luminescence spectra of quadruply charged chromium in $Cr^{4+} : Li_2MgSiO_4$. The Li_2MgSiO_4 structure can have at least two luminescence centers. Undoubtedly, these are a *T*(1) tetrahedron and, probably, also *T*(2) and *T*(3) tetrahedra. The incorporation of Cr^{4+} in the *T*(4) tetrahedron is less probable because of a large difference between the *T*(4)–O distance (2.018 Å) and the Cr^{4+}–O bond length in the structures with tetrahedrally coordinated chromium atoms (1.78 Å) [16, 17]. The presence of at least two luminescence centers is consistent with the fact that the damping curve is described by two exponents [5]. According to [5], the *Dq*/*B* ratio (the ratio of the crystal field strength *Dq* to the Rakah parameter *B*) in the luminescence spectra of $Cr^{4+} : Li_2MgSiO_4$ is larger than the *Dq*/*B* ratio in the spectra of $Cr^{4+} : Mg_2SiO_4$, which is attributed, among other factors, to the lower *B* parameter for lithium magnesium silicate because of a higher degree of covalence of the Cr–O bonds in the compound under study. In fact, as follows from the degree of covalence and the effective charges estimated from the structural data in [17], the effective charges at oxygen atoms in the Li_2MgSiO_4 structure are lower than those in Mg_2SiO_4.

The Li_2MgSiO_4 structure, like $Li_2M^{2+}XO_4$ structures (M^{2+} = Mg, Zn, or Co; *X* = Si or Ge), is based on the γ-Li_3PO_4 structure motif [14, 15]. The polymorphism characteristic of this group of compounds is associated with the fact that the tetrahedral positions can be occupied by the Li^+ and M^{2+} cations either statistically or orderly, the vacancies in the tetrahedral positions, and the types of the occupied position. The polymorphism

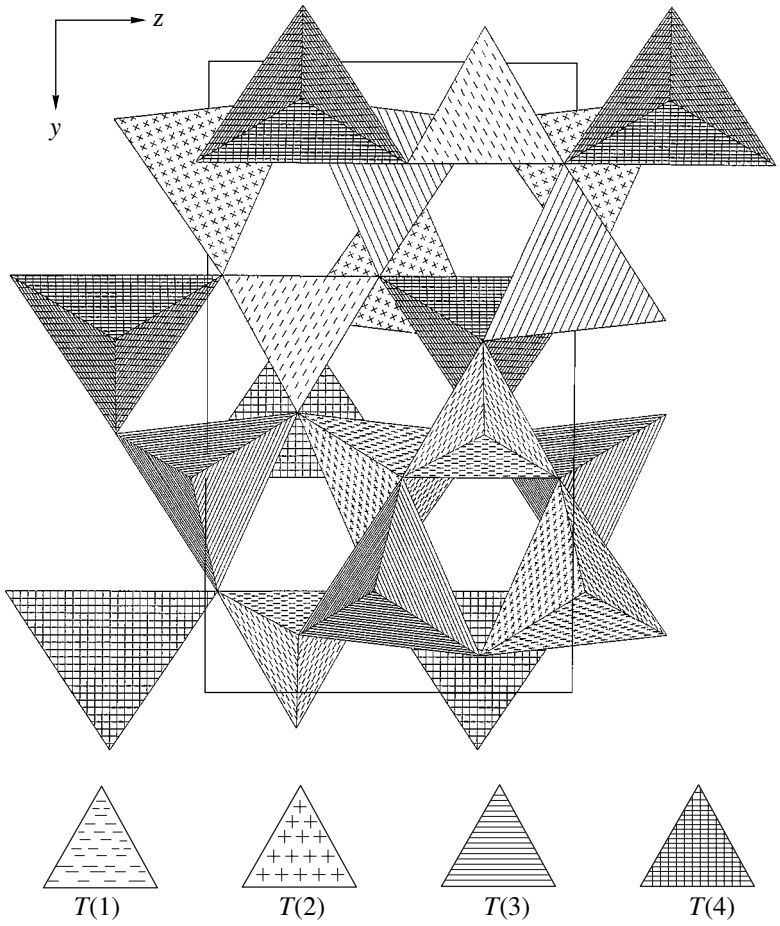

Crystal structure of Li_2MgSiO_4 projected onto the (100) plane.

is one of the facts that result in the failure of all the attempts of growing single crystals of high optical quality of these compounds. The change in the character of the cation distribution over the structure positions in the course of polymorphic transformations, taking place upon lowering of the temperature during the growth process, can give rise to twinning and formation of domain structure in the crystal bulk. Moreover, the attempts to find solvents that would provide the growth of bulk crystals of $Li_2M^{2+}XO_4$ from flux also failed.

In this connection, it seems reasonable to grow these promising Cr^{4+}-activated lasing materials as their films. Single-crystal films of Cr^{4+} : Ga_2GeO_4 were grown on single-crystal substrates of inactivated calcium germanate [19]. It is advantageous to use the forsterite Mg_2SiO_4 single crystal substrates for growth of Cr^{4+} : Li_2MgSiO_4 films, because the corresponding procedure is well developed and ensures growth of high-quality films. Also, one can use the substrates from single crystals of montichellite $CaMgSiO_4$ [10] isostructural to forsterite. The structures of forsterite and Li_2MgXO_4 can be described by a two-layer hexagonal close packing of oxygen atoms, in which the tetrahedral cavities are occupied by the X^{4+} cations. Their unit cells are transformed into the pseudohexagonal unit cells by the matrix

$$\begin{Vmatrix} 0 & 1/2 & -1/2 \\ 0 & 0 & 1 \\ 1 & 0 & 0 \end{Vmatrix}.$$

In the Li_2MgXO_4 structures (X = Si or Ge), the Li and Mg cations are located in the tetrahedral cavities. In the forsterite structure, the M^{2+} cations occupy two positions octahedrally surrounded by oxygen atoms. The unit-cell metrics of forsterite is similar to that of Li_2MgSiO_4. The difference in the unit-cell parameters of lithium magnesium silicate and montichellite $CaMgSiO_4$ (Table 1) is even less. Thus, one can hope that high-quality films can be obtained. Moreover, such films can be obtained at temperatures lower than those used for growth of single crystals, which can be expected to be lower than the phase transition temperatures.

ACKNOWLEDGMENTS

We are grateful to V.V. Dozmarov for providing us with Li_2MgSiO_4 single crystals.

This study was supported by the Russian Foundation for Basic Research, project no. 98-02-17340.

REFERENCES

1. V. V. Dozmarov, V. N. Protopopov, L. D. Iskhakova, and E. M. Dianov, in *Proceedings of the International Conference on Coherent and Nonlinear Optics, Moscow, 1998*, p. 39.
2. V. Petrićević, A. B. Bykov, A. Seas, *et al.*, in *Abstracts of the Conference on Lasers and Electrooptics, 1997*, p. 489.
3. V. V. Dozmarov, L. D. Iskhakova, Yu. A. Velikodnyĭ, *et al.*, Kristallografiya **45** (6), 1146 (2000) [Crystallogr. Rep. **45**, 1059 (2000)].
4. B. Monnaye, Rev. Chim. Miner. **13**, 422 (1976).
5. C. Anino, J. Thery, and D. Vivien, Opt. Mater. **8**, 121 (1997).
6. *Enraf-Nonius CAD-4 Software. Version 5.0* (Enraf-Nonius, Delft, The Netherlands, 1989).
7. L. J. Farrugia, *WinGX98: X-ray Crystallographic Programs for Windows* (University of Glasgow, Glasgow, 1998).
8. Shu-cheng Yu, D. K. Smith, and S. B. Asterman, Am. Mineral. **63**, 1241 (1978).
9. G. M. Sheldrick, *SHELX97: Program for the Solution and Refinement of Crystal Structures* (University of Göttingen, Göttingen, 1997).
10. K. A. Soubbotin, E. V. Zharikov, L. D. Iskhakova, and S. V. Lavrishchev, Kristallografiya **46** (6), 1115 (2001) [Crystallogr. Rep. **46**, 1030 (2001)].
11. J. R. Smyth and R. M. Hazen, Am. Mineral. **58**, 588 (1973).
12. V. A. Efremov, Doctoral Dissertation in Chemistry (Moscow, 1993).
13. A. R. West, PDF, Card Nos. 24-676–24-686, 34-1231; 24-629–24-637.
14. A. R. West and F. P. Glasser, J. Solid State Chem. **4**, 20 (1972).
15. A. R. West, Z. Kristallogr. **141**, 422 (1975).
16. J. A. Gard and A. R. West, J. Solid State Chem. **7**, 422 (1973).
17. K. A. Wilhelm, Ark. Kemi **26**, 157 (1967).
18. V. V. Zuev, *Constitution and Properties of Minerals* (Nauka, Leningrad, 1990).
19. O. N. Gorshkov, E. M. Dianov, N. B. Zvonkov, *et al.*, Pis'ma Zh. Tekh. Fiz. **27** (17), 1 (2001) [Tech. Phys. Lett. **27**, 709 (2001)].

Translated by T. Safonova

Crystallography Reports, Vol. 48, No. 1, 2003, pp. 44–48. Translated from Kristallografiya, Vol. 48, No. 1, 2003, pp. 49–53.

STRUCTURE OF INORGANIC COMPOUNDS

New Hilgardite-Group Polyborate $Pb_2[B_5O_9]Br$ with High Optical Nonlinearity

E. L. Belokoneva*, Yu. K. Kabalov*, O. V. Dimitrova*, and S. Yu. Stefanovich**

** Faculty of Geology, Moscow State University, Leninskie gory, Moscow, 119992 Russia*
e-mail: elbel@geol.msu.ru
*** Karpov Research Institute of Physical Chemistry, ul. Vorontsovo pole 10, Moscow, 103064 Russia*
Received March 22, 2002

Abstract—New anhydrous lead borate $Pb_2[B_5O_9]Br$ (sp. gr. *Pnn*2) was synthesized by the hydrothermal method. The second harmonic generation from polycrystalline samples of $Pb_2[B_5O_9]Br$ is characterized by a higher signal than that observed in powdered LiB_3O_5. The crystal structure of the new hilgardite-group compound was refined by the Rietveld method. Analysis of the known orthorhombic polar varieties of hilgardites, including the new compound, showed that their boron–oxygen frameworks are occupied by the Pb^{2+}, Ca^{2+}, Eu^{2+}, and Ba^{2+} cations; the Cl^-, Br^-, and OH^- anions; and water molecules in combinations determined by their sizes. © *2003 MAIK "Nauka/Interperiodica".*

INTRODUCTION

Although some Pb-containing borates showed promise as nonlinear optical materials, conditions of their preparation, structures, and properties have not been adequately explored. This group includes a few compounds. Of eight known representatives, four compounds exhibit substantial optical nonlinearity, namely, PbB_4O_7 [1], $Pb_5B_3O_8(OH)_3H_2O$ [2], orthorhombic polar hilgardite $Na_{0.5}Pb_2[B_2O_9]Cl(OH)_{0.5}$ [3], and nonaborate $Pb_3(OH)[B_9O_{16}][B(OH)_3]$ [4], which is transformed into PbB_4O_7 upon heating. The group of pentaborates involves a series of polar modifications belonging to a single polytypic hilgardite *OD* family [5]. These are two natural Ca borates with the space groups *Aa* [6] and *P*1 [7] and two synthetic Ca and Eu borates with the space group *Pnn*2 [8, 9]. This study was aimed at the directed synthesis of new Pb-containing varieties of the polar modifications belonging to this family, which have promise as nonlinear optical materials for the transformation of the laser frequency in the UV region. The goal of the study was also to examine the conditions of their formation, determine their crystal structures, and reveal composition–structure–properties relationships.

EXPERIMENTAL

Lead borates were synthesized in the $PbO–B_2O_3–H_2O$ system by the hydrothermal method in standard Teflon-lined autoclaves. Although the conditions for the formation of the natural chloroborates of the hilgardite family correspond to chloride brines [6, 7], the synthetic procedures were developed for the preparation of polar bromine-containing compounds [8, 9]. To search for new hilgardite-like polar compounds, we simulated the physicochemical conditions of their natural formation by varying the main blend composition, as well as the amount and type of the mineralizer. For this purpose, the hydrothermal experiments were carried out with the addition of alkali chlorides, bromides, and iodides to carbonate solutions. The blends were composed of oxide mixtures. The synthesis under mild conditions at 30–300 atm for 20 days at 250°C afforded colorless transparent crystals. Most experiments produced either small prismatic or thin needle-like crystals. In all syntheses, small-size crystals (up to fine-grain powders) were obtained.

The syntheses with the use of alkali bromides gave rise to isometric well-faceted transparent crystals with shiny faces. However, these crystals were too small for single-crystal X-ray analysis. The powder X-ray diffraction pattern of these crystals (DRON-UM1, Co radiation, 40 kV, 25mA) was similar to the pattern of EuB_5O_9Br [9] available in the PDF Database. This was indicative of the formation of a new variety of orthorhombic hilgardite, in which the divalent europium ions are replaced by lead ions.

The test for the second harmonic generation (SHG) in the samples was performed in the reflection mode using a pulsed YAG : Nd laser according to a procedure described in our earlier studies [3, 4]. The second-harmonic intensity $I_{2\omega}$ was measured with respect to a reference powdered sample of α-quartz. The ratio of the signals of the sample under examination and α-quartz was equal to 300, which was unambiguously indicative of the absence of the inversion center in the crystals under examination. The second harmonic signal of the new specimen was approximately three times higher than that of powdered crystals of LiB_3O_5 ($I_{2\omega}$ = 80–

Table 1. Crystallographic data, characteristics of X-ray diffraction study, and details of structure refinement of $Pb_2[B_5O_9]Br$ by the Rietveld method

Characteristic	Value
Unit-cell parameters	
a, Å	11.524(1)
b, Å	11.431(1)
c, Å	6.5399(3)
V_0, Å^3	861.51(1)
Number of formula units, Z	4
Space group	$Pnn2$
2θ range, deg	12–120
Asymmetry, 2θ, deg	60
Number of Bragg reflections	1415
Number of parameters in the refinement	92
R_p, %	1.82
R_{wp}, %	2.35
R_B, %	2.40
R_F, %	2.22
S*	1.19
DWD**	1.58

* Goodness of fit.
** Statistics according to Durbin–Watson.

Table 2. Atomic coordinates and thermal parameters B_j (Å^2) for the $Pb_2[B_5O_9]Br$ structure

Atoms	x/a	y/b	z/c	B_j
Pb(1)	0.2607(4)	0.0425(2)	0	0.53(8)
Pb(2)	0.0280(2)	0.2337(4)	0.663(1)	1.2(1)
Br(1)	0	0	0.893(5)	0.8(6)
Br(2)	0	0.5	0.626(6)	0.8(5)
O(1)	0.247(3)	0.317(2)	0.59(1)	0.3(7)
O(2)	0.209(2)	0.426(2)	0.179(2)	1.0(7)
O(3)	0.276(2)	0.226(2)	0.253(9)	0.7(6)
O(4)	0.078(2)	0.268(3)	0.241(9)	1.0(8)
O(5)	0.286(3)	0.455(2)	0.853(8)	1.3(8)
O(6)	0.388(2)	0.266(3)	0.842(7)	0.2(7)
O(7)	0.184(2)	0.272(2)	0.932(9)	0.3(7)
O(8)	0.418(2)	0.213(2)	0.50(1)	0.5(6)
O(9)	0.238(3)	0.116(2)	0.570(9)	0.7(6)
B(1)	0.275(5)	0.325(4)	0.80(2)	1(1)
B(2)	0.187(4)	0.298(2)	0.16(2)	1(1)
B(3)	0.296(5)	0.217(4)	0.48(2)	1(1)
B(4)	0.461(5)	0.235(6)	0.70(2)	1(1)
B(5)	0.250(6)	0.497(3)	0.03(2)	1(1)

Table 3. Selected interatomic distances (Å) in the $Pb_2[B_5O_9]Br$ structure

Pb(1)-polyhedron		Pb(2)-polyhedron		B-triangles	
Pb(1)–O(1)	2.65(3)	Pb(2)–O(1)	2.73(4)	B(4)–O(4)	1.37(4)
O(2)	2.51(8)	O(3)	2.99(3)	O(6)	1.30(8)
O(3)	2.68(5)	O(4)	2.85(7)	O(8)	1.42(9)
O(5)	2.57(8)	O(6)	2.65(5)	B(5)–O(2)	1.37(7)
O(6)	3.12(4)	O(7)	2.55(5)	O(5)	1.30(8)
O(7)	2.81(4)	O(8)	2.62(8)	O(9)	1.40(3)
O(9)	2.95(6)	O(9)	2.83(3)		
Br(1)	3.12(1)	Br(1)	3.08(1)		
Br(2)	2.92(1)	Br(2)	3.07(1)		
B-tetrahedra					
B(1)–O(1)	1.43(7)	B(2)–O(2)	1.49(3)	B(3)–O(1)	1.48(5)
O(5)	1.52(3)	O(7)	1.54(4)	O(3)	1.47(8)
O(6)	1.49(4)	O(3)	1.45(5)	O(8)	1.42(4)
O(7)	1.48(5)	O(4)	1.40(5)	O(9)	1.47(5)

100 units of SiO_2), which is the currently most efficient nonlinear-optical borate [10].

Earlier, crystals of natural polar Ca-hilgardite with the space group Aa were tested for SHG with the use of a Nd : glass laser [6]. Taking into account that the intensity of the signal was comparable with that of quartz, it was concluded that these crystals exhibit weak optical nonlinearity. The second harmonic generation ($I_{2\omega}$ = 10–12 units of SiO_2) from crystals of $Ba_2[B_5O_9]Cl \cdot 0.5H_2O$, which belong to the hilgardite family and have a structure analogous to the structures described in the

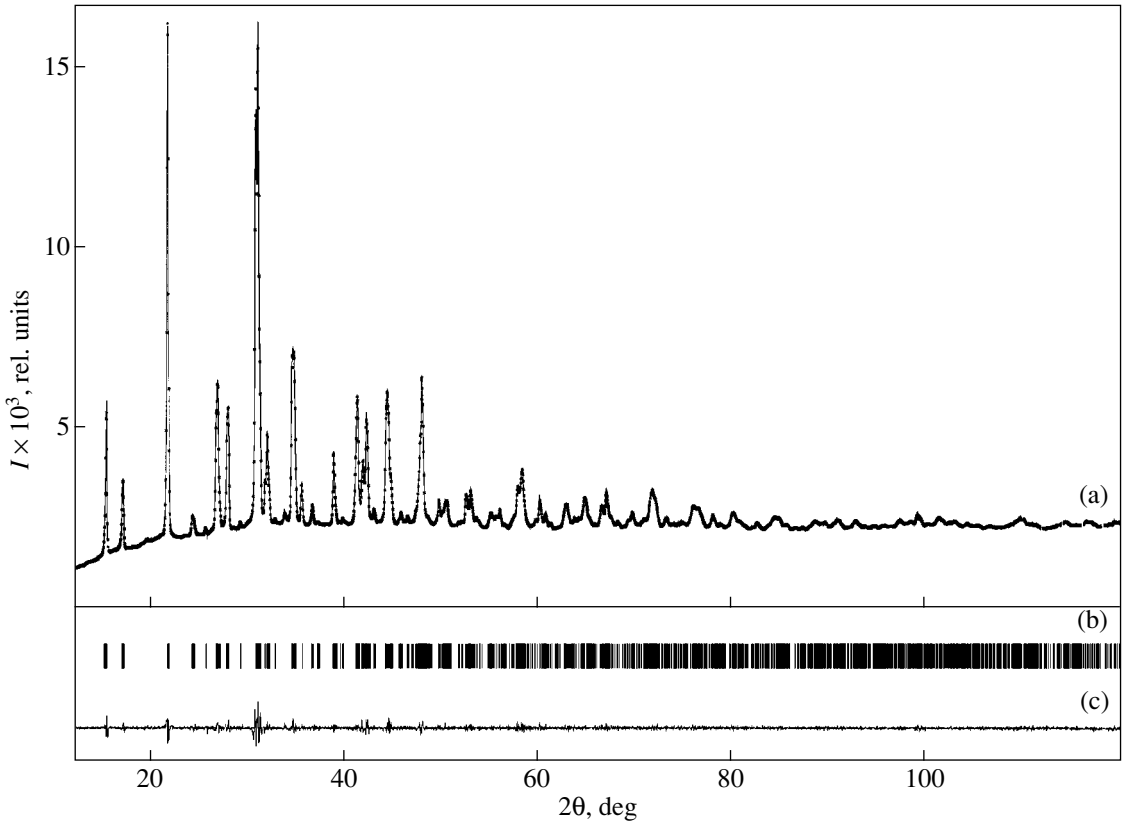

Fig. 1. X-ray diffraction spectrum of $Pb_2[B_5O_9]Br$; (a) experimental (solid curve) and theoretical (asterisks) values; (b) positions of Bragg reflections; (c) the difference spectrum.

studies [3, 8, 9], is an order of magnitude higher [11]. The new Pb,Br-hilgardite synthesized in this study exhibits the most pronounced nonlinear optical properties.

The structure of the new borate was studied by the Rietveld method. The X-ray diffraction spectrum of a powdered sample was measured on an ADP-2 diffractometer (λCu-K_α radiation, Ni filter) using the 2θ scanning technique with a scan step of 0.02° (the exposure time at each point was 15 s). All calculations were carried out with the use of the WYRIET program (version 3.3) [12]. The structure was refined within the space group *Pnn*2. The atomic coordinates of $Eu[B_5O_9]Br$ [9] were used as the starting model. The details of X-ray diffraction study and structure refinement are given in Table 1. The final X-ray diffraction spectrum is shown in Fig. 1. The atomic coordinates and interatomic distances are listed in Tables 2 and 3, respectively.

The peak profiles were approximated by the Pearson VII function with 6FWHM, where FWHM is the average peak width at half-height. The ionic scattering curves were used. The refinement was carried out with the gradual addition of the parameters and the continuous graphical modeling of the background. The refinement of the correction for texture effects with the use of the March–Dollase function demonstrated that the texture of the sample was insignificant. The positions of the Pb and Br atoms were refined with anisotropic thermal parameters. The equivalent isotropic thermal parameters of these atoms are given in Table 2. The refinement of the thermal parameters of the O and B atoms was hampered by the influence of the heavy atoms, the pseudosymmetry of the structure, the acentricity of the space group, and a large number of the parameters in the refinement, which was at the limits of the method. As a result, the resulting individual thermal parameters are at a level of one standard deviation and are approximately equal to 1 Å^2 for each of sort atom.

RESULTS AND DISCUSSION

Among polytypic *OD* modifications of hilgardite, orthorhombic hilgardites were obtained only by synthetic methods, whereas natural specimens are lacking. Four varieties were described in the literature. The new (fifth) synthetic hilgardite $Pb_2[B_5O_9]Br$ has a structure typical of orthorhombic hilgardites. A comparison of the powder X-ray patterns demonstrated that the new variety most closely resembles the Eu-containing analogue. Since the origin of the coordinates in the space group *Pnn*2 can be chosen on different twofold rotation axes, the atomic coordinates of the structures cannot be

Table 4. Unit-cell parameters and coordinates of the cations and anions located in the zeolite cavities in the frameworks of the structures of orthorhombic hilgardites

Unit-cell parameters, Å	$Ca_2[B_5O_9]Br$	$Eu_2[B_5O_9]Br$	$Pb_2[B_5O_9]Br$	$Na_{0.5}Pb_2[B_5O_9]Cl \cdot 0.5(OH)$	$Ba_2[B_5O_9]Cl \cdot 0.5H_2O$
a	11.397	11.503	11.524	11.51	11.716
b	11.255	11.382	11.431	11.45	11.574
c	6.293	6.484	6.540	6.563	6.700
Atom, *x*	Ca(2), 0.2527	Eu(1), 0.2547	Pb(1), 0.2607	Pb(2), 0.2577	Ba(2), 0.2669
y	0.0385	0.0501	0.0425	0.0460	0.0405
z	0	0	0	0	0
Atom, *x*	Ca(1), 0.0334	Eu(2), 0.0307	Pb(2), 0.0280	Pb(1), 0.0560	Ba(1), 0.0188
y	0.2449	0.2374	0.2337	0.2748	0.2188
z	–0.6661*	0.6572	0.6627	0.6875	0.6647
Atom, *x*	Br(2), 0	Br(1), 0	Br(1), 0	Cl(2), 0.071	Cl(2), 0
y	0	0	0	0.056	0
z	–0.8491	0.8769	0.893	0.7325	0.455
Atom, *x*	Br(1), 0	Br(2), 0	Br(2), 0	Cl(1), 0	Cl(1), 0
y	0.5	0.5	0.5	0.5	0.5
z	–0.585	0.6370	0.626	0.5185	0.664
Atom, *x*				Na, 0	
y				0	
z				0.3725	
Atom, *x*				OH, 0	H_2O, 0
y				0	0
z				0.0095	–0.048

* The coordinates are given with a minus sign because of the left-handed coordinate system used in the investigation.

directly compared. The transformation of the coordinates of Ca,Br-, Na,Pb,Cl-, and Ba,Cl-hilgardites [11] (shifts of the origin of coordinates, a change in the directions of the axes, and the determination of the equivalent atoms from the regular point systems) made it possible to compare the positions of the large cations and anions in the channels of all known structures. The results are presented in Table 4. The unit-cell parameters increase monotonically in the series Ca^{2+} (0.99)–Eu^{2+} (1.17)–Pb^{2+} (1.20)–Ba^{2+} (1.34); the ionic radii (Å) according to Shannon's system [13] are given in parentheses. However, the first three members of the series have typical structures, in which halogen atoms are located on twofold rotation axes at heights of ~0.8 and ~0.6 along the *c*-axis only in the presence of the larger Br^- anions (1.96 Å). At the same time, compounds containing the larger Ba^{2+} cation have this structure only in the presence of the smaller Cl^- anion (1.81 Å). From this it follows that the orthorhombic variety of hilgardite is characterized by a rather rigid framework built from B-tetrahedra and B-triangles, and the sizes of the zeolite channels change only slightly on going from one structure to another. Attempts to prepare an orthorhombic modification containing the intraframework Pb^{2+} and Cl^- ions failed. The reason is that, the smaller total size of these ions leads to the incorporation of an additional Na^+ cation from the solution into the cavity of the framework. This cation is coordinated by the Cl(2) atom and an OH group and occupies a new structure position. The Cl(1) position is split, and both the Cl(1) and Cl(2) atoms are located at lower heights along the *c*-axis. In the structure containing the larger Ba^{2+} cation, the Cl(2) position is even more substantially shifted, and the position of the water molecule virtually coincides with the position of the OH group.

In this structure type, all atoms are characterized by the polar distribution along the *c*-axis. This is also true for the boron–oxygen framework, in which all apical vertices of the B-tetrahedra are oriented along the *c*-axis (Fig. 2), and its bases are perpendicular to the

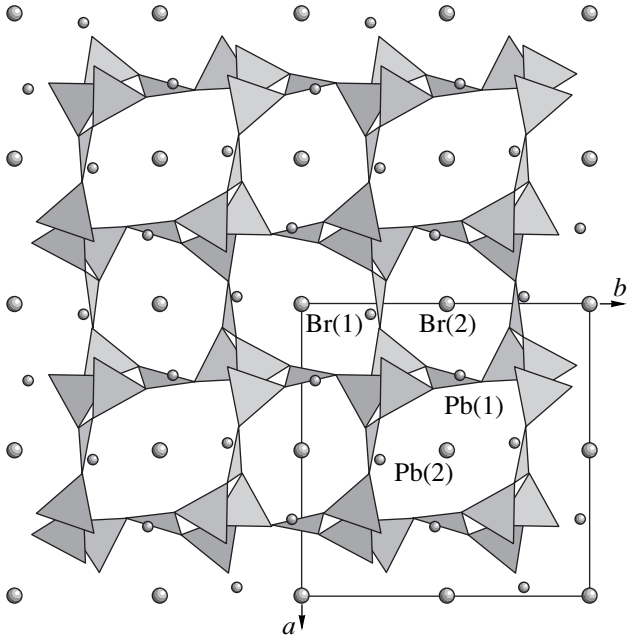

Fig. 2. The structure of $Pb_2[B_5O_9]Br$ projected onto the *ab*-plane. Triangles denote the bases of the B-tetrahedra (parallel to the plane of the projection), whose vertices are directed downward along the *c*-axis. The Pb and Br atoms are indicated by small and large circles, respectively. The unit cell is shown by solid lines.

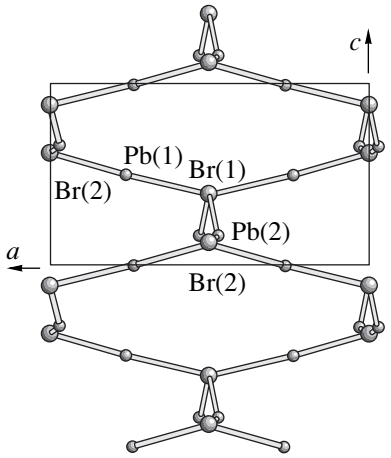

Fig. 3. The structure of $Pb_2[B_5O_9]Br$ projected onto the *ac*-plane. The Pb and Br atoms are indicated by small and large circles, respectively. The polar Pb–Br bonds along the *c*-axis are shown.

c-axis, like in the natural pyroelectric borosilicate tourmaline. In all varieties, the large cations and anions are also characterized by a polar arrangement along the *c*-axis.

The appearance of optical nonlinearity is traditionally related to the presence of strongly asymmetric bonds, such that the polarizable electron density is located predominantly on one side relative to the central atom [1]. The divalent lead cation bearing the highly polarizable lone pair is most characteristic of large cations in this respect. The analysis of the bond lengths and their distributions along the polar *c*-axis (twofold axis) in the $Pb_2[B_5O_9]Br$ structure revealed no polar distribution of the shortest bonds both at Pb(1) (with the O(2) and O(5) atoms) and Pb(2) (with the O(7), O(8), and O(6) atoms). However, the bonds between the Pb(2) and Br atoms are essentially asymmetric (Fig. 3). It can be assumed that the electron densities on the bonds of the divalent Pb cation with a large coordination number are small, whereas the lone-pair density is significant. Most likely, the lone pair is located in free space of the cation, which corresponds to the direction toward the most remote anion involved in coordination to Pb, i.e., toward Br. Unfortunately, the lack of sufficiently large single crystals of $Pb_2[B_5O_9]Br$ did not allow us to examine the electron density and confirm its asymmetrical distribution of the Pb(1) and Pb(2) atoms.

ACKNOWLEDGMENTS

This study was supported by the Russian Foundation for Basic Research, project no. 02-03-33316.

REFERENCES

1. D. L. Corker and A. M. Glazer, Acta Crystallogr., Sect. B: Struct. Sci. **52**, 260 (1996).
2. R. K. Rastsvetaeva, A. V. Arakcheeva, D. Yu. Pushcharovsky, *et al.*, Z. Kristallogr. **213**, 1 (1998).
3. E. L. Belokoneva, T. A. Korchemkina, O. V. Dimitrova, and S. Yu. Stefanovich, Kristallografiya **45** (5), 814 (2000) [Crystallogr. Rep. **45**, 744 (2000)].
4. E. L. Belokoneva, S. Yu. Stefanovich, T. A. Borisova, and O. V. Dimitrova, Zh. Neorg. Khim. **46** (11), 1788 (2001).
5. E. L. Belokoneva, O. V. Dimitrova, T. A. Korchemkina, and S. Yu. Stefanovich, Kristallografiya **43** (4), 864 (1998) [Crystallogr. Rep. **43**, 810 (1998)].
6. S. Ghose and C. Wan, Am. Mineral. **64**, 187 (1979).
7. C. Wan and S. Ghose, Am. Mineral. **68**, 604 (1983).
8. D. J. Lloyd, A. Levasseur, and C. Fouassier, J. Solid State Chem. **6**, 179 (1973).
9. K.-I. Machida, G.-Y. Adachi, and N. Yasioka, Inorg. Chem. **19**, 3807 (1980).
10. P. Becker, Adv. Mater. **10** (13), 979 (1998).
11. O. Ferro, S. Merlino, S. A. Vinogradova, *et al.*, J. Alloys Compd. **305**, 63 (2000).
12. J. Schneider, in *Profile Refinement on IBM-PC's: Proceedings of the IUCr. International Workshop on the Rietveld Method, Petten, 1989*, p. 71.
13. R. D. Shannon, Acta Crystallogr., Sect. A: Cryst. Phys., Diffr., Theor. Gen. Crystallogr. **32**, 751 (1976).

Translated by T. Safonova

Crystallography Reports, Vol. 48, No. 1, 2003, pp. 49–53. Translated from Kristallografiya, Vol. 48, No. 1, 2003, pp. 54–58.

STRUCTURE OF INORGANIC COMPOUNDS

Synthesis and Crystal Structure of New Phosphate $NaFe_4^{2+}Fe_3^{3+}[PO_4]_6$

E. L. Belokoneva, E. A. Ruchkina, and O. V. Dimitrova

Faculty of Geology, Moscow State University, Leninskie gory, Moscow, 119992 Russia

e-mail: elbel@geol.msu.ru

Received March 6, 2002

Abstract—New sodium iron orthophosphate $NaFe_4^{2+}Fe_3^{3+}[PO_4]_6$ was synthesized by the hydrothermal method. The crystal structure (sp. gr. $P\bar{1}$) was established by the heavy-atom method, with the exact chemical formula of the compound being unknown; $R_{hkl} = 0.0492$, $R_{whkl} = 0.0544$, $S = 0.52$. The new compound is analogous to iron phosphate $Fe_3^{2+}Fe_4^{3+}[PO_4]_6$ studied earlier. However, these two compounds differ in the Fe^{2+} and Fe^{3+} contents, because Na^+ ions in the new compound are located at the centers of symmetry not occupied earlier. © *2003 MAIK "Nauka/Interperiodica".*

INTRODUCTION

Among sodium iron phosphates, several compounds are known—$NaFeP_2O_7$ [1, 2], $Na_7Fe_4(P_2O_7)PO_4$ [3], $NaFe_3P_3O_{12}$ [4], $Na_{3.12}Fe_{2.44}(P_2O_7)_2$ [5], $Na_3Fe_2(PO_4)_3$ [6, 7], and $Na_2Fe_3(PO_4)_3$ [8]. Most of these compounds have framework structures with open cavities occupied by Na atoms. The $Na_3Fe_2[PO_4]_3$ compound has three modifications: α (low-temperature monoclinic modification), β (intermediate modification similar to the high-temperature modification), and γ (high-temperature triclinic modification similar to NASICON). Recently, yet another trigonal polymorph of $Na_3Fe_2[PO_4]_3$ has been synthesized and structurally studied [9]. The crystals of Fe,Na phosphates exhibit a number of properties interesting for various applications. For example, the conductivity study [6] showed high cation mobility (sodium) in the β and γ phases of $Na_3Fe_2[PO_4]_3$. The structure of the low-temperature monoclinic modification (α) exhibiting antiferromagnetic properties was established in [7]. Our study was aimed at synthesis of new sodium iron phosphate and determination of its crystal structure.

EXPERIMENTAL

The crystals of the new compound were synthesized by the hydrothermal method in standard 5- to 6-cm^3-large fluoroplastic-lined autoclaves under 70 atm at 280°C. The lower temperature limit was dictated by the kinetics of the reaction, and the upper temperature limit, by the apparatus possibilities. The experiments continued for 20 days to bring the reactions to completion. The coefficient of autoclave filling was chosen in a way to maintain constant pressure. The mixtures of the Na_3PO_4 and $FeCl_3$ salts in equal weight ratios were used as the starting charge. The reaction mixture was placed into an autoclave, and then boric anhydride was added. The solvent was distilled water. As a result, tabular black lusterous crystals were obtained. The crystals had an almost hexagonal habit but belonged (according to their morphology) to the triclinic system. The transverse dimensions of crystals were up to 1.5 mm with the thickness being about 0.4 mm. The test for possible nonlinear optical properties gave a negative result, which indicates that the crystals are centrosymmetric.

Many lines in the powder X-ray diffraction pattern (DRON-UM1 diffractometer, CoK_α radiation, 40 kV, 25 mA) coincide with those observed in the pattern of iron phosphate studied elsewhere [10]. However, the X-ray patterns of these samples have different numbers of reflections, including those in the near region. The composition of the crystals was determined by qualitative X-ray spectral analysis on a CAMSCAN 4DV scanning electron microscope equipped with a LINK attachment for energy-dispersive analysis at the Department of Petrography of the Faculty of Geology of the Moscow State University. The analysis showed that the sample contained Fe, P, and, presumably, also a small amount of Na. The black color of the new phosphate crystals is indicative of the presence of iron atoms of different valence, which is typical, e.g., of magnetite. Apparently, the presence of divalent iron ions can be explained by the fact that crystallization from the hydrothermal solution was accompanied by the formation of intermediate chloride hydrate complexes giving rise to iron reduction [11].

The X-ray diffraction data were collected from a ~0.025-mm-thick single crystal with the transverse

Table 1. Crystallographic data and details of X-ray diffraction study

Sp. gr., Z	$P\bar{1}$, 1
a, Å	6.495(4)
b, Å	9.718(8)
c, Å	8.014(5)
α, deg	115.55(5)
β, deg	101.55(5)
γ, deg	101.12(5)
V, Å^3	424(1)
F(000)	475
Number of atoms per unit cell	38
d_{calcd}, g/cm^3	3.85(1)
Absorption coefficient, μ, cm^{-1}	66.91
Radiation, wavelength	MoK_α, 0.71069
Diffractometer	Syntex P-1
Scan mode	2θ/θ
Scan rate, deg/min	4–12
Number of measured ($I \geq 1.96\sigma(I)$) reflections	2316
Limitations	$F_{hkl} > 4\sigma(F_{hkl})$
Weighting scheme, w	$1/[\sigma(F)^2 + 0.018F^2_{exp}]$
Number of atomic positions	20
Number of parameters in the refinement	175
$2\theta_{max}$, $\sin\theta/\lambda_{max}$	91.69, 1.010
R_{hkl}, R_{whkl}	0.0492, 0.0544
S	0.520

Table 2. Coordinates of the basis atoms and equivalent isotropic thermal parameters, $T = \exp[-1/4(B_{11}a^{*2}h^2 + \ldots 2B_{23}b^*c^*kl)]$; $B_{eq} = 1/3[B_{11}a^{*2}a^2 + \ldots 2B_{23}b^*c^*bc\cos\alpha]$

Atom	x/a	y/b	z/c	$B_{iso/eq}$
Na	0.5	0	0	4.6(3)
Fe(1)	0	0	0	0.66(3)
Fe(2)	−0.0064(1)	0.71407(9)	0.5255(1)	0.64(2)
Fe(3)	0.5205(10	0.47556(9)	0.1942(1)	0.69(2)
Fe(4)	0.2740(1)	0.88843(9)	0.3444(1)	0.56(2)
P(1)	0.5395(2)	0.7662(1)	0.6196(2)	0.38(3)
P(2)	0.7420(2)	0.8323(2)	0.2423(2)	0.45(3)
P(3)	0.0336(2)	0.6274(2)	0.8607(2)	0.60(4)
O(1)	0.6096(7)	−0.0861(5)	0.3752(6)	0.8(1)
O(2)	0.7971(7)	−0.1336(5)	0.1791(6)	1.0(1)
O(3)	−0.0360(7)	0.2415(5)	0.1969(6)	1.0(1)
O(4)	−0.0424(6)	0.8342(5)	0.3682(6)	0.8(1)
O(5)	0.7941(8)	0.5347(5)	0.8252(8)	1.8(1)
O(6)	0.8639(7)	0.4940(5)	0.2616(6)	1.1(1)
O(7)	0.4087(7)	0.3468(4)	0.8956(6)	0.8(1)
O(8)	0.1659(8)	0.7055(6)	0.0759(7)	1.7(2)
O(9)	0.6830(6)	0.2299(4)	0.4914(5)	0.6(1)
O(10)	0.2929(6)	0.0608(4)	0.2530(5)	0.7(1)
O(11)	0.5041(7)	0.2951(5)	0.2407(6)	0.9(1)
O(12)	0.3603(6)	0.3418(5)	0.5256(6)	0.7(1)

dimension ~0.25 mm having the above-described typical habit. Among the vectors found in the study on an automated Syntex P-1 diffractometer, only those corresponding to the triclinic system are consistent with the crystal morphology. The shortest vectors forming obtuse angles were chosen as the basic vectors (Table 1). The shortest a axis is perpendicular to the plane of the tabular crystal. The α angle of ~115° indicates the pseudohexagonal habit of the crystals. The three-dimensional X-ray diffraction data set necessary for the structure determination was collected within a hemisphere of the reciprocal space and included 2386 reflections (together with the reference reflections). The intensities I_{hkl} were processed and converted into F^2_{hkl} using the PROFIT program [12] (see Table 1). All the subsequent computations were performed by the CSD program package.

The crystal structure was solved by the heavy-atom method. The automated search procedure used for locating heavy atoms from the Patterson function P_{uvw} (PATS program) within the sp. gr. $P\bar{1}$ did not meet with success. The arrangement of the heavy atoms was initially established by the direct analysis without considering the symmetry, i.e., within sp. gr. $P1$, as was made in [10]. First, four Fe atoms were located (R was ~0.37). Then the remaining three Fe atoms and six P atoms were located by the method of successive approximations. The structure motif was determined based on the differences in the interatomic distances and the coordination polyhedra typical of both atomic types of coordination (octahedron and tetrahedron). An additional maximum coordinated by six O atoms was also revealed. This maximum corresponds to a sodium atom absent in iron phosphate [10]. The formula of the compound is electroneutral on the condition that the structure contains iron ions of variable valence. The centers of symmetry were readily localized. The origin of the coordinate system was displaced into the Fe atom located in one of these centers. In addition to the Fe(1) atom, only the Na atom is located in a special position at one of the other centers of symmetry in the new

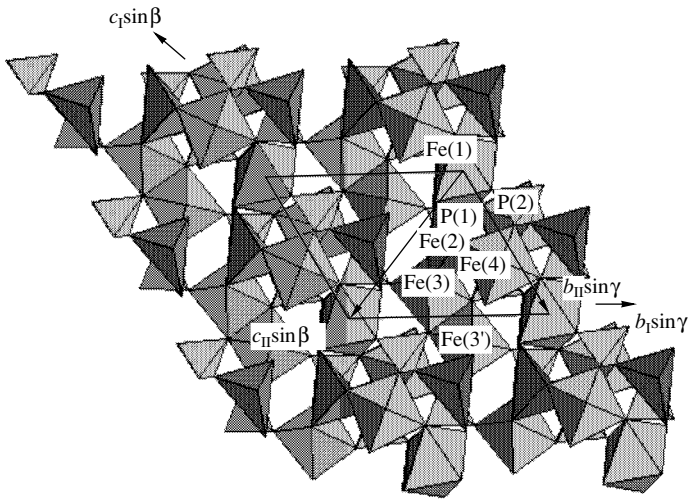

Fig. 1. Crystal structure of **I** projected onto the *bc* plane; the Fe polyhedra and P tetrahedra are shown; the unit vectors of the reference systems of the structure of **II** [10] are indicated by arrows.

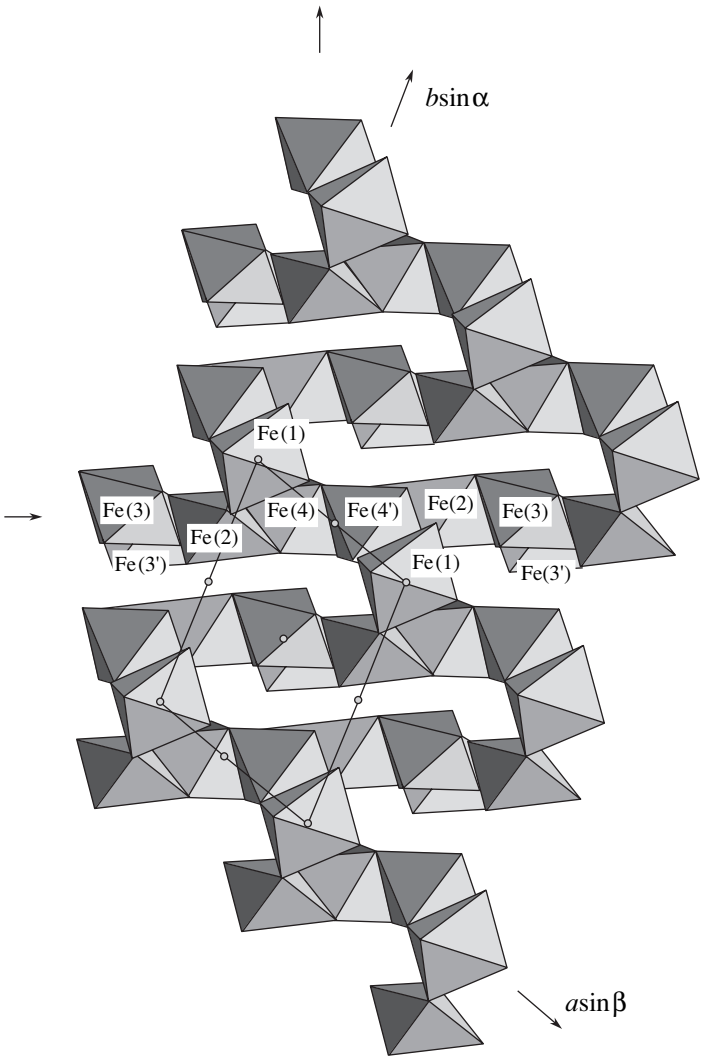

Fig. 2. Crystal structure of **I** projected onto the *ab* plane; the Fe polyhedra are shown; the direction of the ribbons is indicated by the horizontal arrow; the direction perpendicular to the fragments of the close packing is indicated by the vertical arrow.

Table 3. Principal interatomic cation–anion distances (Å) in the $NaFe_4^{2+}Fe_3^{3+}[PO_4]_6$ structure

Na octahedron	
Na–O(2) × 2	2.429(7)
–O(10) × 2	2.576(6)
–O(11) × 2	2.669(8)
Fe octahedron	
Fe(1)–O(2) × 2	2.085(8)
–O(10) × 2	2.251(6)
–O(3) × 2	2.284(8)
Fe(2) five-vertex polyhedron	
Fe(2)–O(3)	2.022(6)
–O(4)	2.065(9)
–O(6)	2.108(7)
–O(9)	2.113(6)
–O(12)	2.167(6)
Fe(3) octahedron	
Fe(3)–O(11)	1.932(10)
–O(5)	1.998(7)
–O(12)	2.032(6)
–O(7)	2.047(6)
–O(6)	2.139(7)
–O(7)	2.146(9)
Fe(4) octahedron	
Fe(4)–O(8)	1.974(7)
–O(1)	2.085(7)
–O(4)	2.089(7)
–O(10)	2.092(9)
–O(1)	2.097(7)
–O(9)	2.101(9)
P(1) tetrahedron	
P(1)–O(11)	1.525(8)
–O(12)	1.547(7)
–O(9)	1.554(6)
–O(10)	1.556(8)
P(2) tetrahedron	
P(2)–O(2)	1.514(9)
–O(1)	1.551(6)
–O(4)	1.546(7)
–O(7)	1.568(8)
P(3) tetrahedron	
P(3)–O(8)	1.521(7)
–O(6)	1.537(7)
–O(3)	1.530(10)
–O(5)	1.540(8)

structure. The final refinement was carried out by the least-squares method with anisotropic thermal parameters of all the atoms with due regard for anomalous scattering of the Mo radiation. The thermal parameters thus obtained corresponded to those typical of the Fe, P, and O atoms, whereas both isotropic and anisotropic thermal parameters of Na, especially *B*(11) and *B*(22), were overestimated. No splitting could be introduced because of too small a distance (0.13 Å) between the peak (0.5017, –0.0003, –0.0003) and the centrosymmetrically related peak in the high-resolution (0.13 Å) synthesis. The empirical absorption correction was applied using the DIFABS program [13]. The crystallographic data, characteristics of the experiment, and the details of the structure refinement are given in Table 1. The atomic coordinates and interatomic distances are listed in Tables 2 and 3, respectively.

RESULTS AND DISCUSSION

The new orthophosphate $NaFe_4^{2+}Fe_3^{3+}[PO_4]_6$ (**I**) is described by the triclinic centrosymmetric space group and is analogous to orthophosphate $Fe_3^{2+}Fe_4^{3+}[PO_4]_6$ (**II**) studied earlier [10] with the exception of the position of the Na atom. The Na atoms were incorporated into the crystal structure of compound **I** because of the different composition of the starting mixture used in the synthesis (Na_3PO_4 in our study and H_3PO_4 in [10]). This gave rise to the change in the ratio of divalent and trivalent iron ions. In compound **I**, the Fe^{2+} content is higher. In the triclinic system, the choice of the unit cells is not limited by the symmetry elements and therefore is somewhat arbitrary. Thus, the initial unit cell of **II** had acute angles. Therefore, the *a* and *c* axes in the crystal structure of the new orthophosphate coincide with the *a* and *b* axes in the structure of **II** [10], whereas the *c* axis in the structure of **II** coincides with the diagonal of the unit cell of **I**. The basic axes corresponding to those used for **II** is shown in Fig. 1. The bond lengths in three independent P tetrahedra in **I**, as those in **II**, vary within a narrow range, 1.514(9)–1.568(8) Å. Of four independent Fe atoms, three atoms have the octahedral coordination, and one Fe atom has coordination number five (trigonal bipyramid). The Na atoms are octahedrally coordinated, with the latter octahedron being more distorted than the Fe octahedra [2.429(7)–2.669(8) Å]. Because of the octahedral configuration of the cavity, the Na octahedron is slightly elongated along the *ab* diagonal, which results in anisotropy of thermal vibrations. The structure of **I** is shown in Figs. 2 and 3. The Fe(3)–Fe(3') and Fe(4)–Fe(4') pairs of the octahedra sharing the O(7)–O(7') and O(1)–O(1') edges, respectively (the centers of symmetry are located at the midpoints of the edges) are linked into chains via five-vertex Fe(2) polyhedra along the O(6)–O(12) and O(4)–O(9) edges. The Fe(4)–Fe(4') pair is parallel to the chain axis (horizontal arrow in Fig. 2),

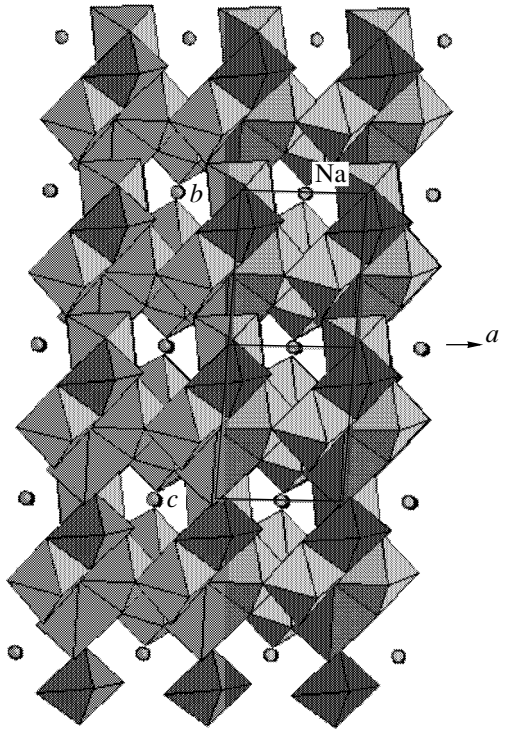

Fig. 3. Crystal structure of **I** projected along the diagonal; the Fe-polyhedra are shown; the Na atoms are represented by circles.

whereas the Fe(3)–Fe(3') pair is perpendicular to it. The Fe(3) and Fe(4) octahedra and the Fe(2) half-octahedron at the layer levels (horizontal in Fig. 2) are "located" on the triangular faces. Their pseudothreefold axes corresponding to the direction of the threefold axis of the fragments of the close packing are located vertically (vertical arrow in Fig. 2). The view along the perpendicular direction demonstrates the similarity of the structure with the structure of corundum-ilmenite. The chains are linked in a close-packed polyhedral framework via the oppositely oriented centrosymmetric F(1) octahedra. As can be seen from Fig. 3, the cavities in the polyhedral framework are located only at the centers of symmetry at a half-height of the *a* axis. These cavities are free in **II** and are occupied by Na atoms in **I**.

The distribution of Fe^{2+} and Fe^{3+} ions over four positions in the structure of **II** was proposed based on the differences in the interatomic distances in the polyhedra. The larger centrosymmetrical Fe(1) octahedron (average Fe–O is 2.235 Å) and the Fe(2) five-vertex polyhedron (average Fe–O is 2.054 Å) are occupied by Fe^{2+}. The smaller Fe(3) and Fe(4) octahedra (average Fe–O are 2.018 and 2.030 Å, respectively) are occupied by Fe^{3+}. This corresponds to the formula $Fe_3^{2+}Fe_4^{3+}[PO_4]_6$. In the structure of **I**, the position of the centrosymmetric Fe(1) octahedron (average Fe–O is 2.207 Å) corresponds to Fe^{2+}. Apparently, the Fe(2) five-vertex polyhedron (average Fe–O is 2.082 Å) is also occupied by Fe^{2+} (in magnetite $Fe^{3+}(Fe^{2+}, Fe^{3+})_2O_4$, the Fe–O distances in the tetrahedra containing Fe^{3+} are shorter and, on the average, are equal to 1.89 Å). More likely, the position of the Fe(4)-octahedron (average Fe–O is 2.049 Å) corresponds to Fe^{3+}. Apparently, the position of the Fe(3) octahedron (average Fe–O is 2.073 Å) is occupied by Fe^{2+} together with Fe^{3+} in the equal ratio (by analogy with the octahedra in magnetite). In magnetite, the "edge bonds" are also present, and the average (Fe^{2+}, Fe^{3+})–O distance is 2.06 Å. The difference in the arrangement of iron ions in **I** and **II** leads to the change in the Fe^{2+} : Fe^{3+} ratio. Thus, this ratio in the structural formula of **I** is 4 : 3, whereas, with due regard for position multiplicities, it is equal to 3 : 4 in **II**. The presence of "edge contacts" in the chain and the interatomic distances does not exclude the variable valence of the Fe atoms (because of exchange interactions) in the positions along the chain. Probably, new orthophosphate **I** possesses magnetic properties. This will be the subject of our future study.

ACKNOWLEDGMENTS

We are grateful to E.A. Guseva for determining the composition of the crystals.

REFERENCES

1. M. Gabelica-Robert, M. Goreaud, P. Labbe, and B. Raveau, J. Solid State Chem. **45**, 389 (1982).
2. R. C. Mercader, L. Terminiello, G. J. Long, *et al.*, Phys. Rev. B **42** (1), 25 (1990).
3. M. De la Rochere, A. Kahn, F. d'Yvoire, and E. Bretey, Mater. Res. Bull. **20**, 27 (1985).
4. D. R. Corbin, J. F. Whitney, W. C. Fultz, *et al.*, Inorg. Chem. **25** (14), 2279 (1986).
5. J. Angenault, J.-C. Couturier, M. Quarton, and F. Robert, Eur. J. Solid State Inorg. Chem. **32**, 335 (1995).
6. M. Pintard-Screpel, F. d'Yvoire, and F. Remy, C. R. Seances Acad. Sci., Ser. C **286**, 381 (1978).
7. N. Fanjat and J. L. Soubeyroux, J. Magn. Magn. Mater. **104–107**, 933 (1992).
8. O. V. Yakubovich, M. A. Simonov, Yu. K. Egorov-Tismenko, and N. V. Belov, Dokl. Akad. Nauk SSSR **236**, 1123 (1977) [Sov. Phys. Dokl. **22**, 550 (1977)].
9. E. L. Belokoneva, E. A. Ruchkina, O. V. Dimitrova, and S. Yu. Stefanovich, Zh. Neorg. Khim. **47** (9) (2002).
10. Yu. A. Gorbunov, B. A. Maksimov, Yu. K. Kabalov, *et al.*, Dokl. Akad. Nauk SSSR **254** (4), 873 (1980) [Sov. Phys. Dokl. **25**, 785 (1980)].
11. H. Remy, *Lehrbuch der anorganischen Chemie* (Geest und Portig, Leipzig, 1961; Mir, Moscow, 1974), Vol. 2.
12. V. A. Strel'tsov and V. E. Zavodnik, Kristallografiya **34** (6), 1369 (1989) [Sov. Phys. Crystallogr. **34**, 824 (1989)].
13. N. Walker and D. Stuart, Acta Crystallogr., Sect. A: Found. Crystallogr. **39**, 158 (1983).

Translated by T. Safonova

Crystallography Reports, Vol. 48, No. 1, 2003, pp. 54–57. Translated from Kristallografiya, Vol. 48, No. 1, 2003, pp. 59–62.

STRUCTURE OF INORGANIC COMPOUNDS

Neutron Diffraction Investigation of the Atomic and Magnetic Structures of MnAs at High Pressures

V. P. Glazkov*, D. P. Kozlenko, K. M. Podurets*, B. N. Savenko**, and V. A. Somenkov***

** Russian Research Centre Kurchatov Institute, pl. Kurchatova 1, Moscow, 123182 Russia*

*** Joint Institute for Nuclear Research, Dubna, Moscow oblast, 141980 Russia*

e-mail: podurets@isssph.kiae.ru

Received January 30, 2002

Abstract—The atomic and magnetic structures of the MnAs compound are investigated using neutron diffraction at high pressures up to 38 kbar in the temperature range 15–300 K. It is found that, as the temperature decreases under high pressure, the MnAs compound undergoes a spin-reorientation transition from the ferromagnetic orthorhombic phase to a new phase whose magnetic moment has both the ferromagnetic and antiferromagnetic components. The structural and magnetic parameters of the high-pressure phases of the MnAs compound are determined. © *2003 MAIK "Nauka/Interperiodica".*

INTRODUCTION

Considerable interest expressed by researchers in the structure and properties of manganese arsenide stems from the fact that the MnAs compound undergoes a large diversity of structural and magnetic phase transitions with an increase in the pressure [1, 2]. Gribanov *et al.* [3] studied the phase diagram of the manganese arsenide MnAs (Fig. 1) in the pressure range up to 32 kbar, primarily from the standpoint of variations in the magnetic properties of this compound. Under normal conditions, the MnAs compound is a ferromagnet and has a hexagonal structure of the NiAs type. The magnetic moments of manganese atoms are oriented perpendicularly to the *c* axis and are equal to 2.7 μ_B at room temperature [3, 4]. As the pressure increases to $P = 4.5$ kbar at room temperature, the MnAs compound undergoes a structural phase transition to an orthorhombic phase with a structure of the MnP type. This phase has a paramagnetic nature in the pressure range up to 20–25 kbar and becomes ferromagnetic at higher pressures [3, 5]. The low-temperature investigations into the magnetic properties of MnAs [3] revealed another ferromagnetic phase at pressures above 8 kbar and temperatures below 80–100 K. However, to the best of our knowledge, no structural studies of the MnAs compound have been performed in the aforementioned ranges of pressures and temperatures. Moreover, Gribanov *et al.* [3] observed different (hypothetically helicoidal) magnetic structures with a decrease in the temperature at pressures ranging from 4.5 to 8 kbar.

Earlier [6], the phase transitions in the MnAs compound were investigated by neutron diffraction methods only in a narrow range of pressures (no higher than 9 kbar). In our recent work [5], the phase transitions in MnAs were examined using neutron depolarization at room temperature in the pressure range up to 80 kbar. It was demonstrated that neutron depolarization due to ferromagnetism first completely disappears in the pressure range 3–15 kbar, then appears again, and increases with an increase in the pressure but does not exceed the initial value. The results obtained in [5] indicate the existence of a high-pressure ferromagnetic phase whose magnetic moment, quite possibly, is also less than the magnetic moment of the initial phase but increases with an increase in the pressure. The neutron depolarization method is particularly convenient for determining the phase boundaries; however, the data on

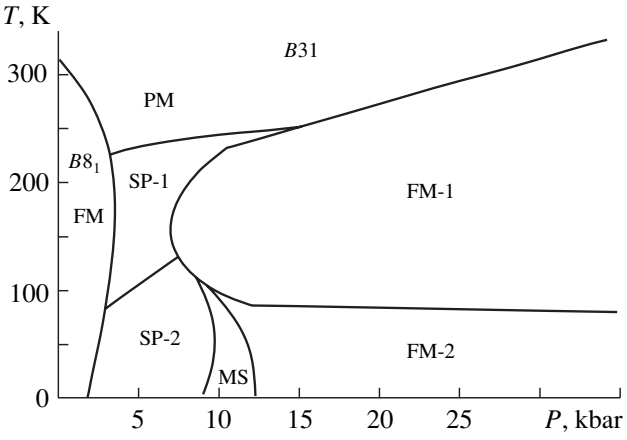

Fig. 1. Schematic phase diagram of the MnAs compound [1, 3]. The regions of the existence of different magnetic phases in the hexagonal ($B8_1$) and orthorhombic ($B31$) modifications of MnAs are shown. Designations: FM is the ferromagnetic phase, PM is the paramagnetic phase, SP is the phase with a helicoidal magnetic structure, and MS is the metastable region.

1063-7745/03/4801-0054$24.00 © 2003 MAIK "Nauka/Interperiodica"

the magnetic structure can be obtained solely by the neutron diffraction method. In this respect, the purpose of the present work was to perform a neutron diffraction investigation of the MnAs compound at high pressures up to 40 kbar in the temperature range 15–300 K.

EXPERIMENTAL

The measurements at high pressures were carried out in high-pressure chambers with sapphire anvils [8] with the use of a DN-12 spectrometer [7] and an IBR-2 pulsed high-flux reactor (Frank Laboratory of Neutron Physics, Joint Institute for Nuclear Research, Dubna). The volume V of the studied samples was approximately equal to 2 mm^3. The diffraction spectra were recorded at the scattering angle $2\theta = 92°$. The resolution of the diffractometer for this scattering angle at the wavelength $\lambda = 2$ Å was $\Delta d/d = 0.02$. The characteristic time taken for one spectrum to be measured was equal to 20 h. The pressure in the chamber was measured from the shift of the ruby luminescence line with an accuracy of 0.5 kbar. A special-purpose cryostat based on a helium refrigerator with a closed circuit was used in the experiments performed in high-pressure chambers at low temperatures (below 15 K). Analysis of the neutron diffraction data was carried out with the MRIA [9] (atomic structure) and Fullprof [10] (atomic and magnetic structures) program packages in the framework of the known structural models [1–4].

RESULTS AND DISCUSSION

It is found that, as the pressure increases, the MnAs compound undergoes a phase transition from the hexagonal modification to the orthorhombic modification in accordance with the results obtained in earlier works [1–3, 6]. Figure 2 shows fragments of the diffraction spectra of the MnAs orthorhombic modification at a pressure of 38 kbar and temperatures of 295 and 15 K.

The diffraction spectrum measured at the pressure $P = 38$ kbar and room temperature corresponds to the ferromagnetic orthorhombic phase of the MnAs compound. The best agreement with the experimental data is achieved in the model according to which the magnetic moments of manganese atoms are aligned parallel to the crystallographic axis *b*. The magnetic moment $\mu_{y\text{-FM}} = 2.3(1)\ \mu_B$ measured at room temperature is slightly less than the magnetic moment ($2.7\ \mu_B$) obtained for the low-pressure phase in [3, 4, 11, 12]. The table presents the structural and magnetic parameters of the ferromagnetic phase of the MnAs compound.

It can be seen from Fig. 2 that, at the pressure $P = 38$ kbar, a decrease in the temperature to $T \approx 110$ K results in the appearance of additional magnetic-structure reflections with $d_{hkl} = 4.99$ and 2.35 Å. A further decrease in the temperature to $T = 15$ K leads to an increase in the intensity of the additional reflections,

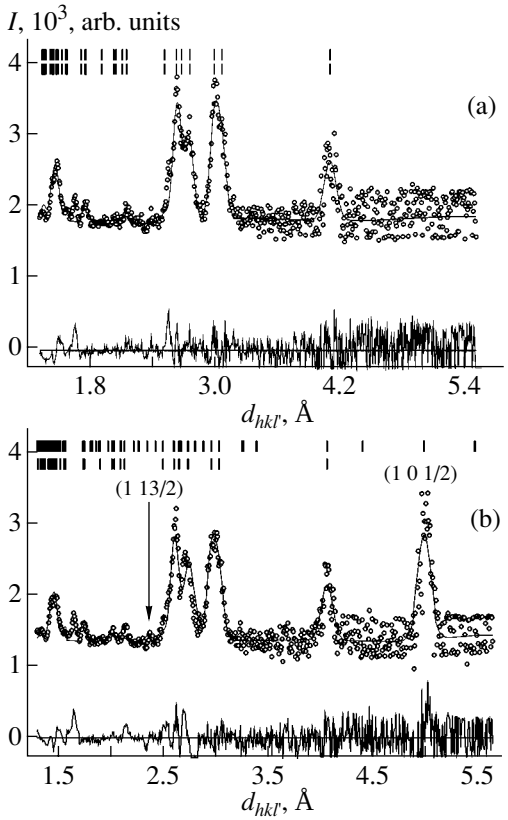

Fig. 2. Fragments of the diffraction spectra of the MnAs compound at $P = 38$ kbar and $T =$ (a) 295 and (b) 15 K. Points are the experimental data, the upper solid lines represent the profiles calculated by the Rietveld method, and the lower solid lines are the difference curves. The upper and lower tic marks indicate the calculated positions of diffraction peaks for the atomic and magnetic structures, respectively. Measurements are performed by the time-of-flight technique using a DN-12 spectrometer.

which suggests the formation of a magnetic superstructure. These reflections can be attributed to a magnetic unit cell with the parameters *a*, *b*, and 2*c* with respect to the initial crystallographic cell; i.e., they correspond to the propagation vector $k = (0, 0, 1/2)$. The arrangement of manganese atoms in this cell can be described by the space group $P2_1/c$ in which the manganese atoms occupy the positions $4(e)_1(x_1, y_1, z_1)$ and $4(e)_2(x_2, y_2, z_2)$, where $x_2 = 1/2 + x_1$, $y_1 = y_2 = 1/4$, and $z_2 = 1/4 - z_1$. According to Izyumov and Ozerov [13], the aforementioned space group corresponds to four Shubnikov color symmetry groups, namely, $P2_1/c$, $P2_1'/c$, $P2_1/c'$, and $P2_1'/c'$. In this case, the screw axis 2_1 and the glide plane *c* do not affect the direction of the magnetic moment, whereas the screw axis $2_1'$ and the glide plane *c*' reverse the direction of the magnetic moment. The best agreement with the diffraction data is achieved in the model described by the space group $P2_1/c$. Within this model, the magnetic moments of manganese atoms

Structural and magnetic parameters of the high-temperature and low-temperature orthorhombic phases of MnAs at $P = 38$ kbar

Parameters	MnAs–FM	MnAs–AFM
T, K	295	15
a, Å	5.495(5)	5.479(5)
b, Å	3.414(5)	3.391(5)
c, Å	6.103(5)	6.068(5)
Mn, Å	$x = 0.015(6)$ $z = 0.200(6)$	$x = 0.035(6)$ $z = 0.200(6)$
As, Å	$x = 0.200(6)$ $z = 0.570(5)$	$x = 0.202(6)$ $z = 0.565(6)$
$\mu_{y\text{-FM}}$, μ_B	2.3(1)	1.9(1)
$\mu_{z\text{-AFM}}$, μ_B	–	2.2(1)
R_{nuc}, %	9.1	7.4
$R_{mag\text{-FM}}$, %	7.1	–
$R_{mag\text{-AFM}}$, %	–	11.4

Note: Mn and As atoms occupy the 4(c) positions (x, 1/4, z), space group *Pnma*. The ferromagnetic component of the magnetic moment of the Mn atoms is directed along the b axis and the antiferromagnetic component of the magnetic moment is aligned along the c axis of the unit cell.

have a ferromagnetic component aligned parallel to the crystallographic axis b and an antiferromagnetic component directed along the crystallographic axis c (Fig. 3): $\mu_{y\text{-FM}} = 1.9(1)\ \mu_B$ and $\mu_{z\text{-AFM}} = 2.2(1)\ \mu_B$ at $T = 15$ K, respectively. This corresponds to the total magnetic moment of manganese atoms $\mu_{Mn} = 2.9(1)\ \mu_B$. We designated this phase as MnAs–AFM. The structural and magnetic parameters of the antiferromagnetic phase are also presented in the table.

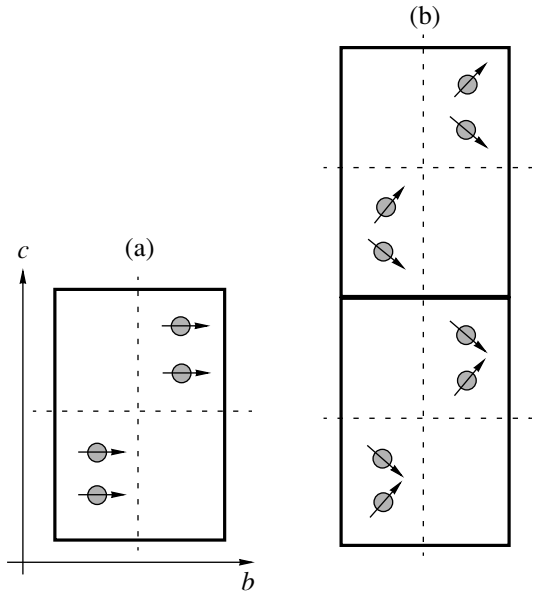

Fig. 3. Magnetic structures of the (a) high-temperature and (b) low-temperature orthorhombic modifications of the MnAs compound at high pressures. Circles are the positions of Mn atoms.

The results obtained in our investigation indicate that, under a high external pressure, a decrease in the temperature leads to a spin-reorientation magnetic phase transition in the MnAs compound, which, in turn, brings about a deviation of the magnetic moments of manganese atoms in the bc plane by an angle of 49.2°. In this case, the ferromagnetic moment decreases. These findings are in agreement with the results of magnetic measurements performed in [3], which demonstrated a decrease in the magnetization with a decrease in the temperature.

The region of the existence of the new magnetic phase MnAs–AFM is identical to the region of the existence of the ferromagnetic phase FM-2. This phase was revealed in the phase diagram of the MnAs compound from the magnetization measurements [3] in the pressure range above 8 kbar and in the temperature range below 80 K (Fig. 1). The temperature of the magnetic phase transition to the MnAs–AFM phase ($T \approx 110$ K at $P = 38$ kbar) is comparable to the temperature of the magnetic phase transition to the FM-2 ferromagnetic phase ($T \approx 75$ K at $P = 35$ kbar [3]). The total magnetic moment of manganese atoms in the high-pressure phase at a low temperature, i.e., $\mu_{Mn} = 2.9(1)\ \mu_B$, is slightly less than the total magnetic moment in the low-pressure hexagonal phase $\mu_{Mn} = 3.3(1)\ \mu_B$ [4].

It should be noted that, as the temperature decreases, the structure parameters of manganese and arsenic atoms remain unchanged to within the limits of experimental error (except for the x parameter of manganese atoms, which slightly increases with a decrease in the temperature). Although this increase in the x parameter is small, it can appear to be significant, because the distance between the nearest neighbor manganese atoms does not depend on the x parameter, whereas the distance between the next-to-nearest neighbor atoms decreases with an increase in the x parameter. This implies that the presence of a soft structure parameter can affect the magnetic interactions between the nearest and next-to-nearest neighbor atoms and can be considered a factor responsible for the magnetic phase transition.

ACKNOWLEDGMENTS

We are grateful to V.I. Voronin for supplying the samples used in our investigations.

This work was supported by the Russian Foundation for Basic Research (project nos. 00-02-17077 and 01-02-17286), the State Program of Support for Leading Scientific Schools of the Russian Federation (project nos. 00-15-96778 and 00-15-96712), and the State Scientific and Technical Program "Topical Directions in the Physics of Condensed Matter: Neutron Investigations of Condensed Matter."

REFERENCES

1. N. Menyuk, J. A. Kafalas, K. Dwight, and J. B. Goodenough, Phys. Rev. **177**, 942 (1969).
2. K. Maki, T. Kaneko, H. Hiroyoshi, and K. Kamigaki, J. Magn. Magn. Mater. **177–181**, 1361 (1998).
3. I. F. Gribanov, É. A. Zavadskiĭ, and A. P. Sivachenko, Fiz. Nizk. Temp. **5**, 1219 (1979) [Sov. J. Low Temp. Phys. **5**, 577 (1979)].
4. N. N. Sirota, E. A. Vasilev, and G. A. Govor, J. Phys. (Paris) **32** (2–3), 1 (1971).
5. K. M. Podurets, S. A. Klimko, V. V. Runov, *et al.*, Physica B (Amsterdam) **297**, 258 (2001).
6. N. N. Sirota and G. A. Govor, Dokl. Akad. Nauk SSSR **196**, 155 (1971).
7. V. L. Aksenov, A. M. Balagurov, V. P. Glazkov, *et al.*, Physica B (Amsterdam) **265**, 258 (1999).
8. V. P. Glazkov and I. N. Goncharenko, Fiz. Tekh. Vys. Davleniĭ **1**, 56 (1991).
9. V. B. Zlokazov and V. V. Chernyshev, J. Appl. Crystallogr. **25**, 447 (1992).
10. J. Rodríguez-Carvajal, Physica B (Amsterdam) **192**, 55 (1993).
11. E. L. Hall, L. H. Schwartz, G. P. Felcher, and D. H. Ridgley, J. Appl. Phys. **41**, 939 (1970).
12. L. H. Schwartz, E. L. Hall, and G. P. Felcher, J. Appl. Phys. **42**, 1621 (1971).
13. Yu. A. Izyumov and R. P. Ozerov, *Magnetic Neutron Diffraction* (Nauka, Moscow, 1966; Plenum, New York, 1970).

Translated by O. Borovik-Romanova

Crystallography Reports, Vol. 48, No. 1, 2003, pp. 58–60. Translated from Kristallografiya, Vol. 48, No. 1, 2003, pp. 63–65.

STRUCTURE OF ORGANIC COMPOUNDS

Synthesis and the Crystal Structure of Aqua-Dioxo-Nitrato-(2,2',6',2''-Terpyridine)-Neptunium(V) $[NpO_2(NO_3)(Terpy)(H_2O)]$

N. A. Budantseva*, G. B. Andreev*, A. M. Fedoseev*, M. Yu. Antipin, and J.-C. Krupa*****

** Institute of Physical Chemistry, Russian Academy of Sciences, Leninskiĭ pr. 31, Moscow, 119991 Russia*

e-mail: budants@ipc.rssi.ru

*** Nesmeyanov Institute of Organoelement Compounds, Russian Academy of Sciences, ul. Vavilova 28, Moscow, 119991 Russia*

**** Institut de Physique Nucléaire, CNRS-IN2P3, 91406 Orsay Cedex, France*

Received April 1, 2002

Abstract—The crystal structure of the $[NpO_2(NO_3)(Terpy)(H_2O)]$ complex between pentavalent neptunium and 2,2',6',2"-terpyridine is determined. The crystal data are as follows: a = 11.130(3) Å, b = 7.916(2) Å, c = 18.324(5) Å, β = 100.873(6)°, V = 1585.5(8) Å^3, Z = 4, space group is $P2_1/n$, R = 0.044, and $wR(F^2)$ = 0.092. The coordination polyhedron of the Np atom is a pentagonal bipyramid whose equatorial plane includes three nitrogen atoms of the *Terpy* molecule and two oxygen atoms of the nitrate ion and the water molecule. © *2003 MAIK "Nauka/Interperiodica".*

INTRODUCTION

Continuing our studies on the structure and properties of the coordination compounds of pentavalent neptunium with various pyridine derivatives [1–5], we performed X-ray structure analysis of a complex between Np(V) and 2,2',6',2"-terpyridine (*Terpy*). No structural data on the actinide(V) and (VI), even uranyl, compounds with this ligand are available in the literature.

EXPERIMENTAL

Compound $[NpO_2(NO_3)(Terpy)(H_2O)]$ (**I**) was synthesized by the following procedure. Freshly precipitated Np(V) hydroxide was dissolved in HNO_3. The solution was evaporated at a temperature below 40°C, and the precipitate was dissolved in ethanol. Then, a solution of an equimolar amount (0.1 mol/l) of 2,2',6',2"-terpyridine in ethanol was added. Green crystals of compound **I** precipitated at room temperature.

The experimental data were obtained on a Bruker SMART diffractometer at 110 K. The crystal was $0.08 \times 0.10 \times 0.16$ mm in size. The data were corrected for absorption with the SADABS procedure. The structure was solved by the direct method. All the nonhydrogen atoms were refined in the full-matrix anisotropic approximation on F^2 using all the 4595 unique reflections. The hydrogen atoms of the *Terpy* molecule were introduced into the calculated positions and refined isotropically, and the hydrogen atoms of the water molecules were not located. The main crystal data and parameters of the structure refinement are summarized in Table 1. The atomic coordinates and equivalent thermal parameters are listed in Table 2.

Table 1. Main crystal data and parameters of structure refinement

Crystal system	Monoclinic
a, Å	11.130(3)
b, Å	7.916(2)
c, Å	18.324(5)
β, deg	100.873(6)
Space group	$P2_1/n$
Z	4
V, Å^3	1585.5(8)
ρ_{calcd}, g/cm^3	2.439
Radiation (λ, Å)	MoK_α (0.71073)
Scan mode	θ/2θ
$2\theta_{max}$, deg	60
Number of reflections	16048
Number of unique reflections ($I > 2\sigma(I)$)	2942
Number of parameters refined	278
R, $wR(F^2)$	0.044, 0.092

Table 2. Atomic coordinates and equivalent thermal parameters

Atom	*x*	*y*	*z*	U_{eq}, Å^2	Atom	*x*	*y*	*z*	U_{eq}, Å^2
Np(1)	0.06751(2)	0.65932(2)	0.19504(2)	0.01386(9)	C(15)	–0.2211(8)	0.6145(10)	0.2446(4)	0.021(2)
N(1)	0.1648(6)	0.6353(8)	0.0783(3)	0.018(2)	O(1)	0.0660(4)	0.4269(6)	0.1911(3)	0.0129(9)
N(2)	–0.0696(6)	0.7325(8)	0.0676(3)	0.018(2)	O(2)	0.0781(5)	0.8903(7)	0.1972(3)	0.018(1)
N(3)	–0.1678(6)	0.6710(8)	0.1889(3)	0.018(2)	O(3)	0.2850(5)	0.6604(7)	0.2534(3)	0.018(1)
N(4)	0.0127(6)	0.6952(9)	0.3694(3)	0.021(2)	O(4)	–0.0079(5)	0.6471(7)	0.4298(3)	0.025(1)
C(1)	0.2761(7)	0.5702(11)	0.0827(4)	0.023(2)	O(5)	–0.0082(6)	0.8427(7)	0.3473(3)	0.032(1)
C(2)	0.3338(9)	0.5543(11)	0.0230(5)	0.026(2)	O(6)	0.0546(5)	0.5888(8)	0.3267(3)	0.025(1)
C(3)	0.2746(8)	0.6093(11)	–0.0448(5)	0.025(2)	H(1)	0.320(6)	0.513(9)	0.136(4)	0.05(2)
C(4)	0.1586(7)	0.6738(10)	–0.0517(4)	0.019(2)	H(2)	0.400(8)	0.533(9)	0.019(5)	0.05(2)
C(5)	0.1070(7)	0.6874(9)	0.0106(4)	0.016(2)	H(3)	0.291(6)	0.615(8)	–0.089(4)	0.05(2)
C(6)	–0.0185(7)	0.7576(9)	0.0066(4)	0.017(2)	H(4)	0.115(6)	0.708(8)	–0.098(4)	0.05(2)
C(7)	–0.0768(7)	0.8496(10)	–0.0546(4)	0.019(2)	H(7)	–0.038(6)	0.878(8)	–0.095(4)	0.05(2)
C(8)	–0.1901(8)	0.9224(11)	–0.0520(5)	0.024(2)	H(8)	–0.230(6)	0.998(9)	–0.093(4)	0.05(2)
C(9)	–0.2424(8)	0.8974(11)	0.0093(5)	0.022(2)	H(9)	–0.308(6)	0.933(9)	0.013(4)	0.05(2)
C(10)	–0.1827(7)	0.7972(9)	0.0674(4)	0.016(2)	H(12)	–0.405(8)	0.826(9)	0.096(5)	0.05(2)
C(11)	–0.2421(7)	0.7506(9)	0.1309(4)	0.018(2)	H(13)	–0.477(9)	0.742(9)	0.184(6)	0.05(2)
C(12)	–0.3651(7)	0.7722(11)	0.1294(5)	0.022(2)	H(14)	–0.376(9)	0.616(9)	0.279(5)	0.05(2)
C(13)	–0.4161(8)	0.7139(11)	0.1878(5)	0.024(2)	H(15)	–0.178(6)	0.569(9)	0.278(4)	0.05(2)
C(14)	–0.3437(8)	0.6314(11)	0.2460(5)	0.024(2)					

RESULTS AND DISCUSSION

In structure **I** (figure), the coordination polyhedron of the neptunium atom is a pentagonal bipyramid. Its equatorial plane is formed by three nitrogen atoms of the terpyridine molecule and oxygen atoms of the monodentate nitrate ion and the coordinationally bound water molecule.

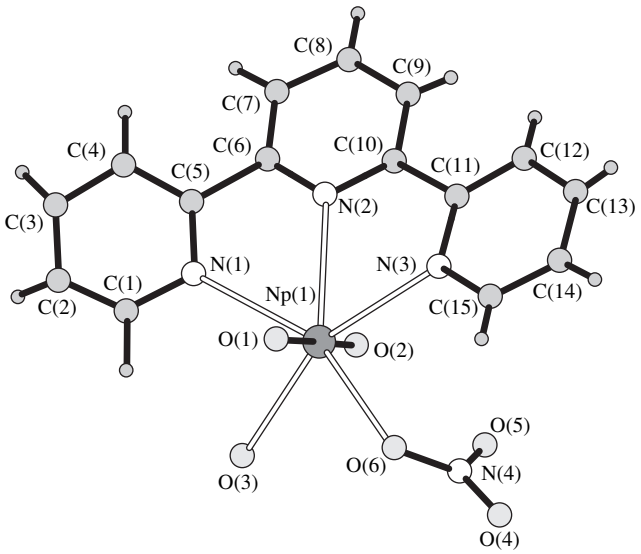

A fragment of the crystal structure $[NpO_2(NO_3)(Terpy)(H_2O)]$.

The distances from the neptunium atom to the equatorial atoms are different. The distance to the oxygen atom of the water molecule is the shortest, 2.455(5) Å. The distance to the oxygen atom of the nitrate ion is somewhat longer, 2.506(5) Å. The Np–N bond lengths have normal values and lie in the range 2.580(5)–2.602(5) Å. The largest atomic deviation from the rms equatorial plane is 0.360 Å. The distance between the neptunium nearest neighbor atoms is 5.757 Å.

The NpO_2 group is nearly linear and symmetric: the Np–O distances are 1.841(5) and 1.832(5) Å, and the O–Np–O bond angle is 176.5(2)°.

The terpyridine molecule and the neptunium atom form two conjugated metallocycles in which the endocyclic angles at the metal atom are 62.6(2)° and 62.5(2)°. The *T*1, *T*2, and *T*3 pyridinium rings containing the N(1), N(2), and N(3) atoms, respectively, form dihedral angles of 19.0°, 26.4°, and 20.4° with the rms equatorial plane of the coordination polyhedron of the Np atom. The largest atomic deviations from the rms planes of the pyridinium rings are 0.011 (*T*1), 0.027 (*T*2), and 0.004 (*T*3) Å. The dihedral angles between the planes of the rings are 14.5° (*T*1–*T*2), 22.6° (*T*1–*T*3), and 16.0° (*T*2–*T*3).

The lengths of the N–C and C–C bonds in the three rings are 1.33(1)–1.35(1) and 1.36(1)–1.38(1) Å (*T*1), 1.359(9)–1.360(9) and 1.37(1)–1.39(1) Å (*T*2), and 1.350(10)–1.370(9) and 1.376(12)–1.381(11) Å (*T*3), respectively. These values agree with those observed in the structure of the uncoordinated terpyridine mole-

cule, 1.32–1.35 and 1.35–1.40 Å [6]. In structure **I** and in a free *Terpy* molecule, the distances between the C atoms of the neighboring pyridinium rings are 1.49(1) Å.

The nitrate ion acts as a monodentate ligand. The lengths of the N–O bonds differ from those in the free ion. The N–O distances in the free ion are 1.245 Å [7]. In structure **I**, the distance to the coordinated oxygen atom is 1.296(8) Å and the distances to the uncoordinated atoms are 1.231(8) and 1.243(8) Å.

REFERENCES

1. G. B. Andreev, A. M. Fedoseev, N. A. Budantseva, and M. Yu. Antipin, Mendeleev Commun., No. 2, 58 (2001).
2. G. B. Andreev, M. Yu. Antipin, A. M. Fedoseev, and N. A. Budantseva, Koord. Khim. **27** (3), 231 (2001).
3. G. B. Andreev, J.-C. Krupa, M. Yu. Antipin, *et al.*, in *31emes Journess des Actinides: Programme and Abstracts, Saint-Malo, France, 2001*, p. 6.
4. G. B. Andreev, M. Yu. Antipin, A. M. Fedoseev, and N. A. Budantseva, Dokl. Akad. Nauk **374** (3), 343 (2000).
5. G. B. Andreev, V. N. Khrustalev, M. Yu. Antipin, *et al.*, Koord. Khim. **26** (11), 878 (2000).
6. C. A. Bessel, R. F. See, D. L. Jameson, *et al.*, J. Chem. Soc., Dalton Trans., 3223 (1992).
7. A. Wells, *Structural Inorganic Chemistry* (Clarendon, Oxford, 1984; Mir, Moscow, 1988), Vol. 1.

Translated by I. Polyakova

Crystallography Reports, Vol. 48, No. 1, 2003, pp. 61–67. Translated from Kristallografiya, Vol. 48, No. 1, 2003, pp. 66–72.

STRUCTURE OF ORGANIC COMPOUNDS

Molecular and Crystal Structures of the Product of the Reaction between Tetrafluoroborate tris[Triphenylphosphinegold(I)]oxonium and Calix[4]arene

L. G. Kuz'mina*, A. V. Churakov*, G. G. Sadikov*, and J. A. K. Howard**

** Kurnakov Institute of General and Inorganic Chemistry, Russian Academy of Sciences, Leninskiĭ pr. 31, Moscow, 119991 Russia*

*** Chemistry Department, Durham University, Durham DH1 3LE, England*

e-mail: kuzmina@igic.ras.ru

Received April 25, 2002

Abstract—The molecular and crystal structures of a complex salt in which the cation is tris[triphenylphosphinegold(I)]oxonium and the anion is deprotonated calix[4]arene are determined. The tris[triphenylphosphinegold(I)]oxonium cation forms a centrosymmetric, doubly charged, hexanuclear dimer. The oxonium oxygen atoms are characterized by a nonplanar bond configuration: the Au–O–Au bond angles vary in the range 92.2(2)°–101.8(2)° due to aurophilic interactions (Au···Au) occurring at distances in the range 2.9650(4)–3.1836(4) Å. The monomers are joined into dimers via pairs of Au···Au interactions at a distance of 3.1880(5) Å. The anion adopts a cone conformation. The deprotonated oxygen atom of the anion is involved in the formation of two hydrogen bonds as a proton acceptor. In the crystal, two anions and one cation form a cluster in which the large-sized dimer cation is capped by the two calix[4]arene anions on opposite sides: {*A*–*K*–*A*}. In turn, these clusters form zigzag chains due to stacking interactions involving one of the benzene rings. © *2003 MAIK "Nauka/Interperiodica".*

INTRODUCTION

Calixarenes belong to the class of macrocyclic compounds. At present, these compounds have been intensively studied as objects of supramolecular chemistry [1–9]. Since flexible molecules of calixarenes are capable of adopting their shape for many molecules, ions, and molecular fragments, they can be used as three-dimensional building blocks in the design of highly selective host molecules. Among compounds of this class, the structure and properties of calix[4]arenes are best understood. The structure of calix[4]arenes involves four phenol groups linked by orthomethylene bridges. For 16-membered macrocyclic fragments of calix[4]arenes, there exist four stable conformations that can transform into one another with a moderate expenditure of energy. Owing to the presence of OH functional groups in flexible macrocyclic fragments of calix[4]arenes, they can enter into electrostatic interactions with the guest molecule, whereas the aryl groups provide π-type interactions with the guest molecule. This renders calix[4]arenes most suitable for use as model objects in the elucidation of the nature of guest–host interactions that play a central role in molecular recognition, which is important for biochemistry [1–9].

Great interest expressed by researchers in gold(I) complexes is associated with their unusual luminescent properties, on the one hand, and the interesting pharmacological properties [10–19], on the other hand. Recent investigations revealed a correlation between the photochemical and photophysical properties of these compounds and the occurrence of different-type secondary interactions with the participation of gold atoms, such as aurophilic interactions (Au···Au), Au·π-system interactions, and Au···heteroatom interactions [20–23].

Research into the elements belonging to different molecular systems but combined into a single system, which have been extensively studied in supramolecular chemistry, is of special interest. Investigation of combined molecular systems is currently directed toward the search for new materials with unusual properties. This explains our interest in the products of the replacement of hydroxyl protons of calix[4]arenes by the isolobal cation fragment $AuPPh_3$, i.e., in the complexes in which either of their two constituents is of interest by itself from both theoretical and practical points of view.

This paper reports on the results of X-ray structure investigation of the product of the reaction between calix[4]arene and a well-known aurating agent, namely, $[O(AuPPh_3)_3]BF_4$. We assumed that, during the reaction, one or several protons of the calix[4]arene hydroxyl groups should be replaced by the $AuPPh_3$ cationic complexes. In the aforementioned molecular system, the distance between the gold atoms should be short enough for these atoms to participate in an aurophilic and (or) another weak interaction.

Details of the chemical experiment performed in this work will be described in a separate paper.

1063-7745/03/4801-0061$24.00 © 2003 MAIK "Nauka/Interperiodica"

Table 1. Crystal data, data collection, and refinement parameters for the crystal structure studied

Empirical formula	$C_{26}H_{68}Au_3O_5P_3 \cdot Sol$
Solvate (experiment *1*/experiment *2*)	$2C_4H_4O \cdot 2H_2O/4C_4H_4O$
Molecular weight	1961.27/1817.17
Crystal system	Triclinic
Space group	$P\bar{1}$
a, Å	15.8804(3)/15.9106(1)
b, Å	16.7883(3)/16.7675(2)
c, Å	17.0711(3)/17.2650(1)
α, deg	93.207(1)/93.634(1)
β, deg	114.107(1)/113.136(1)
γ, deg	90.047(1)/90.018(1)
V, Å^3	4146.4(1)4225.42(6)
Z	2/2
ρ_{calcd}, g/cm^3	1.571/1.428
F(000)	1908/1764
$\mu(MoK_\alpha)$, mm^{-1}	5.404/5.295
Crystal size, mm	$0.46 \times 0.32 \times 0.28/0.40 \times 0.40 \times 0.26$
Radiation type (wavelength, Å)	MoK_α (0.71073)
Scan mode/θ range, deg	ω/1.22, 27.00 / ω/1.22–27.00
Index ranges	$-20 \le h \le 19/-20 \le h \le 20$
	$-21 \le k \le 21/-16 \le k \le 21$
	$-21 \le l \le 22/-22 \le l \le 22$
Number of measured reflections	34650/29927
Number of unique reflections	17978 [R_{int} = 0.0606]/18329 [R_{int} = 0.0525]
Number of reflections with $I > 2\sigma(I)$	15793/16112
Transmission factor (min/max)	0.27986/0.62579 / 0.52044/0.86244
Number of refined parameters	891/919
R factors for reflections with $I > 2\sigma(I)$	R_1 = 0.0484, wR_2 = 0.1221/R_1 = 0.0695, wR_2 = 0.1705
R factors for all reflections	R_1 = 0.0904, wR_2 = 0.1523/R_1 = 0.1038, wR_2 = 0.2673
Goodness-of-fit on F^2	1.036/1.042
Extinction coefficient	0.00000(7)/0.0011(3)
Residual electron density (min/max), e/Å^3	–2.008/1.780/ –1.320/3.756

EXPERIMENTAL

X-ray diffraction analysis of the compound under investigation was carried out using crystals grown at different temperatures (~270 and ~250 K) from tetrahydrofuran (THF), which, in the former case, was not subjected to dehydration. In the latter case, the crystallization was performed with a dried tetrahydrofuran.

The most important parameters of experiments *1* and *2* are presented in Table 1. In both cases, a colorless single crystal in the form of a prism was covered with a perfluorinated oil and placed in a Bruker SMART CCD diffractometer at a temperature of 150.0(2) K. Experimental reflections were measured in the ω scan mode (exposure time per frame, 15 s).

Correction for X-ray absorption by the studied crystal was introduced using a semiempirical method [24] for a large set of equivalent reflections.

The structure was solved by direct methods and refined using the least-squares procedure for F^2. The hydrogen atoms and the electron-density peaks for solvate molecules were located from the difference Fourier synthesis. In experiment *1*, the solvate molecules were identified as two tetrahydrofuran molecules and,

most probably, two water molecules. The tetrahydrofuran molecules were disordered, and the oxygen atoms of the water molecules only partially occupied their positions. The isolated peaks were assigned to the oxygen atoms of the solvate molecules on the basis of the results of analyzing the short intermolecular contacts formed by these atoms either with the O(3) oxygen atom of the anion (2.94 Å) or with each other (2.63 Å). The observed contacts are characteristic of hydrogen bonds. Moreover, as was noted above, the tetrahydrofuran used in this experiment was not subjected to dehydration.

In experiment *2*, the solvate molecules were identified as four tetrahydrofuran molecules. These molecules are also disordered and are characterized by partial site occupation. No isolated peaks that could be attributed to water molecules were revealed.

The final refinement of the structure was performed using the least-squares procedure in the anisotropic approximation for all the non-hydrogen atoms of the host molecular ions and in the isotropic approximation for the atoms of the solvate molecules. The positions of the hydrogen atoms were refined within a riding model. All the peaks of the residual electron density were located either in the vicinity of the gold atoms or in the cavities of the crystal packing. This does not exclude the possibility that the crystal structure can involve additional solvate molecules disordered over their positions with a low occupancy.

All the calculations were carried out with the SHELXS86 [25] and SHELXL93 [26] software packages. The crystal data have been deposited in the Cambridge Structural Database.

In both experiments, we obtained close sizes of the unit cell of the studied crystal, the same atomic coordinates, and identical geometric parameters for the cation and the anion. The results of experiment *1*, which were obtained with a higher accuracy, will be discussed below.

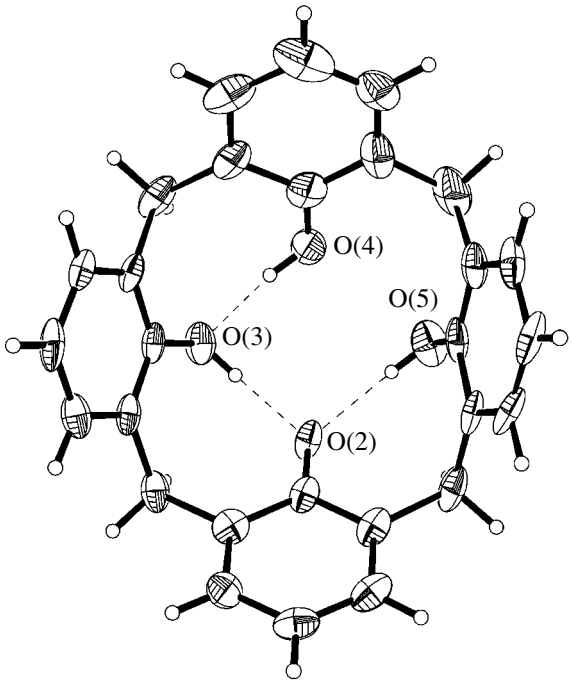

Fig. 1. Structure of the calix[4]arene anion. Thermal ellipsoids for atoms are drawn at the 40% probability level.

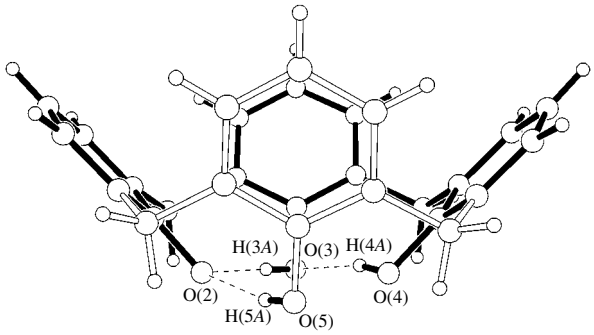

Fig. 2. Side projection of the calix[4]arene anion.

RESULTS AND DISCUSSION

Contrary to the expectations, the reaction of calix[4]arene with $[O(AuPPh_3)_3]BF_4$ resulted in the cation exchange rather than in the replacement of one or several protons of the calix[4]arene hydroxyl groups by the isolobal cationic complexes $AuPPh_3^+$. Compound **I** is a complex salt in which the anion is deprotonated calix[4]arene and the cation is $[O(AuPPh_3)_3]^+$. The selected bond lengths and angles are listed in Table 2.

Structure of the Anion

The structure of the calix[4]arene anion with thermal ellipsoids is shown in Fig. 1. Figure 2 depicts the side projection of the anion, in which the conformation of the macrocycle is clearly seen. The macrocycle adopts a cone conformation, i.e., one of the four stable conformations typical of calix[4]arene molecules [9]. This cone is not symmetric. The dihedral angles between the planes of the C(1)···C(6), C(8)···C(13), C(15)···C(20), and C(22)···C(27) benzene rings and the mean plane through the O(2), O(3), O(4), and O(5) oxygen atoms are equal to 46.1°, 57.6°, 45.6°, and 70.1°, respectively. This feature of the calix[4]arene anion is most likely associated with the packing effects and nonsymmetric hydrogen bonds (see below) and indicates a high conformational flexibility of the molecular skeleton of calix[4]arene.

The auration leads to deprotonation of only one hydroxyl group. This corresponds to the charge balance in the unit cell of the studied crystal and is confirmed by

Table 2. Selected bond lengths (Å) and angles (deg)

Bond/angle	*d*/ω	Bond/angle	*d*/ω
Au(1)–Au(2)	3.1836(4)	C(8)–C(13)	1.37(1)
Au(2)–Au(3)	3.0905(4)	C(8)–C(9)	1.38(1)
Au(1)–Au(3)	2.9650(4)	C(9)–C(10)	1.39(1)
Au(2)–Au(3)$^{\#1}$	3.1880(5)	C(10)–C(11)	1.34(2)
Au(1)–P(1)	2.221(2)	C(11)–C(12)	1.40(2)
Au(2)–P(2)	2.228(2)	C(12)–C(13)	1.38(1)
Au(3)–P(3)	2.228(2)	C(13)–C(14)	1.51(2)
Au(1)–O(1)	2.032(5)	C(14)–C(16)	1.52(2)
Au(2)–O(1)	2.071(5)	C(15)–C(20)	1.42(2)
Au(3)–O(1)	2.083(6)	C(15)–C(16)	1.45(2)
O(2)–C(1)	1.34(1)	C(16)–C(17)	1.40(2)
O(3)–C(8)	1.37(1)	C(17)–C(18)	1.41(2)
O(4)–C(15)	1.36(2)	C(18)–C(19)	1.39(2)
O(5)–C(22)	1.38(1)	C(19)–C(20)	1.37(2)
C(1)–C(6)	1.40(1)	C(20)–C(21)	1.49(2)
C(1)–C(2)	1.42(1)	C(21)–C(23)	1.50(2)
C(2)–C(3)	1.37(2)	C(22)–C(23)	1.41(2)
C(2)–C(7)	1.54(1)	C(22)–C(27)	1.43(2)
C(3)–C(4)	1.40(2)	C(23)–C(24)	1.40(2)
C(4)–C(5)	1.37(2)	C(24)–C(25)	1.42(2)
C(5)–C(6)	1.39(2)	C(25)–C(26)	1.35(2)
C(6)–C(28)	1.56(2)	C(26)–C(27)	1.36(2)
C(7)–C(9)	1.54(2)	C(27)–C(28)	1.50(2)
Au(3)–Au(1)–Au(2)	60.22(1)	Au(1)–O(1)–Au(2)	101.8(2)
Au(1)–Au(2)–Au(3)	56.38(1)	Au(1)–O(1)–Au(3)	92.2(2)
Au(2)–Au(3)–Au(1)	63.40(1)	Au(2)–O(1)–Au(3)	96.1(2)
Au(3)–Au(2)–Au(3)$^{\#1}$	90.97(1)	O(1)–Au(1)–P(1)	175.6(2)
Au(1)–Au(2)–Au(3)$^{\#1}$	110.16(1)	O(1)–Au(2)–P(2)	178.3(1)
Au(1)–Au(3)–Au(2)$^{\#1}$	110.63(1)	O(1)–Au(3)–P(3)	177.3(2)
Au(2)–Au(3)–Au(2)$^{\#1}$	89.03(1)		

Note: The symmetry operation used for generating equivalent atoms: $^{\#1}$ $-x + 2, -y + 1, -z$.

the presence of electron-density peaks in the difference Fourier map in the vicinity of the O(3), O(4), and O(5) oxygen atoms (which were identified as hydrogen atoms) and by the absence of the electron-density peak in the vicinity of the O(2) oxygen atom. Moreover, despite the relatively large errors, the O(2)–C(1) bond [1.34(1) Å] proves to be systematically shorter than the other three C–O bonds in the anion [1.37(1), 1.36(2), and 1.38(1) Å]. It should also be noted that it is this O(2) oxygen ion with a larger negative charge that participates in the formation of two hydrogen bonds as a proton acceptor.

The deprotonation causes a disturbance of the cyclic hydrogen-bonded network, which is inherent in calixarenes with a cone conformation [27]. The O(2) deprotonated atom with an extra negative charge is involved in the formation of two hydrogen bonds (as a proton acceptor) with protons of the adjacent hydroxyl groups. The O(2)···O(3) and O(2)···O(5) distances (2.569 and 2.749 Å, respectively) [as well as the O(2)···H(3A) and O(2)···H(5A) distances (1.729 and 1.923 Å, respectively)] characterize hydrogen bonds of different strengths: one of these two bonds is a hydrogen bond of moderate strength, and the other bond is a weak hydro-

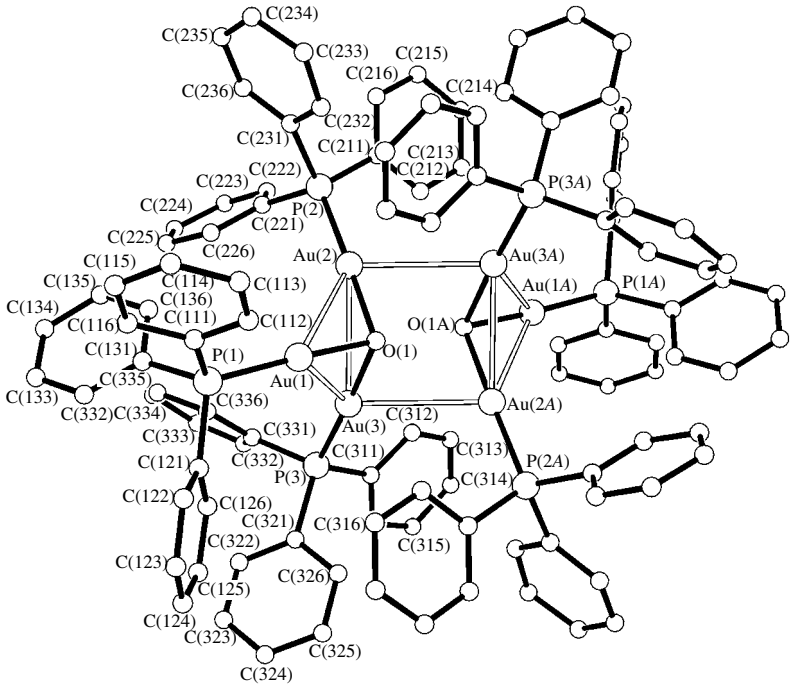

Fig. 3. Structure of the centrosymmetric, doubly charged, hexanuclear dimer cation $[O(AuPPh_3)_3]_2^{2+}$. The numbering of carbon atoms is shown only for the symmetrically independent moiety of the molecule. Hydrogen atoms are omitted for clarity.

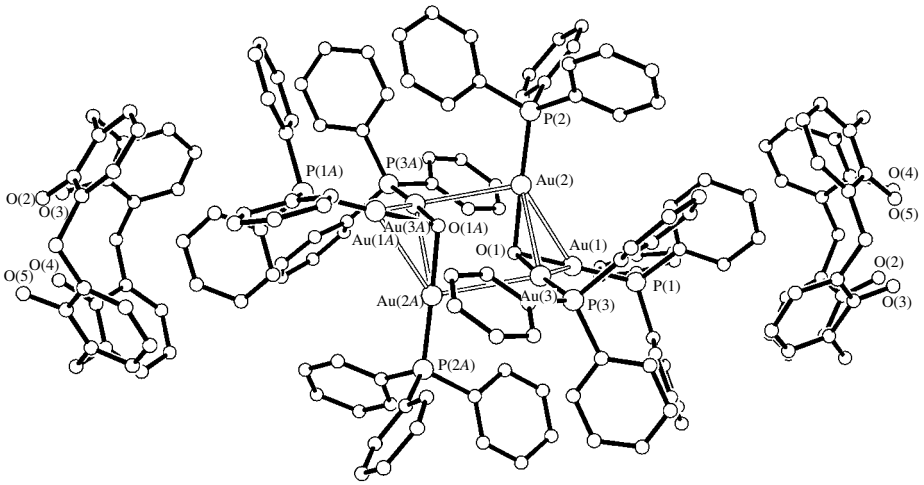

Fig. 4. A supramolecular cluster consisting of two anions and one dimer cation in the crystal.

gen bond. The bond angles at the H(3*A*) and H(5*A*) atoms (178.2° and 166.5°, respectively) correspond to a linear hydrogen bond. As regards the third hydrogen bond in the calix[4]arene anion, namely, the O(4)···H(4*A*)–O(3) bond, its parameters (2.573 Å, 1.740 Å, and 166.1°) are close to those of the stronger hydrogen bond formed by the O(2) oxygen atom. The spacing between the oxygen atoms (2.750 Å), which are not involved in hydrogen bonds, is a direct consequence of the closure of the cyclic fragment.

Structure of the Cation

The tris[triphenylphosphinegold(I)]oxonium cation with a dimer structure occupies a special position at the center of inversion of the crystal lattice under investigation. The structure of this cation is shown in Fig. 3. The oxonium oxygen atoms O(1) and O(1*A*) are characterized by a nonplanar bond configuration. In this case, the bond angles at each atom are equal to 92.2(2)°, 96.1(2)°, and 101.8(2)°. This geometry is typical of oxonium oxygen atoms involved in cationic complexes.

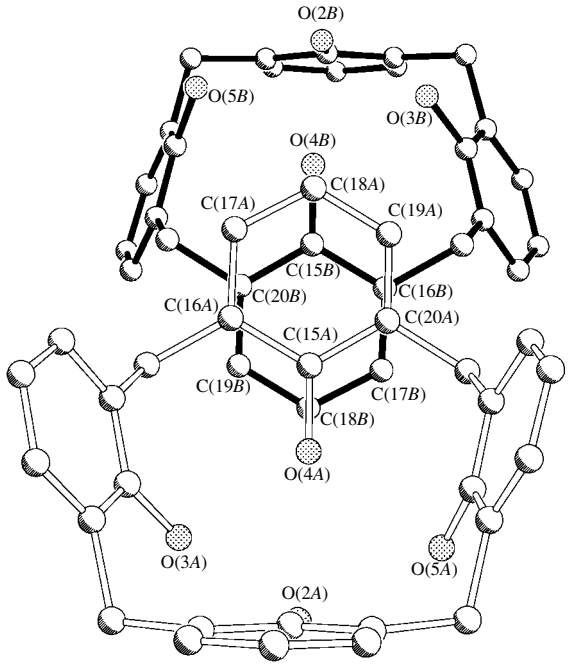

Fig. 5. Projection of a stacking pair onto the mean plane of the C(15*A*)··C(20*A*) benzene ring.

According to the Cambridge Structural Database (Version 5.22) [28], which contains information on the structures of 12 similar cationic complexes, the bond angles at the oxonium oxygen atoms in these structures vary in the range 90.9°–98.3°; i.e., these angles are less than the tetrahedral value (109.5°). It is interesting to note that, in triaurated thiooxonium, the bond angle at the central sulfur atom is less than 90°. Unlike the triaurated oxonium, its isolobal analogue, namely, trimercurated oxonium, has a nearly planar structure [29]. Such a distortion in the molecular geometry at the central atom in gold compounds is due to intramolecular aurophilic interactions [19–23], which occur in triaurated oxonium and thiooxonium structures at comparable distances. In triaurated oxonium and thiooxonium structures, the Au···Au distances can be identical only in the case when the bond angles at the sulfur atoms are smaller than those at the oxygen atoms, because the Au–S bond (~2.30 Å [28]) is longer than the Au–O bond (~2.03 Å [28]). Similar interactions between metal atoms are not characteristic of doubly charged mercury cations. Therefore, the geometry of the bonds in the studied molecule is governed by weak aurophilic interactions.

In the studied compound, the monomer units are joined into centrosymmetric dimers through aurophilic interactions. The Au···Au distances are equal to 2.9650(4), 3.0905(4), and 3.1836(4) Å in each monomer and 3.1880(5) Å between the monomer units. All the distances fall within the range corresponding to aurophilic interactions [19, 20].

As in all the known dimer structures of triaurated oxonium and thiooxonium, the gold atoms in the stud-

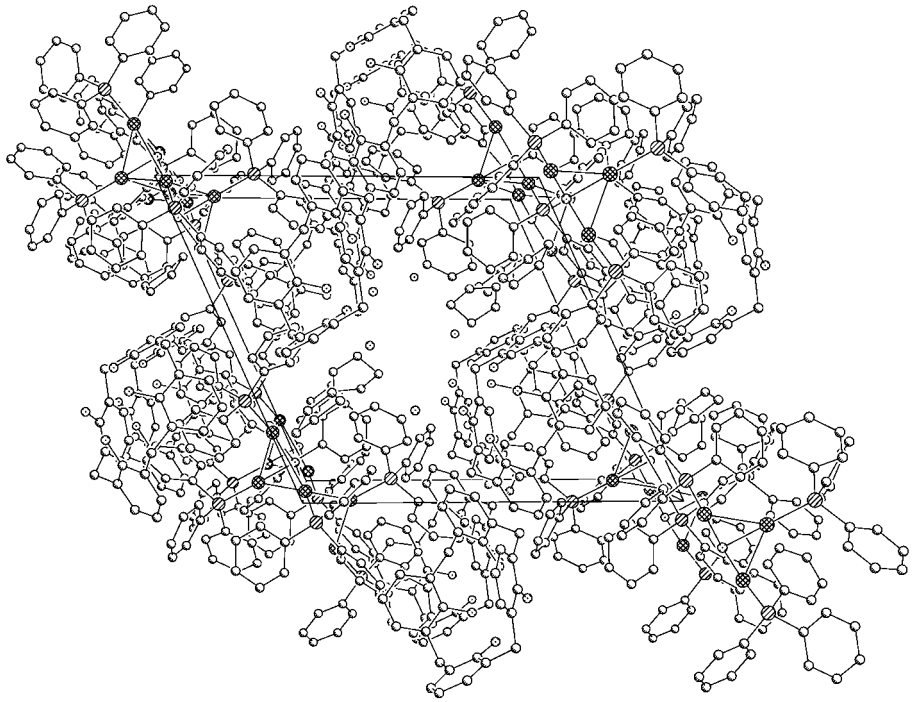

Fig. 6. Projection of a fragment of the crystal packing.

ied compound form a chair-shaped cage:

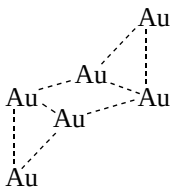

The oxygen atoms deviate from the planes of the Au_3 triangles toward each other, i.e., toward the central four-membered Au_4 ring.

The Au–O and Au–P bonds have standard lengths [2.032(5), 2.071(5), 2.083(6) and 2.221(2), 2.228(2), 2.228(2) Å, respectively]. The deviations from linear coordination of the gold atoms are very small [175.6(2)°, 178.3(1)°, and 177.3(2)°].

Packing of Structural Units in the Crystal

The mutual arrangement of the cations and anions in the studied crystal is also of considerable interest. It should be noted that the size of the dimer cation is substantially larger than that of the calix[4]arene anion. Consequently, it is this dimer that is the main structure-forming element of crystal packing. In this compound, according to the terminology accepted in supramolecular chemistry [1], just the dimer cation is the host, whereas the calix[4]arene anion has the role of a guest, which is not typical of calix[4]arenes.

In the crystal, two anions and one cation form a cluster in which the large-sized cation is capped by the two calix[4]arene anions on opposite sides, as is shown in Fig. 4. In turn, the {*A*–*K*–*A*} clusters form zigzag chains due to stacking interactions between one of the benzene rings of each anion and the centrosymmetrically related benzene ring of the adjacent cluster. Figure 5 shows the projection of a stacking pair onto the mean plane of the C(15*A*)···C(20*A*) benzene ring. The interplanar distance in this pair (3.425 Å) corresponds to stacking interactions in aromatic compounds.

The zigzag chains are packed in the crystal in such a way as to form extended cavities in the structure. In Fig. 6, such a cavity is located along the axis of projectivity at the center of the unit cell of the crystal lattice under investigation. It is these cavities of crystal packing that contain all the solvate molecules.

A comparison of the results obtained in the above two experiments allows us to draw the conclusion that the cavities formed in crystal packing are large enough to house different-type solvate molecules. Moreover, these cavities permit a disordered arrangement of the solvate molecules in the structure or incomplete occupation of their positions in the crystal.

ACKNOWLEDGMENTS

We are grateful to K.I. Grandberg for synthesizing the compound studied in our work.

This work was supported by the Russian Foundation for Basic Research (project nos. 99-07-90133 and 01-03-32474) and the Royal Society.

REFERENCES

1. J.-M. Lehn, *Supramolecular Chemistry: Concepts and Perspectives* (VCH, Weinheim, 1995).
2. C. D. Gutsche, *Calixarenes* (Royal Society of Chemistry, Cambridge, 1989).
3. J. L. Atwood, G. W. Orr, K. D. Robinson, and F. Hamada, Supramol. Chem. **2**, 309 (1993).
4. E. van Dienst, W. I. Iwema Bakker, J. F. Engbersen, *et al.*, Pure Appl. Chem. **65**, 387 (1993).
5. C. D. Gutsche, Aldrichimica Acta **28**, 3 (1995).
6. V. Böhmer, Angew. Chem., Int. Ed. Engl. **34**, 713 (1995).
7. C. D. Gutsche, in *Calixarenes*, Ed. by J. F. Stoddart (Royal Society of Chemistry, Cambridge, 1998).
8. A. Ikeda and S. Shinkae, Chem. Rev. **97**, 1713 (1997).
9. B. P. Hay, J. B. Nicholas, and D. Feller, J. Am. Chem. Soc. **122**, 10083 (2000).
10. R. F. Ziolo, S. Lipton, and Z. Dor, J. Chem. Soc., Chem. Commun., 1124 (1970).
11. J. C. Vickery, M. M. Olmstead, E. Y. Fung, and A. L. Balch, Angew. Chem., Int. Ed. Engl. **36**, 1179 (1997).
12. R. E. Allan, M. A. Beswick, M. A. Paver, *et al.*, Angew. Chem., Int. Ed. Engl. **35**, 208 (1996).
13. A. Bauer, W. Schneider, and H. Schmidbaur, Inorg. Chem. **36**, 2225 (1997).
14. Z. Assefa, R. J. Staples, and J. P. Fackler, Jr., Inorg. Chem. **33**, 2790 (1994).
15. I. J. B. Lin, C. W. Liu, I.-K. Liu, and Y.-Sh. Wen, Organometallics **11**, 1447 (1992).
16. S. F. Rice, S. J. Midler, H. B. Gray, *et al.*, Coord. Chem. Rev. **43**, 349 (1980).
17. D. C. Smith and H. B. Gray, Coord. Chem. Rev. **100**, 169 (1990).
18. Sh. Sh. Tang, Ch.-P. Chang, I. B. Lin, *et al.*, Inorg. Chem. **36**, 2294 (1997).
19. L. G. Kuz'mina, Koord. Khim. **25** (9), 643 (1999).
20. H. Shmidbaur, Gold Bull. **23**, 11 (1990).
21. P. Pyykkö and Yongfang Zhao, Angew. Chem., Int. Ed. Engl. **30** (5), 604 (1991).
22. P. Pyykkö, N. Runeberg, and F. Mendizabal, Chem.-Eur. J. **3** (9), 1451 (1997).
23. M. Barysz and P. Pyykkö, Chem. Phys. Lett. **285**, 398 (1998).
24. *Siemens Analytical X-ray Instruments* (1995).
25. G. M. Sheldrick, Acta Crystallogr., Sect. A: Found. Crystallogr. **46**, 467 (1990).
26. G. M. Sheldrick, *SHELXL97: Program for the Refinement of Crystal Structures* (Univ. of Göttingen, Göttingen, 1997).
27. D. M. Rudkevich, Chem.-Eur. J. **6** (15), 2679 (2000).
28. F. H. Allen and O. Kennard, Chem. Design Autom. News **8**, 1 (1993).
29. D. Grdenič, M. Sikirika, D. Matkovič-Calogovič, and A. Nagl, J. Organomet. Chem. **253** (3), 283 (1983).

Translated by O. Borovik-Romanova

Crystallography Reports, Vol. 48, No. 1, 2003, pp. 68–72. From Kristallografiya, Vol. 48, No. 1, 2003, pp. 73–77.

STRUCTURE OF ORGANIC COMPOUNDS

Crystal Structure Analysis of (Morpholino)(Phenyl)(Dicyclohexylamino) Phosphiniminocyclotrithiazene[1]

Srinivas Janaswamy*, G. Sreenivasa Murthy*, T. Mohan, and M. N. Sudheendra Rao****

** Department of Physics, Indian Institute of Technology Madras, Chennai, 600036 India*

*** Department of Chemistry, Indian Institute of Technology Madras, Chennai, 600036 India*

e-mail: srinivas@foodsci.purdue.edu

Received March 20, 2002

Abstract—The title compound $(C_6H_5)(C_4H_8NO)[N(C_6H_{11})_2]P{=}N{-}S_3N_3$ crystallizes in a triclinic crystal system with unit cell parameters a = 9.8884(4) Å, b = 10.6075(1) Å, c = 14.2276(2) Å, α = 78.14(3)°, β = 79.31(1)°, γ = 65.42(2)°, V = 1319.44(6) Å^3, Z = 2, and space group $P\bar{1}$. The cyclotrithiazene ring adopts a "distorted chair" conformation with a deviation of 0.682(7) Å for the tricoordinated sulfur atom. Remarkably, a short exocyclic S–N bond length 1.489(4) Å along with a large P–N–S angle 136.2(3)° are observed with the iminophosphorus moiety. *© 2003 MAIK "Nauka/Interperiodica".*

INTRODUCTION

Phosphiniminocyclotrithiazenes are the novel examples of monosubstituted cyclotrithiazenes [1–3]. Systematic structural study of these heterocycles helps to understand the bonding pattern in the cyclotrithiazene ring with different substituents attached to the phosphorus atom. Since the first crystal structure on triphenyl phosphiniminocyclotrithiazene [1] was reported, many new compounds of this family have been synthesized [4–6] and a few crystal structures were reported [7–9]. We have embarked on a systematic crystal structure determination of these heterocyclic systems [10–16] in order to understand the effect of various groups on the conformation of the cyclotrithiazene ring. Of the three groups attached to the phosphorus atom, only one has been varied, keeping the other two the same so as to study the conformational changes in the cyclotrithiazene ring, as well as in the iminonitrogen moiety. The two common substituents in this series are phenyl and dicyclohexylamino groups. The variant is an alicyclic ammo group, namely, pyrrolidino, piperidino, and morpholino in each of the compounds. The corresponding compounds have been labeled as *PYDPPC*, *PIDPPC*, and *MORPPC*, respectively, for brevity in the subsequent discussion. In this article we report the crystal structure of (morpholino)(phenyl)(dicyclohexylamino) phosphiniminocyclotrithiazene and compare the salient features with the reported structures.

EXPERIMENTAL

The compound was prepared from the reaction of S_4N_4 with the phosphine $(C_6H_5)(C_4H_8NO)[N(C_6H_{11})_2]P$

Table 1. Crystallographic data for *MORPPC*

Crystal system	Triclinic	μ, mm^{-1}	0.368
Space group	$P\bar{1}$	Crystal dimensions, mm	$0.12 \times 0.16 \times 0.30$
a, Å	9.8884(4)	θ range, deg	2–25
b, Å	10.6075(1)	Reflections measured/unique	3678
c, Å	14.2276(2)	Reflections observed [$I \geq 3\sigma(I)$]	3202
α, deg	78.14(3)	Number of parameters refined	438
β, deg	79.21(1)	$GOOF(F^2)$	1.109
γ, deg	65.42(2)	R_1	0.0592
V, Å^3	1319.44(6)	wR_2	0.1706
Z	2	$\Delta\rho_{max}/\Delta\rho_{min}$, e Å^{-3}	0.67/ –0.44
ρ_{calcd}, g/cm^3	1.326		

[1] This article was submitted by the authors in English.

1063-7745/03/4801-0068$24.00 © 2003 MAIK "Nauka/Interperiodica"

Table 2. Coordinates ($\times 10^4$) and isotropic thermal parameters U_{eq}/U_{iso} ($\times 10^3$ Å^2) for *MORPPC*

Atom	*x*	*y*	*z*	U_{eq}/U_{iso}	Atom	*x*	*y*	*z*	U_{eq}/U_{iso}
P	3886(1)	8352(1)	7777(1)	38(1)	H(2)	3150(60)	5840(60)	10880(40)	62(2)
S(1)	7033(1)	7687(2)	7842(1)	59(1)	H(3)	970(90)	5480(80)	10540(60)	120(3)
S(2)	8822(2)	8048(2)	6159(1)	95(1)	H(4)	380(80)	6160(70)	9040(50)	90(2)
S(3)	9033(3)	5382(2)	6991(3)	152(1)	H(5)	1730(50)	7250(50)	5890(40)	38(1)
N(1)	7219(5)	8613(5)	6777(4)	66(1)	H6)	3950(60)	9380(60)	7850(40)	47(1)
N(2)	9611(8)	6417(8)	6267(4)	126(1)	H(7)	5560(60)	8370(50)	5630(40)	63(1)
N(3)	7481(6)	6099(5)	7647(5)	94(2)	H(8)	3770(50)	9030(50)	4460(40)	54(1)
N(4)	5398(4)	8231(4)	8172(3)	48(1)	H(9)	2760(60)	8670(50)	5220(40)	49(2)
N(5)	4050(4)	7834(4)	6737(3)	48(1)	H(10)	4020(60)	5340(60)	5830(40)	59(2)
N(6)	2681(4)	9992(3)	7684(4)	38(1)	H(11)	2650(70)	6460(60)	6080(50)	83(2)
O	4086(5)	7011(4)	4968(3)	72(1)	H(12)	4290(50)	5910(50)	7230(40)	49(1)
C(1)	4313(6)	8640(6)	5807(3)	50(1)	H(13)	5770(60)	6030(50)	6430(40)	58(1)
C(2)	3573(8)	8443(6)	5066(4)	59(1)	H(14)	1280(50)	9490(50)	7270(30)	38(1)
C(3)	3800(9)	6231(7)	5856(4)	72(2)	H(15)	−109(50)	11350(50)	8480(40)	49(1)
C(4)	4594(8)	6336(5)	6621(4)	63(2)	H(16)	410(60)	9620(60)	8840(40)	62(1)
C(5)	3066(5)	7273(4)	8643(3)	46(1)	H(17)	−2159(70)	11050(60)	8610(50)	72(2)
C(6)	1916(6)	6983(5)	8453(4)	55(1)	H(18)	−1329(60)	9960(60)	7900(40)	53(2)
C(7)	1201(7)	6314(6)	9170(5)	69(2)	H(19)	−2899(80)	11900(60)	6960(40)	81(2)
C(8)	1628(7)	5913(6)	10076(5)	72(2)	H(20)	−2029(60)	12550(60)	7300(40)	50(2)
C(9)	2806(8)	6164(6)	10279(4)	68(2)	H(21)	−859(60)	12480(60)	5800(40)	56(2)
C(10)	3495(8)	6838(6)	9557(4)	56(1)	H(22)	−629(60)	11090(60)	6000(40)	55(2)
C(11)	1167(5)	10299(5)	7437(3)	43(1)	H(23)	1500(60)	11320(60)	6080(40)	65(2)
C(12)	−46(6)	10558(6)	8307(4)	55(1)	H(24)	660(50)	12340(50)	6770(30)	35(1)
C(13)	−1536(7)	10776(9)	8010(6)	76(2)	H(25)	1810(40)	11930(40)	7970(30)	21(1)
C(14)	−2001(7)	11894(1)	7181(6)	82(2)	H(26)	4070(70)	9970(60)	9200(40)	74(2)
C(15)	−796(7)	11723(9)	6315(5)	73(2)	H(27)	2530(60)	10540(60)	9480(40)	59(2)
C(16)	709(6)	11503(6)	6605(4)	52(1)	H(28)	1710(80)	13140(70)	9380(50)	100(2)
C(17)	2803(5)	11149(4)	8063(3)	40(1)	H(29)	3030(80)	11940(70)	9950(50)	80(2)
C(18)	3036(7)	10877(7)	9118(4)	61(1)	H(30)	4970(90)	12240(80)	8790(50)	100(2)
C(19)	2944(8)	12234(9)	9412(6)	81(2)	H(31)	3950(70)	13530(80)	8920(50)	80(2)
C(20)	4052(7)	12766(8)	8764(7)	93(3)	H(32)	4550(90)	13140(70)	7510(50)	100(2)
C(21)	3808(7)	13009(6)	7740(6)	76(2)	H(33)	2790(60)	13800(60)	7750(40)	63(2)
C(22)	3906(7)	11706(6)	7408(5)	55(1)	H(34)	3840(70)	11790(60)	6760(50)	72(2)
H(1)	4030(50)	6970(50)	9630(30)	21(1)	H(35)	4620(60)	11160(50)	7430(40)	37(2)

in acetonitrile at room temperature [6]. Red parallelepiped crystals were obtained by slow evaporation from the mixture of CH_2Cl_2–CH_3CN (1 : 2). A crystal of dimensions 0.12 × 0.16 × 0.30 mm was selected for data collection. The intensity data were collected at room temperature in ω/2θ-scan mode on an Enraf-Nonius CAD-4 diffractometer using graphite monochromated λMoK_α radiation and corrected for Lorentz and polarization effects. The structure was solved by direct methods using SHELXS86 [17] and refined by the full-matrix least squares method using SHELXL97 [18]. All the non-hydrogen atoms were refined with anisotropic thermal parameters and the hydrogen atoms, located from the difference electron density maps during the intermediate stages of refinement, were refined with isotropic displacement parameters. The crystal data, along with the details of structure refinement, are listed in Table 1.

Table 3. Selected bond lengths *d* (Å), bond angles ω (deg) and torsion angles φ (deg) for *MORPPC*

Bond	*d*	Bond	*d*
S(1)–N(1)	1.652(5)	P–N(4)	1.641(4)
S(1)–N(3)	1.623(6)	P–N(5)	1.640(4)
S(1)–N(4)	1.489(4)	P–N(6)	1.644(4)
S(2)–N(1)	1.597(5)	P–C(5)	1.817(4)
S(2)–N(2)	1.561(8)	P…….S(1)	2.91(1)
S(2)–N(2)	1.558(7)	S(3)–N(3)	1.610(6)
Bond angle	ω	Bond angle	ω
N(1)–S(1)–N(3)	106.7(3)	N(4)–P–N(5)	118.7(2)
S(1)–N(1)–S(2)	116.3(3)	N(4)–P–N(6)	109.3(2)
N(1)–S(2)–N(2)	114.0(3)	N(5)–P–N(6)	106.2(2)
S(2)–N(2)–S(3)	125.1(4)	N(4)–P–C(5)	108.5(2)
N(2)–S(3)–N(3)	115.4(3)	N(5)–P–C(5)	104.5(2)
S(3)–N(3)–S(1)	117.7(3)	N(6)–P–C(5)	109.4(2)
N(1)–S(1)–N(4)	105.8(2)	P–N(4)–S(1)	136.2(3)
N(3)–S(1)–N(4)	105.7(3)		
Torsion angle	φ	Torsion angle	φ
S(1)–N(1)–S(2)–N(2)	35.8(5)	N(1)–S(2)–N(2)–S(3)	−6.9(9)
S(2)–N(2)–S(3)–N(3)	1.2(9)	N(2)–S(3)–N(3)–S(2)	−24.9(7)
S(3)–N(3)–S(1)–N(1)	49.9(5)	N(3)–S(1)–N(1)–S(1)	−56.0(4)

RESULTS AND DISCUSSION

The title compound is the third in the series $(R)(C_6H_5)[N(C_6H_{11})_2]P{=}N{-}S_3N_3$, for which the crystal structure has been determined. The alicyclic amino-group *R* is C_4H_8N (pyrrolidino) [10] and $C_5H_{10}N$ (piperidino) [12] for the earlier reported examples. The fractional coordinates and equivalent isotropic thermal parameters with their standard deviations for all the atoms of the title compound are listed in Table 2. The molecular structure [19] with the atom numbering scheme is shown in the figure. Selected bond lengths, bond angles and torsion angles are summarized in Table 3. The dissimilar bond distances found with the skeletal sulfur atoms are presumably due to different hybridization they invoke in the bond formation. These distances can be broadly categorized into three groups: (i) 1.652(5) and 1.623(6) Å, (ii) 1.610(6) and 1.597(5) Å, and (iii) 1.561(8) and 1.558(7) Å. Similar S–N bond distances are also evidenced in other members of phosphiniminocyclotrithiazenes [10–16], $(C_6H_5)_3As{=}N{-}S_3N_3$, [20] $(p\text{-}CH_3C_6H_4)_3As{=}N{-}S_3N_3$ [21] and some acyclic sulfur-nitrogen compounds [22]. Strikingly, the two long bonds [of group (i)] in the heterocycles involve the tricoordinated sulfur atom S(1); this feature is consistent in the phosphiniminocyclotrithiazenes family. The shortest bond observed in the ring [1.578(6) *PYDPPC*, 1.560(4) *PIDPPC*, and 1.558(7) Å *MORPPC*] is close to S=N double bond distance 1.55 Å [23]. The pK_α values [24] of the variant amines in the corresponding compounds are 11.31, 11.12, and 8.49 respectively. It can be seen that as the basicity of the amine increases, the sulfur-nitrogen bond tends to approach the double bond distance. The six endocyclic bond angles agree well in all the three compounds. The tricoordinated sulfur atom deviates from the mean plane of the other five atoms by 0.682(7) Å. This value agrees well with the other two members of the series (0.656 Å in *PYDPPC* and 0.686 Å in *PIDPPC*). The trend of the signs of the torsion angles (Table 3) reveals that the puckering in the ring is towards a distorted chair conformation. Only the anion $S_3N_3^-$ has a planar conformation [25].

In the present case, morpholino moiety has also brought noticeable changes to the P–N(4)=S(1) fragment. It is seen that the S(1)–N(4) bond distance has decreased significantly from 1.580(4) Å (in *PYDPPC*) to 1.490(4) Å (in *MORPPC*). Correspondingly, the P–N(4)=S(1) bond angle increase from 120.8(2)° (in *PYDPPC*) to 136.2(3)° (in *MORPPC*) is observed. Interestingly, the non-bonded P⋯S(1) distance also shows a corresponding increase in the present structure, 2.76(1) Å (*PYDPPC*) and 2.91(1) Å (*MORPPC*). This trend can be attributed to the reverse donation [26, 27]

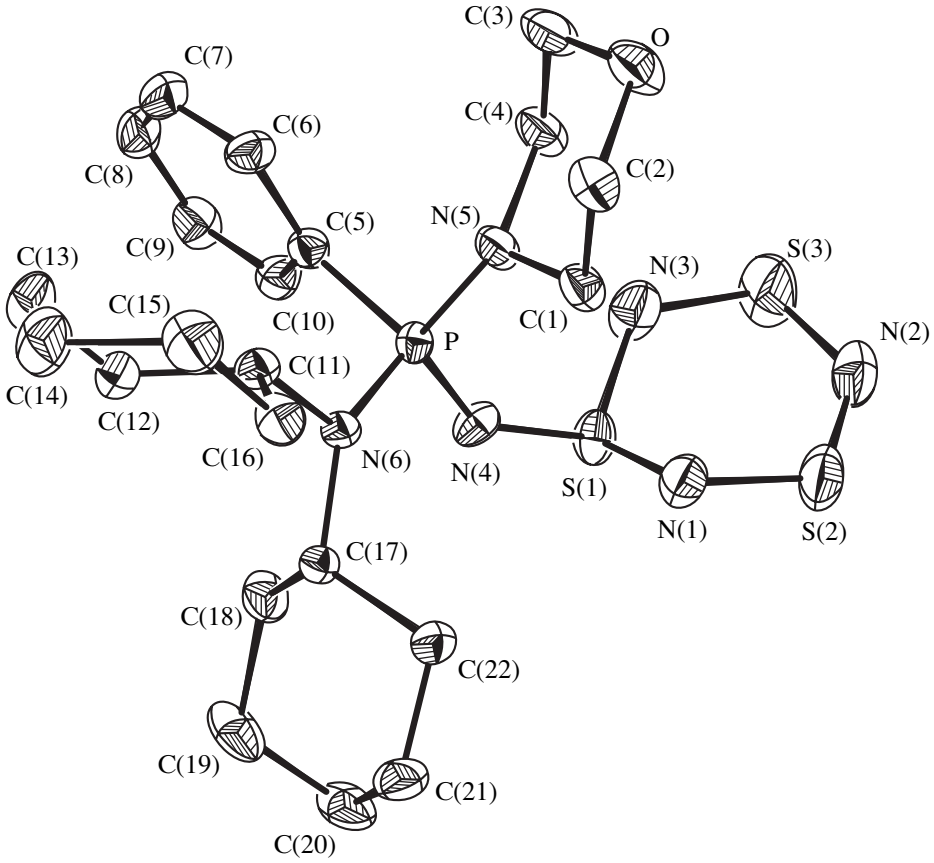

The ORTEP-13 [19] of $(OC_4H_8N)(C_6H_5)[N(C_6H_{11})_2]P{=}N{-}S_3N_3$. The thermal ellipsoids are at 50% probability level (the H atoms are omitted).

ability of nitrogen of a lone electron pair to the phosphorus, that is influenced by the substituents attached to phosphorus, as one would anticipate. The interaction of P–N=S moiety with the π-bonding feature of the cyclotrithiazene ring may also be important in explaining the trends observed in the bonding characteristics.

The phosphorus–nitrogen distances arising from the two amino groups attached to phosphorus are considerably shorter than the expected $P(sp^3)$–$N(sp^2)$ bond length 1.77 Å [28] but resemble those observed in phosphazenes [29, 30]. The trend is suggestive of the presence of a π-character in these bonds. The phosphorus atom has a distorted tetrahedral geometry. The phenyl ring is planar. The dicyclohexylamino and morpholino groups adopt a chair conformation with normal bond lengths and angles. In the structure, no hydrogen bonds or short contacts are observed, and the molecules are held by van der Waals forces.

ACKNOWLEDGMENTS

S. Janaswamy is grateful to Dr. Babu Varghese and Sri M.V. Rao for their encouragement and helpful discussions. We thank the management, RSIC, HI Madras, Chennai, for the use of the Enraf-Nonius GAD-4 diffactometer.

REFERENCES

1. E. M. Holt and S. L. Holt, J. Chem. Soc. Dalton Trans., 1990 (1974).
2. T. Chivers, R. T. Oakley, A. W. Cordes, and W. T. Pinnington, J. Chem. Soc. Chem. Commun., 1214 (1981).
3. C. Spang, F. T. Edelmann, M. Noltemeyer, and H. W. Roesky, Chem. Ber. **122**, 1247 (1986).
4. A. J. Elias and M. N. S. Rao, Inorg. Chim. Acta **164**, 45 (1989).
5. C. J. Thomas and M. N. S. Rao, Heteroatom. Chem. **3**, 321 (1992).
6. T. Mohan and M. N. S. Rao, Heteroatom. Chem. **8**, 225 (1997).
7. S. W. Liblong, R. T. Oakly, A. W. Cordes, and M. C. Noble, Can. J. Chem. **61**, 2062 (1983).
8. A. J. Elias, M. N. S. Rao, and Varghese Babu, Polyhedron **9**, 1433 (1990).
9. C. J. Thomas, K. K. Bhandary, L. M. Thomas, *et al.*, Bull. Chem. Soc. Jpn. **66**, 1830 (1993).
10. J. Srinivas, G. S. Murthy, T. Mohan, and M. N. S. Rao, Acta Crystallogr., Sect. C: Cryst. Struct. Commun. **52**, 1250 (1996).

11. J. Srinivas, G. S. Murthy, L. M. Thomas, and M. N. S. Rao, J. Chem. Cryst. **26** (6), 403 (1996).
12. J. Srinivas, G. S. Murthy, T. Mohan, and M. N. S. Rao, Z. Kristallogr. **212**, 323 (1997).
13. J. Gopalakrishnan, M. N. S. Rao, J. Srinivas, and G. S. Murthy, Polyhedron **16** (7), 1089 (1997).
14. J. Gopalakrishnan, J. Srinivas, G. S. Murthy, and M. N. S. Rao, Proc.-Indian Acad. Sci., Chem. Sci. **110** (2), 89 (1998).
15. J. Gopalakrishnan, J. Srinivas, G. S. Murthy, and M. N. S. Rao, Indian J. Chem. A **37** (12), 1052 (1998).
16. J. Srinivas, G. S. Murthy, U. Swarnalatha, and M. N. S. Rao, J. Chem. Cryst. **31** (5), 323 (2002).
17. G. M. Sheldrick, *SHELXS86: Program for the Solution of Crystal Structures* (University of Göttingen, Göttingen, 1986).
18. G. M. Sheldrick, *SHELXL97: Program for the Refinement of Crystal Structures* (University of Göttingen, Göttingen, 1997).
19. L. J. Farrugia, J. Appl. Crystallogr. **30**, 565 (1997).
20. E. M. Holt, S. L. Holt, and K. J. Watson, J. Chem. Soc. Dalton Trans., 514 (1977).
21. C. J. Thomas, R. Cea-Olivares, G. Espinosa-Pérez, and R. W. Turner, J. Organomet. Chem. **493**, 101 (1995).
22. A. Haas, Ch. Klare, P. Betz, *et al.*, Inorg. Chem. **35**, 1918 (1996).
23. J. W. Bats, P. Coppens, and T. P. Koetzle, Acta Crystallogr., Sect. B: Struct. Crystallogr. Cryst. Chem. **33**, 37 (1977).
24. J. A. Dean, *Handbook of Organic Chemistry* (McGraw-Hill, New York, 1987).
25. J. Bojes, T. Chivers, W. G. Laidlaw, and M. Trsic, J. Am. Chem. Soc. **101**, 4517 (1979).
26. D. P. Craig and N. L. Paddock, J. Chem. Soc., 4118 (1962).
27. C. A. Coulson, Nature **221**, 1106 (1969).
28. D. W. J. Cruickshank, Acta Crystallogr. **17**, 671 (1964).
29. A. Kilic, S. Beges, Z. Kilic, and T. Hokelek, J. Mol. Struct. **516**, 255 (2000).
30. J. Brinek, M. Alberti, J. Marek, *et al.*, Polyhedron **17** (8), 3235 (1998).

Crystallography Reports, Vol. 48, No. 1, 2003, pp. 73–83. Translated from Kristallografiya, Vol. 48, No. 1, 2003, pp. 78–88.

STRUCTURE OF ORGANIC COMPOUNDS

Design of Molecules and Noncentrosymmetric Crystals of 3-(4-Nitrophenyl)-2-Phenylacrylic Acid Derivatives

L. N. Kuleshova, V. N. Khrustalev, K. Yu. Suponitskiĭ, M. Yu. Antipin, D. V. Gusev, and E. S. Bobrikova

Nesmeyanov Institute of Organoelement Compounds, Russian Academy of Sciences, ul. Vavilova 28, Moscow, 119991 Russia

e-mail: lukul@xrlab.ineos.ac.ru

Received December 25, 2001

Abstract—The derivatives of 3-(4-nitrophenyl)-2-phenylacrylic acid are synthesized. It is shown that the chemical modification of this acid results in a change in the symmetry of the supramolecular fragment formed by molecules in the crystal. In turn, this change leads to a change in the crystal symmetry and favors the formation of a noncentrosymmetric crystal structure. The crystal structures of 3-(4-nitrophenyl)-2-phenylacrylic acid (**I**), 3-(4-nitrophenyl)-2-phenyl-triethyl aminoacrylate (**II**), and 3-(4-nitrophenyl)-2-phenylacrylic acid (3-methoxy)phenyl ester (**III**) are investigated by X-ray diffraction. © *2003 MAIK "Nauka/Interperiodica".*

INTRODUCTION

As is known, molecular first-order nonlinear optical effects can be observed in organic asymmetric conjugate chromophore molecules. Manifestation of the nonlinear optical effect in a condensed phase requires a noncentrosymmetric arrangement of molecules in the crystal or in the polymeric matrix. Unfortunately, an obvious direct way of attaining an acentric molecular order on the macroscopic level—the growth of noncentrosymmetric crystals of compounds capable of exhibiting molecular nonlinear properties—is not the easiest and most efficient method. This can be explained by the fact that, for the most part, organic compounds crystallize in the centrosymmetric space groups [1], which exclude the manifestation of the nonlinear optical activity in the solid phase. Moreover, it turns out that the acentric crystal structure is a necessary but not sufficient condition, because the optimum arrangement of nonlinear optically active molecules with respect to the polar direction in the crystal is required to achieve a nonlinear optical effect.

Although the empirical approaches to the preparation of acentric crystals have long been known (some of them are described in detail in monograph [2]), researchers sometime face insurmountable obstacles in producing noncentrosymmetric crystals of promising molecular compounds. It should be noted that the reason for the predominance of centrosymmetric crystalline compounds remains unclear. Furthermore, it was revealed that centrosymmetric structures are not thermodynamically preferable [3] and that their formation is not governed by the dipole molecule moment as a factor compensating for the parallel dipole orientation [4]. This implies that the decrease in the dipole molecule moment (recommended in [2]) is not an efficient method of designing the noncentrosymmetric crystal structures. Moreover, it was demonstrated that hydrogen bonds play an important role in the formation of noncentrosymmetric crystals; however, this contribution of hydrogen bonds is determined by the formation of acentric local packing fragments [5, 6] rather than by the decrease in the dipole molecule moment due to the formation of intermolecular hydrogen bonds, as was assumed in [2]. In other words, the ability of molecules to form strong noncentrosymmetric local fragments through intermolecular hydrogen bonds or other specific interactions leads to an increase in the probability of forming noncentrosymmetric crystal structures.

In the present work, we attempted to obtain noncentrosymmetric crystals of 3-(4-nitrophenyl)-2-phenylacrylic acid derivatives by way of changing the symmetry of a local supramolecular fragment. Moreover, we performed an X-ray diffraction investigation of the crystal structures of 3-(4-nitrophenyl)-2-phenylacrylic acid 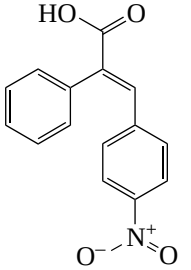 (**I**), 3-(4-nitrophenyl)-2-phenyl-

1063-7745/03/4801-0073$24.00 © 2003 MAIK "Nauka/Interperiodica"

triethyl aminoacrylate 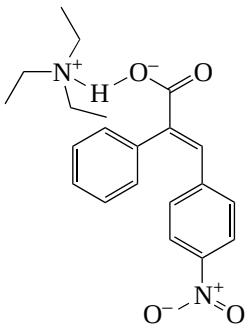 (**II**), and 3-(4-nitrophenyl)-2-phenylacrylic acid (3-methoxy)phenyl ester 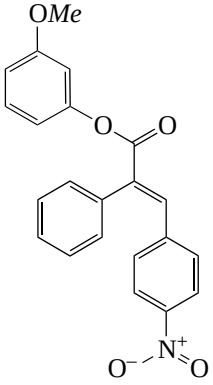 (**III**).

EXPERIMENTAL

Synthesis. Acid **I** was synthesized according to the procedure described in [7]. Needle-shaped, light yellow crystals of compound **I** (T_m = 214°C) precipitated from isopropanol.

Bulk platelike, light yellow crystals of compound **II** (T_m = 100–104°C) were grown by a slow evaporation of a solution containing acid **I** (0.1 g, 0.0004 mol), isopropanol (1 ml), and triethylamine (0.22 g, 0.3 ml, 0.002 mol).

Compound **III** was prepared as follows. Chloroform (6 ml) and thionyl chloride (0.71 g, 0.44 ml, 0.006 mol) were added to acid **I** (1.34 g, 0.005 mol). The mixture was boiled for 4 h. The dark yellow transparent solution obtained was evaporated under vacuum. The precipitate was dissolved in chloroform (10 ml). Then, pyridine (0.61 g, 0.005 mol) was added, and the mixture was boiled for 5 min. The prepared solution was sequentially washed in a 5% HCl solution, water, 5% NaOH solution, and water. Thereafter, the product was evaporated under vacuum and recrystallized from a toluene–petroleum ether mixture. The yield was 1.31 g (70%). Light yellow, prismatic crystals **III** (T_m = 142°C) were grown from isopropanol.

X-ray diffraction analysis. Crystals **I** ($C_{15}H_{11}NO_4$, M = 269.25) are monoclinic, space group $P2_1/c$, at 110 K: a = 11.475(6) Å, b = 5.641(3) Å, c = 19.150(10) Å, β = 98.439(11)°, V = 1226.3(11) Å^3, Z = 4, d_{calcd} = 1.458 g/cm^3, $F(000)$ = 560, and μ = 0.107 mm^{-1}.

Crystals **II** ($C_{21}H_{26}N_2O_4$, M = 370.44) are triclinic, space group $P\bar{1}$, at 298 K: a = 12.441(2) Å, b = 12.957(2) Å, c = 13.709(2) Å, α = 79.604(5)°, β = 80.343(5)°, γ = 63.065(4)°, V = 1928.4(6) Å^3, Z = 4, d_{calcd} = 1.276 g/cm^3, $F(000)$ = 792, and μ = 0.089 mm^{-1}.

Crystals **III** ($C_{22}H_{17}NO_5$, M = 375.37) are monoclinic, space group Pn, at 298 K: a = 6.0176(12) Å, b = 12.572(3) Å, c = 12.865(3) Å, β = 102.97(3)°, V = 948.4(3) Å^3, Z = 2, d_{calcd} = 1.314 g/cm^3, $F(000)$ = 392, and μ = 0.094 mm^{-1}.

The unit cell parameters and the intensities of 6328, 5613, and 2478 reflections (for structures **I**, **II**, and **III**, respectively) were measured on a SMART CCD 1000 automated diffractometer (compound **I**; T = 110 K; λMoK_α; ω scan mode; step width, 0.3°; exposure time per frame, 10 s; θ_{max} = 25°) and a Siemens P3/PC automated diffractometer (compounds **II** and **III**, T = 298 K, λMoK_α, $\theta/2\theta$ scan mode, θ_{max} = 23° for **II** and 28° for **III**). The structures were solved by direct methods and refined using the full-matrix least-squares procedure in the anisotropic approximation for the nonhydrogen atoms. In crystal **II**, the ethyl groups in one of the two independent triethylammonium cations are disordered over two positions with equal occupancies.

For the most part, the hydrogen atoms were independently located from the difference Fourier syntheses and refined in the isotropic approximation. The exceptions were the hydrogen atoms of the ethyl groups of two independent triethylammonium cations in compound **II**, whose positions were geometrically calculated and refined in the isotropic approximation with fixed positional (a riding model) and thermal parameters: $U_{iso}(H) = 1.5U_{eq}(C)$ for CH_3 groups and $U_{iso}(H) = 1.2U_{eq}(C)$ for CH_2 groups. The final discrepancy factors are as follows: R_1 = 0.0625 for 1388 independent reflections with $I > 2\sigma(I)$ and wR_2 = 0.1630 for all 2165 independent reflections for structure **I**, R_1 = 0.0891 for 2867 independent reflections with $I > 2\sigma(I)$ and wR_2 = 0.2438 for all 4801 independent reflections for structure **II**, and R_1 = 0.0421 for 2125 independent reflections with $I > 2\sigma(I)$ and wR_2 = 0.1115 for all 2478 independent reflections for structure **III**.[1] All the calculations were performed with the SHELXTL PLUS (Version 5.10) software package [8]. The atomic coordinates are listed in Tables 1–3.

RESULTS AND DISCUSSION

The choice of the 4-nitrophenyl derivatives of acrylic acid as model systems for designing molecules and noncentrosymmetric crystals was motivated by the possibility of easily modifying the molecular structure and tendency for these compounds to undergo cocrys-

[1] The relatively large factor R for structure **II** was explained by the poor quality of the crystal, which, in addition, slowly decomposed in the course of data collection.

tallization with organic amines and other electron-donor systems [9–12]. The crystal structure of 4-nitrophenylacrylic acid was investigated by Kageyama *et al.* [13]. This compound exists in the form of an *E* isomer with respect to the double bond, the molecule is planar (the mean deviation of atoms from the root-mean-square plane of the molecule is equal to 0.003 Å), and the atoms of the carboxyl group are involved in a common molecular conjugate chain. As in the majority of other carboxylic acids, the molecules of 4-nitrophenylacrylic acid in the crystal are linked into centrosymmetric dimers through intermolecular hydrogen bonds between the carboxyl groups, which is responsible for the formation of centrosymmetric crystals. Recent attempts have been made to prevent the formation of centrosymmetric dimers (and, thus, to obtain acentric crystals) through cocrystallization with organic bases (amines) [9] and a number of donor–acceptor systems [10–12]. However, these attempts have failed, even though this approach, as applied to other compounds, often leads to good results.

In this work, we attempted to avoid the formation of centrosymmetric dimers characteristic of carboxylic acids through the screening of the carbonyl group in the derivatives of acid **I**. For this purpose, we grew crystal **II** (by cocrystallization of acid **I** with triethylamine). Moreover, we synthesized (3-methoxy)phenyl ester **III** and methyl ester **IV** of acid **I**. According to the Cambridge Structural Database, ester **IV** was studied earlier by Tinant *et al.* [14]. For this reason, we carried out X-ray diffraction analysis only for crystals of ester **III**.

Molecular geometry. A general view of the studied molecules and the atomic numbering are given in Fig. 1. The main geometric characteristics are presented in Table 4. The bond lengths and bond angles in the molecules have typical values [15, 16]. As a whole, the molecular structures of all the compounds synthesized (including ester **IV**) differ insignificantly. The alternation of bond lengths is clearly observed in the C(1)–C(2)=C(3)–C(4) chain. As in the aforementioned 4-nitrophenylacrylic acid, the carboxyl groups are likely involved in the conjugation. However, the C(1)–C(2) bond length in the independent molecules in crystal **II** is actually equal to the length of the C–C single bond [15, 16]. Furthermore, in the 2-phenyl derivatives of acrylic acid, the mean atomic deviations from the root-mean-square plane passing through the O(1), O(2), C(1)–C(10), and N(1) atoms are relatively large and equal to 0.147 Å in **I**, 0.192 and 0.128 Å in **II**, 0.166 Å in **III**, and 0.151 Å in **IV**. The C(9)–C(4)–C(3)–C(2) torsion angles indicate that virtually planar acrylic acid and *p*-nitrophenyl fragments in the molecules are rotated with respect to each other by 26.4(4)° in **I**, –37.1(7)° and 35.4(6)° in **II**, 29.3(4)° in **III**, and 161.4° in **IV**. The dihedral angles are equal to 28.3°, 40.9° and 23.3°, 144.8°, and 157.5°, respectively. The plane of the phenyl ring at the C(2) atom is rotated with respect to the root-mean-square plane of the other part of the molecule through an angle of 68.6° in molecule **I**, 118.1° and 60.5° in independent molecules **II**, 114.3° in molecule **III**, and 68.0° in molecule **IV**, which excludes the conjugation. The methoxy group at the C(20) atom in molecule **III** is also rotated relative to the root-mean-square plane of the molecule by an angle of 68.6°.

Table 1. Atomic coordinates ($\times 10^4$) and isotropic equivalent (isotropic for H atoms) thermal parameters (Å^2, $\times 10^3$) for structure **I**

Atom	*x*	*y*	*z*	U_{eq}/U_{iso}
O(1)	9153(2)	7595(4)	229(1)	35(1)
O(2)	9695(2)	6251(3)	–774(1)	36(1)
O(3)	4016(2)	18383(4)	–1939(1)	42(1)
O(4)	4014(2)	19321(4)	–841(1)	44(1)
N(1)	4356(2)	18112(4)	–1303(1)	35(1)
C(1)	9138(2)	7664(5)	–467(2)	32(1)
C(2)	8390(2)	9536(5)	–846(2)	29(1)
C(3)	7778(2)	10974(5)	–469(2)	31(1)
C(4)	6905(2)	12790(5)	–717(2)	29(1)
C(5)	6716(2)	14607(5)	–246(2)	31(1)
C(6)	5885(2)	16358(5)	–430(2)	32(1)
C(7)	5235(2)	16266(5)	–1093(2)	29(1)
C(8)	5372(2)	14471(5)	–1571(2)	31(1)
C(9)	6215(2)	12762(5)	–1379(2)	31(1)
C(10)	8385(2)	9684(5)	–1626(2)	30(1)
C(11)	8868(2)	11655(5)	–1913(2)	31(1)
C(12)	8883(3)	11787(5)	–2639(2)	34(1)
C(13)	8392(2)	10010(5)	–3073(2)	35(1)
C(14)	7902(3)	8047(5)	–2793(2)	35(1)
C(15)	7907(2)	7876(5)	–2073(2)	33(1)
H(1O)	9600(30)	6350(60)	403(16)	45(9)
H(3)	7980(30)	10860(50)	32(17)	36(8)
H(5)	7200(30)	14680(60)	228(17)	45(9)
H(6)	5760(20)	17710(50)	–112(4)	35(8)
H(8)	4860(30)	14450(50)	–2017(16)	37(8)
H(9)	6350(20)	11480(50)	–1685(14)	28(7)
H(11)	9190(20)	12950(50)	–1603(14)	27(7)
H(12)	9220(30)	13130(60)	–2823(15)	40(8)
H(13)	8420(20)	9990(50)	–3575(16)	26(7)
H(14)	7540(30)	6830(60)	–3108(16)	44(9)
H(15)	7520(20)	6580(50)	–1895(14)	30(7)

Molecular packing. As could be expected, molecules **I** in the crystal form characteristic centrosymmetric dimers through the OH···O bonds between the carboxyl groups [O(1)···O(2), 2.673(4) Å; H(10)···O(2), 1.77(4) Å; angle at the H atom, 173(3)°]. These dimers are joined into ribbons along the O*X* axis owing to the weaker but also centrosymmetric pairs of the contacts

Table 2. Atomic coordinates (Å $\times 10^4$; for H atoms, $\times 10^3$) and isotropic equivalent (isotropic for H atoms) thermal parameters (Å^2, $\times 10^3$) for structure **II**

Atom	*x*	*y*	*z*	U_{eq}/U_{iso}
O(1)	320(3)	3284(2)	1239(2)	48(1)
O(2)	517(3)	1502(3)	1190(2)	42(1)
O(3)	−5208(3)	884(3)	5979(2)	43(1)
O(4)	−4477(3)	1614(3)	6843(2)	46(1)
N(1)	−4545(3)	1321(3)	6065(3)	34(1)
C(1)	49(4)	2443(4)	1533(3)	36(1)
C(2)	−971(4)	2644(3)	2378(3)	33(1)
C(3)	−1337(4)	1804(4)	2699(3)	33(1)
C(4)	−2219(3)	1747(3)	3548(3)	29(1)
C(5)	−2931(4)	1181(3)	3495(3)	31(1)
C(6)	−3715(4)	1062(3)	4307(3)	31(1)
C(7)	−3755(4)	1481(3)	5176(3)	28(1)
C(8)	−3060(4)	2047(4)	5247(4)	33(1)
C(9)	−2296(4)	2164(4)	4426(3)	32(1)
C(10)	−1541(4)	3775(3)	2800(3)	31(1)
C(11)	−2780(4)	4469(4)	2787(3)	37(1)
C(12)	−3348(4)	5511(4)	3214(3)	37(1)
C(13)	−2672(4)	5871(4)	3643(3)	40(1)
C(14)	−1445(4)	5197(4)	3654(3)	41(1)
C(15)	−873(4)	4169(4)	3222(3)	36(1)
N(2)	1952(3)	2845(3)	−345(3)	42(1)
C(16*A*)	2054(9)	3891(8)	−754(7)	39(2)
C(16*B*)	2760(10)	3496(9)	−251(9)	56(3)
C(17)	2195(5)	4506(6)	101(4)	75(2)
C(18*A*)	3024(10)	1781(11)	36(9)	34(3)
C(18*B*)	2763(13)	1638(12)	−334(12)	50(3)
C(19*A*)	3628(12)	1248(11)	−1227(10)	67(4)
C(19*B*)	4057(12)	1246(12)	−757(12)	67(4)
C(20*A*)	1465(7)	2456(7)	−1170(6)	29(2)
C(20*B*)	1219(9)	3496(9)	−1136(8)	55(3)
C(21)	283(6)	3117(5)	−1296(4)	71(2)
O(1')	−5659(3)	6814(3)	8477(2)	46(1)
O(2')	−5346(2)	8143(2)	9055(2)	41(1)
O(3')	166(3)	9133(3)	4180(2)	47(1)
O(4')	−574(3)	8470(3)	3266(3)	47(1)
N(1')	−512(3)	8717(3)	4071(3)	36(1)
C(1')	−5112(4)	7417(4)	8446(6)	35(1)
C(2')	−4100(4)	7303(3)	7616(3)	34(1)
C(3')	−3717(4)	8138(4)	7376(3)	34(1)
C(4')	−2862(3)	8250(3)	6533(3)	28(1)
C(5')	−2101(4)	8753(3)	6629(3)	30(1)
C(6')	−1310(4)	8888(3)	5830(3)	31(1)
C(7')	−1309(3)	8545(3)	4931(3)	30(1)
C(8')	−2050(4)	8048(3)	4815(4)	33(1)
C(9')	−2831(4)	7914(4)	5618(3)	33(1)
C(10')	−3555(3)	6228(3)	7106(3)	31(1)

Table 2. (Contd.)

Atom	*x*	*y*	*z*	U_{eq}/U_{iso}
C(11')	−2311(4)	5523(4)	7109(3)	36(1)
C(12')	−1747(4)	4526(4)	6625(3)	40(1)
C(13')	−2435(5)	4233(4)	6124(3)	42(1)
C(14')	−3649(4)	4932(4)	6101(3)	41(1)
C(15')	−4224(4)	5909(4)	6606(3)	36(1)
N(2')	−7032(3)	7908(3)	10418(3)	35(1)
C(16')	−6625(4)	6637(4)	10791(4)	41(1)
C(17')	−5461(5)	6125(6)	11242(5)	63(2)
C(18')	−7168(4)	8648(4)	11199(3)	40(1)
C(19')	−8085(5)	8645(5)	12071(4)	43(1)
C(20')	−8159(4)	8341(4)	9895(3)	34(1)
C(21')	−8545(5)	9585(4)	9394(4)	44(1)
H(3)	−96(3)	115(4)	241(3)	26(11)
H(5)	−288(3)	88(3)	283(3)	41(12)
H(6)	−422(4)	69(4)	423(3)	41(11)
H(8)	−319(3)	232(3)	587(3)	36(12)
H(9)	−184(3)	255(3)	452(3)	34(11)
H(11)	−322(3)	423(3)	252(3)	16(9)
H(12)	−419(4)	597(3)	319(3)	24(10)
H(13)	−311(4)	659(4)	398(4)	59(14)
H(14)	−97(3)	546(3)	400(3)	38(11)
H(15)	4(4)	364(4)	317(3)	39(11)
H(2N)	126(3)	300(3)	36(3)	28(10)
H(3')	−407(4)	873(4)	779(3)	47(13)
H(5')	−208(3)	900(3)	730(3)	30(10)
H(6')	−78(4)	923(4)	590(3)	41(12)
H(8')	−208(3)	785(3)	416(3)	19(9)
H(9')	−337(3)	757(3)	557(3)	23(9)
H(11')	−190(4)	574(3)	750(3)	36(11)
H(12')	−92(4)	402(3)	667(3)	23(10)
H(13')	−199(4)	358(4)	576(3)	35(11)
H(14')	−414(4)	472(4)	576(3)	44(12)
H(15')	−509(4)	646(3)	656(3)	30(10)
H(2'N)	−632(4)	795(3)	979(3)	41(11)
H(16*A*)	−656(4)	627(4)	1015(4)	51(13)
H(16*B*)	−724(3)	663(3)	1125(3)	14(9)
H(17*A*)	−559(5)	648(5)	1188(4)	79(19)
H(17*B*)	−470(6)	628(5)	1075(5)	110(20)
H(17*C*)	−514(4)	530(5)	1139(4)	63(15)
H(18*A*)	−730(3)	949(3)	1082(2)	20(9)
H(18*B*)	−629(4)	834(3)	1139(3)	34(10)
H(19*A*)	−788(4)	778(4)	1246(3)	51(12)
H(19*B*)	−887(4)	889(4)	1185(3)	48(13)
H(19*C*)	−812(4)	920(4)	1244(4)	63(15)
H(20*A*)	−794(4)	780(4)	935(3)	56(13)
H(20*B*)	−888(3)	832(3)	1039(2)	16(8)
H(21*A*)	−785(3)	957(3)	892(3)	27(10)
H(21*B*)	−880(4)	1016(4)	983(3)	46(13)
H(21*C*)	−929(4)	980(4)	906(4)	63(14)

Table 3. Atomic coordinates ($\times 10^4$) and isotropic equivalent (isotropic for H atoms) thermal parameters (Å^2, $\times 10$) for structure **III**

Atom	*x*	*y*	*z*	U_{eq}/U_{iso}	Atom	*x*	*y*	*z*	U_{eq}/U_{iso}
O(1)	−2419(4)	7869(2)	11128(2)	77(1)	C(18)	−5919(7)	8398(4)	13038(3)	88(1)
O(2)	−4209(6)	6378(2)	10518(2)	99(1)	C(19)	−4694(7)	7900(3)	13917(3)	81(1)
O(3)	2365(4)	9558(2)	5207(2)	87(1)	C(20)	−2754(6)	7352(2)	13878(2)	68(1)
O(4)	5419(4)	9933(2)	6371(2)	87(1)	C(21)	−1977(5)	7321(2)	12936(2)	62(1)
O(5)	−1707(6)	6867(2)	14802(2)	109(1)	C(22)	75(17)	6174(6)	14789(6)	140(2)
N(1)	3491(4)	9574(2)	6124(2)	61(1)	H(3)	−190(50)	8530(20)	10020(20)	51(7)
C(1)	−3015(5)	7087(2)	10397(2)	57(1)	H(5)	3090(60)	9180(30)	9550(30)	82(10)
C(2)	−1951(4)	7232(2)	9462(2)	51(1)	H(6)	4880(60)	9690(30)	8190(30)	69(9)
C(3)	−616(4)	8073(2)	9424(2)	53(1)	H(8)	−50(60)	8480(30)	5960(30)	74(9)
C(4)	448(4)	8409(2)	8552(2)	51(1)	H(9)	−1800(60)	7760(30)	7240(30)	72(9)
C(5)	2426(5)	9006(2)	8800(2)	65(1)	H(11)	700(60)	5840(30)	8910(30)	63(8)
C(6)	3482(5)	9377(2)	8026(2)	65(1)	H(12)	0(90)	4550(40)	7570(40)	127(17)
C(7)	2453(4)	9159(2)	6973(2)	52(1)	H(13)	−3660(70)	4310(30)	6490(30)	88(11)
C(8)	482(5)	8588(2)	6691(2)	59(1)	H(14)	−6250(90)	5340(40)	6780(40)	120(16)
C(9)	−510(5)	8197(2)	7482(2)	59(1)	H(15)	−5820(70)	6690(30)	8100(30)	74(9)
C(10)	−2454(4)	6381(2)	8637(2)	51(1)	H(17)	−6090(80)	8740(40)	11560(40)	106(14)
C(11)	−702(6)	5729(2)	8481(2)	65(1)	H(18)	−7280(110)	8900(50)	13090(50)	134(18)
C(12)	−1099(8)	4964(3)	7672(3)	85(1)	H(19)	−5250(80)	7910(30)	14530(40)	105(12)
C(13)	−3195(8)	4854(3)	7031(3)	90(1)	H(21)	−710(70)	6970(30)	12900(30)	86(11)
C(14)	−4935(8)	5478(4)	7182(3)	90(1)	H(22*A*)	−510(130)	5510(60)	14420(60)	170(30)
C(15)	−4597(5)	6246(3)	7994(3)	71(1)	H(22*B*)	470(110)	5840(50)	15410(60)	150(20)
C(16)	−3261(5)	7828(2)	12058(2)	59(1)	H(22*C*)	1380(90)	6490(40)	14600(50)	108(18)
C(17)	−5226(6)	8361(3)	12077(3)	76(1)					

Table 4. Selected bond lengths (Å) and bond angles (deg) in the studied compounds

Compound	NPAC [13]	**I**	**II**		**III**	4 [14]
			(*A*)	(*B*)		
C(1)–O1	1.276	1.330(3)	1.261(5)	1.239(5)	1.352(3)	1.323
C(1)–O(2)	1.248	1.225(3)	1.232(5)	1.273(5)	1.177(3)	1.182
C(1)–C(2)	1.465	1.482(4)	1.528(6)	1.522(6)	1.495(3)	1.486
C(2)–C(3)	1.321	1.349(4)	1.340(6)	1.339(5)	1.336(3)	1.334
C(3)–C(4)	1.457	1.463(4)	1.475(6)	1.467(6)	1.472(3)	1.456
C(7)–N(1)	1.467	1.464(4)	1.478(5)	1.463(5)	1.471(4)	1.487
C(1)–C(2)–C(3)	123.6	118.4(3)	118.9(4)	120.3(4)	119.7(2)	116.7
C(1)–C(2)–C(10)	–	116.5(3)	118.9(4)	117.3(4)	115.5(2)	119.0
C(2)–C(3)–C(4)	126.1	129.2(3)	129.0(4)	128.0(4)	128.6(2)	131.8
C(5)–C(4)–C(9)	118.6	118.2(3)	118.8(4)	118.9(4)	118.3(2)	117.4
C(6)–C(7)–C(8)	122.2	122.5(3)	121.7(4)	122.0(4)	122.4(2)	123.6

Note: NPAC is nitrophenylacrylic acid.

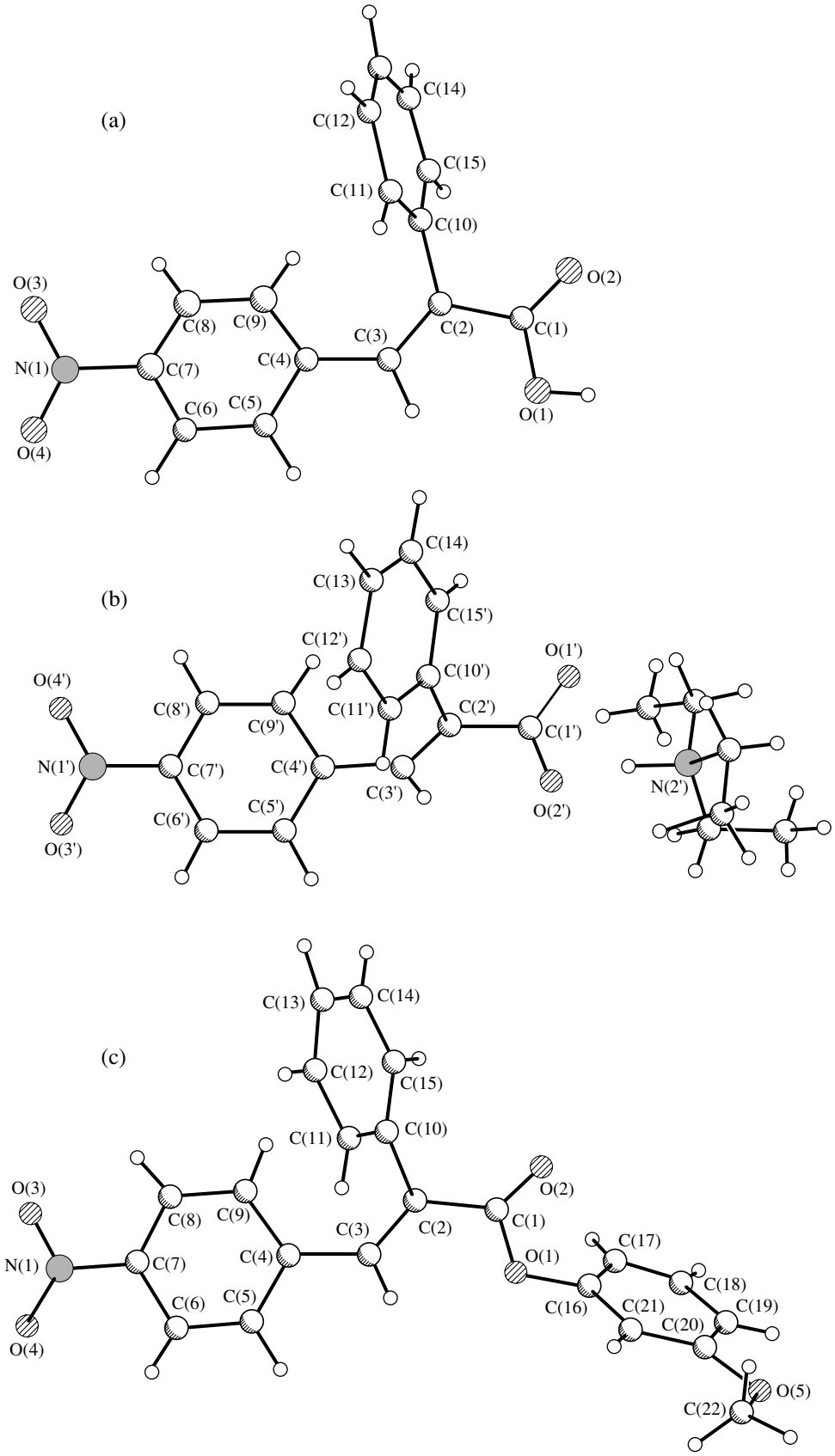

Fig. 1. A general view of molecules (a) **I**, (b) **II**, and (c) **III** and the atomic numbering.

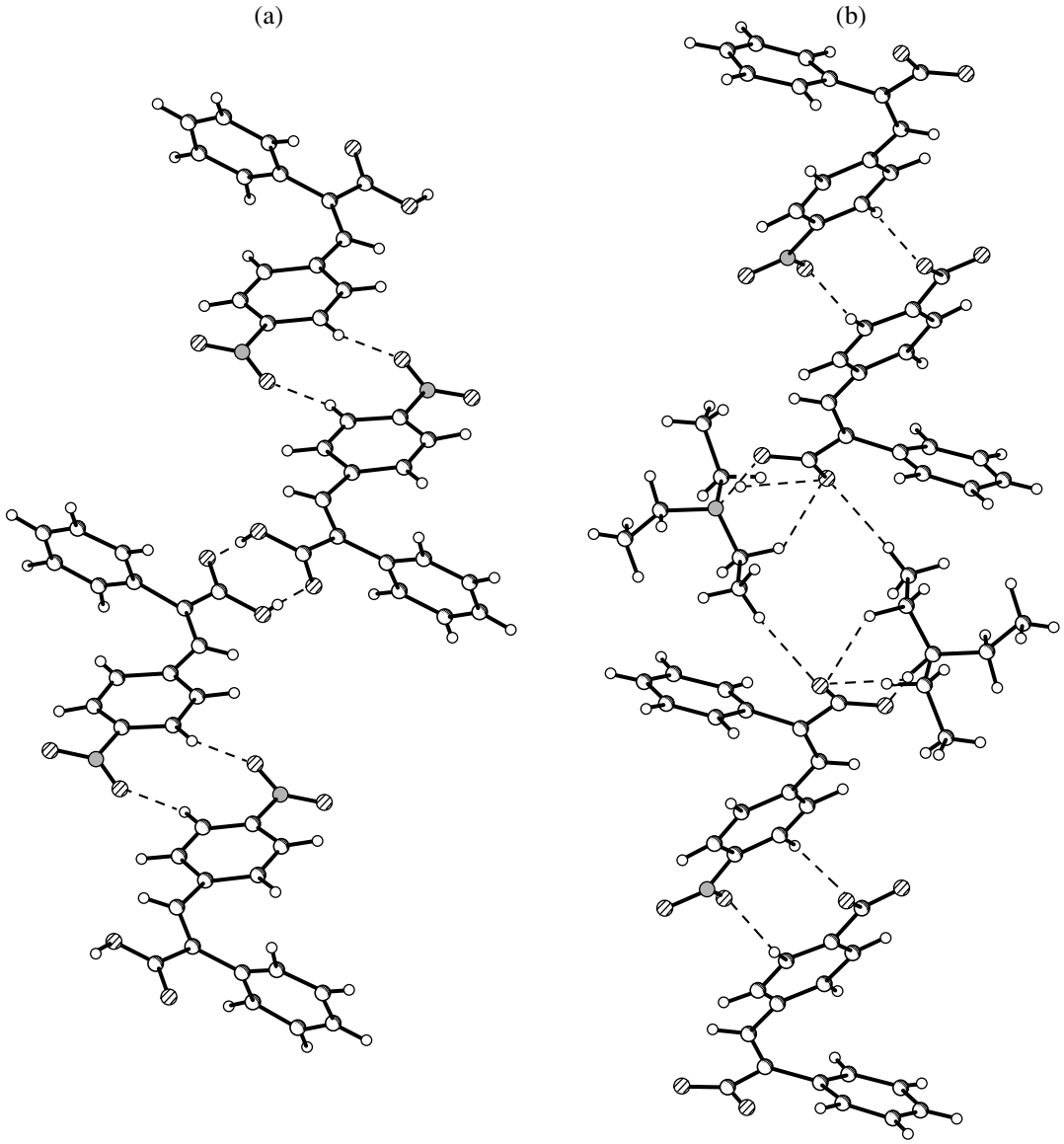

Fig. 2. Molecular associates formed by molecules in crystals (a) **I** and (b) **II**.

$C_{ar}H\cdots O(NO_2)$ [H···O, 2.46(4) Å] (Fig. 2a). In turn, the centrosymmetric ribbons are linked to form the centrosymmetric crystal structure. In order to prevent the formation of centrosymmetric dimers, we cocrystallized initial acid **I** with triethylamine in the hope that this donor–acceptor pair between the acid anion and the protonated organic base could be more energetically favorable. Unfortunately, as in the aforementioned works [9–12], the prepared binary crystal also turned out to be centrosymmetric. It can be seen from Fig. 2b that, although the triethylamine group is incorporated between the carboxyl groups of the adjacent molecules owing to the sufficiently strong hydrogen bonds [N(2)H···O(1), 2.662(4) Å; H···O, 1.50(4) Å; angle at the H atom, 176(4)° and N(2')H···O(2'), 2.654(4) Å; H···O, 1.52(4) Å; <*D*H*A*>, 170(4)°], the system of hydrogen bonds formed remains centrosymmetric.

Table 5. Components of the first-order nonlinear optical susceptibility tensor d_{ijk} (pm/V) for the crystals studied

Compound	D_{xxx}	d_{xxz}	d_{xzz}	d_{zzz}	d_{yyz}	d_{xyy}
3	0.5	3.1	0.0	0.2	1.4	0.5
4	26.9	13.4	6.7	3.3	6.7	14.1

Another attempt to screen the carboxyl group by synthesizing methyl ester **IV** and (3-methoxy)phenyl ester **III** has met with success. The crystals of methyl ester **IV** crystallize in the racemic but noncentrosymmetric space group *Cc*, and the crystals of ester **III** crystallize in the space group *Pn* (Fig. 3). The molecular packings in the crystals of both compounds are very

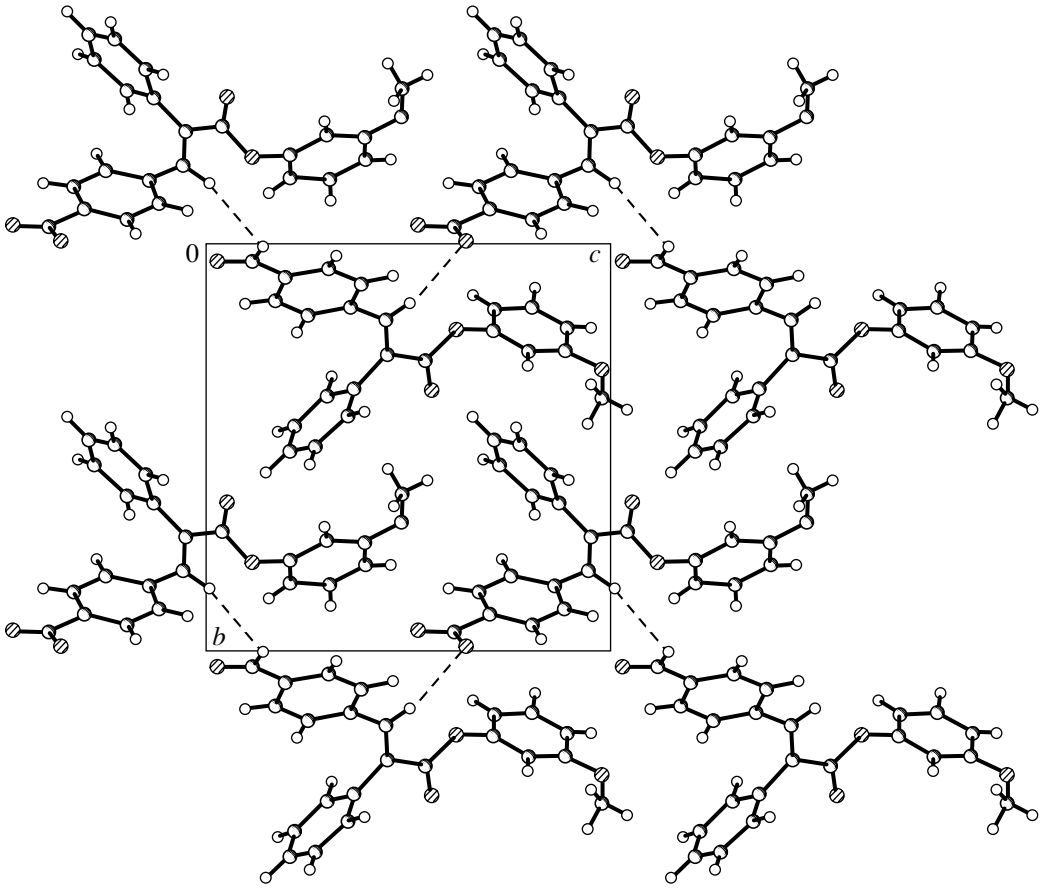

Fig. 3. Molecular packing in crystal **III**.

similar to each other. The stacks of parallel molecules are formed along the direction of the smallest lattice parameter in both crystals.

Calculation of the susceptibilities of the studied crystals. Since we succeeded in preparing noncentrosymmetric crystals **III** and **IV**, it was expedient to evaluate their first-order nonlinear susceptibilities *d*. To accomplish this, we first calculated the molecular hyperpolarizabilities β. The calculations were performed in the framework of the finite-field theory approximation [17–20] included in the MOPAC program package [21] (the AM1 parametrization [22]). The data derived from the MOPAC program were processed according to the HYPER program [23] with the aim of determining the molecular hyperpolarizability tensor components β_{ijk}, which were required to calculate the susceptibility of the crystals under investigation.

For compound **III**, the molecular hyperpolarizability, which is determined by the relationship

$$\beta_{vec} = \sqrt{(\beta_{xxx} + \beta_{xyy} + \beta_{xzz})^2 + (\beta_{yxx} + \beta_{yyy} + \beta_{yzz})^2 + (\beta_{zxx} + \beta_{zyy} + \beta_{zzz})^2},$$

proves to be relatively low: $\beta_{vec} = 2.0 \times 10^{-30}$ cm^3/B^2. This can be associated with both the nonplanar molecular structure and the presence of the bulky substituent at the O(1) atom. For a more planar and less bulky molecule of compound **IV**, the hyperpolarizability β_{vec} is equal to 17.0×10^{-30} cm^3/B^2.

The components of the first-order nonlinear optical susceptibility tensor for the crystals were evaluated using the NLOP program based on the oriented-gas model [24, 25].[2] According to this model, the tensor components d_{IJK} can be written in the form

$$d_{IJK} = \frac{1}{V} f_I f_J f_K \times \sum_{n=1}^{Z} \left[\sum_{i=1}^{3} \sum_{j=1}^{3} \sum_{k=1}^{3} \cos\theta_{iI}^{n} \cos\theta_{jJ}^{n} \cos\theta_{kK}^{n} \beta_{ijk} \right],$$

[2] The algorithm of the program developed by K.Yu. Suponitskiĭ, M.Yu. Antipin, and T.V. Timofeeva will be published in a separate paper.

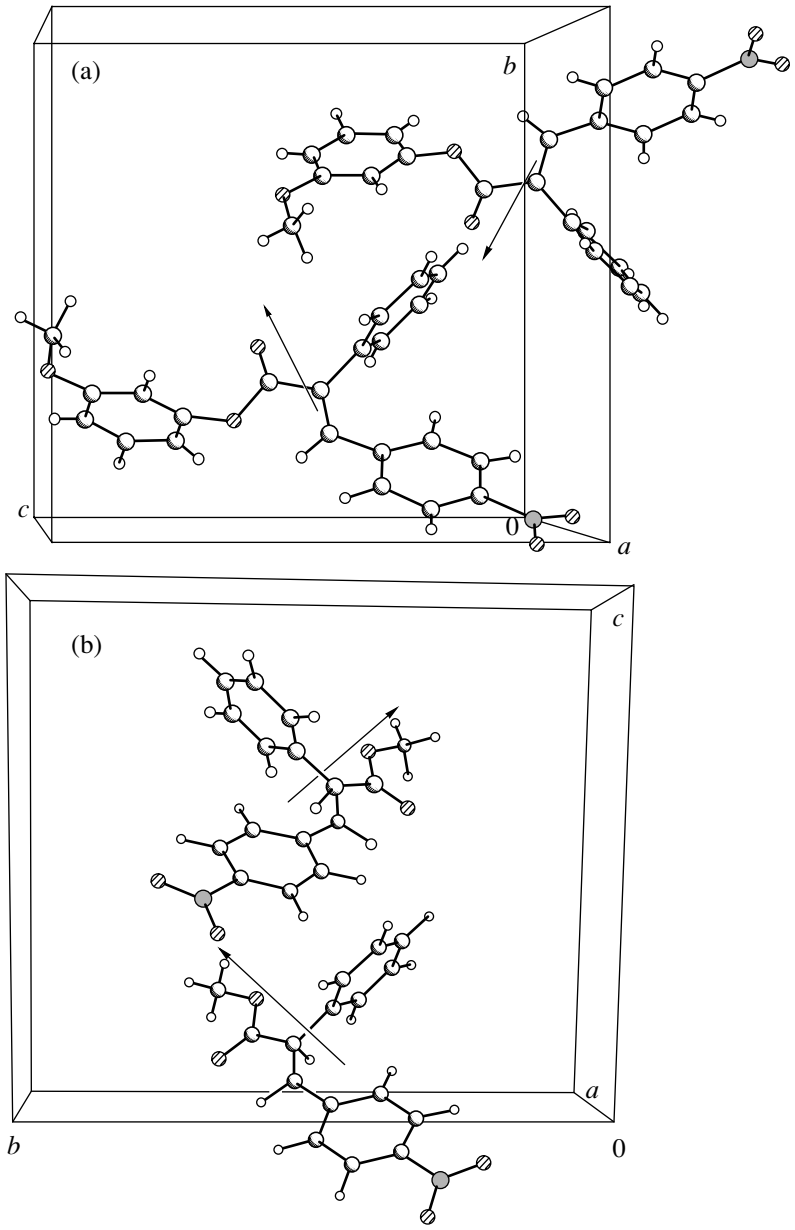

Fig. 4. Relative orientation of the vector parts of the molecular hyperpolarizabilities β_{vec} in crystals (a) **III** and (b) **IV**.

where V is the unit cell volume, Z is the number of molecules per cell, $\cos\theta_{ij}$ are the direction cosines relating the local molecular (*ijk*) and crystal (*IJK*) coordinate systems, β_{ijk} are the components of the molecular hyperpolarizability tensor, and f_i are the local-field factors.[3] The results of calculations are given in Table 5. As follows from the results obtained, crystals **IV** are characterized by comparatively large values of d_{ijk}; hence, they are promising for use in further investigation. Moreover, the molecular orientation in crystal **IV** (Fig. 4) is close to the optimum orientation: the angle between the direction of the vector part of the molecular hyperpolarizability and the polar direction in the crystal (the O*Y* axis) is 57.9°. According to the calculation carried out by Oudar and Zyss [24, 25], the angle equal to 54.74° is optimum for the maximum nonlinear optical activity in noncentrosymmetric monoclinic crystals. In crystal **III**, this angle is equal to only 28°. Consequently, the nonlinear optical effect in this crystal cannot exceed 51% of the maximum effect.

[3] The factors f_i are usually estimated from the refractive indices according to the Lorenz formula $f_i = [n_i^2 + 2]/3$. To the best of our knowledge, these data for the studied compounds are unavailable. For this reason, we used the empirical relationship $f_i f_j f_k = 3$ [26].

CONCLUSIONS

Thus, the results obtained have demonstrate that compounds of this class hold promise for use in further investigation. It is of interest to synthesize other esters of the acid under study (for example, ethyl ester). It is also instructive to perform a precision X-ray diffraction analysis of methyl ester **IV** with the aim of refining the results of calculations of the susceptibility of this compound, specifically on the basis of the experimental electron density distribution.

ACKNOWLEDGMENTS

This work was supported by the Russian Foundation for Basic Research, project nos. 00-03-32840a, 00-15-97359, and 01-03-06143.

REFERENCES

1. A. I. Kitaĭgorodsky, *Molecular Crystals* (Nauka, Moscow, 1971).
2. *Nonlinear Optical Properties of Organic Molecules and Crystals*, Ed. by D. S. Chemla and J. Zyss (Academic, New York, 1987), Vols. 1, 2.
3. A. Gavezzotti and G. Filippini, J. Am. Chem. Soc. **117**, 12299 (1995).
4. J. K. Whitsell, R. E. Davis, L. L. Sanders, *et al.*, J. Am. Chem. Soc. **113**, 3267 (1991).
5. G. R. Desiraju, *Crystal Engineering* (Elsevier, Amsterdam, 1989).
6. L. N. Kuleshova and V. N. Khrustalev, Kristallografiya **45** (1), 84 (2000) [Crystallogr. Rep. **45**, 78 (2000)].
7. G. Bakunin, Gazz. Chim. Ital. **25**, 146 (1905).
8. G. M. Sheldrick, *SHELXTL'97, Versions 5.10: An Integrated System for Solving, Refining, and Displaying Crystal Structures from Diffraction Data* (Bruker AXS, Madison, 1997).
9. H. Koshima, S. Honke, and J. Fujita, J. Org. Chem. **64**, 3916 (1999).
10. G. R. Desiraju and J. A. R. P. Sarma, Chem. Commun. **48**, 45 (1983).
11. J. A. R. P. Sarma and G. R. Desiraju, J. Chem. Soc., Perkin Trans. 2, 1905 (1985).
12. C. V. K. Sharma, K. Panneerselvam, T. Pilati, *et al.*, J. Chem. Soc., Perkin Trans. 2, 2209 (1993).
13. Y. Kageyama, T. Iwamoto, M. Haisa, *et al.*, Acta Crystallogr., Sect. C: Cryst. Struct. Commun. **49**, 833 (1993).
14. B. Tinant, R. Touillaux, M. Declerc, *et al.*, Bull. Soc. Chim. Belg. **92**, 865 (1983).
15. F. H. Allen, O. Kennard, D. G. Watson, *et al.*, J. Chem. Soc., Perkin Trans. 2, S1 (1987).
16. A. G. Orpen, L. Brammer, F. H. Allen, *et al.*, J. Chem. Soc., Dalton Trans. 1, S1 (1989).
17. M. J. S. Dewar and J. J. P. Stewart, Chem. Phys. Lett. **111**, 416 (1984).
18. H. A. Kurtz, J. J. P. Stewart, and K. M. Dieter, J. Comput. Chem. **11**, 82 (1990).
19. J. Zyss, J. Chem. Phys. **70**, 3333 (1979).
20. J. Zyss, J. Chem. Phys. **70**, 3341 (1979).
21. QCPE; MOPAC: Quantum Chemistry Program Exchange. Version 6 (1990).
22. B. H. Cardelino, C. E. Moore, and R. E. Stickel, J. Phys. Chem. **95**, 8645 (1991).
23. M. J. S. Dewar, E. G. Zoebish, E. F. Healy, *et al.*, J. Am. Chem. Soc. **107**, 3902 (1985).
24. J. L. Oudar and J. Zyss, Phys. Rev. A **26**, 2016 (1982).
25. J. Zyss and J. L. Oudar, Phys. Rev. A **26**, 2028 (1982).
26. M. Barzoukas, D. Josse, P. Femaux, *et al.*, J. Opt. Soc. Am. B **4**, 977 (1987).

Translated by O. Borovik-Romanova

Crystallography Reports, Vol. 48, No. 1, 2003, pp. 8–11. Translated from Kristallografiya, Vol. 48, No. 1, 2003, pp. 14–16.

STRUCTURE OF INORGANIC COMPOUNDS

Three-Dimensionally Modulated Incommensurate Crystal Structure of Lazurite from the Baikal Region

N. B. Bolotina*, R. K. Rastsvetaeva*, A. N. Sapozhnikov, A. A. Kashaev***, A. Schöenleber****, and G. Chapuis******

** Shubnikov Institute of Crystallography, Russian Academy of Sciences, Leninskiĭ pr. 59, Moscow, 119333 Russia*

e-mail: rast@ns.crys.ras.ru

*** Vinogradov Institute of Geochemistry, Siberian Division, Russian Academy of Sciences, ul. Favorskogo 1a, Irkutsk, 664033 Russia*

**** Irkutsk Institute for Engineers of Railway Transport, ul. Chernyshevskogo 15, Irkutsk, 664074 Russia*

***** Institute of Crystallography, University of Lausanne, BSP, Lausanne, 1015 Switzerland*

Received September 19, 2002

Abstract—The three-dimensionally modulated incommensurate crystal structure of lazurite from the Baikal region was determined for the first time. The structure was solved within the cubic system with the unit-cell parameter a_{cub} = 9.077(1) Å and the (3+2)-dimensional superspace group $Pnn2(\mathbf{q}_1, \mathbf{q}_2)$ under the assumption of a twin model consisting of three orthorhombic components related by a threefold axis along the [111] direction. The structure was refined using 257 main reflections and 2392 first-order satellite reflections with the isotropic thermal parameters to wR_0 = 1.98% and wR_1 = 7.50% respectively. *© 2003 MAIK "Nauka/Interperiodica".*

Lazurite belongs to the sodalite group of minerals, which includes, along with sodalite, also nosean and hauyne. Minerals of the sodalite group are described by the general formula $(Na, Ca, K)_8(AlSiO_4)_6(SO_4, S, OH, Cl)_2$ and cubic unit cells with lattice parameters of about 9 Å. The X-ray diffraction patterns of some sodalites have additional reflections indicative of distortions of the basic cubic structure. For example, the commensurately modulated structures of triclinic [1] and orthorhombic [2] lazurites have orthorhombic superstructures (in terms of the metrics) with the unit-cell parameters $a = na_{cub}\sqrt{2}$ (where n is an integer), $b = a_{cub}\sqrt{2}$, and $c = a_{cub}$.

The X-ray diffraction pattern of a new lazurite specimen from the Baikal region is extremely complicated because of the three-dimensional incommensurate modulation. Earlier, we solved the averaged structure of this mineral within the cubic unit-cell with the parameter a_{cub} = 9.077(1) Å based on only the main reflections within the sp. gr. $P23$ [3]. In the present study, the incommensurate three-dimensionally modulated structure of this lazurite specimen was established for the first time with the involvement of the satellite reflections within the superspace group.

The X-ray diffraction data were collected on a four-circle Oxford Xcalibur diffractometer equipped with a CCD detector at the University of Lausanne (Switzerland) and processed using the CrysAlis RED program to obtain a set of integrated intensities with six-digit indices *hklmnp*.

The X-ray diffraction pattern of the crystal has intense satellite reflections oriented along the [110] diagonal of the reciprocal cubic lattice and located at distances of $\gamma a^*_{cub}\sqrt{2}$, $\gamma = 0.2154(1) \cong 3/14$ from the main reflections, indicative of an incommensurate modulation. In addition to the satellite reflections $\{hkl110\}$, the X-ray pattern also has numerous much weaker satellites $\{hkl211\}$ and also high-order satellites.

The analysis of the X-ray pattern showed that the true symmetry of this lazurite specimen is lower than cubic and that, apparently, the symmetry of the X-ray diffraction pattern is attributable to twinning with respect to the elements of the cubic symmetry. In the earlier study [4], it was assumed that twinning could be responsible for the satellites observed along the [110] directions in cubic hauyne. Twinning of domains with the orthorhombic superstructure was also considered [4]. In our case, there were no grounds for using the orthorhombic setting, because no main reflections distorting the cubic lattice of sodalite were observed, and the modulation was incommensurate with the periods of both lattices. Hence, we retained the same unit cell with a cubic metrics but chose the simplest twin model consisting of three orthorhombic components related by the threefold axis along the [111] direction, which

allowed us to pass to a modulated structure. We assumed that each orthorhombic component of the twin has a two-dimensional modulation along two mutually perpendicular [110] and $[\bar{1}10]$ directions in the *xy*-plane with the wavevectors $\mathbf{q}_1 = \gamma\mathbf{a}^* + \gamma\mathbf{b}^*$ and $\mathbf{q}_2 = -\gamma\mathbf{a}^* + \gamma\mathbf{b}^*$, respectively.

The five-digit *hklm*0 and *hkl*0*m* indices were ascribed to the satellites along the face diagonals of the reciprocal cubic lattice based on the set of five wavevectors $\mathbf{a}^*$, $\mathbf{b}^*$, $\mathbf{c}^*$, $\mathbf{q}_1$, and $\mathbf{q}_2$ (each reflection was indexed in the coordinate system of its own twin component). Assuming that the complicated X-ray diffraction pattern containing numerous satellites has the reflections from the domains of different types, we performed the computations using not only the main reflections but also the most representative group of first-order satellites with the index $m = \pm 1$ which were located along the diagonals. The intensities of these satellite reflections indicate that they are responsible for the domains comprising a large part of the specimen.

Analysis of systematic absences made it possible to choose between the symmetry groups *P*222 (no systematic absences) and *Pnn*2. For lazurite, the major difference between *P*222 and *Pnn*2 reduces to the positions of sulfur at the vertices and centers of the cubes in the sp. gr. *Pnn*2, which are identical and have a degree of freedom along the *z* axis, whereas the same positions in the sp. gr. *P*222 are nonequivalent and are fixed along the *z* axis. Based on all the aforesaid and taking into account that only the 003 reflection (weak in comparison with even axial reflections) of all the reflections with one nonzero index and several weak satellites are inconsistent with the *Pnn*2 symmetry, we chose the (3+2)-dimensional space group $Pnn2(\mathbf{q}_1, \mathbf{q}_2)$. The modulation displacement functions of all the structure parameters were given by the sum of two harmonics with the wavevectors $\mathbf{q}_1$ and $\mathbf{q}_2$. The amplitudes and phases of the harmonics were refined by the least-squares method simultaneously with the parameters of the basic structure using the JANA program [5].

Taking into account the cubic symmetry of the X-ray diffraction pattern, the volumes of the twin components were chosen to be equal to each other, and the structural computations were carried out using the reflections averaged within the X-ray diffraction class *m*3. Since the main reflections contain the contributions from all the domains, different scale factors (S_0 and S_1) were used for the main and the satellite reflections, respectively. The refined scale factors are related as $S_0/S_1 = 1.254$. The modulated structure was solved with the isotropic thermal parameters because of the correlations between the anisotropic thermal parameters and the modulation parameters. The final *R* factors were $wR_0 = 1.98\%$ and $wR_1 = 7.50\%$, calculated using 257 main reflections and 2392 satellites, respectively, which were rejected based on the condition $|F_{calcd} - F_{obs}| < 50\sigma(F_{obs})$.

One of the six-membered rings forming the framework of the structure is shown in the figure. The second harmonic was fixed in the phase $u = 0$, and the modulations of the atomic coordinates of the ring were treated as a function of the phase *t* of the first harmonic with the wavevector $\mathbf{q}_1$. The values of the functions were the atomic displacements (Å) from the points of the basic lattice. As to the *z* coordinates, all the symmetrically independent framework atoms, except for O(1) and O(4), modulate in phase with equal amplitudes. The modulations along the *x* and *y* axes do not occur in phase and have weaker amplitudes. However, the *x* coordinates of the pair of the O(3) and O(6) atoms and the *y* coordinates of the pair of the O(2) and O(5) atoms modulate in phase to a much greater extent that the remaining atoms. Moreover, the O(6), O(5), and O(1) triad and the O(3), O(2), and O(4) triad modulate in phase with respect to the *x*, *y*, and *z* coordinates, with the difference in phases between the two triads being rather small. Assuming that each oxygen atom occupies a vertex shared by two adjacent $(AlSi)O_4$ tetrahedra, the modulation of the framework reduces mainly to mutual rotations of the tetrahedra resulting in the change in the configuration of the intraframework cavity bounded by the O(1)–O(6) six-membered ring.

One of the two independent Na (Ca) cations is located on the [111]-directed diagonal in the center of the ring shown in the figure. Another independent cation is located on the same diagonal in the center of the adjacent ring at an average distance of $0.5a_{cub}\sqrt{3}$ from the first cation. Each cation position in the averaged structure is split into three subpositions. In the modulated structure, the cation positions are also split. The Na(1), Na(2), and Na(3) subpositions correspond to the first cation. The Na(4), Na(5) (Ca(5)), and Ca subpositions correspond to the second cation. The refined total occupancy of the Na(1)–Na(3) subpositions is slightly higher than unity, apparently, because of the fact that calcium atoms replace a small number of sodium atoms. Almost all the calcium cations are located in the mixed Na(5) (Ca(5)) position and pure calcium position on another half of the body diagonal. The modulations of the *z* coordinates of the cations in the Na(1)–Na(3) positions correlate in phase not only with each other but also with the modulations in the *z* coordinates of the atoms from the adjacent six-membered ring. Therefore, well-matched strong modulations of the atoms of cubic lazurite are observed along the direction perpendicular to the plane of propagation of the modulation waves. The same characteristic feature was observed earlier in triclinic and orthorhombic lazurites [1, 2].

The most substantial difference between the results of our study and the data obtained earlier concerns the positions of the sulfur atoms. In the studies of cubic lazurites from the Afghanistan and the Baffin Island [6, 7], the positions of the sulfur atoms of sulfate and sulfide occupying the vertices and center of the cube were discussed, whereas the positions on the unit-cell

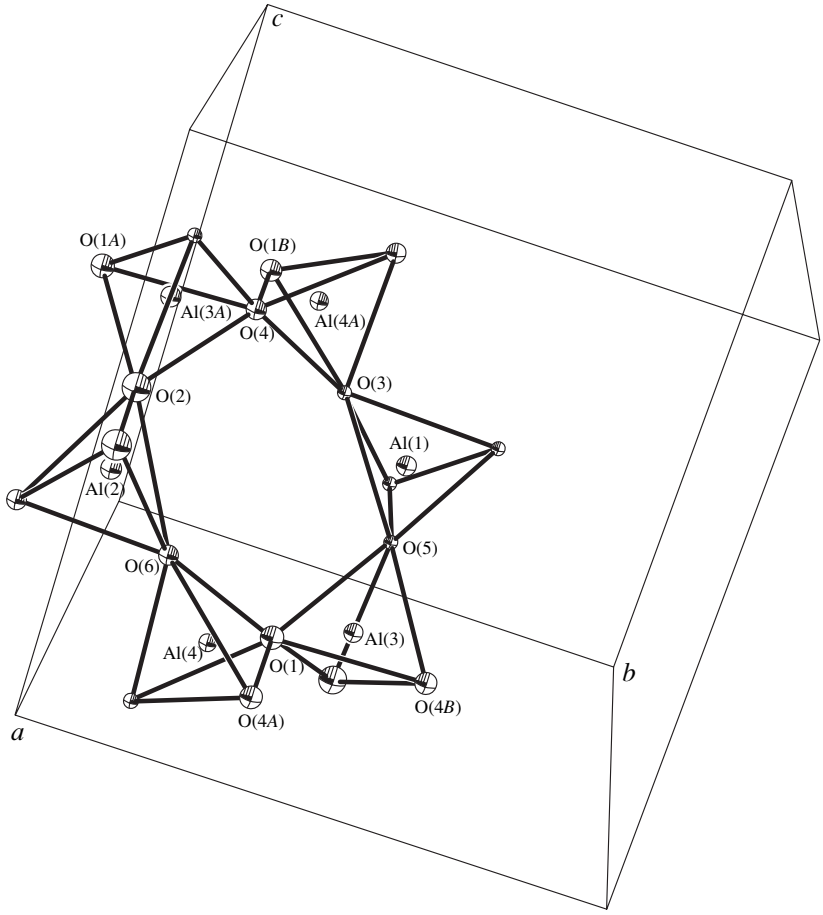

Six-membered ring as the major structural unit of the tetrahedral framework.

edges were ignored. However, the "edge positions" are clearly seen for the lazurite specimen from the Baikal region. In contrast, the oxygen atoms located on the [111] diagonals and involved in the formation of the $(SO_4)^{-2}$ sulfate groups together with the S(1) atoms are poorly localized in the modulated structure. Therefore, the occupancies of the O(7) and O(8) positions were not refined and were specified based on the refined occupancy of the S(1) position. The positions of the oxygen atoms surrounding the sulfur atoms are displaced as compared to those in the averaged structure [3]. Microprobe chemical analysis revealed a substantially higher oxygen content than was established for the O(7) and O(8) positions by X-ray diffraction analysis (1.73 of $(SO_4)^{-2}$ instead of 0.84). It can be assumed that the S(2)–S(5) positions are partly occupied by the oxygen atoms, which are involved either in sulfate groups or directly in the coordination environment of the Na and Ca cations. Moreover, the refined total occupancy of the S(2)–S(5) positions on the edges is 1.54 atoms per unit cell rather than 0.9 indicated for the analogous positions in [3].

To summarize, the results obtained allowed us to draw a conclusion about the nature of modulations in cubic lazurite. It can be reliably stated that the main reason for the modulations is not the formation of clusters of different sizes as was indicated in [6] but the nature of ordering of intraframework ions in any part of the specimen, which determines the gradient of the modulation displacements, i.e., the directions of wave propagation in different domains, whereas the modulation period is determined by the framework which is identical in all the domains.

ACKNOWLEDGMENTS

We are grateful to Prof. V.I. Simonov for his continuous interest in our work and valuable advice.

This study was supported by the Russian Foundation for Basic Research (project nos. 01-05-64604 and 00-02-16636) and the Russian Federation Government Program for Support of Leading Scientific Schools (project no. 00-15-96633).

REFERENCES

1. V. G. Evsyunin, R. K. Rastsvetaeva, A. N. Sapozhnikov, and A. A. Kashaev, Kristallografiya **43** (6), 1057 (1998) [Crystallogr. Rep. **43**, 999 (1998)].
2. V. G. Evsyunin, A. N. Sapozhnikov, A. A. Kashaev, and R. K. Rastsvetaeva, Kristallografiya **42** (6), 1014 (1997) [Crystallogr. Rep. **42**, 938 (1997)].
3. R. K. Rastsvetaeva, N. B. Bolotina, A. N. Sapozhnikov, *et al.*, Kristallografiya **47** (3), 449 (2002) [Crystallogr. Rep. **47**, 404 (2002)].
4. H. Xu and D. R. Veblen, Am. Mineral. **80**, 87 (1995).
5. V. Petricek and M. Dusek, *JANA98: The Crystallographic Computing System. User Manual* (Institute of Physics, Academy of Sciences of the Czech Republic, Prague, 2000).
6. I. Hassan, Am. Mineral. **85**, 1383 (2000).
7. A. N. Sapozhnikov, V. L. Tauson, and L. N. Matveeva, Zap. Vseross. Mineral. O–va **130** (2), 121 (2001).

Translated by T. Safonova

Crystallography Reports, Vol. 48, No. 1, 2003, pp. 84–91. Translated from Kristallografiya, Vol. 48, No. 1, 2003, pp. 89–96.

STRUCTURE OF ORGANIC COMPOUNDS

Crystal Structures of Cesium and Dimethylammonium Cupradecaborates, $Cs[CuB_{10}H_{10}]$ and $(CH_3)_2NH_2[CuB_{10}H_{10}]$

I. N. Polyakova, E. A. Malinina, and N. T. Kuznetsov

Kurnakov Institute of General and Inorganic Chemistry, Russian Academy of Sciences, Leninskiĭ pr. 31, Moscow, 119991 Russia

e-mail: sokol@igic.ras.ru

Received February 20, 2002

Abstract—The crystal structures of $Cs[CuB_{10}H_{10}]$ (**I**) and $(CH_3)_2NH_2[CuB_{10}H_{10}]$ (**II**) are studied (R = 0.0398 and 0.0510 for 1225 and 2728 observed reflections in **I** and **II**, respectively). Crystals **I** and **II** are built of $[(CuB_{10}H_{10})^-]_\infty$ anionic chains and cations. The distorted tetrahedral coordination of the Cu^+ ions is formed by four pairs of B–H atoms from two polyhedral anions. The Cu–B bond lengths in **I** and **II** are 2.159–2.287(6) and 2.130–2.285(9) Å, respectively. The coordination of the Cu^+ ions in **II** includes only edges between apical and equatorial vertices of the anions. In **I**, both the edges of the apical belt and those between two equatorial vertices are involved in coordination. The ability of the $B_{10}H_{10}^{2-}$ anion to coordinate metals by the equatorial edge is established for the first time. © *2003 MAIK "Nauka/Interperiodica".*

INTRODUCTION

It is known that polyhedral *closo*-boron hydride anions $B_nH_n^{2-}$ (n = 6, 10, or 12) are able to form bonds with transition metals. The coordination compounds of the $B_{10}H_{10}^{2-}$ anion are of particular interest, because this polyhedral anion contains vertices of different types (bound to four and five neighboring vertices), which makes possible different variants of its binding with metal. Earlier [1], the series of $Cat[CuB_{10}H_{10}]$ compounds, where $Cat = Cs^+$ or $R_{4-n}NH_n^+$ (n = 0, 1, or 2; $R = CH_3$, C_2H_5, or C_4H_9), was prepared by redox reactions of alkylammonium and cesium decaborates with Cu(II) salts in aqueous solutions. The mechanism of formation and physicochemical properties of these compounds, as well as the brief data on the crystal structures of $CsCu[B_{10}H_{10}]$ (**I**) and $(CH_3)_2NH_2[CuB_{10}H_{10}]$ (**II**), were reported in [2]. In the present paper, crystal structures **I** and **II** are discussed in more detail.

EXPERIMENTAL

The sets of intensities $I(hkl)$ for crystals **I** and **II** were obtained on a CAD4 automated diffractometer ($\lambda Mo K_\alpha$, graphite monochromator, ω scan mode). The structures were solved by the direct method with the SHELXS97 program [3]. All the H atoms in the $B_{10}H_{10}^{2-}$ anions in both structures and most of the H atoms in the dimethylammonium cations in **II** were located from the difference Fourier syntheses. The coordinates of the missing H atoms were calculated. The non-hydrogen atoms were refined in the anisotropic approximation, and the H atoms were refined within a riding model with isotropic thermal parameters larger than the U_{eq} values of the corresponding non-hydrogen atoms by a factor of 1.2. The refinement was performed with the SHELXL97 program [4]. The main crystallographic characteristics and parameters of data collection and structure refinement are summarized in Table 1. The atomic coordinates are listed in Table 2.

RESULTS AND DISCUSSION

Crystals **I** and **II** are built of $[(CuB_{10}H_{10})^-]_\infty$ anionic chains and Cs^+ (**I**) or $[(CH_3)_2NH_2]^+$ (**II**) cations. The structures of the chains and the atomic numberings in structures **I** and **II** are shown in Figs. 1 and 2, respectively. In crystal **II**, the unit cell contains four crystallographically independent Cu^+, $B_{10}H_{10}^{2-}$, and $[(CH_3)_2NH_2]^+$ units. The Cu^+ cations and $B_{10}H_{10}^{2-}$ anions are divided into two independent chains, Cu(1)–[B(10)–B(19)]H_{10}–Cu(2)–[B(20)–B(29)]H_{10}– and –Cu(3)–[B(30)–B(39)]H_{10}–Cu(4)–[B(40)–B(49)]H_{10}–. The Cu atoms form three-center two-electron bonds with four pairs of B–H atoms from two anions. In **II**, both B–B edges that coordinate the Cu atom in each anion link the apical (B_a) and equatorial (B_e) vertices. Edges of this type are involved in Cu coordination also in cupradecaborates $Cu_2B_{10}H_{10}$ (**III**) [5] and $[Cu(Ph_3P)_2]_2B_{10}H_{10} \cdot CHCl_3$ (**IV**) [6] studied earlier. In **I**, one of the coordinating edges of the polyhedron also belongs to the B_a–B_e type, whereas the other edge

Table 1. Main crystal data and parameters of data collection and structure refinement for **I** and **II**

Parameter	**I**	**II**
Empirical formula	$H_{10}B_{10}CsCu$	$C_2H_{18}B_{10}CuN$
M	314.63	227.81
Space group	*Pbcn*	$P\bar{1}$
a, Å	21.212(4)	12.838(4)
b, Å	9.216(3)	13.421(5)
c, Å	9.657(3)	14.889(6)
α, deg	90	65.80(3)
β, deg	90	89.32(3))
γ, deg	90	88.09(3)
V, Å^3	1887.8(9)	2339(1)
Z	8	8
ρ_{calcd}, g/cm^3	2.214	1.294
Crystal size, mm	$0.03 \times 0.21 \times 0.56$	$0.07 \times 0.18 \times 0.85$
μ_{Mo}, mm^{-1}	6.031	1.813
θ_{max}, deg	32	25
No. of reflections:		
unique	2977	8219
with $I > 2\sigma(I)$ (N_{obs})	1225	2728
R_1, wR_2 for N_{obs}	0.0398, 0.0967	0.0510, 0.1302
GOOF	0.952	0.971
$\Delta\rho_{min}$ and $\Delta\rho_{max}$, e/Å^3	–1.664 and 1.654	–0.652 and 0.894

links the equatorial vertices of two tetragonal pyramids. Thus, the Cu(1) atom is coordinated by three B–H groups [B(1), B(2), and B(3)] that are located at the vertices of the same tetragonal pyramid and one B–H group [B(7)] lying in the base of the other pyramid. Metal chelation by a B_e–B_e edge of the decaborate anion is observed for the first time.

The Cu atoms in **I** and **II** have distorted tetrahedral environments. The B–Cu–B coordination planes are twisted by 72.0° in **I** and 70.9°–75.5° in **II**. The endocyclic B–Cu–B angles are 45.8(2)° and 47.0(2)° in **I** and 45.2(3)°–46.1(3)° in **II**. In all the chelate rings of compounds **I** and **II**, with the exception of the Cu(3)–H(31)–B(31)–B(32)–H(32) in **II**, two Cu–B distances are nonequivalent (the difference is 0.081 and 0.059 Å in **I** and 0.04–0.16 Å in **II**). In **I**, the Cu(1)–B(1) bond with apical B atom [2.159(6) Å] is significantly shorter than three bonds with the equatorial B atoms [2.228–2.287(6) Å], which correlates with the larger negative charge at the apical vertices of the $B_{10}H_{10}^{2-}$ anion [7]. In compound **III**, conversely, the Cu–B_a bonds (2.21–2.32 Å) are longer than the Cu–B_e bonds (2.13–2.18 Å), which can be explained by the participation of both apical B–H groups in the coordination of two Cu atoms. In **II** and **IV**, no dependence between the Cu–B bond length and the type of vertices is observed. In **II**, the ranges of the Cu–B_a and Cu–B_e bond lengths substantially overlap [2.145–2.285(9) and 2.130–2.268(9) Å, respectively]. In **IV**, bond lengths of both types are approximately identical [2.28–2.32(1) Å]. The sets of vertices that are involved in binding with Cu atoms are different for compounds **I**–**IV**: 1, 2, 3, 7 in **I**; 1, 2, 7, 10 and 1, 2, 8, 10 in **II**; 1, 2, 4, 8, 9, 10 in **III**; and 1, 2, 9, 10 in **IV**.

In crystal **I**, the binding of the Cu atoms by edges of different types results in the formation of zigzag chains running along the screw axes in the *c* direction. The chains, which are related by the *c* glide planes, are packed to form three-sheet packets parallel to the *bc* plane (Fig. 3). The inner sheet of the packet consists of Cu atoms, and the outer sheets are formed of polyhedral anions. The Cs^+ ions are situated in "hollows" of the outer sheets and, due to the relative shift of the neighboring packets, form bonds with "hills" of the adjacent sheet, thus connecting the packets into a three-dimensional framework. The environment of the Cs(1) atom includes eight H atoms from five polyhedral anions at the distances 2.95–3.44 Å (mean 3.20 Å). For comparison, in the cubic structures of $Cs_2B_{12}H_{12}$ [8] and $Cs_2B_6H_6$ [9], in which the environments of the Cs atoms consist of twelve symmetrically related H atoms from four polyhedral anions, the Cs–H distances are 3.13 and 3.38 Å, respectively.

Table 2. Atomic coordinates and thermal parameters U_{eq} (U_{iso} for H atoms) in structures **I** and **II**

Atom	*x*	*y*	*z*	U_{eq}/U_{iso}, Å^2
		I		
Cs(1)	0.07506(2)	0.23588(4)	0.49879(5)	0.0385(1)
Cu(1)	0.25546(4)	0.23855(9)	0.20942(9)	0.0440(2)
B(1)	0.3068(3)	0.1251(6)	0.3693(7)	0.022(1)
B(2)	0.3344(3)	0.2988(7)	0.3524(7)	0.023(1)
B(3)	0.2888(2)	0.2380(5)	0.5014(7)	0.0205(9)
B(4)	0.3406(3)	0.0822(6)	0.5238(7)	0.023(1)
B(5)	0.3867(3)	0.1391(7)	0.3727(7)	0.025(1)
B(6)	0.3423(3)	0.3905(6)	0.5163(7)	0.023(1)
B(7)	0.3468(3)	0.2383(6)	0.6378(6)	0.021(1)
B(8)	0.4158(3)	0.1668(7)	0.5453(7)	0.025(1)
B(9)	0.4126(3)	0.3190(8)	0.4253(8)	0.025(1)
B(10)	0.4101(3)	0.3439(8)	0.5983(8)	0.028(1)
H(1)	0.2779	0.0664	0.3062	0.026
H(2)	0.3190	0.3756	0.2919	0.028
H(3)	0.2359	0.2657	0.5021	0.025
H(4)	0.3387	−0.0256	0.5760	0.028
H(5)	0.4182	0.0761	0.3102	0.031
H(6)	0.3257	0.4974	0.5385	0.027
H(7)	0.3390	0.2038	0.7415	0.026
H(8)	0.4556	0.0884	0.5733	0.030
H(9)	0.4480	0.3710	0.3747	0.030
H(10)	0.4417	0.4080	0.6647	0.033
		II		
Cu(1)	0.93488(8)	0.56127(7)	0.24334(8)	0.0609(4)
Cu(2)	0.95284(9)	0.07972(8)	0.19809(8)	0.0718(4)
Cu(3)	0.52621(9)	0.28745(7)	0.30407(8)	0.0636(4)
Cu(4)	0.56223(8)	0.80950(7)	0.25440(8)	0.0608(4)
B(10)	0.9843(7)	0.2519(6)	0.1429(6)	0.044(2)
B(11)	0.9550(7)	0.3815(6)	0.3176(6)	0.045(2)
B(12)	0.9310(6)	0.4309(6)	0.1954(7)	0.040(2)
B(13)	1.0611(7)	0.3725(6)	0.2492(6)	0.046(3)
B(14)	0.9974(6)	0.2520(6)	0.3368(7)	0.039(2)
B(15)	0.8674(7)	0.3121(6)	0.2823(6)	0.038(2)
B(16)	1.0210(7)	0.3736(6)	0.1334(7)	0.040(2)
B(17)	1.0650(7)	0.2468(7)	0.2339(7)	0.046(2)
B(18)	0.9298(7)	0.2044(7)	0.2573(7)	0.044(2)
B(19)	0.8821(7)	0.3286(6)	0.1568(6)	0.040(2)
B(20)	0.8823(7)	−0.3065(7)	0.2819(7)	0.045(2)
B(21)	1.0517(7)	−0.0682(7)	0.2101(8)	0.054(3)
B(22)	0.9193(7)	−0.0761(7)	0.1991(7)	0.044(2)
B(23)	1.0138(7)	−0.1387(6)	0.1450(7)	0.040(2)
B(24)	1.0839(7)	−0.2034(6)	0.2636(7)	0.043(2)
B(25)	0.9906(7)	−0.1389(7)	0.3182(7)	0.042(2)
B(26)	0.8846(7)	−0.1914(6)	0.1781(7)	0.040(2)
B(27)	1.0002(7)	−0.2816(7)	0.2234(7)	0.045(2)
B(28)	0.9825(7)	−0.2817(7)	0.3446(7)	0.046(2)
B(29)	0.8677(6)	−0.1912(6)	0.2999(6)	0.035(2)
B(30)	0.5346(7)	0.6977(6)	0.1818(6)	0.039(2)
B(31)	0.4944(7)	0.4149(7)	0.3574(6)	0.040(2)
B(32)	0.5460(7)	0.4647(7)	0.2436(7)	0.048(3)

Table 2. (Contd.)

Atom	*x*	*y*	*z*	U_{eq}/U_{iso}, Å^2
		II		
B(33)	0.4138(7)	0.5006(7)	0.2670(6)	0.041(2)
B(34)	0.4628(6)	0.5319(6)	0.3678(6)	0.038(2)
B(35)	0.5972(6)	0.4919(6)	0.3448(6)	0.036(2)
B(36)	0.4877(6)	0.5942(6)	0.1611(6)	0.035(2)
B(37)	0.4274(7)	0.6398(7)	0.2503(6)	0.041(2)
B(38)	0.5577(6)	0.6349(6)	0.3052(6)	0.032(2)
B(39)	0.6160(7)	0.5859(7)	0.2159(7)	0.040(2)
B(40)	0.4291(7)	1.1565(7)	0.2872(7)	0.046(2)
B(41)	0.6040(7)	0.9746(7)	0.2201(7)	0.047(3)
B(42)	0.4854(6)	0.9525(6)	0.2763(6)	0.036(2)
B(43)	0.5977(6)	0.9914(6)	0.3283(7)	0.037(2)
B(44)	0.6208(7)	1.1042(6)	0.2057(6)	0.038(2)
B(45)	0.5084(6)	1.0631(6)	0.1538(7)	0.037(2)
B(46)	0.4656(6)	1.0231(6)	0.3537(7)	0.037(2)
B(47)	0.5595(6)	1.1301(6)	0.3058(6)	0.031(2)
B(48)	0.4977(6)	1.1804(6)	0.1813(7)	0.037(2)
B(49)	0.4037(6)	1.0741(6)	0.2323(6)	0.034(2)
N(1)	0.2692(6)	0.3217(6)	0.0873(5)	0.077(2)
N(2)	0.7591(8)	0.6174(7)	0.5078(7)	0.128(4)
N(3)	0.3220(6)	0.8242(6)	0.0332(5)	0.080(2)
N(4)	0.7754(7)	1.098(1)	0.5945(8)	0.134(4)
C(1)	0.3108(7)	0.4297(7)	0.0348(6)	0.073(3)
C(2)	0.2444(7)	0.2657(7)	0.0228(6)	0.067(3)
C(3)	0.8146(7)	0.5178(7)	0.5558(7)	0.069(3)
C(4)	0.7631(8)	0.7041(7)	0.5418(6)	0.084(3)
C(5)	0.2389(6)	0.7511(7)	0.0459(7)	0.070(3)
C(6)	0.2960(7)	0.9242(7)	0.0490(7)	0.079(3)
C(7)	0.8136(8)	1.040(1)	0.5343(8)	0.104(4)
C(8)	0.743(1)	1.2081(9)	0.5355(8)	0.119(5)
H(10)	0.9831	0.2012	0.1044	0.052
H(11)	0.9579	0.4163	0.3640	0.054
H(12)	0.9172	0.5076	0.1463	0.048
H(13)	1.1251	0.4101	0.2606	0.056
H(14)	1.0129	0.2056	0.4085	0.047
H(15)	0.7807	0.3161	0.3057	0.046
H(16)	1.0562	0.4342	0.0729	0.049
H(17)	1.1413	0.2027	0.2400	0.055
H(18)	0.8980	0.1154	0.2911	0.053
H(19)	0.8157	0.3486	0.1003	0.048
H(20)	0.8510	−0.3846	0.3112	0.054
H(21)	1.0950	0.0024	0.1925	0.065
H(22)	0.8813	−0.0021	0.1691	0.053
H(23)	1.0304	−0.1228	0.0709	0.048
H(24)	1.1641	−0.2353	0.2834	0.051
H(25)	0.9983	−0.1233	0.3780	0.051
H(26)	0.8292	−0.1815	0.1188	0.048
H(27)	1.0376	−0.3341	0.1909	0.054
H(28)	1.0075	−0.3324	0.4142	0.056
H(29)	0.8161	−0.1844	0.3589	0.042
H(30)	0.5483	0.7842	0.1350	0.047

Table 2. (Contd.)

Atom	*x*	*y*	*z*	U_{eq}/U_{iso}, Å^2
		II		
H(31)	0.4765	0.3332	0.4132	0.047
H(32)	0.5802	0.4234	0.1993	0.058
H(33)	0.3254	0.4895	0.2547	0.049
H(34)	0.4266	0.5364	0.4334	0.046
H(35)	0.6729	0.4643	0.3938	0.043
H(36)	0.4456	0.6137	0.0854	0.042
H(37)	0.3620	0.7006	0.2396	0.049
H(38)	0.5759	0.6747	0.3483	0.038
H(39)	0.7019	0.5950	0.1895	0.048
H(40)	0.3851	1.2261	0.3029	0.056
H(41)	0.6481	0.9254	0.1972	0.056
H(42)	0.4348	0.8754	0.2915	0.043
H(43)	0.6464	0.9551	0.3877	0.045
H(44)	0.6905	1.1431	0.1682	0.045
H(45)	0.4974	1.0753	0.0826	0.045
H(46)	0.4367	0.9853	0.4306	0.045
H(47)	0.6203	1.1785	0.3315	0.037
H(48)	0.4940	1.2610	0.1120	0.045
H(49)	0.3295	1.0715	0.2086	0.041
H(11N)	0.2156	0.3266	0.1272	0.092
H(12N)	0.3233	0.2788	0.1301	0.092
H(21N)	0.6845	0.6015	0.5211	0.154
H(22N)	0.7576	0.6397	0.4392	0.154
H(31N)	0.3439	0.8464	–0.0312	0.096
H(32N)	0.3807	0.7870	0.0692	0.096
H(41N)	0.8256	1.1027	0.6370	0.160
H(42N)	0.7221	1.0642	0.6337	0.160
H(1*A*)	0.3657	0.4239	0.0115	0.087
H(1*B*)	0.3127	0.4704	0.0748	0.087
H(1*C*)	0.2610	0.4737	–0.0208	0.087
H(2*A*)	0.2229	0.1954	0.0552	0.080
H(2*B*)	0.1933	0.3109	–0.0267	0.080
H(2*C*)	0.3084	0.2650	–0.0173	0.080
H(3*A*)	0.8082	0.4892	0.6207	0.083
H(3*B*)	0.8873	0.5301	0.5364	0.083
H(3*C*)	0.7941	0.4614	0.5316	0.083
H(4*A*)	0.8319	0.7064	0.5654	0.101
H(4*B*)	0.7170	0.6839	0.5973	0.101
H(4*C*)	0.7463	0.7654	0.5034	0.101
H(5*A*)	0.2639	0.6863	0.0350	0.084
H(5*B*)	0.2212	0.7184	0.1189	0.084
H(5*C*)	0.1814	0.7826	0.0105	0.084
H(6*A*)	0.2503	0.9679	0.0043	0.095
H(6*B*)	0.3613	0.9613	0.0509	0.095
H(6*C*)	0.2693	0.9000	0.1179	0.095
H(7*A*)	0.7706	1.0513	0.4845	0.125
H(7*B*)	0.8185	0.9594	0.5810	0.125
H(7*C*)	0.8858	1.0579	0.5166	0.125
H(8*A*)	0.6923	1.2095	0.4882	0.143
H(8*B*)	0.8029	1.2461	0.5004	0.143
H(8*C*)	0.7113	1.2480	0.5791	0.143

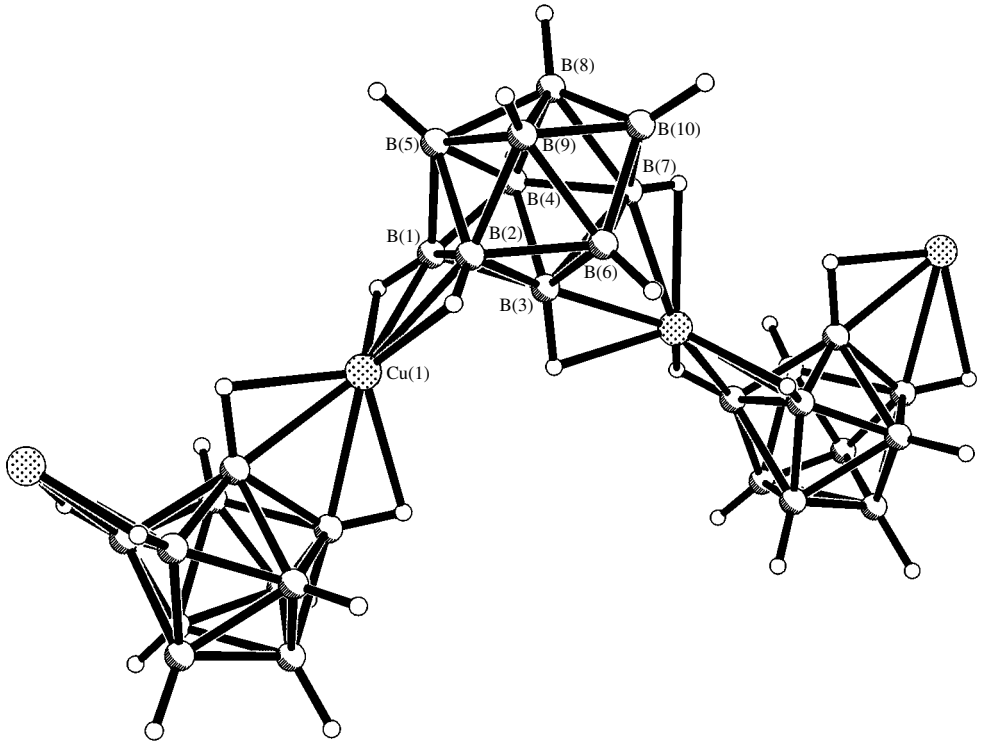

Fig. 1. A fragment of the chain and the atomic numbering in structure **I**.

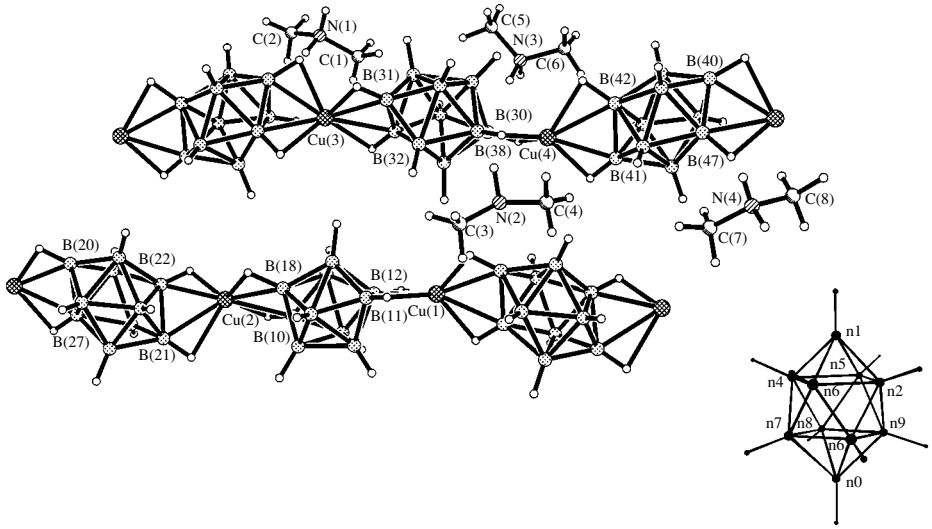

Fig. 2. A fragment of structure **II**. In the polyhedral anions, only B atoms that are involved in Cu coordination are labeled. The scheme of numbering of the B atoms is shown in the inset.

In structure **II**, the metal coordination by the edges of the apical belts only results in the formation of straight $[(CuB_{10}H_{10})^-]_\infty$ chains that run along the *b* axis, (Fig. 4). In both independent chains, the polyhedra that coordinate the Cu atoms by the 1–2 and 7–10 edges alternate with those coordinating Cu atoms by the 1–2 and 8–10 edges; that is, the edges of a polyhedron involved in coordination are related by the S_8^3 or S_8^5 symmetry operations. The symmetrically related chains are packed into layers parallel to the *bc* plane. Different layers alternate along the *a* axis. The $[(CH_3)_2NH_2]^+$ cat-

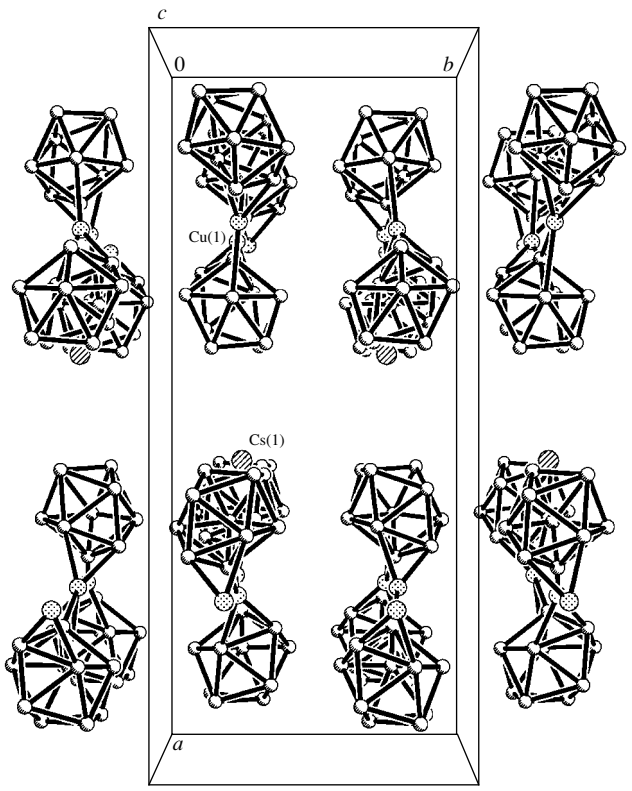

Fig. 3. Projection of structure **I** onto the *ab* plane. The H atoms are omitted.

ions are located between the anionic layers and participate in the N–H··H–B specific interactions with polyhedral anions. Similar interactions of the *closo*-decaborate anion with organic cations have already been observed, and their existence was supported by the spectral studies [10, 11]. The sets of vertices that are involved in specific interactions are different for all the nitrogen atoms. The N(1) atom is bound to the B(17), B(16), B(48), and B(49) atoms; N(2), to B(20), B(29), B(31), and B(34); N(3), to B(44), B(45), B(30), and B(37); and N(4), to B(25), B(21), B(46), and B(49). Thus, each cation in **II** links two chains: the cations containing the N(3) atom bridges the symmetrically related –Cu(3)–[B(30)–B(39)]H_{10}–Cu(4)–[B(40)–B(49)]H_{10}– chains, and the rest of the cations bridge different chains. The dimethylammonium cations with the N(1) and N(3) atoms form shorter N··B contacts [3.30–3.54(1) and 3.36–3.46(1) Å, respectively] as compared to those formed by the two other cations [3.43–3.75(1) and 3.43–3.56(1) Å for N(2) and N(4), respectively]. Apparently, the arrangement of the cations in the unit cell violates the crystallographic equivalence of the anionic chains.

Thus, the X-ray diffraction studies of crystals **I** and **II** revealed that, in the compounds with monovalent copper, the decahydro-*closo*-decaborate anion acts as a ligand. Metal coordination is achieved by the B–H pairs of atoms that are linked by the common edge. Com-

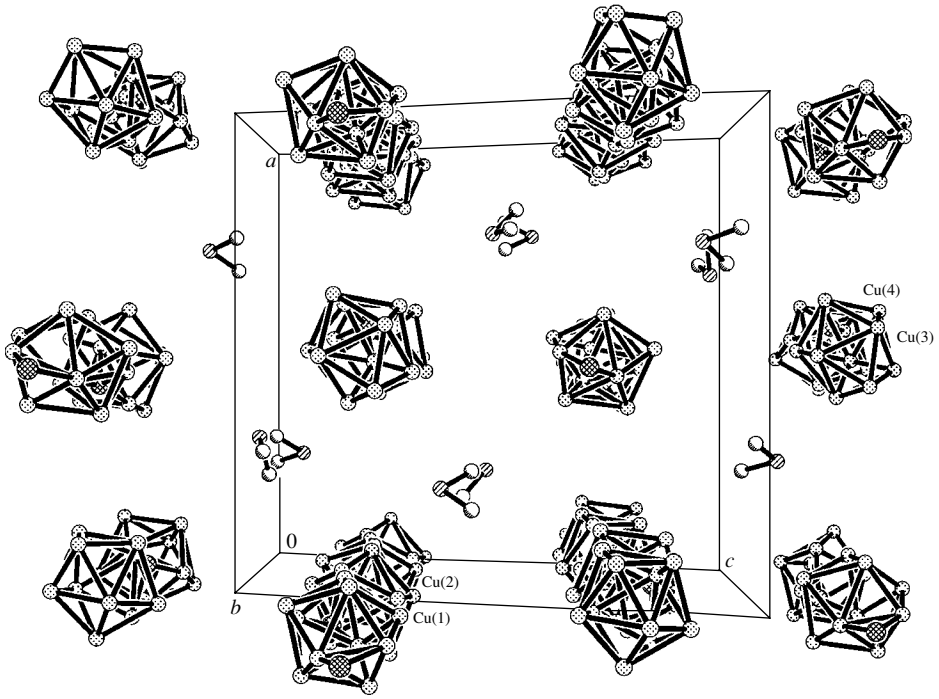

Fig. 4. Projection of structure **II** onto the *ac* plane. The H atoms are omitted.

pound **I** provides the first example of the $B_{10}H_{10}^{2-}$ anion that coordinates metal by an edge of the equatorial belt.

ACKNOWLEDGMENTS

This study was supported by the Russian Foundation for Basic Research, project nos. 99-03-32589 and 00-15-97394.0. We also acknowledge the support of the Russian Foundation for Basic Research in the payment of the license for using the Cambridge Structural Database, project no. 99-07-90133.

REFERENCES

1. E. A. Malinina, L. V. Goeva, K. A. Solntsev, and N. T. Kuznetsov, Zh. Neorg. Khim. **38** (1), 38 (1993).
2. E. A. Malinina, K. Yu. Zhizhin, L. V. Goeva, *et al.*, Dokl. Akad. Nauk **378** (3), 351 (2001).
3. G. M. Sheldrick, *SHELXS97: Program for the Solution of Crystal Structures* (Univ. of Göttingen, Göttingen, 1997).
4. G. M. Sheldrick, *SHELXL97: Program for the Refinement of Crystal Structures* (Univ. of Göttingen, Göttingen, 1997).
5. R. D. Dobrott and W. N. Lipscomb, J. Chem. Phys. **37** (8), 1779 (1962).
6. J. T. Gill and S. J. Lippard, Inorg. Chem. **14** (4), 751 (1975).
7. W. N. Lipscomb, *Boron Hydrides* (Benjamin, New York, 1963), p. 110.
8. I. Tiritiris, T. Schleid, K. Müller, and W. Preetz, Z. Anorg. Allg. Chem. **626**, 323 (2000).
9. I. Yu. Kuznetsov, D. M. Vinitskiĭ, K. A. Solntsev, *et al.*, Zh. Neorg. Khim. **32** (12), 3112 (1987).
10. C. T. Chantler and E. N. Maslen, Acta Crystallogr., Sect. B: Struct. Sci. **45** (3), 290 (1989).
11. A. V. Virovets, N. N. Vakulenko, V. V. Volkov, and N. V. Podberezskaya, Zh. Strukt. Khim. **35** (3), 72 (1994).

Translated by I. Polyakova

Crystallography Reports, Vol. 48, No. 1, 2003, pp. 92–97. Translated from Kristallografiya, Vol. 48, No. 1, 2003, pp. 97–102.

STRUCTURE OF ORGANIC COMPOUNDS

X-ray Diffraction Studies of 5-Functionalized Substituted 1,2,3,4-Tetrahydropyrimidin-2-ones(thiones): I. Molecular Structures of 5-Acetyl-4-Ethyl-6-Methyl-1,2,3,4-Tetrahydropyrimidine-2-Thione, 5-Acetyl-6-Methyl-4-(4-Methylphenyl)-1,2,3,4-Tetrahydropyrimidine-2-Thione, and 5-Acetyl-4-(4-Methoxyphenyl)-6-Methyl-1,2,3,4-Tetrahydropyrimidin-2-one

G. V. Gurskaya*, V. E. Zavodnik, and A. D. Shutalev*****

** Énglehardt Institute of Molecular Biology, Russian Academy of Sciences, ul. Vavilova 32, Moscow, 119991 Russia*

e-mail: gurskaya@eimb.ru

*** Karpov Research Institute of Physical Chemistry, State Scientific Center, ul. Vorontsovo pole 10, Moscow, 103064 Russia*

**** Lomonosov State Academy of Fine Chemical Technology, pr. Vernadskogo 86, Moscow, 117571 Russia*

Received March 15, 2002

Abstract—The structures of three 5-acetyl-1,2,3,4-tetrahydropyrimidin-2-ones(thiones), namely, 5-acetyl-4-ethyl-6-methyl-1,2,3,4-tetrahydropyrimidine-2-thione, 5-acetyl-6-methyl-4-(4-methylphenyl)-1,2,3,4-tetrahydropyrimidine-2-thione, and 5-acetyl-4-(4-methoxyphenyl)-6-methyl-1,2,3,4-tetrahydropyrimidin-2-one, which are potential medicinals, are studied by X-ray diffraction. The conformational features of the molecules studied are analyzed. For these compounds, the dependence of the conformation of the tetrahydropyrimidine ring on the orientation of the substituent at the C(4) atom with respect to the heterocycle is found. *© 2003 MAIK "Nauka/Interperiodica".*

INTRODUCTION

At present, 5-functionalized substituted 1,2,3,4-tetrahydropyrimidin-2-ones and their 2-thioxo analogues (**I**) have attracted considerable attention of researchers due to a wide spectrum of biological properties exhibited by compounds of this type.

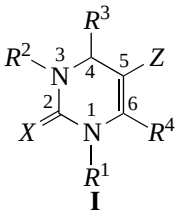

I

X = O, S

Z = COOR, COOH, C(O)NR_2, CN, NO_2, C(O)R

Recently, highly active antihypertensive agents, inhibitors of kinesin *Eg*5, antiviral and antibacterial agents, selective antagonists of α_{1a} adrenoreceptors, etc. [1–8] have been found among esters of 2-oxo- and 2-thioxo-1,2,3,4-tetrahydropyrimidine-5-carboxylic acids (**I**, Z = COOR), which are known as Biginelli compounds [1]. In this respect, much effort of scientists has been directed toward the investigation into the dependence of the biological activity of Biginelli compounds on the chemical and three-dimensional structure of their molecules [6–8].

Compounds of type **I**, which contain functional groups other than the ester group at the C(5) atom, specifically, the acyl group [Z = C(O)R] [7], have been studied to a considerably lesser degree because of the lack of a unified convenient approach to their chemical synthesis. Earlier [9, 10], we developed a new simple procedure of preparing 5-acyl-1,2,3,4-tetrahydropyrimidin-2-ones(thiones) with the use of the reaction between α-tosyl substituted ureas or thioureas and 1,3-dicarbonyl compounds in the presence of bases, followed by dehydration of the 5-acyl-4-hydroxyhexahydropyrimidin-2-ones(thiones) formed. In this paper, we report the results of the X-ray diffraction studies of three 5-acetyl-1,2,3,4-tetrahydropyrimidin-2-ones(thiones), namely, 5-acetyl-4-ethyl-6-methyl-1,2,3,4-tetrahydropyrimidine-2-thione (**II**), 5-acetyl-6-methyl-4-(4-methylphenyl)-1,2,3,4-tetrahydropyrimidine-2-thione (**III**),

1063-7745/03/4801-0092$24.00 © 2003 MAIK "Nauka/Interperiodica"

and 5-acetyl-4-(4-methoxyphenyl)-6-methyl-1,2,3,4-tetrahydropyrimidin-2-one (**IV**).

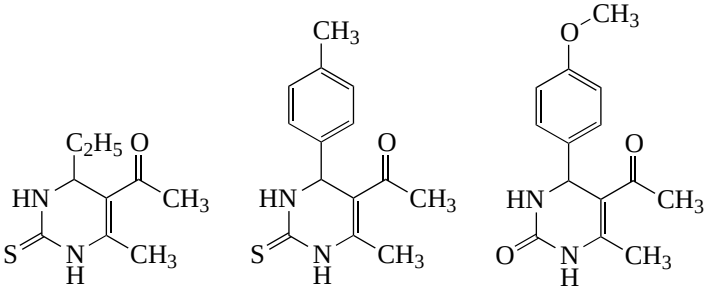

II **III** **IV**

EXPERIMENTAL

Racemic compounds **II**–**IV** were synthesized according to the procedure described in [9, 10]. Crystals suitable for X-ray diffraction analysis were prepared by slow evaporation of a solvent from saturated alcoholic solutions of the corresponding compounds. The stereoisomers of compound **IV** separated in the course of crystallization.

The crystallographic parameters and three-dimensional sets of intensities of reflections with $I > 2\sigma(I)$ for all the crystals studied were obtained on a CAD4 four-circle automated diffractometer (MoK_α radiation, β filter, θ/2θ scan mode).

The main crystallographic parameters are as follows:

Crystals **II** are triclinic, $a = 7.246(1)$ Å, $b = 7.929(2)$ Å, $c = 9.201(2)$ Å, $\alpha = 95.59(3)°$, $\beta = 99.97(3)°$, $\gamma = 94.48(3)°$, $V = 515.7(2)$ Å^3, $Z = 2$, $d_{calcd} = 1.279$ g/cm^3, and space group $P\bar{1}$.

Crystals **III** are triclinic, $a = 7.219(1)$ Å, $b = 8.164(2)$ Å, $c = 13.080(3)$ Å, $\alpha = 105.76(2)°$, $\beta = 91.73(2)°$, $\gamma = 107.06(2)°$, $V = 704.2(3)$ Å^3, $Z = 2$, $d_{calcd} = 1.228$ g/cm^3, and space group $P\bar{1}$.

Crystals **IV** are orthorhombic, $a = 7.437(2)$ Å, $b = 14.817(3)$ Å, $c = 23.782(5)$ Å, $V = 2620.6(10)$ Å^3, $Z = 8$, $d_{calcd} = 1.319$ g/cm^3, and space group $P2_12_12_1$.

The structures were solved by the direct method, and the non-hydrogen atoms were refined by the full-matrix least-squares procedure in the anisotropic approximation. The hydrogen atoms were located from difference Fourier syntheses and refined by the least-squares procedure in the isotropic approximation. The discrepancy factors R have the following values: in structure **II**, $R = 0.029$ for 1733 reflections with $I > 2\sigma(I)$; in structure **III**, $R = 0.031$ for 1519 reflections; and in structure **IV**, $R = 0.022$ for 1171 reflections. The coordinates and isotropic equivalent thermal parameters of the non-hydrogen atoms in structures **II**–**IV** are listed in Table 1. All the calculations concerned with the solution and refinement of the structures were performed with the SHELX97 program package [11].

RESULTS AND DISCUSSION

It is known that the biological activity of 1,2,3,4-tetrahydropyrimidin-2-ones(thiones) depends on both the chemical nature of the substituents and the three-dimensional structure of molecules [1–5]. Compounds **II**–**IV** differ mainly in the substituent at the C(4) atom (the alkyl group in **II** and the aryl groups in **III** and **IV**). This allows us to use the X-ray structural data in analyzing the effect of different substituents at the C(4) atom on the conformation of the pyrimidine ring. However, correlation between the three-dimensional structures and the biological activity is not discussed in this paper, because the activity of compounds **II**–**IV** has not been studied yet.

The molecular structures of compounds **II**–**IV** and the atomic numbering schemes used in this paper are shown in Figs. 1–3, respectively. The bond lengths and angles in the structures studied are in agreement within the accuracy of their determination and are close to those available in the literature; therefore, we dwell below only on the analysis of the conformations. The main conformational parameters of molecules **II**–**IV** are given in Tables 2 and 3. The graphical calculations and the calculation of the rms planes were performed with the SHELXTL81 program. The torsion angles and the geometry of the hydrogen bonds were calculated with the PARST93 program [12].

In studies of the correlation between the biological activity and the three-dimensional molecular structure in the series of 1,2,3,4-tetrahydropyrimidin-2-ones(thiones), it is conventional to describe the conformation of the pyrimidine rings in terms of a boat-type conformation [8]. Below, we follow this pattern but will use also another, simpler approach. The conformational differences in the pyrimidine rings can be easily seen from the changes in the dihedral angle (ϕ) between two obviously planar atomic groups, namely, the N(1)N(3)C(2)S[O] (thio)ureide fragment and the N(1)C(6)C(5)C(4) group, which contains the C(5)=C(6) double bond. The rms atomic deviations from these planes are less than those in the planar C(2)N(3)C(5)C(6) fragment of the boat, and, therefore, the interpretation of conformations is more accurate.

Table 1. Coordinates ($\times 10^4$) and equivalent isotropic thermal parameters ($Å^2 \times 10^3$) of the non-hydrogen atoms in structures **II**, **III**, and **IV**

Structure **II**					Structure **III**				
Atom	*x*/*a*	*y*/*b*	*z*/*c*	U_{eq}	Atom	*x*/*a*	*y*/*b*	*z*/*c*	U_{eq}
S	7547(1)	9157(1)	999(1)	43(1)	S	8033(1)	6161(1)	4664(1)	47(1)
O(51)	15819(2)	7398(3)	4298(2)	78(1)	O(51)	1433(2)	9406(2)	3280(2)	56(1)
N(1)	9355(2)	7761(2)	3267(1)	36(1)	N(1)	7417(3)	8451(2)	3704(2)	39(1)
N(3)	11174(2)	8685(2)	1668(1)	37(1)	N(3)	4704(2)	6663(3)	4150(2)	36(1)
C(2)	9475(2)	8502(2)	1997(2)	33(1)	C(2)	6619(3)	7117(3)	4146(2)	34(1)
C(4)	12713(2)	7733(2)	2305(2)	35(1)	C(4)	3396(3)	7188(3)	3522(2)	32(1)
C(41)	12618(2)	5984(2)	1429(2)	45(1)	C(41)	2577(3)	5778(3)	2461(2)	39(1)
C(42)	12745(3)	6058(3)	–191(2)	54(1)	C(42)	3769(5)	5265(4)	1720(2)	66(1)
C(43)					C(43)	2986(8)	3998(5)	741(3)	93(1)
C(44)					C(44)	1018(7)	3223(4)	466(3)	87(1)
C(45)					C(45)	–163(6)	3706(5)	1214(4)	90(1)
C(46)					C(46)	599(4)	4955(4)	2199(3)	63(1)
C(47)					C(47)	160(20)	1910(8)	–622(5)	162(4)
C(5)	12624(2)	7629(2)	3928(2)	35(1)	C(5)	4456(3)	8998(3)	3375(2)	32(1)
C(51)	14447(2)	7524(2)	4884(2)	44(1)	C(51)	3156(3)	9982(3)	3167(2)	37(1)
C(52)	14705(3)	7573(3)	6536(2)	57(1)	C(52)	3785(4)	11589(4)	2777(3)	51(1)
C(6)	10913(2)	7548(2)	4328(2)	34(1)	C(6)	6422(3)	9515(3)	3426(2)	33(1)
C(61)	10394(2)	7240(3)	5794(2)	47(1)	C(61)	7771(3)	11155(4)	3223(3)	50(1)

Structure **IV**

Molecule 1					Molecule 2				
Atom	*x*/*a*	*y*/*b*	*z*/*c*	U_{eq}	Atom	*x*/*a*	*y*/*b*	*z*/*c*	U_{eq}
O(1)	1821(4)	6437(2)	4897(1)	40(1)	O(1*a*)	6711(4)	6389(2)	4680(1)	41(1)
O(41)	–227(5)	1480(2)	4501(2)	64(1)	O(41*a*)	9610(5)	2711(2)	6391(2)	68(1)
O(51)	232(5)	4632(3)	2636(1)	70(1)	O(51*a*)	8547(6)	7211(3)	7120(2)	88(1)
N(1)	3350(6)	5890(3)	4147(2)	39(1)	N(1*a*)	5255(5)	6516(2)	5514(2)	39(1)
N(3)	291(5)	5780(3)	4182(2)	39(1)	N(3*a*)	8314(6)	6637(2)	5477(1)	36(1)
C(2)	1791(6)	6051(2)	4436(2)	33(1)	C(2*a*)	6798(6)	6501(3)	5195(2)	34(1)
C(4)	274(6)	5104(3)	3731(2)	36(1)	C(4*a*)	8393(6)	6462(3)	6085(2)	35(1)
C(41)	160(5)	4148(3)	3955(2)	35(1)	C(41*a*)	8652(5)	5458(3)	6193(2)	36(1)
C(42)	1227(7)	3839(3)	4385(2)	49(1)	C(42*a*)	9984(6)	5003(4)	5901(2)	46(1)
C(43)	1166(7)	2956(3)	4583(2)	53(1)	C(43*a*)	10244(7)	4092(4)	5978(2)	54(1)
C(44)	–16(6)	2364(3)	4344(2)	49(1)	C(44*a*)	9207(6)	3603(3)	6353(2)	46(1)
C(45)	–1104(7)	2652(4)	3903(2)	55(2)	C(45*a*)	7890(7)	4043(3)	6644(2)	50(1)
C(46)	–1032(6)	3536(3)	3718(2)	47(1)	C(46*a*)	7633(6)	4973(4)	6561(2)	46(1)
C(47)	924(9)	1151(5)	4934(3)	74(2)	C(47*a*)	8647(9)	2193(4)	6788(3)	69(2)
C(5)	1905(6)	5250(3)	3362(2)	35(1)	C(5*a*)	6753(6)	6859(3)	6363(2)	37(1)
C(51)	1653(7)	4979(3)	2771(2)	47(1)	C(51*a*)	7037(7)	7219(3)	6926(2)	50(1)
C(52)	3054(11)	5114(7)	2324(3)	86(2)	C(52*a*)	5562(9)	7594(5)	7283(2)	60(2)
C(6)	3416(6)	5599(3)	3596(2)	36(1)	C(6*a*)	5205(6)	6818(3)	6068(2)	35(1)
C(61)	5262(7)	5704(5)	3345(3)	56(1)	C(61*a*)	3328(7)	7043(5)	6255(2)	51(1)

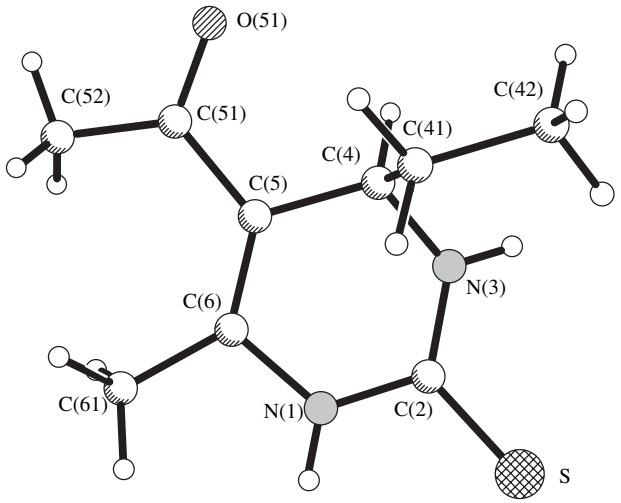

Fig. 1. Structure of molecule **II**.

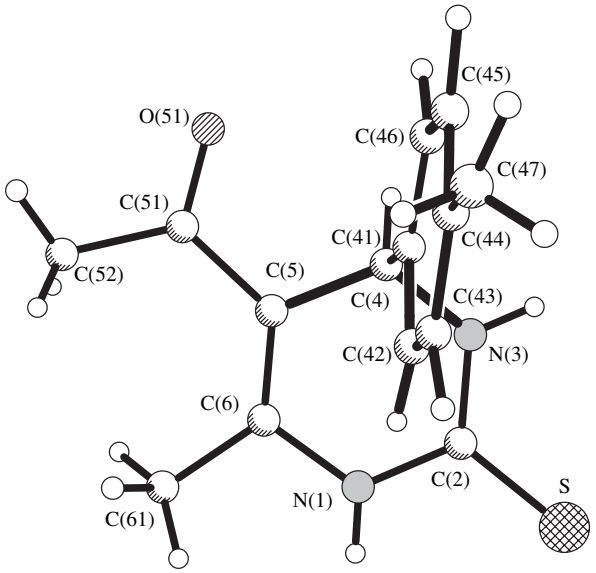

Fig. 2. Structure of molecule **III**.

The non-hydrogen atoms of the substituents at the C(4) and C(5) atoms in the molecules of compounds **II**–**IV** form planar groups. These are the acetyl groups, the C(4)C(41)C(42) ethyl fragment in **II**, the methylphenyl substituent in **III**, and the methoxyphenyl group in **IV**. In the last structure, the atoms involved in the C(44)C(47)O(41) and C(44*a*)C(47*a*)O(41*a*) methoxy groups in molecules 1 and 2 actually lie in the planes of the corresponding phenyl rings with a mean atomic deviation of 0.01 Å and the angles between the planes of the methoxy groups and the benzene rings are only 2.4° in molecule 1 and 3.2° in molecule 2.

It can be seen from Table 2 that the planes of the substituents at the C(4) atom, that is, the C(4)C(41)C(42) ethyl fragment or the aryl fragments, are almost perpendicular to the C(2)N(3)C(5)C(6) plane of the pyrimidine ring (the plane of the bottom of the boat). However, these fragments show different orientations relative to the N(3)–C(4) and C(4)–C(5) bonds of the heterocyclic ring. In the molecules of compound **III** and molecules 1 of compound **IV**, the aryl fragments are situated over the plane of the pyrimidine ring (Figs. 2, 3) and, in accordance with the N(3)–C(4)–C(41)–C(42) (–60.0° and –47.2°) and C(5)–C(4)–C(41)–C(42) (63.1° and 75.8°) torsion angles (Table 3), exhibit a *gauche* orientation. In the molecules of compound **II** and molecules 2 of compound **IV** (Figs. 1, 3), the methyl and aryl fragments are placed aside from the planes of the pyrimidine rings and, in accordance with the corresponding torsion angles (59.5° and 48.6°; –178.8° and 172.0°; Table 3), show a *trans* orientation.

At the same time, the type of conformation of the substituent at the C(4) atom in the molecules of the pyrimidines studied correlates with the degree of puckering of the pyrimidine ring. Actually, in the molecules of compound **II** and molecules 2 of compound **IV** with the *trans* orientation of the alkyl and aryl fragments, the puckering of the pyrimidine ring is more pronounced than that in the molecules of compound **III** and molecules 1 of compound **IV** with the *gauche* orientation of the aryl groups. The deviations of the N(1) and C(4) atoms from the C(2)N(3)C(5)C(6) plane of the ring are

Table 2. Conformational parameters of the molecules of compounds **II**–**IV**

Conformation	**II**	**III**	**IV**	
			Molecule 1	Molecule 2
Deviations of the N(1) and C(4) atoms (Å) from the C(2)N(3)C(5)C(6) plane	0.164 0.442	0.123 0.339	0.128 0.412	0.157 0.489
ϕ angles (deg) between the N(1)C(2)S[O]N(3) and N(1)C(6)C(5)C(4) planes in the pyrimidine ring	21.0	15.8	17.6	21.3
Angles (deg) between the planes of the C(2)N(3)C(5)C(6) pyrimidine fragment and the C(5)C(51)C(52)O(51) acetoxy group	21.2	7.9	18.2	15.4
Angles (deg) between the planes of the C(2)N(3)C(5)C(6) pyrimidine fragment and the ethyl or aryl fragment	83.7	89.4	86.6	86.1

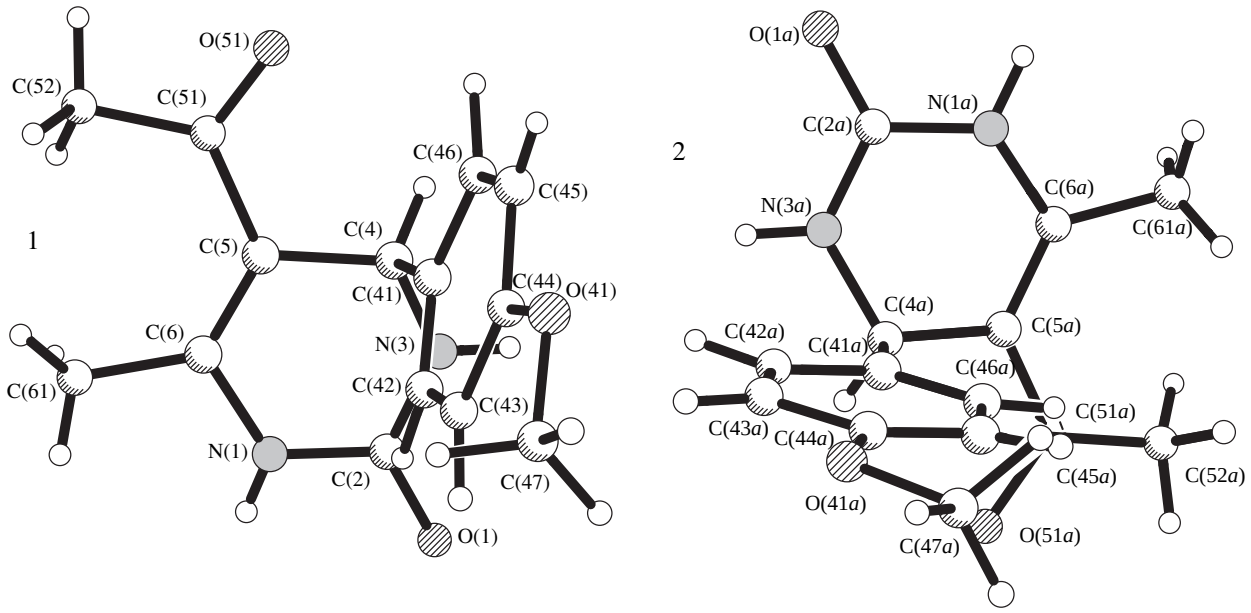

Fig. 3. Structure of crystallographically independent molecules 1 and 2 in compound **IV**.

0.164, 0.157 and 0.442, 0.489 Å, respectively, in the former molecules and 0.123, 0.128 and 0.339, 0.412 Å, respectively, in the latter molecules (Table 2). The degree of puckering of the pyrimidine rings is more clearly manifested by the dihedral angle (ϕ) between the N(1)C(2)S[O]N(3) and N(1)C(6)C(5)C(4) planes in pyrimidine. In the molecules with the *trans* orientation of the substituents at the C(4) atom, the ϕ angles are 21.0° and 21.3°; in the molecules with the *gauche* orientation, these angles are 15.8° and 17.6° (Table 2).

Note also that, in going from the alkyl substituent at the C(4) atom in the molecules of compound **II** to the aryl substituent in the molecules of the two other compounds, the angle between the planes of the C(5)C(51)C(52)O(51) acetyl group and the C(2)N(3)C(5)C(6) fragment of pyrimidine slightly

Table 3. Main torsion angles (deg) characterizing the conformation of the pyrimidine rings and the relative orientations of the substituents at the C(4) and C(5) atoms in the molecules of compounds **II**, **III**, and **IV**

Torsion angle	**II**	**III**	**IV**	
			Molecule 1	Molecule 2
N(1)–C(6)–C(5)–C(4)	−7.3(2)	−5.6(3)	−6.3(6)	−7.3(6)
C(6)–C(5)–C(4)–N(3)	32.8(2)	25.1(3)	29.8(6)	36.0(5)
C(5)–C(4)–N(3)–C(2)	−39.8(2)	−30.8(3)	−38.0(6)	−45.3(5)
C(4)–N(3)–C(2)–N(1)	18.1(2)	14.2(4)	19.7(6)	22.4(6)
N(3)–C(2)–N(1)–C(6)	13.9(2)	10.6(4)	9.8(7)	11.9(6)
C(2)–N(1)–C(6)–C(5)	−18.8(2)	−14.4(4)	−16.1(7)	−19.4(6)
N(3)–C(4)–C(41)–C(42)	59.5(2)	−60.0(3)	−47.2(6)	48.6(5)
C(5)–C(4)–C(41)–C(42)	−178.8(2)	63.1(3)	75.8(5)	172.0(4)
N(3)–C(4)–C(41)–C(46)	–	120.0(3)	134.1(4)	−130.9(5)
C(5)–C(4)–C(41)–C(46)	–	−116.9(3)	−102.8(5)	−7.6(6)
N(3)–C(4)–C(5)–C(51)	−150.8(1)	−156.0(2)	−150.6(4)	−145.6(4)
N(1)–C(6)–C(5)–C(51)	176.8(1)	175.7(2)	174.2(4)	174.5(4)
C(4)–C(5)–C(51)–O(51)	−5.5(2)	10.1(3)	−3.3(6)	3.0(7)
C(6)–C(5)–C(51)–O(51)	170.6(2)	−171.2(2)	176.2(4)	−178.8(5)
C(4)–C(5)–C(51)–C(52)	174.2(2)	−166.9(2)	176.3(5)	−176.5(4)
C(6)–C(5)–C(51)–C(52)	−9.7(3)	11.8(4)	−4.2(8)	1.7(8)

Table 4. Geometric parameters of the intermolecular hydrogen bonds in structures **II**–**IV**

D–H··*A* bond*	*D*··*A* distance, Å	H··*A* distance, Å	*D*–H··*A* angle, deg	Symmetry operation for *A*
II				
N(3)–H···S	3.342(2)	2.49(2)	165(3)	(2 –*x*, 2 – *y*, –*z*)
N(1)–H···O(51)	2.886(2)	2.05(2)	172(5)	(*x* – 1, *y*, *z*)
III				
N(3)–H···S	3.329(3)	2.49(2)	165(3)	(1 –*x*, 1 – *y*, 1 – *z*)
N(1)–H···O(51)	2.886(3)	2.12(3)	161(5)	(1 +*x*, *y*, *z*)
IV				
N(1)–H···O(1*a*)	2.898(5)	2.19(4)	167(4)	(*x*, *y*, *z*)
N(1*a*)–H···O(1)	2.948(5)	2.07(5)	177(4)	(*x*, *y*, *z*)
N(3)–H···O(1*a*)	3.050(5)	2.26(4)	170(5)	(*x* – 1, *y*, *z*)
N(3*a*)–H···O(1)	2.965(5)	2.06(4)	171(4)	(*x* + 1, *y*, *z*)
C(46*a*)–H···O(51)	3.379(6)	2.55(5)	152(4)	(0.5 –*x*, 1 – *y*, 0.5 + *z*)
C(47*a*)–H···O(51*a*)	3.332(8)	2.60(5)	127(5)	(2 – *x*, *y* – 0.5, 1.5 – *z*)

* *D* is a donor, *A* is an acceptor, and H is a hydrogen atom.

decreases. The carbonyl oxygen of the acetyl group in all the structures studied is situated *trans* relative to the C(5)=C(6) double bond of pyrimidine.

The characteristic feature of the crystal structures studied is the trend of the tetrahydropyrimidine molecules to form dimers. In crystals **II** and **III**, the molecules related by the centers of symmetry are linked into dimers through two N(3)–H···S intermolecular hydrogen bonds (Table 4). In the three-dimensional crystal structure, the dimers are interlinked through a system of the N(1)–H···O(51) intermolecular hydrogen bonds and van der Waals forces. In crystal **IV**, the dimers consist of two crystallographically independent molecules, which are linked through the N(1)(*x*; *y*; *z*)–H··O(1*a*)(*x*; *y*; *z*) and N(1*a*)(*x*; *y*; *z*)–H··O(1)(*x*; *y*; *z*) hydrogen bonds. The dimers are interlinked through a system of the N(3)[N(3*a*)]–H··O(1*a*)[O(1)] intermolecular hydrogen bonds and van der Waals forces to form the crystal structure. Probably, the C–H··O intermolecular hydrogen bonds also contribute to the stabilization of this structure. The oxygen atoms of all the acetyl and methoxy groups can be involved in these bonds. The geometric parameters of some possible C–H··O bonds are listed in Table 4.

ACKNOWLEDGMENTS

This study was supported by the Russian Foundation for Basic Research, project no. 00-15-74835. We also acknowledge the support of the Russian Foundation for Basic Research in the payment of the license for using the Cambridge Structural Database, project no. 02-07-90322.

REFERENCES

1. C. O. Kappe, Tetrahedron **49**, 6937 (1993).
2. K. S. Atwal, B. N. Swanson, S. E. Unger, *et al.*, J. Med. Chem. **34**, 806 (1991).
3. G. J. Grover, S. Dzwonczyk, D. M. McMullen, *et al.*, J. Cardiovasc. Pharmacol. **26**, 289 (1995).
4. S. J. Haggarty, T. U. Mayer, D. T. Miyamoto, *et al.*, Chem. Biol. **7**, 275 (2000).
5. D. Nagarathnam, S. W. Miao, B. Lagu, *et al.*, J. Med. Chem. **42**, 4764 (1999).
6. G. C. Rovnyak, S. D. Kimball, B. Beyer, *et al.*, J. Med. Chem. **38**, 119 (1995).
7. C. O. Kappe, Acc. Chem. Res. **33**, 879 (2000).
8. C. O. Kappe, W. M. F. Fabian, and M. A. Semones, Tetrahedron **53**, 2803 (1997).
9. A. D. Shutalev and V. A. Kuksa, Khim. Geterotsikl. Soedin., No. 1, 97 (1995).
10. A. D. Shutalev, E. A. Kishko, N. V. Sivova, and A. Yu. Kuznetsov, Molecules **3**, 100 (1998).
11. G. M. Sheldrick, *SHELX97: Program for the Solution and Refinement of Crystal Structures* (University of Göttingen, Göttingen, 1997).
12. M. Nardelli, Comput. Chem. **7**, 95 (1993).

Translated by I. Polyakova

Crystallography Reports, Vol. 48, No. 1, 2003, pp. 98–105. Translated from Kristallografiya, Vol. 48, No. 1, 2003, pp. 103–110.

STRUCTURE OF MACROMOLECULAR COMPOUNDS

Solution Structures of Human Immunoglobulins IgG and IgM and Rheumatoid Factor IgM-RF

V. V. Volkov*, R. L. Kayushina*, V. A. Lapuk, E. V. Shtykova*, E. Yu. Varlamova***, M. Malfois****, and D. I. Svergun*******

** Shubnikov Institute of Crystallography, Russian Academy of Sciences, Leninskiĭ pr. 59, Moscow, 119333 Russia*

e-mail: vvo@ns.crys.ras.ru

*** Zelinskiĭ Institute of Organic Chemistry, Russian Academy of Sciences, Leninskiĭ pr. 47, Moscow, 119991 Russia*

**** Hematology Research Center, Russian Academy of Medical Sciences, Novozykovskiĭ proezd 4a, Moscow, 125167 Russia*

***** Netherlands Organization for Scientific Research, Grenoble, France*

****** European Molecular Biology Laboratory, c/o DESY, Notkestrasse 85, Hamburg, 22603 Germany*

Received July 1, 2002

Abstract—The low-resolution structures of human immunoglobulins M (IgM) and G (IgG) and the rheumatoid factor (IgM-RF) in solution were determined from synchrotron-radiation small-angle X-ray scattering by the method of dummy atom modeling (bead models). The structural models of IgM determined on the assumption that the molecule has a fivefold symmetry axis are in good agreement with the atomic structure of this protein proposed earlier. The molecular structure of the rheumatoid factor IgM-RF reconstructed by dummy atom modeling differs from the model of the IgM molecule: the $F(ab)_2$ regions in the IgM-RF pentamer are asymmetric. This result confirms the earlier assumption that these regions in IgM-RF are different both structurally and biochemically. The typical shape of the IgG molecule in solution was demonstrated to be closer to the *Y* type, with the maximum size being larger than the size of the known crystallographic models. © *2003 MAIK "Nauka/Interperiodica".*

INTRODUCTION

Immunoglobulins belong to the family of glycoproteins produced in mammals. The main functions of most of these proteins are reduced to specific recognition and binding of foreign substances (antigens) and performance of effector functions [1]. There are five classes of immunoglobulins found in most of higher mammals which differ in the molecular size, charge, amino-acid composition, and carbohydrate content. Immunoglobulins IgG comprise 70–75% of all serum immunoglobulins. Immunoglobulins IgM account for 10% of the total pool of serum immunoglobulins. Immunoglobulin M that exhibits rheumatoid activity (IgM-RF) forms the autoimmune complex with IgG of the same organism. The rheumatoid factor IgM-RF is present in blood serum of most of the patients suffering from rheumatoid arthritis. A topical problem is to reveal the relation between the structure and pathologic function of IgM-RF, which is necessary for the development of the approaches to diagnostics and treatment of rheumatoid arthritis and other autoimmune diseases.

Recently, the three-dimensional structures of several intact monoclonal immunoglobulins IgG were established at 0.28–0.4 nm resolution [2–4]. All the attempts to grow the crystals of immunoglobulins of other classes, such as IgA, IgD, IgE, and IgM, failed. Their molecular structures were studied by electron microscopy, atomic force microscopy, NMR, and other physicochemical methods. Some of these methods require special treatment of the samples, which, in turn, can change the structures of the constituent molecules.

Small-angle X-ray scattering (SAXS) allows one to study the structures of biological macromolecules in solutions under the conditions close to physiological ones. The intensity curves in SAXS are determined by the shape of the molecules at about 2–3 nm resolution; in other words, small-angle X-ray scattering enables one to study the conformation of biopolymers in solution [5].

Comparing experimental scattering curves with the intensities calculated for high-resolution structures determined by the crystallographic methods allows one to estimate the difference in the structures of the molecules in crystal and solution [6–12] and to verify the adequacy of hypothetical molecular models.

EXPERIMENTAL

Preparation of immunoglobulin solutions. The IgG solutions were prepared from the chemical pur-

1063-7745/03/4801-0098$24.00 © 2003 MAIK "Nauka/Interperiodica"

chased by Sigma (USA). Human monoclonal IgM (Waldenström's disease) and monoclonal IgM-RF were prepared according to procedures developed elsewhere [13–14]. Solutions of these proteins with the concentrations 2.5–14.0 mg/ml were prepared using a Tris buffer, pH 8.3–8.4 (Merck, Germany). The concentrations of the proteins in solutions were measured by spectrophotometry using absorption values $A^{1\%}_{280/1\ \mathrm{cm}}$ equal to 12.0 for IgM and IgM-RF and 14.0 for IgG. The aggregation level of the proteins in solutions was estimated using a Spinko E analytical ultracentrifuge (Beckman, USA). The aggregation contents did not exceed 5%. All the solutions were filtered through a membrane (pore size 0.45 μm; Schleicher and Schuell, Germany) directly prior the experiments.

Small-angle X-ray scattering measurements. Synchrotron-radiation small-angle X-ray scattering data were collected [15–17] on an X33 camera of the European Molecular Biology Laboratory (EMBL) at the DORIS III storage ring (DESY, Hamburg, Germany) using a standard procedure and a multichannel proportional delay-line detector. Synchrotron radiation was used because of its high intensity, which allowed us to measure the intensities with a good signal-to-noise ratio. Data of such quality cannot be obtained on laboratory apparatus equipped with conventional X-ray tubes because of the weak scattering power of the solutions of biomolecules. The intensity data were measured in the angular range $0.1 < s < 5$ nm^{-1}, where $s = 4\pi\sin\theta/\lambda$ (2θ is the scattering angle and $\lambda = 0.152$ nm is the radiation wavelength). To cover the above-mentioned angular range, the measurements were made at two different sample-detector distances (2.9 and 4 m). The complete scattering pattern was obtained by combining both data sets obtained. The angular calibration of the camera was carried out with the use of the collagen and tripalmitate standards. The detector was calibrated using a synchrotron beam from a ^{55}Fe-source.

The samples were placed in to 1-mm-thick cells with 20 μm thick mica windows. The measurements were made at 20°C. The results of 10–15 successful measurements made within 1 min each were combined and the data thus obtained were first normalized to the intensity of the incident beam and then statistically averaged and corrected for the detector sensitivity. After subtraction of scattering from the cell containing the pure solvent, the resulting curves were normalized to the solution concentrations.

Determination of the integrated parameter of the IgM and IgM-RF molecules in solution. The radii of gyration R_g were calculated based on the SAXS data in the Guinier approximation $I_{\exp}(s) = I(0)\exp(-s^2R_g^2/3)$ valid in the region $(sR_g) < 1.3$ [5] and also based on the distance distribution function $p(r) = r^2\gamma(r)$ calculated from the experimental data using the indirect inverse Fourier transforms program GNOM [18–19] according to the equation

$$\gamma(r) = \frac{1}{2\pi^2}\int_{s=0}^{\infty} s^2 I(s)\frac{\sin(sr)}{sr}ds. \qquad (1)$$

The $p(r)$ function was also used to determine the maximum sizes $D_{\max}$ of the dissolved molecules.

The molecular weights of the immunoglobulins were evaluated by extrapolating the small-angle scattering curves to the intensities observed at the zero scattering angle $I(0)$. The $I(s)$ values were normalized to the scattering from the solution of the reference protein, bovine albumin (Sigma USA). The accuracy of the determination of the molecular weights by the small-angle scattering method depends primarily on the accuracy of the measured solution concentrations. For immunoglobulins, the accuracy was 5–15%.

Modeling of low-resolution molecular structures based on small-angle scattering data. The intensities of scattering from the system of monodisperse particles in dilute solutions are proportional to the spherically averaged intensity of scattering by one particle [5]:

$$I(s) = \langle A^2(\mathbf{s})\rangle_\Omega = 4\pi\int_{r=0}^{\infty} r^2\langle\rho(\mathbf{r})\otimes\rho(\mathbf{r})\rangle_\omega\frac{\sin(sr)}{sr}dr, \qquad (2)$$

where $A(\mathbf{s})$ is the scattering amplitude, $\langle\cdot\rangle_\Omega$ and $\langle\cdot\rangle_\omega$ denote averaging over angles in the reciprocal and direct spaces, respectively, associated with random orientations of molecules in the solution, and $\otimes$ indicates the convolution operation. The three-dimensional model of the particle is described by the scattering distance distribution function $\rho(r)$. In the case of X-ray radiation, this function is proportional to the difference between the electron densities of the molecule and the solvent (contrast). It is seen from Eq. (2) that the structure function $\rho(r)$ cannot be reconstructed directly from the experimental data by the inverse Fourier transformation. However, one can calculate the scattering intensity $I(s)$ from any three-dimensional model structure, evaluate the difference between the scattering intensity from the model and the experimental intensities, and minimize this difference by varying the model parameters by the method of nonlinear optimization and, thus, reconstruct the three-dimensional scattering-density distribution. In our study, we used dummy atom modeling (bead model), which provides the reconstruction of the low-resolution structures of macromolecules in solution [5, 20]. The method is based on the representation of the particle structure by a set of small spheres (dummy atoms) arranged in space. The main advantage of this method is the absence of any limitations on the complexity of the particle structure. The immunoglobulin molecules were described by a one-phase model consisting of spheres with equal (unity) densities. In this approach, the absolute value of the density is of no importance. Thus, the small-angle scat-

tering intensity can be calculated by the following equation:

$$I(s) = 2\pi^2 \sum_{l=0}^{\infty} \sum_{m=-l}^{l} [A_{lm}(s)]^2, \quad (3)$$

where

$$A_{lm}(s) = i^l \sqrt{2/\pi} f(s) \sum_{j=1}^{N} j_l(sr_j) Y^*_{lm}(\Omega_j) \quad (4)$$

is the amplitude of scattering from the structure consisting of N spheres with the unity density, r_j and Ω_j are the polar coordinates, $f(s)$ is the amplitude of scattering from one sphere, $j_l(x)$ are spherical Bessel functions, and $Y_{lm}(\Omega)$ are the spherical harmonics.

To search for the spatial arrangement of the three-dimensional elements, the DAMMIN program was modified [21] for solving the nonlinear least-squares problem by global minimization based on the method of simulation of annealing. According to this method, the search is started based on a particular structural model consisting of spheres (usually, from two to five thousand spheres) randomly arranged at the knots of the closest packing in space. These knots are located within a bounded spherical region with a diameter equal to the maximum molecular size. The maximum size of the region is preliminarily determined based on the experimental data and the $p(r)$ function using the GNOM program. Each three-dimensional knots contains a sphere with the solvent density (0) or the protein density (1). The size of the spheres used had to be, on the one hand, sufficiently small so that the step of their packing had no substantial effect on the shape of the scattering curve in the angular range under study and, on the other hand, sufficiently large so that the number of spheres within the search area was not too large (generally, not more than 5000 spheres). The latter requirement is necessary for saving computer time. In the course of the search, the minimization program transforms the density of a randomly chosen sphere, i.e., changes the particle density (1) in to the solvent density (0) or vice versa. After each modification, the program calculates the SAXS intensity curve for the current structure and also the weighted total quadratic deviation from the experimental scattering curve constructed by M points:

$$\chi^2 = \sum_{j=1}^{M} [(I_{\text{exp}}(s_j) - I(s_j))/\sigma(s_j)]^2, \quad (5)$$

where $\sigma(s_j)$ is the estimated experimental error at the jth point. The above sum is complemented with the penalty functions which reflect the requirements of the structure continuity $w_D P_D$ and the absence of lone spheres $w_L P_L$ [21]. The weighting coefficients w_D and w_L were taken to be equal to 0.02 so that the contributions of χ^2 and penalty functions at the minimum of the functional $F = \chi^2 + w_D P_D + w_L P_L$ were approximately equal. The penalty function P_D is calculated as the ratio of the total number of spheres in the structure to the number of spheres in the largest domain formed by the atoms contacting each other. The P_L function is calculated according to the equation $P_L = 1 - \langle 1 - \exp(-N_e) + \exp(-12)\rangle_N$, where 12 is the maximum number of contacts of a sphere with its nearest neighbors, N_e is the actual number of contacts formed by this sphere in the structure, and $\langle\rangle_N$ is the number of contacts per one sphere averaged over the whole structure.

If the value of the target function F is lower than that obtained at the previous step ($\Delta = F_k - F_{k-1} < 0$, k is the number of the step), the structure is stored. The procedure of the annealing simulation consists in that, at each step, the structure characterized by the worst F value is taken to be (with a certain probability) the "best" structure. The probability is set by the "temperature" T; i.e., if $\Delta > 0$, the structure is stored with the probability $\exp(-\Delta/T)$. Upon each $100N$ steps (or $10N$ steps with $\Delta < 0$) the parameter T is reduced ($T_{k+1} = 0.9T_k$), which allows the program to store unreliable structures more and more rarely. The necessity of annealing procedure is associated with the fact that the target function F can have several local minima. The possibility of taking an erroneous step as the solution of the problem allows the program not to stop at the intermediate solutions. The final three-dimensional configuration of the spheres is treated as the true structural model of the molecule in solution. In the general case, it is impossible to estimate analytically the closeness of the final model to the global minimum, because the parameters of the structural model (coordinates of the centers of spheres) depend nonlinearly on the intensities (2). Therefore, the calculations for each scattering curve were performed independently several times.

If no additional requirements are imposed on the structural model, one can easily find numerous structures characterized by almost the same minimum deviation (5) but substantially different from one another. In some cases, the use of some additional information on the characteristic structural features allows one to increase the reliability of the structure reconstruction. In this study, such an additional requirement to the structure was the existence of a fivefold symmetry axis in the case of the IgM and IgM-RF molecules and a twofold symmetry axis in the case of the IgG molecule.

Procedure for calculations of SAXS intensities from atomic-resolution molecular structures. Only the crystal structures of the IgG molecule [4] (Brookhaven Protein Data Bank, codes 1IGY and 1IGT) and its fragments (1MCO and 2IG2) were established at the 2.8–4.0 Å resolution. The pentameric structure of immunoglobulin IgM consisting of 71 domains in solution was studied by Perkins *et al.* [22] based on the small-angle X-ray scattering data and was modeled with the use of a molecular graphics program. In [22], the scattering curves of IgM were compared with the curves calculated from the three-dimen-

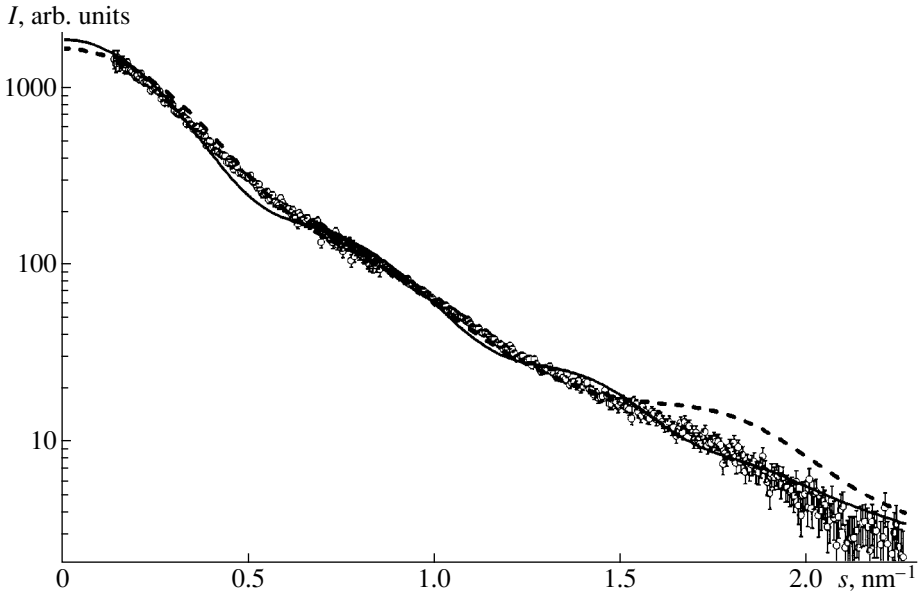

Fig. 1. Comparison of the experimental small-angle scattering curve from a solution of immunoglobulin IgG (with error bars) and curves calculated from the known high-resolution structures of IgG_{1k} (Mab61.1.3, structure code 1IGY; dashed curve) and IgG_{2ak} (Mab231, structure code 1IGT; solid curve).

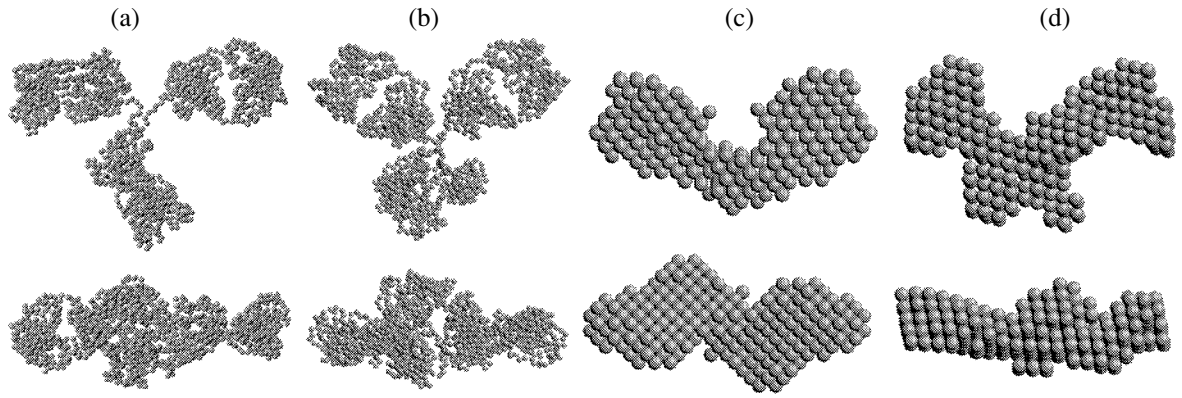

Fig. 2. Known crystallographic models of the (a) IgG_{2ak} (Mab231, structure code 1IGT) and (b) $IIgG_{1k}$ (Mab61.1.3, structure code 1IGY) molecules [4], (c) the structure reconstructed from the small-angle scattering data taking into account the twofold symmetry axis, and (d) the model reconstructed without allowance for additional symmetry. Each structure is shown in two mutually perpendicular orientations.

sional models constructed based on the published α-carbon coordinates of the fragments of an IgG molecule. The complete structure of the pentameric IgM molecule obtained under the assumption of the coplanar arrangement of the $F(ab)_2$ and $(Fc)_5$ fragments showed the best agreement with the experimental curves. Each IgG-like monomer of this pentameric structure consists of 14 domains formed by four polypeptide chains. The model of IgM was consistent with the hydrodynamic and sedimentation data [22].

The SAXS intensities obtained from the atomic structures were calculated using the CRYSOL program [23]. This program provides the computation of scattering curves based on the form factors of real atoms with due regard for scattering from the excluded volume and the outer hydration shell.

RESULTS AND DISCUSSION

Integrated structure parameters of immunoglobulins. According to the SAXS data, the average molecular weights of immunoglobulins determined for samples with different concentrations under different conditions of data collection (the camera lengths were 4 and 2.9 m) were 146 ± 10 kDa for IgG, 760 ± 40 kDa for IgM, and 690 ± 20 kDa for IgM-RF. According to

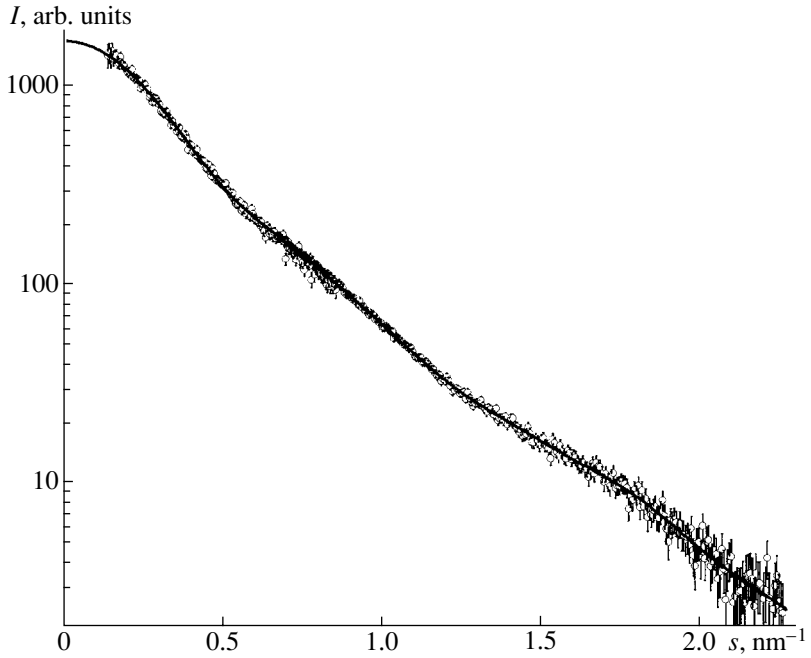

Fig. 3. Comparison of the experimental scattering data from an IgG solution (with error bars) with a typical scattering curve from the model structure (solid curve) calculated using the DAMMIN program (see Figs. 2c and 2d).

the published data, the molecular weights of IgG and IgM are 146 and 970 kDa, respectively [24]. Despite the substantial errors in the molecular weights determined, this parameter for rheumatoid factor is systematically lower than that for IgM. The underestimated molecular weights are also indicative of the absence of noticeable aggregation of molecules in solution. The radii of gyration calculated from the experimental curves reflect the same tendency, namely, the molecule of rheumatoid factor is smaller than IgM. The maximum sizes of the molecules D_{max} calculated by the GNOM program are 17, 37, and 36 nm for IgG, IgM, and IgM-RF, respectively. The average radii of gyration R_g under the above-mentioned conditions are 5.9 ± 0.1, 11.4 ± 0.6, and 10.9 ± 0.4 nm for IgG, IgM, and IgM-RF, respectively. According to the published data, the average radii R_g are 12.17 ± 0.34 nm [22], 12.0 and 12.1 nm [25] for IgM, and 5.84 ± 0.4 nm for IgG [26].

Solution structure of IgG. The IgG molecules have structures typical of antibodies and consist of four polypeptide chains, namely, two identical light chains and two identical heavy chains (with varying and constant regions), which form altogether 12 domains and comprise two Fab regions and one Fc region [22, 24]. The flexibility inherent in immunoglobulins can give rise to a broad spectrum of molecular conformations. According to the crystallographic data [4], the IgG molecule in the crystal can adopt both symmetric and asymmetric *T* and *Y* conformations. In solution, antibodies can have conformations intermediate between these main conformations. The SAXS curves from an IgG solution and the scattering curves calculated for the crystal structures of IgG_{1k} (Mab61.1.3, structure code 1IGY) and IgG_{2ak} (Mab231, structure code 1IGT) [3] are shown in Fig. 1. The χ value for 1IGY (2.1) is lower than that for I1GT (2.8). Hence, it can be assumed that, on the average, the shape of the IgG molecules in solution is closer to the *Y* conformation.

To test this assumption, the shape of the IgG particles was determined from the experimental scattering data using the DAMMIN program [14]. The maximum size (D_{max}) of the IgG macromolecules, which was evaluated from the distance-distribution function $p(r)$, was 17 nm. To estimate the stability of the problem solution, the protein structure was reconstructed several times. The shape of IgG in solution was reconstructed using an arbitrarily located twofold symmetry axis. One of the typical models reconstructed from the small-angle scattering data and the crystallographic model in two mutually perpendicular orientations are shown in Fig. 2. For comparison, the shape of IgG reconstructed without imposing any restrictions on the particle anisometry is also shown in Fig. 2. Fitting of the model scattering curves to the experimental data is illustrated by Fig. 3.

The reconstructed structures, including the model obtained without any restrictions on the symmetry of macromolecules, have larger linear dimensions that the dimension of the atomic model of 1IGY (17 and 14.7 nm, respectively). With due regard for the correction for the thickness of the hydration shell (0.3 nm), the determined dimension corresponds to the maximum distance in the 1IGT structure (16.4 nm). Hence, it can be assumed that the IgG molecules in solution have a

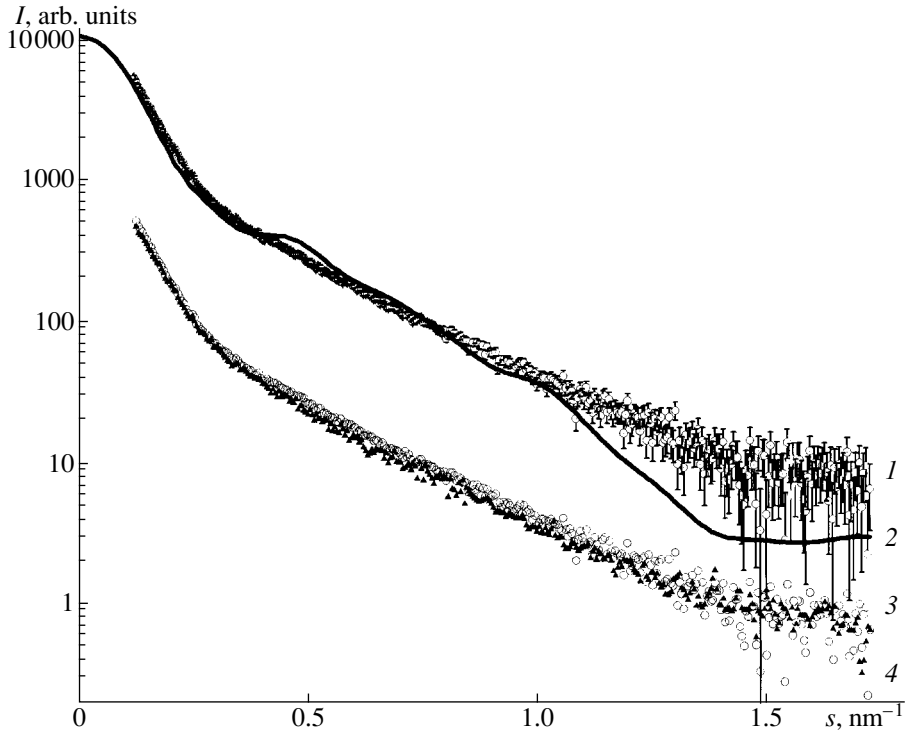

Fig. 4. Comparison of the experimental small-angle scattering curve from an IgM solution (*1*, with error bars) with the intensities calculated using the CRYSOL program from the atomic model of IgM proposed in [22] (*2*, solid curve). Comparison of the normalized experimental scattering curves from solutions of IgM (*3*, circles) and IgM-RF (*4*, solid triangles). For clarity, the pairs of curves (*1* and *2*) and (*3* and *4*) are shifted in the vertical direction.

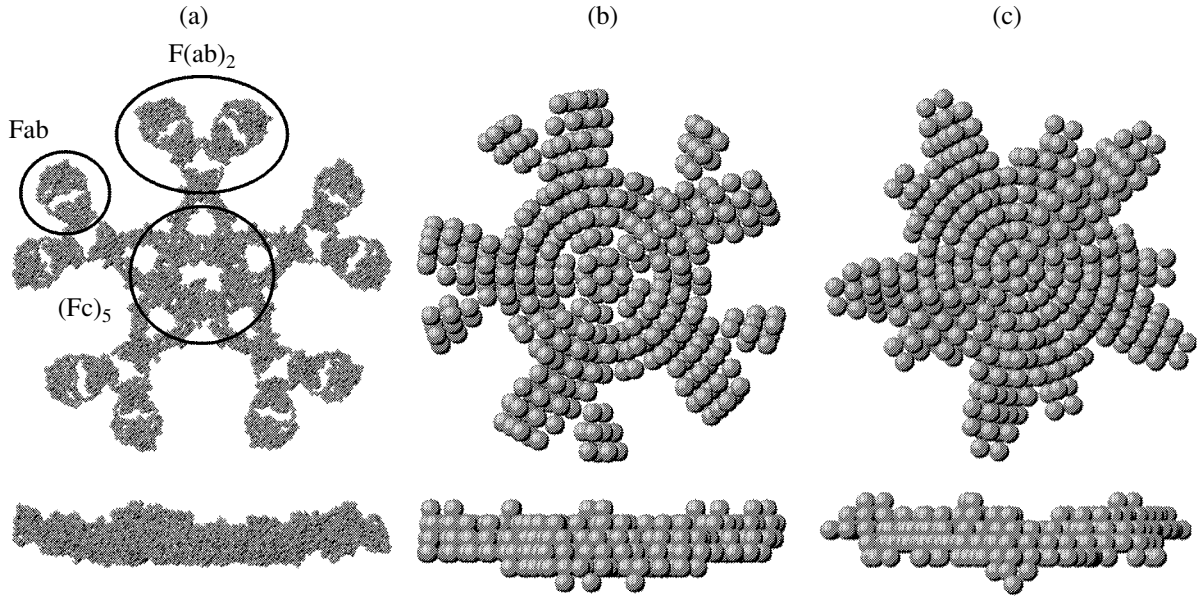

Fig. 5. Comparison of (a) the atomic structure of the IgM molecule proposed in [22] with two typical structures obtained using of the DAMMIN program, namely, the (b) IgM and (c) IgM-RF models. Each structure is shown in two mutually perpendicular orientations.

"wider" conformation than the conformation of 1IGY. In turn, the *V*-shaped models found using the DAMMIN program differ from the shape of 1IGT and are closer to the *Y* conformation. The scattering from the dummy-atom models obtained in this study is consistent with the experimental data without systematic deviations with $\chi = 0.8 \pm 0.1$ (Fig. 3). The experimental curve is smoother than the theoretical scattering profiles calcu-

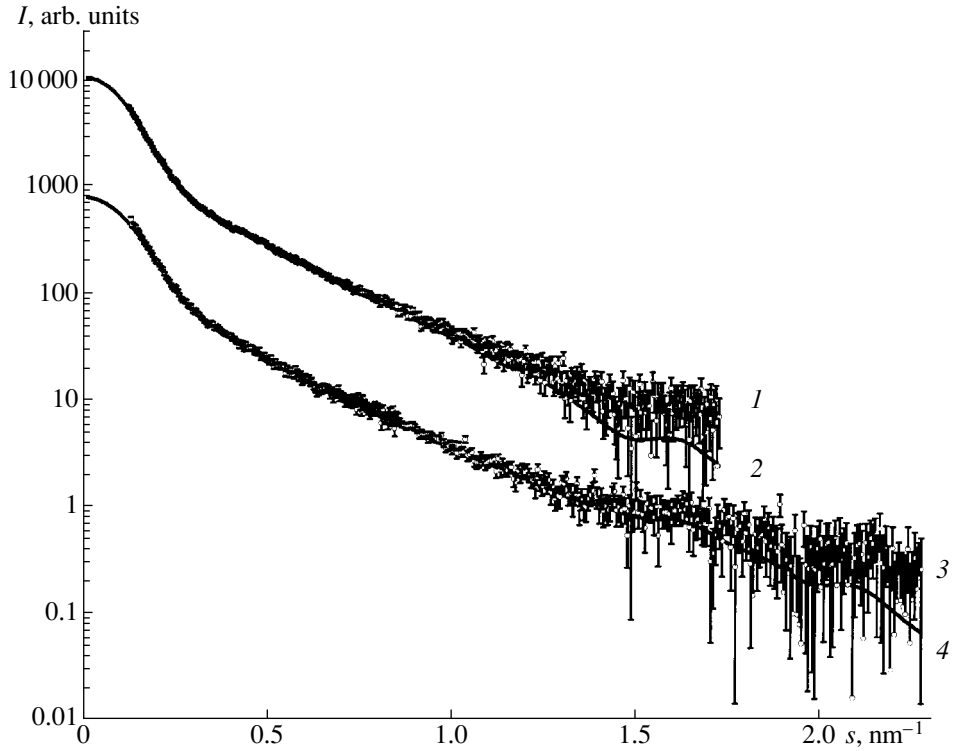

Fig. 6. Comparison of (*1*) the experimental scattering data from an IgM solution (with error bars) with (*2*) the typical scattering curve from the model structure (solid curve) calculated using the DAMMIN program (see Fig. 5b). Analogous comparison for the curves for the structure of IgM-RF (curves *3* and *4*). For clarity, the pair of the curves (*1* and *2*) and the pair of the curves (*3* and *4*) are shifted in the vertical direction.

lated for the atomic structures, which is attributed to the fact that the solutions can simultaneously include molecules adopting various conformations.

Solution structure of IgM. Figure 4 presents the experimental scattering curves from IgM in solution and the theoretical scattering curves calculated from the symmetric pentameric atomic model of IgM [22] (the data were kindly provided by S. Perkins) using the CRYSOL program as was described above. The general scheme of the IgM molecule formed by five IgG-like regions is shown in Fig. 5a. In the small-angle region (s is up to 1 nm^{-1}), the calculated data are in the satisfactory agreement with the experimental data. A substantial discrepancy observed at high angles is associated with scattering from the inner structure of the particle in the symmetric model. The symmetry of the molecule in solution can be changed because of its flexibility, and the experimental scattering curve becomes more monotonic because of averaging.

One of the typical reconstructions of the symmetric IgM structure based on the small-angle scattering data by the DAMMIN program is shown in Fig. 5b. On the whole, the IgM model found under the minimum assumptions about the structure agrees satisfactorily with the model proposed by S. Perkins.

Solution structure of IgM-RF. Similar calculations were performed based on the scattering from IgM-RF. The maximum size of a molecule of the rheumatoid factor in solution determined from the profile of the size-distribution function was less (36 nm) than that of IgM (37 nm). As can be seen from Fig. 4, the scattering curves of an the IgM(*3*) solution differ only slightly from the curve of an IgM-RF(*4*) solution. One of IgM-RF structures reconstructed as was described above is shown in Fig. 5c. The curves obtained by fitting the scattering curves from the models to the experimental data are presented in Fig. 6.

In all the reconstructed structures, the $F(ab)_2$ regions of the molecule appear to be asymmetric, namely, one of the Fab fragments in each pair has a reduced volume. This is consistent with the lower molecular weight and smaller size of IgM-RF compared to the corresponding parameters of IgM and is in agreement with the earlier assumption that the Fab regions in the molecule of the rheumatoid factor have different structures and functions [27]. The difference in the Fab regions of monoclonal immunoglobulin IgM and the rheumatoid factor IgM has been found earlier by the method of differential scanning microcalorimetry [28]. The comparison of the parameters of thermal denaturation of the Fab and $(Fc)_5$ fragments of IgM and IgM-RF led to the conclusion that the $(Fc)_5$ fragments of both proteins are thermodynamically similar, whereas the characters of inter-

actions between the domains in their Fab fragments are different.

CONCLUSIONS

To summarize, the reconstruction of the molecular shape from small-angle X-ray scattering data demonstrated that the solution structure of rheumatoid factor IgM-RF differs from that of IgM by the asymmetry of the $F(ab)_2$ regions and a lower molecular weight. The shape of the IgG molecules in solution is close to the *Y*-type structure but is characterized by a wider conformation.

ACKNOWLEDGMENTS

This study was supported by the Russian Foundation for Basic Research (project no. 01-02-17040) and INTAS (project no. 00-243).

REFERENCES

1. M. W. Turner, in *Structure and Functions of Antibodies*, Ed. by L. E. Glynn and M. W. Steward (Wiley, Chichester, 1981; Mir, Moscow, 1983).
2. L. J. Harris, S. B. Larson, K. W. Hasel, *et al.*, Nature **360**, 369 (1992).
3. L. J. Harris, E. Skaletsky, and A. McPherson, J. Mol. Biol. **275**, 861 (1998).
4. L. J. Harris, S. B. Larson, and A. McPherson, Adv. Immunol. **72**, 191 (1998).
5. D. I. Svergun and L. A. Feĭgin, *Small-Angle X-ray and Neutron Scattering* (Nauka, Moscow, 1987).
6. J. Ninio, V. Luzatti, and M. Yaniv, J. Mol. Biol. **71**, 217 (1972).
7. M. Y. Pavlov and B. A. Fedorov, Biopolymers **22**, 1507 (1983).
8. G. Grossmann, Z. H. L. Abraham, E. T. Adman, *et al.*, Biochemistry **32**, 7360 (1993).
9. D. I. Svergun, C. Barberato, M. H. Koch, *et al.*, Proteins **27**, 110 (1997).
10. A. E. Aleshin, M. Malfois, X. Liu, *et al.*, Biochemistry **38**, 8359 (1999).
11. D. I. Svergun, M. V. Petoukhov, M. H. J. Koch, *et al.*, J. Biol. Chem. **275**, 297 (2000).
12. I. K. Feil, M. Malfois, J. Hendle, *et al.*, J. Biol. Chem. **276**, 12024 (2001).
13. V. A. Lapuk, N. M. Khatiashvili, A. I. Chukhrova, and E. D. Kaverzneva, Biokhimiya **50**, 237 (1985).
14. V. A. Lapuk, A. I. Chukhrova, E. V. Chernokhvostova, *et al.*, Biokhimiya **57**, 617 (1992).
15. M. H. J. Koch and J. Bordas, Nucl. Instrum. Methods **208**, 461 (1983).
16. C. Boulin, R. Kempf, M. H. J. Koch, and S. M. McLaughlin, Nucl. Instrum. Methods Phys. Res. A **249**, 399 (1986).
17. C. Boulin, R. Kempf, A. Gabriel, and M. H. J. Koch, Nucl. Instrum. Methods Phys. Res. A **269**, 312 (1988).
18. D. I. Svergun, A. V. Semenyuk, and L. A. Feigin, Acta Crystallogr., Sect. A: Found. Crystallogr. **24**, 244 (1988).
19. D. I. Svergun, J. Appl. Crystallogr. **25**, 495 (1992).
20. Yu. A. Rol'bin, R. L. Kayushina, L. A. Feĭgin, and B. M. Shchedrin, Kristallografiya **18** (4), 701 (1973) [Sov. Phys. Crystallogr. **18**, 442 (1973)].
21. D. I. Svergun, Biophys. J. **76** (6), 2879 (1999).
22. S. J. Perkins, A. S. Nealis, B. J. Sutton, and A. Feinstein, J. Mol. Biol. **221**, 1345 (1991).
23. D. I. Svergun, C. Barberato, and M. H. J. Koch, J. Appl. Crystallogr. **28**, 768 (1995).
24. I. Roitt, J. Brostoff, and D. Male, *Immunology* (Mosby, London, 1998; Mir, Moscow, 2000).
25. P. Wilhelm, I. Pilz, K. Goral, and W. Palm, Int. J. Biol. Macromol. **2**, 13 (1980).
26. I. Pilz, E. Schwarz, and W. Palm, Eur. J. Biochem. **75**, 195 (1977).
27. V. A. Lapuk, V. Ya. Chernyak, and N. N. Magretova, Biokhimiya **61**, 61 (1996).
28. I. I. Protasevich, B. Ranjbar, E. Yu. Varlamova, *et al.*, Biokhimiya **62**, 1066 (1997).

Translated by T. Safonova